Max-Planck-Institut für Meteorologie
*Max Planck Institute for Meteorology*

# Simulation of the climate impact of Mt. Pinatubo eruption using ECHAM5

Manu Anna Thomas

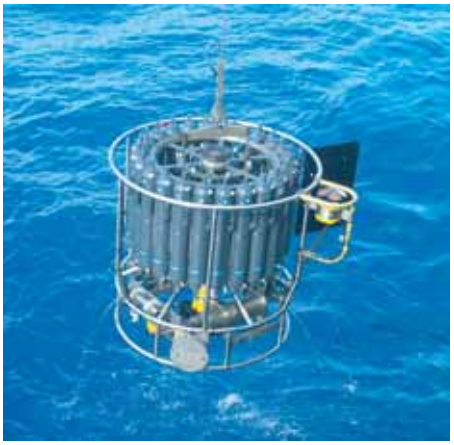

Berichte zur Erdsystemforschung 52/2008

*Reports on Earth System Science*

## Hinweis

Die Berichte zur Erdsystemforschung werden vom Max-Planck-Institut für Meteorologie in Hamburg in unregelmäßiger Abfolge herausgegeben.

Sie enthalten wissenschaftliche und technische Beiträge, inklusive Dissertationen.

Die Beiträge geben nicht notwendigerweise die Auffassung des Instituts wieder.

Die "Berichte zur Erdsystemforschung" führen die vorherigen Reihen "Reports" und "Examensarbeiten" weiter.

## *Notice*

*The Reports on Earth System Science are published by the Max Planck Institute for Meteorology in Hamburg. They appear in irregular intervals.*

*They contain scientific and technical contributions, including Ph. D. theses.*

*The Reports do not necessarily reflect the opinion of the Institute.*

*The "Reports on Earth System Science" continue the former "Reports" and "Examensarbeiten" of the Max Planck Institute.*

## Anschrift / Address

Max-Planck-Institut für Meteorologie
Bundesstrasse 53
20146 Hamburg
Deutschland

Tel.: +49-(0)40-4 11 73-0
Fax: +49-(0)40-4 11 73-298
Web: www.mpimet.mpg.de

## Layout:

Bettina Diallo, PR & Grafik

Titelfotos:
vorne:
Christian Klepp - Jochem Marotzke - Christian Klepp
hinten:
Clotilde Dubois - Christian Klepp - Katsumasa Tanaka

Berichte zur Erdsystemforschung 52/2008

# Simulation of the climate impact of Mt. Pinatubo eruption using ECHAM5

Dissertation zur Erlangung des Doktorgrades der Naturwissenschaften
im Departement Geowissenschaften der Universität Hamburg
vorgelegt von

Manu Anna Thomas
aus Kottayam, Indien

Hamburg 2008

*Reports on Earth System Science* 52/2008

ISSN 1614-1199

Manu Anna Thomas
Max-Planck-Institut für Meteorologie
Bundesstrasse 53
20146 Hamburg
Germany

Als Dissertation angenommen
vom Departement Geowissenschaften der Universität Hamburg

auf Grund der Gutachten von
Prof. Dr. Guy Brasseur
und
Dr. Claudia Timmreck

Hamburg, den 22. Januar 2008
Prof. Dr. Kay-Christian Emeis
Leiter des Departements für Geowissenschaften

ISSN 1614-1199

# Simulation of the climate impact of Mt. Pinatubo eruption using ECHAM5

Lower stratospheric temperature anomaly at 30 hPa (K)

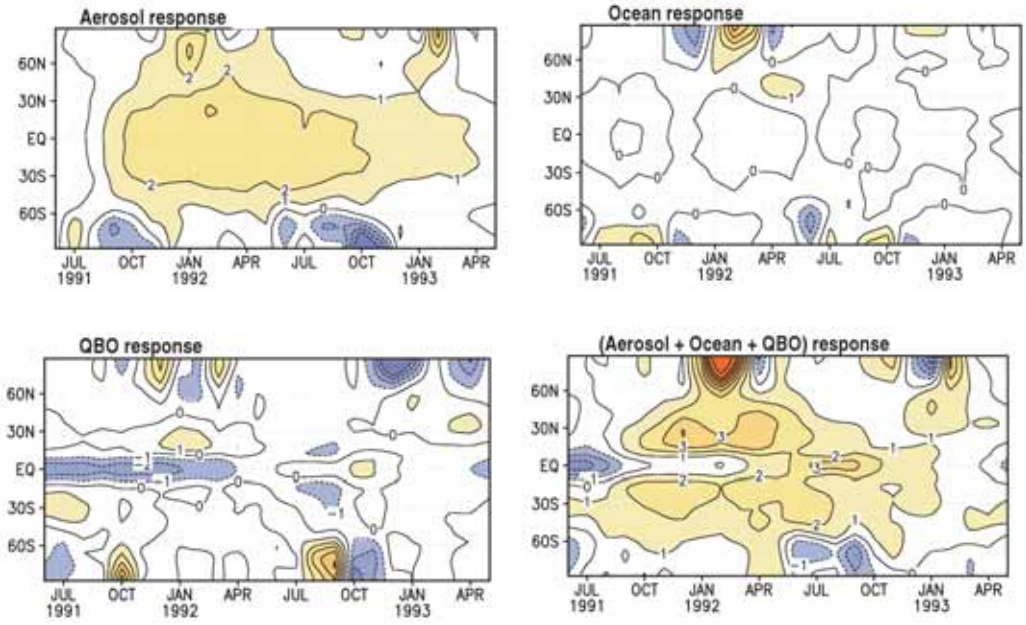


Manu Anna Thomas

Hamburg 2008

# Contents

# Abstract

Large volcanic eruptions provide an excellent opportunity to study the response of the climate system to a global radiative perturbation and to test the climate models to assess this response. The eruption of Mt. Pinatubo in Philippines in June 1991 was one of the strongest volcanic eruptions in the recent history. In this study, most comprehensive simulations to date of climate impact of Mt. Pinatubo eruption are carried out with prescribed volcanic aerosols including observed SSTs, QBO and volcanically induced ozone anomalies (a) to analyze individual and combined response of these boundary conditions to volcanic forcing and (b) to assess sensitivity of climate response to the change of QBO phase using the middle atmosphere version of ECHAM5. ECHAM5.3 was overestimating the SW heating rate anomalies and hence, the lower stratospheric temperature response in the simulations with Pinatubo aerosols. Hence, few improvements are made in the radiative transfer parameterization scheme of ECHAM5 to include the effects of multiple reflection and the aerosol gas interactions in case of high volcanic aerosol loadings. Both these effects contradict one another and the dominance of either of them depends on the aerosol optical properties and their concentration. In this study, the multiple reflection effect overrides the aerosol-gas interaction effect since the sulfate aerosols are mostly scattering in the solar spectrum.

In order to understand the individual and combined, radiative and dynamical responses of observed SSTs and QBO to volcanic forcing, the climate response of Mt. Pinatubo eruption is evaluated under varying boundary conditions, including one at a time. Among all these experiments, it is seen that the experiment that includes the most realistic set up (with observed SST, QBO and ozone anomalies) with the volcanic forcing simulates the climate impact most realistically. The analysis shows that the pure lower stratospheric tropical aerosol responses are insensitive to the boundary conditions. The pure El Niño-related stratospheric temperature anomalies exhibit tropical cooling and subtropical warming and the pure QBO-related temperature anomalies show a cooling during the easterly QBO and warming during the westerly QBO phase. The pure effects of El Niño and QBO is known from other studies and are realistically simulated in this study too. The QBO-related 30 hPa geopotential height anomalies show a strengthening of the polar vortex during the westerly phase of the QBO and vice versa. The magnitude and pattern of the anomalously strong polar vortex is more or less captured in the second winter in the combined responses of volcanic forcing with QBO and observed SST+QBO. However, the polar vortex is disturbed during the first winters and this is due to the enhanced wave propagation during El Niño winters. The dynamical response manifested as the "volcanic winter pattern" is not simulated in either of the individual or combined mean responses, although 30% of the ensemble members do show the dynamical response. The results also show that the ocean response in the surface temperature anomalies in the two winters are so strong that it masks the effects due to volcanoes in the model. Apart from this, inconsistencies are seen

in the planetary wave propagation characteristics in the model climatology in comparison with ERA40 climatology. The results show that the vertical wave activity flux values of the stationary waves at 200 hPa are 48% less in the model climatology than in the ERA40 climatology.

Further, the climate response to Mt. Pinatubo eruption is investigated, if the eruption had occurred in the opposite phase of the QBO. Mt. Pinatubo erupted during the easterly QBO phase and the phase change occurred 14 months after the eruption. Here, the winds in the model are forced by the opposite QBO phase. The results show that the QBO-related lower stratospheric temperature responses are simulated realistically depending on the QBO phase encountered. The polar vortex is disturbed in the first winter irrespective of the QBO phase due to the increased vertical wave activity during El Ni$\tilde{n}$o winters. The simulated "volcanic winter pattern" for the first winter following the eruption is independent of the QBO phase as the El Ni$\tilde{n}$o effects modulate the response and override the effects due to the change of phase of QBO. Finally, all these results highlight the degree of efficiency of ECHAM5.4 in simulating such large perturbations, although the simulation of the dynamical response still remains a major challenge.

# Chapter 1

# Introduction and motivation

## 1.1 Introducing large volcanic eruptions

Large volcanic eruptions cause short term climate changes and contribute to natural climate variability (e.g. *Robock* [2000]; *Zielinski* [2000]). For instance, average global surface temperatures dropped about half a degree Celsius after the eruption of Mt. Pinatubo (*Jones and Briffa* [1992]). Very cold temperatures in the summer of 1816 following the Tambora eruption resulted in crop failures and famine in North America and Europe. This year was known as the "year without summer" (*Stommel and Stommel* [1983]; *Robock* [1994]). The 1883 Krakatoa eruption produced erratic weather events and proxy records show that the NH [1] temperatures were lowered by as much as $0.7^oC$ (*Robock* [2005]). These explosive volcanic eruptions affect the global climate system. This is explained schematically in Figure 1.1. Massive volcanic eruptions can inject significant amounts of gases such as water vapor, $CO_2$, $SO_2$, HCl, HF and particulate matter into the stratosphere (*Textor et al.* [2003]). The particulate matter mainly consists of silicate particles and hence, is removed from the atmosphere by gravitational sedimentation on time scales of minutes to a few weeks. HCl and HF are efficiently removed from the atmosphere by dissolution in liquid water (*Robock* [2000]; *Textor et al.* [2003]). $SO_2$ and $H_2S$ are less soluble in water and hence the resident time is much longer. Sulfate aerosols are produced when $SO_2$ is chemically transformed into $H_2SO_4$ on a time scale of weeks. These sulfate particles spread globally depending upon the latitude, altitude and time of the year of the volcanic eruption (*Strong* [1984]; *Stowe et al.* [1992]). They affect the Earth's radiative balance and disturb the stratospheric chemical equilibrium.

Volcanic eruptions can alter the climate of the Earth both directly and indirectly, for both short and long periods of time. The sulfate aerosols are purely scatterers in the visible part of the solar spectrum, thus scattering the incoming radiation partially back to space,

[1] NH: Northern Hemisphere

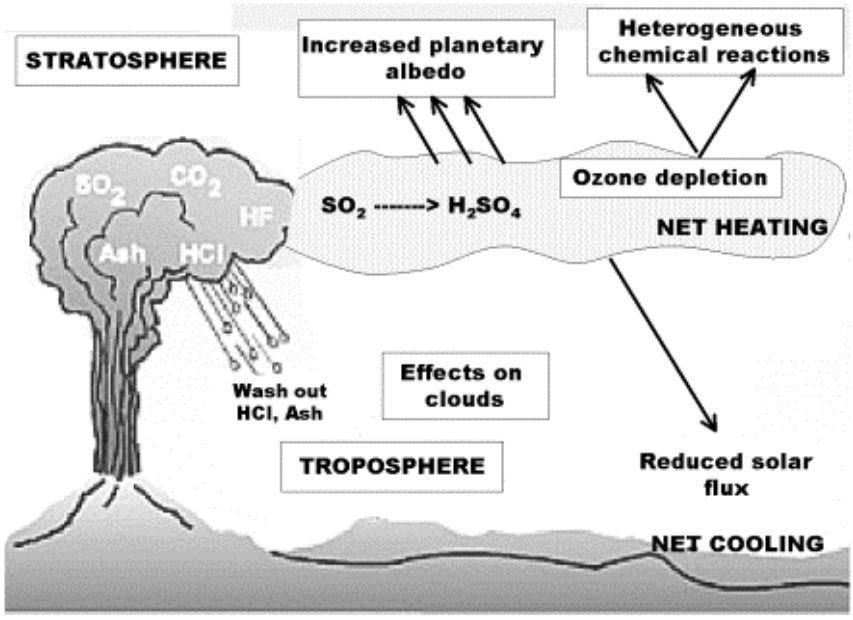


Figure 1.1: Schematic of the volcanic inputs to the atmosphere and their effects.

leading to a cooling of the Earth's surface. They are also good absorbers in the near infrared (near IR) and in the infrared region (IR), thus, warming the aerosol containing layers significantly.

Volcanic aerosols have the potential to change not only the radiative flux in the stratosphere, but also the chemistry. Sulfate aerosols produced by volcanic eruptions can trigger ozone depletion in the stratosphere through heterogeneous chemical reactions (*Crutzen* [1976]; *Tie and Brasseur* [1995]; *Tie et al.* [1996]). This lowers absorption of ultraviolet radiation and reduces the radiative heating in the lower stratosphere, but, the net effect is still heating.

Furthermore, the sulfate aerosols fall into the accumulation mode of the aerosol-size distribution spectrum and hence can act as cloud condensation nuclei, thus modifying the microphysical properties of clouds (*Menon and Saxena* [1998]; *Menon et al.* [2002]; *Lohmann et al.* [2003]). The prominent dynamical impact of large tropical volcanic eruptions is the "winter warming" phenomenon (substantial warming of the NH continents and cooling over the Middle east and Greenland in winter) in the Northern Hemisphere associated with the enhancement of the northern polar vortex for two boreal winters following a tropical eruption.

Aerosols injected into the stratosphere cause a rapid cooling of the lower atmosphere and hence can lead to changes in ocean heat content and sea level. It is estimated that large volcanic eruptions result in rapid reductions in ocean heat content and global mean sea level (*Gregory et al.* [2004]; *Church et al.* [2005]; *Gleckler et al.* [2006]) because of the

net reduction of solar flux at the ocean surface. The recovery to pre-eruption levels can take up to decades, depending upon the intensity of the volcanic eruption.

They can also cause substantial perturbations to the global carbon cycle, particularly its terrestrial component. Sulfate particles and ash from the eruption reduce the sunlight reaching the surface, making the radiation less direct and more diffuse. Additionally, they can result in a reduction in the growth rate of carbon-dioxide levels globally (*Gu et al.* [2003]). This is due to the fact that plants photosynthesize more efficiently in diffuse sunlight, thereby taking in more carbon-dioxide out of the air (*Gu et al.* [2003], *Farquhar and Roderick* [2003]), particularly in the tropics. The opposite is observed in the mid-latitudes due to the unavailability of both diffuse and direct solar radiation after volcanic eruptions. Understanding how volcanoes affect the global carbon cycle can lead to valuable insights into the dynamics of atmospheric $CO_2$ concentration and its relation to climate. How strong the climate impact of large volcanic eruptions will be, depends upon several factors such as the $SO_2$ emission, geographical location of the eruption, injection height, duration of the eruption and season of the year.

Large explosive volcanic eruptions with VEI [2](VEI ranges from 0-8) of 7 or 8, (such as the Toba eruption about 75,000 years ago) alter the landscape considerably and can severely impact the global climate for decades (*Self* [2006]). Some first attempts have been made to assess the climatic response of such huge volcanic eruptions. *Timmreck and Graf* [2006] used an atmospheric model with $SO_2$ gas input 100 times larger than that of the Mt. Pinatubo eruption, located at Yellowstone. They found that the season of injection is important, with a global spread of the aerosol cloud in NH summer and the all-sky net radiative flux was as low as -32 $W/m^2$ at the surface. Model simulations in response to the Toba eruption (*Jones et al.* [2005]) indicate severe short term cooling with global surface temperatures reduced by up to $10^oC$.

Considering these large perturbations to climate over a relatively short period of time, accurate and realistic simulations of these effects can serve as important guidelines for understanding anthropogenic influences on climate such as the effects of increasing greenhouse gases, aerosols in the stratosphere and ozone depleting chemicals. Studying the climatic responses would also help us to evaluate the important radiative and dynamical processes that respond to both natural and anthropogenic forcings. Furthermore, modeling the effects of volcanic eruptions would facilitate us to improve the climate models.

In this study we will concentrate on the Mt. Pinatubo eruption as it was the best observed large volcanic eruption that ever happened. The following sections give a general overview of this eruption.

[2]VEI: Volcanic Explosivity Index: a measure to describe the magnitude of explosive volcanic eruptions.

## 1.2 The Mt. Pinatubo eruption and its climatic impact

Mount Pinatubo volcano on Luzon Island in the Philippines (15.1N; 120.4E) erupted on June 15, 1991 injecting about 17 Mt of $SO_2$ into the stratosphere (*Bluth et al.* [1992]). SAGE II [3] satellite measurements showed that the Pinatubo aerosols in the tropics reached as high as 30 km altitude with most of the cloud between 20 and 25 km and the optically thick portion covered the latitudes from 10S to 30N (*McCormick and Veiga* [1992]; *Long and Stowe* [1994]). The volcanic aerosol encircled the Earth in 21 days due to the easterly winds prevailing at this time in the tropical stratosphere. It covered about 42% of the Earth's surface area after two months (*Stowe et al.* [1992]) straddling the equator extending from 15N to 15S. The SAGE II optical depths of this eruption in figure 1.2 shows the spread and evolution of aerosols after a month.

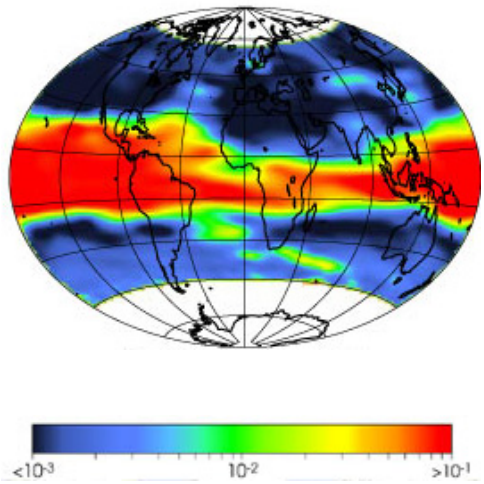


Figure 1.2: Integrated SAGE II stratospheric optical depth at wavelength 1020 nm one month after the Mt. Pinatubo eruption. Increasing values from blue to red (Image by Pat Mc Cormick, Langley Research Center).

These aerosol particles are relatively long lived in the stratosphere. The estimated e-folding residence time in mid-latitudes is about one year and between one and two years in the tropical latitudes (*McCormick et al.* [1978]; *Yue et al.* [1991]). This was the largest volcanic eruption of the last century with a VEI of 6. The availability of satellite borne sensors (TOMS [4], MLS [5] and SAGE II) provided useful information and this is the only eruption of this scale that is well documented so far. This huge eruption that affected the weather around the whole globe inspired scientists to look into the possible relations between volcanic eruptions and the Earth's atmosphere and to understand the microphysical, chemical and radiative properties of sulfate aerosols (*Hervig et al.* [1993]; *Grant et al.* [1994];

[3]SAGE: Stratospheric Aerosol Gas Experiment
[4]TOMS: Total Ozone Mapping Spectrometer
[5]MLS: Microwave Limb Sounder

*Lambert et al.* [1997]). Since then, there has been numerous studies, both observational and modeling (e.g. *Graf et al.* [1993]; *Stenchikov et al.* [1998]; *Timmreck et al.* [1999]; *Yang and Schlesinger* [2002]; *Soden et al.* [2002]; *Robock* [2005]), investigating the climate impact of Mt. Pinatubo eruption. Much of the literature refers to the progress in the understanding of atmospheric chemistry, dynamics and in climate modeling. The following subsections briefly describe the observed radiative, dynamical and chemical responses of Mt. Pinatubo eruption.

### 1.2.1 Radiative forcing

Radiative forcing is a commonly used metric to evaluate the change in solar irradiance in the Earth-atmosphere system due to an external perturbation. Here, in this study, aerosol radiative forcing is interpreted as the change in the net fluxes and radiative heating rates due to aerosols. As mentioned in the introduction, volcanic aerosols scatter visible radiation, reflect and absorb in the near-infrared bands and absorb and emit thermal radiation rendering significant radiative forcing of the climate system. Global pyrheliometer observations at the surface indicated a net reduction of solar fluxes for more than a year which caused a global surface cooling of 0.5 K (*Dutton and Christy* [1992]). The global mean forcing at the top of the atmosphere was -3 $Wm^{-2}$ for August/September 1991 determined using ERBE [6] radiometer data and this was the first direct measurements of large scale volcanic forcing (*Minnis et al.* [1993]). *Hansen et al.* [1992] predicted a net global radiative loss of the Earth-atmosphere system, peaking at about 4.5 $Wm^{-2}$ in late 1992. The radiative forcing using prescribed aerosol optical depth was simulated by many general circulation models and it was shown that the maximum aerosol radiative forcing amounts to -6 $Wm^{-2}$ at the surface (*Stenchikov et al.* [1998]; *Timmreck et al.* [1999]; *Kirchner et al.* [1999]). The net aerosol heating rate of 0.2 - 0.3 K/day was computed in the thickest portion of the aerosol cloud in August 1991 (*Kinne et al.* [1992]; *Pitari* [1993]).

### 1.2.2 Atmospheric response

Observations have shown that following Mt. Pinatubo eruption, the stratosphere temperature anomaly peaked as high as 2.5 K. Several modeling studies have shown that volcanically induced ozone anomalies and the QBO effects cools the stratosphere considerably, which otherwise would have been around 4 K (*Kirchner et al.* [1999]; *Stenchikov et al.* [2002]). The absorption of solar near IR radiation contributes significantly to the stratospheric heating (*Stenchikov et al.* [1998]). *Kirchner et al.* [1999] pointed out that aerosol radiative forcing, stratospheric thermal response and summer tropospheric cooling do not depend significantly on the type of SST, climatological or observed, used as boundary conditions. *Timmreck*

[6] ERBE: Earth Radiation Budget Experiment

*et al.* [1999] performed interactive and non-interactive simulations with aerosols and chemistry using the MAECHAM4 model and showed that an interactive coupling of the aerosol with the radiation scheme is necessary to adequately describe the observed transport characteristics over the first months of the eruption.

The Mauna Loa observatory measurements of downward direct and diffuse radiation indicated that the reduction in direct downward shortwave radiation was almost matched by an enhancement of the downward diffuse flux at this latitude (*Dutton and Christy* [1992]; *Robock* [2000]). Climate records showed that this eruption was followed by a $0.5^oC$ decrease in mean global temperatures (*Hansen et al.* [1996]), a 33% increase in diffuse radiation and a 3% decrease in global solar radiation. The rate of increase of atmospheric carbon-dioxide concentration after Mt. Pinatubo eruption was about half the average rate ( 0.72 ppm/year) and this reduction has been attributed to an increase in the net ecosystem productivity of the terrestrial biosphere due to an increase in the fraction of diffuse radiation (*Sarmiento* [1993]).

### 1.2.3 Ocean response

For Mt. Pinatubo eruption, a reduction of about $3x10^{22}$ J in global ocean heat content and a global mean sea level fall of 5 mm and a decrease in evaporation of up to 0.1 mm/day were estimated (*Church et al.* [2005]). Though the solar net flux reduction owing to the eruption had recovered to the pre-eruption values within a span of up to 3 years, the recovery period for the global ocean heat content and global mean sea level is relatively slow (*Church et al.* [2005]). *Gleckler et al.* [2006] carried out coupled ocean atmosphere simulations with and without volcanic forcing and it was seen that the simulated heat content with volcanic forcing is in closer agreement with observations with an abrupt drop in the heat content after the 1883 Krakatoa eruption. The recovery owing to 1991 Pinatubo eruption was more rapid due to its smaller amplitude and anthropogenic influences than after the recovery after 1883 Krakatoa eruption. *Delworth et al.* [2005] using a global coupled ocean atmosphere model conducted experiments independently with anthropogenic aerosol forcing, natural (volcanic and solar) forcing and well mixed greenhouse gases. They show that the natural and anthropogenic aerosols have substantially delayed and reduced the total amount of global ocean warming and hence, sea level rise that would have risen purely in response to increasing greenhouse gases. The anthropogenic aerosols and the effects of volcanic aerosols reduced the simulated ocean warming by approximately two-thirds (*Brasseur and Roeckner* [2005]).

### 1.2.4 Dynamic response

As mentioned in section 1.1, a noticeable climatic impact of explosive tropical volcanic eruptions is the "winter warming" phenomenon in the Northern Hemispheric winter that

has been observed for two winters following Pinatubo eruption. This effect is referred to as the positive phase of the AO [7] which is associated with the enhancement of the north polar vortex and thus strengthening the signal in the troposphere (e.g. *Graf et al.* [1993]; *Labitzke* [1994]; *Robock and Mao* [1995]; *Thompson and Wallace* [1998]). The Arctic Oscillation is the dominant mode of interannual variability of Northern Hemisphere circulation and a positive mode corresponds to a stronger than normal polar vortex. The strengthening of the AO is associated with positive temperature anomalies over North America, Europe and Siberia and negative temperature anomalies over Alaska, Greenland, Middle east and China.

The winter warming pattern is understood as a dynamical response to volcanically produced temperature gradients in the lower stratosphere from aerosol heating and ozone depletion (*Grainger et al.* [1993]; *Kirchner and Graf* [1995]; *Stenchikov et al.* [2002]). Their proposed mechanism can be explained schematically as shown in figure 1.3: Volcanic aerosols reflect the solar radiation, thereby cooling the Earth's surface and decreasing the tropospheric temperature difference between equator and North Pole. In the stratosphere, the volcanic aerosols absorb solar radiation, warm the lower stratosphere and hence, increase the stratospheric temperature difference between equator and North Pole. These gradients strengthen the westerly winds in the lower stratosphere. This modulates the planetary wave activity in such a way that a positive phase of the Arctic Oscillation is produced in the troposphere.

*Stenchikov et al.* [2002] showed that the heating forced by Pinatubo aerosols in the lower tropical stratosphere is not the only forcing that contributes to a positive AO response, but, ozone depletion due to volcanic aerosols can also force a positive phase. Ozone depletion in this case took place in the high latitudes in NH, thereby causing polar cooling, thus increasing the equator to pole temperature gradient in the stratosphere and creating a positive phase of the AO. Many climate models (*Stenchikov et al.* [1998]; *Kirchner et al.* [1999]; *Stenchikov et al.* [2002]; *Stenchikov et al.* [2004]) have reproduced this winter warming pattern when forced with observed aerosols and ozone changes, but, with climatological sea surface temperatures as boundary conditions. However, the magnitude was much weaker compared to observations. Also, the recent IPCC [8] models used for the same analysis could not reproduce this dynamical response (*Stenchikov et al.* [2006]), thereby highlighting the non-linearity in the system and/or the unknown processes.

A decrease of meridional temperature gradient in the troposphere leads to a decrease in mean zonal energy and amplitude of tropospheric waves that result in a decrease of vertical wave activity flux to the stratosphere. The vertical component of wave activity flux, characterized by Eliassen-Palm flux, at 400 hPa and in 30-60N latitude band decreased by 5-6% and this reduced wave activity thereby accelerating the polar vortex (*Stenchikov*

[7] AO: Arctic Oscillation
[8] IPCC: Intergovernmental Panel on Climate Change

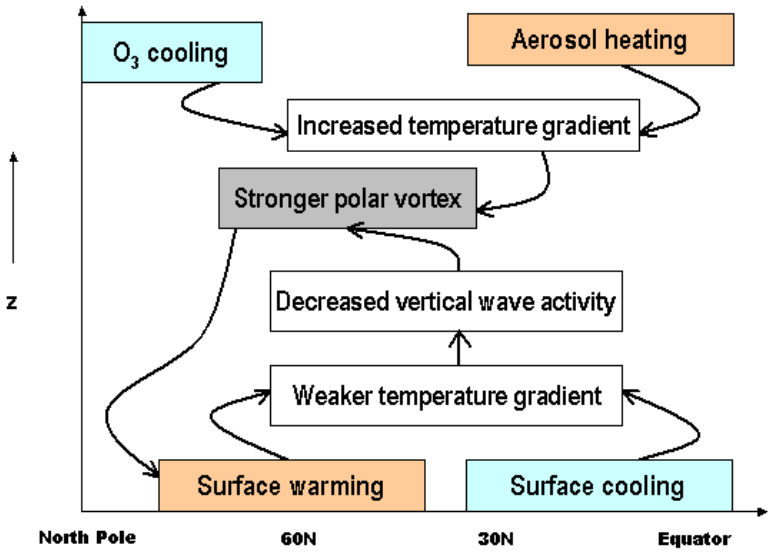


Figure 1.3: Schematic of how the tropospheric and stratospheric gradient mechanisms are triggered by volcanic aerosols (taken from *Stenchikov et al.* [2002]).

*et al.* [2002]). But, a recent study by *Graf et al.* [2007] shows that much more planetary wave energy produced in the troposphere passes into the lower and upper stratosphere in volcanically disturbed winters compared to strong polar vortex episodes without volcanic perturbation, thus contradicting earlier studies (*Graf et al.* [1993]; *Kirchner and Graf* [1995]; *Stenchikov et al.* [2002]).

### 1.2.5 Ozone effects

Satellite data and radiosonde measurements show significant stratospheric ozone losses after Mt. Pinatubo eruption, particularly in the middle and low latitudes (e.g. *Gleason et al.* [1993]; *Randel et al.* [1995]; *Solomon* [1999]) and ozone losses began approximately a month following the eruption, consistent with the time required to convert $SO_2$ to sulfuric acid aerosol (*Schoeberl et al.* [1993]; *Chandra* [1993]). These losses are due to the production of active $ClO_x$ (oxides of chlorine) facilitated by the sulfate aerosols, thus effectively reducing the ozone concentration. The column ozone concentration anomaly changed from 2% in the tropics to 7% in the mid-latitudes (*Angell* [1997a]). *Grant et al.* [1992] estimated the decrease due to the presence of Pinatubo aerosols in the 16-28 km altitude level to be 13-20 DU and this value was later refined to a decrease of 27 DU below 28 km and an increase of 5.4 DU between 28 and 32 km with the use of SAGE II climatological data (*Grant et al.* [1994]). This decrease was also shown by *Kinne et al.* [1992] using Mauna Loa Observatory lidar aerosol data. The reduction in ozone concentration resulted in a decrease in UV ab-

sorption, thus modifying the net aerosol heating effect (*Rosenfield et al.* [1997]). Modeling studies estimated the cooling of the stratosphere by 1 - 1.5 K due to this volcanically induced ozone depletion (*Stenchikov et al.* [2002]).

During the first several months, vertical uplifting and compensating temperature response were the major effects of the aerosol heating (*Kinne et al.* [1992]; *Timmreck et al.* [1999]). *Brasseur and Granier* [1992] used a 2D model with heterogeneous chemistry to compute Pinatubo related ozone loss and their results suggested that ozone column loss in the tropics occurred mainly as a result of uplifting. *Rozanov et al.* [2002] performed the first simulation of the effects of the Pinatubo eruption by a Stratosphere-Troposphere GCM with interactive aerosols and chemistry. *Timmreck et al.* [2003], using a 3D chemistry climate model showed that the tropical ozone concentration decreases below 30 Km due to heterogeneous chemistry and upward transport, and increases above 30 Km due to a decrease in $NO_x$ concentration.

### 1.2.6 QBO effects

The QBO [9] in the zonal wind is a very prominent feature of interannual variability of the tropical stratospheric circulation. Satellite observations revealed that the QBO has an important influence on the transport from tropical stratospheric reservoirs to mid latitudes (*Trepte and Hitchman* [1992]; *Trepte et al.* [1993]; *Baldwin et al.* [2001]). Once the aerosols reach the stratosphere, the detrainment of the aerosols depends upon the intensity of planetary wave activity and on the phase of the QBO. In the easterly phase of the QBO, the planetary wave activity is much less in low latitudes and hence the aerosols are trapped in the equatorial reservoir, whereas in the westerly phase, the tracers are mixed by planetary wave induced motions (*Trepte et al.* [1993]). The temporal evolution of the distribution of aerosol in the stratospheric region after the eruption of Pinatubo was observed from 1992-1995 by the Haloe experiment aboard UARS. Mt. Pinatubo erupted during the descending QBO's easterly shear where the aerosols tend to remain near the equator, whereas during the westerly shear, the aerosols tend to spread poleward. The changeover from westerly to easterly phase took place from April to May 1991 at 30 hPa and from June to July at 50 hPa (*Labitzke and McCormick* [1992]). It has been shown that the QBO reduced the volcanically induced stratospheric temperature response at the equator at 50 hPa by 0.5 K due to the stronger upwelling induced by the QBO in the easterly shear layer. *Stenchikov et al.* [2004] developed a version of the SKYHI troposphere-stratosphere-mesosphere model that assimilates observed zonal mean winds in the tropical stratosphere to simulate a realistic QBO and the resulting analysis shows that volcanic perturbations of the tropospheric winter circulation are affected significantly by the phase of the QBO, with a westerly QBO phase in the lower stratosphere resulting in an enhancement of the aerosol effect on the

[9] QBO: Quasi-Biennial Oscillation

Arctic Oscillation.

### 1.2.7 El Niño effects

ENSO [10] events affect the weather around the globe as the tropical Pacific is a major heat source that drives the atmospheric circulation. Small changes in this heat source can have widespread consequences (*Philander* [1990]). The simultaneous/subsequent evolution of El Niño in the Pacific after large volcanic eruptions such as Agung in 1963, El Chichón in 1982 and Mt. Pinatubo in 1991 raised many questions as to whether there exists a strong relation between El Niño events and explosive volcanic eruptions or whether the occurrence was purely coincidental. Many hypothesis were suggested on plausible mechanisms (*Schatten et al.* [1984]; *Strong* [1986]; *Handler* [1986]; *Hirono* [1988]), but, none of the modeling studies could explain any of the hypotheses. *Robock and Free* [1995] found no significant correlation between SOI [11] and any volcanic indices. *Self et al.* [1997] examined every large eruption of the past 150 years and showed that in none of the cases El Niño occurred as a consequence of an eruption. Recently, *Adams et al.* [2003] correlated the two volcanic indices, Volcanic Explosivity Index and Ice core Volcanic Index with SOI. In this study, only the largest eruptions were included and showed that there was a recognizable El Niño like response in the 3 consecutive years after large explosive volcanic eruptions followed by a weaker La-Nina like state in next 3 years. He concluded that volcanic eruptions do not trigger El Niño events, but they can force the climate system to a state where El Niño like conditions are favored.

*Mass and Portman* [1989] examined the influences on surface temperature of nine major volcanic eruptions during 1883-1982 and the ENSO events that occurred near the times of these eruptions and found that the ENSO signal can either enhance or mask the volcanic signal. After removing the ENSO signals they found only modest cooling of up to $0.2^0$ for 1-2 years following these eruptions. *Yang and Schlesinger* [2001] using singular value decomposition analysis removed the 1991-1992 and 1993 ENSO signals from observed surface air temperature anomalies over Eurasia, North America, South America and Africa following the eruption and found that ENSO signals were weak over Eurasia, but, relatively strong over the other continents. Over North America, the 1991-92 El Niño event contributed more than 50% of the observed total cooling of about -1$^o$C in JJA 1992.

## 1.3 Objectives and outline of the present study

The main objective of this study is to investigate the climatic impact of the Mt. Pinatubo eruption on the tropical and extratropical circulation. To better understand the anomalies

[10] ENSO: El Niño and Southern Oscillation
[11] SOI: Southern Oscillation Index

in the circulation as observed after Mt Pinatubo eruption, the internal variability of the system and effects of El Niño and the QBO will be investigated and discussed in detail. For this purpose, the effects are simulated with the ECHAM5 GCM[12].

This study aims to reveal the generalized climatic response to Mt. Pinatubo eruption under varying boundary conditions, including one at a time, thereby assessing the individual and combined radiative and dynamical responses of volcanic effects, El Niño and QBO. This experiment gives us an overview on how the climate responds to a scenario in which one or the other boundary conditions are included. This is the first study that includes all the known processes such as the effects of QBO, SST and volcanically induced ozone anomalies for the simulation of Mt. Pinatubo eruption and to analyze the responses to individual and combined forcings using the same model with high vertical resolution.

The QBO has a profound effect on the global atmospheric response to volcanic radiative forcing and it has been shown that the QBO reduced the stratospheric temperature response by 0.5 K at 50 hPa during Mt. Pinatubo eruption. The QBO is simulated in the model by assimilating the observed zonal mean winds at Singapore in the tropical stratosphere (*Giorgetta and Bengtsson* [1999]). Mt. Pinatubo erupted during the easterly phase of QBO at 30 hPa and the phase change to westerlies took place 14 months after the eruption. In this study, a sensitivity analysis is carried out to explain if there is any systematic difference of the effect of the QBO phase on the response of the circulation to the Mt. Pinatubo eruption. Moreover, the individual responses to the observed phase of QBO and the opposite phase of QBO are investigated.

The description of the model set up and a brief description of the data sets used in this study is described in chapter II. Before answering all these scientific questions, it is important to assess how good the model simulates this natural climate experiment. Attempts to simulate the radiative effects of aerosols and the limitations of the radiation schemes in the model and hence, the improvements made are introduced in chapter III. Chapter IV presents the sensitivity of the model to simulate volcanically induced radiative and dynamical response to varying boundary conditions. The sensitivity of the atmospheric effects of Mt. Pinatubo eruption to the phase of QBO is is presented in chapter V. Chapter VI presents the summary and conclusions.

[12]GCM: General Circulation Model

# Chapter 2

# Description of model and dataset used

## 2.1 Model description

The experiments are performed with the most recent version of the fifth generation atmospheric general circulation model ECHAM5 developed at Max Planck Institute for Meteorology, Hamburg (Special section "Climate models at the Max-Planck Institute for Meteorology" in Journal of Climate, 2006, 19, Issue-16, 3769-3987 ). The model is based on the spectral weather prediction model of ECMWF. The spatial resolution is based on a triangular truncation of spherical harmonics at wave numbers 21, 31, 42, 63, 85, 106 and higher and hybrid sigma pressure co-ordinate representation in the vertical. In the standard configuration, the model has 19 or 31 vertical layers with the top level at 10 hPa. The middle atmosphere version, known as MAECHAM5, is available with either 39 (*Manzini et al.* [2006]) or 90 layers (*Giorgetta et al.* [2006]), with the topmost level at 0.01 hPa. The 90 layer grid allows the simulation of the quasi-biennial oscillation. The numerics and physics of ECHAM5 is described in *Roeckner et al.* [2003].

Since radiative transfer is the major process linking the general circulation to volcanic aerosols in the stratosphere, the radiation schemes in both SW and LW are mentioned briefly here. The SW radiative transfer scheme of ECHAM5 follows *Fouquart and Bonnel* [1980] and the LW radiative transfer follows the RRTM (Rapid Radiative Transfer Model) scheme (*Mlawer et al.* [1997]) as implemented in cycle 23 release 1 of the IFS model of ECMWF (*Morcrette et al.* [1998]). The number of spectral bands in the shortwave has been increased from 2 in ECHAM4 to 4 in ECHAM5 and recently to 6 (*Cagnazzo et al.* [2007]) (Table 2.1). The Near IR range is resolved by three bands and the UV/VIS range is also resolved by three bands, to account better for the wavelength dependencies of optical properties of aerosols and will be explained in more detail in chapter 3. The near-IR bands

in the 4-spectral band of ECHAM5 and the 6-spectral band of ECHAM5 remains the same. The main difference is in the split up of the UV/VIS bands. The 4 band ECHAM5 had 1 band in the UV/VIS (0.25-0.69).

The RRTM scheme is based on a two stream approximation instead of the emissivity method of *Morcrette et al.* [1998] that is used in ECHAM4. Radiative transfer is divided into 16 bands (instead of 6 in ECHAM4) in the longwave (table of the LW spectral wavelengths are shown in Appendix-A) and the scheme is computationally more efficient at higher resolutions because the CPU time increases linearly with the number of layers compared to the quadratic dependency of the emissivity schemes used in ECHAM4. The radiative transfer calculations are made every two hours independent of time step and resolution. Radiative heating rates are estimated at every time step based on the 2 hourly radiative flux calculations and the solar incidence that is calculated at every time step.

The radiative transfer calculation requires profiles of active gases, aerosols, cloud water and ice and cloud cover. Water vapor, cloud water and ice are prognostic variables. $CO_2$, $CH_4$, $N_2O$ and CFCs are prescribed with a constant mixing ratio, and ozone is prescribed following the zonally averaged monthly climatology of *Fortuin and Kelder* [1998] which is based on the observation over a period 1980 - 1991. Optionally, $CH_4$ and $N_2O$ can be prescribed as a vertical profile with decreasing mixing ratios in the stratosphere for the middle atmosphere configuration of ECHAM5. However, in this study, constant mixing ratios are prescribed for $CH_4$ and $N_2O$. Aerosol distributions are prescribed following *Tanre et al.* [1984]. This climatology distinguishes spatial distributions of optical thickness at 0.55 micrometers of sea, land, urban and desert aerosols and well mixed tropospheric and stratospheric background aerosols.

| *Band* | *Spectral interval* | *Type* |
|---|---|---|
| 1 | 0.185 - 0.25 | UV |
| 2 | 0.25 - 0.44 | UV |
| 3 | 0.44 - 0.69 | VIS |
| 4 | 0.69 - 1.19 | Near-IR |
| 5 | 1.19 - 2.38 | Near-IR |
| 6 | 2.38 - 4.00 | Near-IR |

Table 2.1: Spectral intervals ($\mu$m) and band type in the shortwave in ECHAM5

## 2.2 Pinatubo aerosol data sets

Two types of aerosol datasets, PADS [1] and SAD [2] are used in this study. Sato developed a global stratospheric aerosol database for the period 1850-1993 (*Sato et al.* [1993]) and SAD refers to this dataset. But, for this study, both these data sets have been compiled

[1]Pinatubo Aerosol Data Set
[2]Sato Aerosol Data

by Gera Stenchikov (*Stenchikov et al.* [1998]) from SAGE [3] and UARS [4] satellite data for different ECHAM resolutions. The main difference is that PADS make use of the SAGE retrievals at 1.02 $\mu$m, whereas SAD make use of the retrievals at 0.55 $\mu$m to calculate the aerosol parameters. The difference between these two data sets and the model sensitivity to them are discussed in chapter 3. These aerosol data sets consist of zonally averaged values of extinction cross sections, single scattering albedo and asymmetry factor for two years following the Pinatubo eruption. SAD will be adapted for specific model versions and resolutions.

The observed aerosol cloud followed a zonal structure within a few weeks after the eruption and varied smoothly in time (*McCormick et al.* [1995]. Hence, the Pinatubo aerosol data set is calculated with zonal mean aerosol parameters and a one month time step. The SAGE II optical depths for four layers in the lower stratosphere and the UARS effective radii (*Lambert et al.* [1997]) were used to calculate the aerosol parameters. The optical depths and effective radii characterize the aerosol particle density and size distribution. They depend on the altitude, latitude and time and are provided on different spatial and temporal grids. The aerosol spectral optical characteristics are calculated using the Mie code (*Wiscombe* [1980]) and refractive indices for a 75% solution of sulfuric acid (*Palmer and Williams* [1975]). The aerosol parameters are given as monthly mean data and are interpolated for each time step of the model run.

The aerosol optical depth at 0.55 $\mu$m for two years after the eruption is shown in figure 2.1. The spread of the aerosol cloud six months after the eruption is evident. This is due to the enhanced meridional northward transport in fall, which is associated with an amplification of planetary scale waves in high latitudes. These waves transport the volcanic aerosol from the tropics to high latitudes.

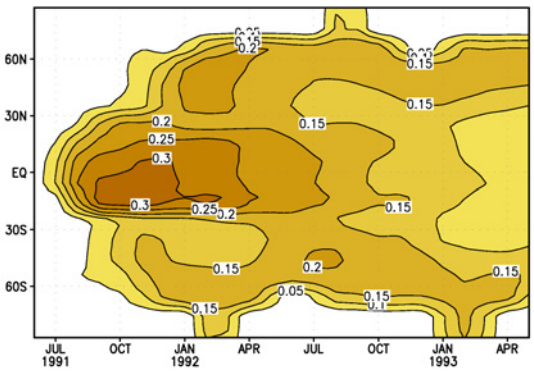


Figure 2.1: Zonally averaged Pinatubo aerosol optical depth at 0.55 $\mu$m for two years after the eruption.

[3] SAGE: Stratospheric Aerosol and Gas Experiment
[4] UARS: Upper Atmosphere Research Satellite

## 2.3 Ozone anomaly data set

The ozone anomalies owing to Mt. Pinatubo eruption has been compiled by Gera Stenchikov (*Stenchikov et al.* [2002]) from in-situ ozonesonde observations. Observations from around 20 stations in the mid and high latitudes and from two stations in the tropics were used in the preparation of the data set and is validated with the TOMS column observations (*Randel et al.* [1995]).

Figure 2.2 shows the vertical structure of ozone anomalies in $\mu$g/g for several months after Pinatubo eruption. The evolution of ozone loss in the stratosphere owing to the eruption and the recovery by December 1992 can be seen in this figure. There is an ozone loss of up to 1.2 $\mu$g/g after July 1991 in the equatorial lower stratosphere between 10 and 50 hPa. In the middle and high latitudes, maximum ozone loses extend beyond the 10 - 50 hPa band. An increase in ozone amount is revealed in the southern hemisphere in July 1992. This is due to an increase in photolysis rates because of UV reflection from the aerosol layer and $NO_x$ consumption (*Solomon* [1999]). Positive ozone anomalies are visible in the equatorial region above 10 hPa especially during the westerly phase of QBO from Dec 1992 through May 1993.

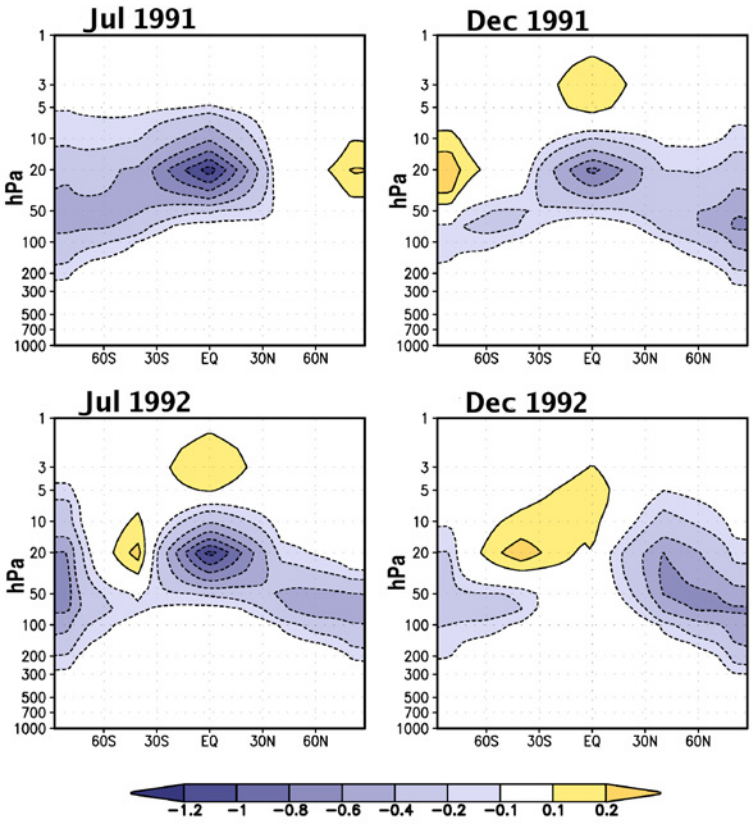


Figure 2.2: Zonal mean cross-section volcanically induced ozone mixing ratio anomalies ($\mu$g/g) calculated from ozonesonde data.

To produce the ozone data set for our simulations, the monthly mean and zonal ozone anomaly data set is first interpolated to the model grid and these anomalies were then applied to the zonal mean ozone distribution used in ECHAM5.

## 2.4 Experimental set up

As mentioned in the previous chapter, model runs are carried out with both climatological and observed SST as boundary conditions and also with different QBO phases. The setup for each of the experiments are given below.

In this study, we carry out ensembles of the model runs. An ensemble, in this case, is a collection of runs using the same model, but varying slightly in their initial conditions. Ensemble simulations are based on the MAECHAM5 model at resolution T42L39. This model does not simulate the QBO, unless the QBO is assimilated. The mean response is then evaluated by comparing the means of different ensembles. Moreover, ensembles also allow to quantify the internal variability of the model.

**Volcanic effects only**
An ensemble of 10 two-year simulations with climatological sea surface temperature (SST) and sea ice (SIC) is performed using MAECHAM5 with Pinatubo aerosol perturbation (aerosol run). The initial conditions for these runs are chosen arbitrarily from the a 15-year control run simulation with climatological SST and SIC distribution (control run) after spinup. Thus, we have ten independent realizations. The ensemble mean response is calculated as an average of the difference between the individual ensemble members and the control run mean.

**Combined effects of El Ni$\tilde{n}$o and Pinatubo**
Similarly, ensemble runs have been performed with observed SST and SIC as boundary conditions (from AMIP [5]). Ten two-year experiments are carried out with Pinatubo aerosol perturbation (aerosol run) and without the aerosol perturbation (control run). For both cases, the initial conditions are taken from the 15 year control run made with climatological SST and SIC as boundary conditions and a spinup of 17 months using the observed lower boundary conditions of Jan 1990 to May 1991 is made before the beginning of the aerosol and control runs. The response in this case is calculated as a one-to-one difference of the ensemble means of the perturbed and the unperturbed ensembles.

**Combined effects of Pinatubo, El Ni$\tilde{n}$o and QBO**
For the runs including the QBO, a similar procedure as above is adopted. In this case, a

[5] AMIP: Atmospheric Model Intercomparison Project

spinup of 17 months is carried out with observed SST and with the observed QBO phase. To include the QBO forcing in this study, the zonal mean zonal winds in the tropics are nudged towards the prevailing zonal wind observations at Singapore (*Giorgetta and Bengtsson* [1999]). The nudging is applied uniformly in a core domain and extends with decreasing nudging rate to the boundary of the domain. The latitudinal core domain specified for the study here is 7N-7S and the domain boundary is 10N-10S. In the vertical the core domain and the boundary is over the levels extending from 70 hPa to 10 hPa. The nudging rate is $(10 \text{ days})^{-1}$.

The evolution of the simulated zonal mean zonal wind averaged over 5N - 5S over the period June 1991 - May 1993 is investigated both from observations and simulations. The evolution of the simulated zonal mean zonal wind averaged over 5N - 5S in figure 2.3 (b) compares reasonably well with the observations from Singapore used for the assimilation in 2.3 (a). It shows the downward propagation of easterlies and westerlies associated with QBO. The observed phase and amplitude is simulated well by the model. The easterly phase of the QBO simulated by the model from June 1991 to Oct 1992 is slightly weak below 30 hPa (25 m/s (observed) versus 20 m/s (simulated)). The westerly phase of the QBO at 30 hPa from Oct 1991 to the end of the simulation period is also slightly weak.

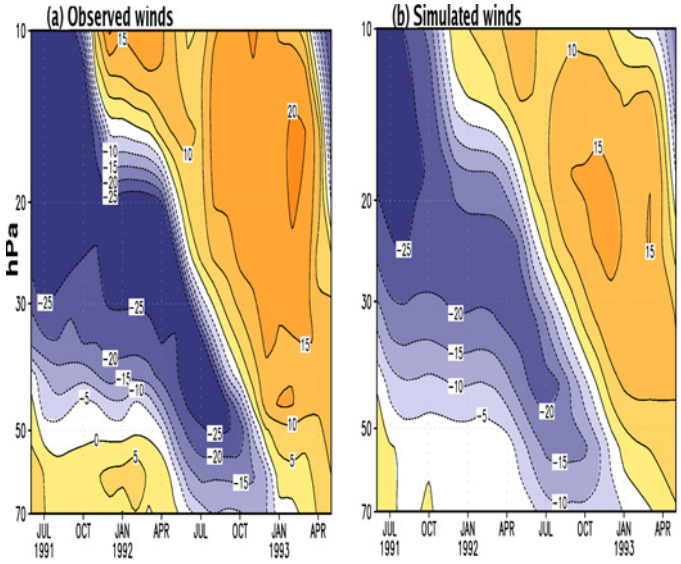


Figure 2.3: Zonally averaged zonal wind anomalies averaged over the latitudinal band from 5N-5S (m/s) from (a) Singapore observations that is assimilated in the model and (b) simulated zonal mean zonal winds.

To obtain information about the aerosol induced radiative forcing, the radiation routine in the model is called twice in our simulations including Pinatubo aerosols. Radiative forcing and net radiative fluxes related to the volcanic aerosols are calculated at every time step from the difference between the radiation calculations with aerosols and those without Pinatubo aerosols. Calculations are made for both clear sky and cloudy sky conditions.

# Chapter 3

# Radiative effects of aerosols - Model limitations and improvements

## 3.1 Introduction

Volcanic eruptions and their subsequent climate response are relatively short-lived perturbations to the climate system. They provide an excellent opportunity to understand the feedback mechanisms of the climate system and to test the climate models. Volcanic eruptions can be considered as a natural climate experiment. Hence, the well observed episode of Mt. Pinatubo eruption and the subsequent weather and climatic changes are an interesting case to study the functioning of the climate system.

As explained in the previous chapter, the Pinatubo volcanic plume reached a maximum height of 40 km, with the bulk of aerosol centered around 25 km, affecting the whole globe through the interactions with radiation, chemistry and dynamics. So, in order to simulate such an event, the first step is to see how well the model responds to such large perturbations. In this chapter, the efficiency of the model in simulating the radiative forcing of Mt. Pinatubo eruption is ascertained. The model limitations in simulating the aerosol induced radiative forcing and the resulting lower stratospheric temperature response are presented and the effect of model improvements on forcing and response are discussed in this chapter. A brief overview on the radiative properties of the sulfate aerosols and the treatment of aerosols and gases in the ECHAM5 radiation scheme are also pointed out in this chapter.

## 3.2 Radiative properties of sulfate aerosols

As mentioned in the previous chapter, most of the explosive volcanic eruptions are a major source of sulfate aerosols, which are produced when sulfur dioxide ($SO_2$) and hydrogen sulfide ($H_2S$) are chemically transformed into sulfuric acid ($H_2SO_4$) within a time scale of weeks (e.g. *Bluth et al.* [1992]). The aerosols thus formed remain in the stratosphere for several years. Sulfate aerosols have been deemed important for climate change because the estimated strength of their direct forcing is appreciable. Hence, in this section, the radiative properties of sulfate aerosols are discussed. The radiative properties of the aerosols can be characterized by their optical properties such as extinction co-efficient, single scattering albedo and asymmetry. Another most commonly used metric is aerosol optical depth (AOD) that gives an estimate how optically thick the aerosol layer is. In other words, AOD gives a measure of how opaque the medium is to radiation passing through it. The higher the AOD value means more aerosols are within a column.

The variation of single scattering albedo, extinction co-efficient and absorption co-efficient with wavelength for varying mean sulfate aerosol radii is shown in figure 3.1. These values are results of Mie calculations using refractive indices from *Palmer and Williams* [1975] for a weight percentage of 75% (means a sulfuric acid solution of 75%) and for a lognormal distribution with a varying mean radius (R) and a constant size distribution of 1.86 (C. Timmreck, personal communication). The extinction co-efficient, which denotes the fraction of light attenuated by scattering and absorption, is shown in figure 3.1(a). In other words, it is the sum of scattering co-efficient and absorption co-efficient. There is a wide range of extinction co-efficients evident for varying radii in the visible spectral band and this range decreases at high solar wavelengths.

The single scattering albedo (ssa) determines the fraction of the total attenuation by scattering (ssa=0 means complete absorption, while ssa=1 means complete scattering). The sulfate aerosols are purely scattering in the UV and visible band of the solar spectrum (single scattering albedo (ssa) = 1) and mostly scattering in the near-IR band, thus increasing the planetary albedo. They are good absorbers in the middle and far solar infrared and in the thermal infrared region as seen in figure 3.1(b).

The asymmetry parameter (g) parameterizes the scattering distribution in terms of forward versus backward scattering (g=0 for equal amounts of forward and backward scattering as is the case for Rayleigh scattering). Positive values of g (g>0) indicate that scattering is more prominent in the forward direction. The range of the values of asymmetry parameter for varying mean aerosol radii is shown in figure 3.1(c). Typical values are around 0.6 - 0.7 at visible wavelengths and a wide range of values is seen for varying radii at near-IR spectral wavelengths.

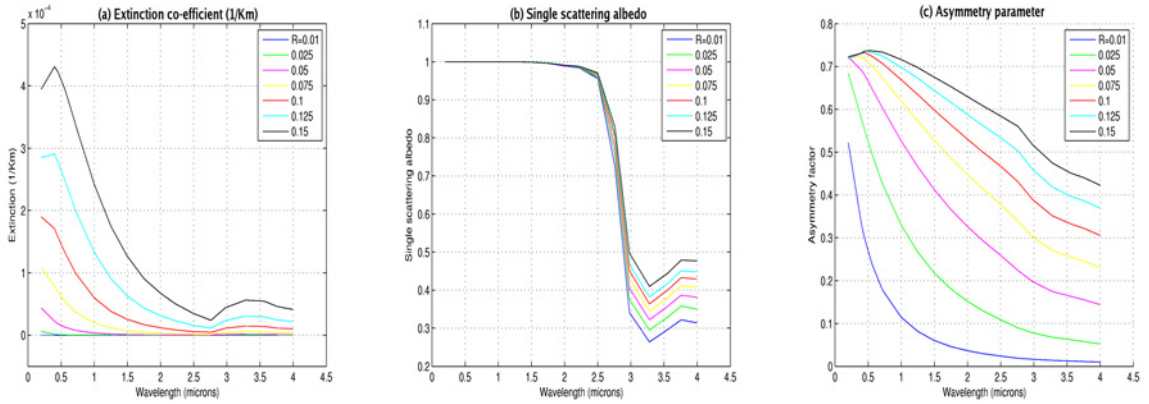


Figure 3.1: The variation of (a) extinction co-efficient (1/km), (b) single scattering albedo and (c) asymmetry parameter at solar wavelengths in ECHAM5 SW spectral range for varying mean sulfate aerosol radii (R) in micrometers

## 3.3 Over-estimation of climatic response

As a first step, the lower stratospheric (20-22 km) radiative heating and the resulting temperature anomalies are evaluated in simulations with prescribed time dependent distributions of aerosol optical depths, as derived from observations, to determine how good the model can capture the processes and the dynamical and energetic response in comparison with observations.

A first model simulation is performed with ECHAM5 at T42L19 resolution, which has the highest full level at 10 hPa ($\sim$ 30 km) with climatological SST as boundary condition. The model is run for only 8 months (Jun 1991 - Jan 1992) following the eruption. In order to isolate the radiative response to aerosol perturbation, the time dependent forcings such as SST, ozone depletion and QBO are excluded in this simple simulation though they play an important role in modulating the climate in the tropical stratosphere. Studies (*Kirchner et al.* [1999]; *Stenchikov et al.* [2002]) have shown that ozone anomalies resulting from Pinatubo eruption and QBO effects related to the QBO phase in 1991 thereafter reduce the stratospheric temperature anomalies by 1.5-2K when compared to the expected temperature response in the simulations that neglect these effects. Here, the main focus is on the tropical response. The observed values of temperature anomalies are calculated from NCEP re-analysis [1] with respect to the 1968-1996 climatology. Shown in figure 3.2 is the zonally averaged lower stratospheric temperature anomaly from observations with respect to the NCEP climatology (a) and from the model simulation with respect to the climatology over 5 years using the same boundary conditions (b). The observed lower stratospheric temperature anomaly shows a warming of 2-3 K in the tropics. Large anomalies up to 7 K

[1]NCEP Re-analysis: This data developed by NCEP and NCAR that has 40-year record (1958-1998) of global analysis of atmospheric fields (see *Kalnay and coauthors* [1996])

are also observed in the SH springtime high latitudes in 3.2(a) and these are presumably related to the stratospheric warmings owing to the breakdown of the polar vortex that is more stronger and persistent compared to the polar vortex in the NH.

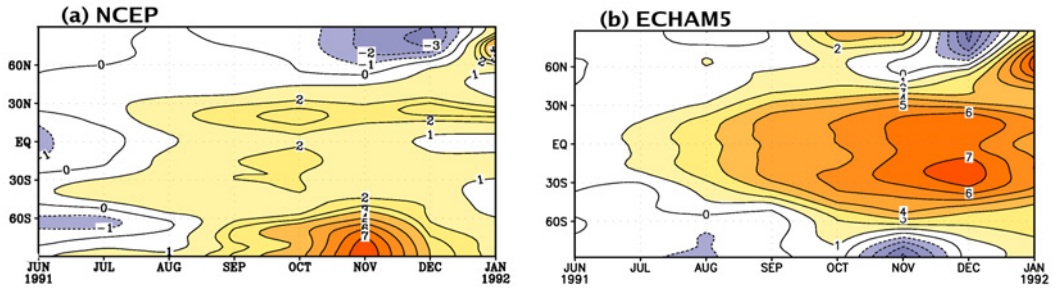


Figure 3.2: Zonally averaged 50 hPa temperature anomalies (K) calculated from NCEP reanalysis and (b) simulated in the run with climatological SST for the period Jun 1991 - Jan 1992

In the simulated run, shown in figure 3.2(b), the maximum temperature anomaly in the tropics reaches around 7K, seven months after the eruption. If the ozone and QBO effects were included, the temperature anomaly would be around 5K, which is still 3K higher than the observations (figure 3.2(a)). To diagnose this overestimation, the radiative forcing anomalies in solar and thermal bands are analyzed separately. The longwave and shortwave heating rate anomalies in Kelvin/day (K/d) for Aug 1991 and the comparison with previous studies by *Stenchikov et al.* [1998] (hereafter referred to as ST-98) are presented in figure 3.3.

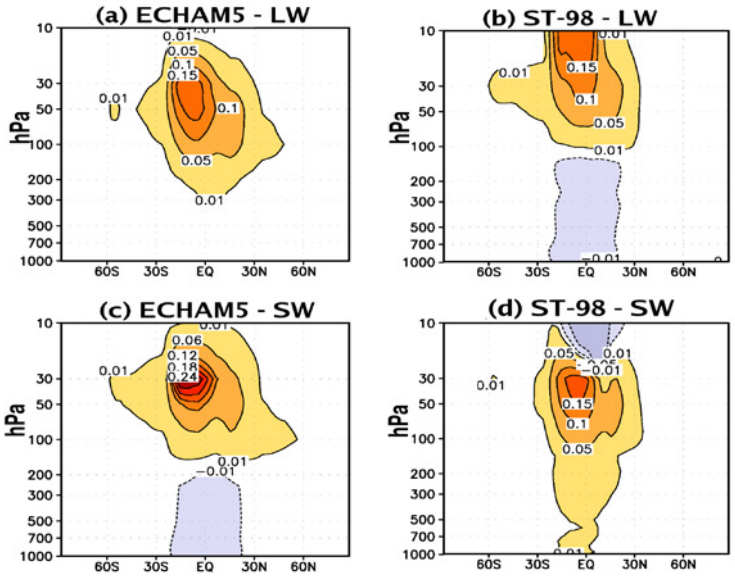


Figure 3.3: Radiative heating rate anomalies (K/d) for Aug 1991 in the thermal spectral range from (a) ECHAM5 simulation and (b) *Stenchikov et al.* [1998] and in the solar spectral range from (c) ECHAM5 simulation and (d) *Stenchikov et al.* [1998] .

From figure 3.3, it is evident that the simulated long wave radiative heating rate anomalies (figure 3.3(a)) agree well in magnitude with that of the previous studies shown in figure 3.3(b). The region of the maximum LW heating rate anomalies are however, lower in ECHAM5 compared to ST-98, where the maximum anomalies are at the topmost level of the model. The over-estimation is more pronounced in the simulated solar radiative forcing anomalies with Pinatubo aerosols (refer figure 3.3(c) and figure 3.3(d)). The shortwave heating rate anomaly from the model simulation is two times higher than that of the previous studies from ST-98 and is the cause of the too strong temperature response in the lower stratosphere.

In the following sections the SW radiation scheme will be discussed in more detail in order to understand better the reasons of this over-estimation and the improvements implemented in the scheme for more realistic results.

## 3.4 ECHAM5 shortwave radiation scheme

The SW radiative transfer of ECHAM5 follows *Fouquart and Bonnel* [1980] as implemented in cycle 23 release 1 (CY23R1) of the IFS model of ECMWF (*Roeckner and co authors* [2003]; ECMWF-Technical Memorandum 165) The flow chart of the SW radiation scheme in ECHAM5 is shown in figure 3.4. The main shortwave routine is given by *SW* that carries out the calculations of the absorber amounts of the gases (*SWU*) and the radiative transfer in visible (*SW-VIS*) and Near-IR (*SW-NIR*) spectral bands. *SW-VIS* and *SW-NIR* branches carry out the calculations for both clear sky (*SWCLR*) and cloudy sky (*SWR*) conditions independently. Radiative transfer calculations based on the delta-Eddington approximation are carried out in the *SWDE* routine. Each routine is discussed in detail in the following sections.

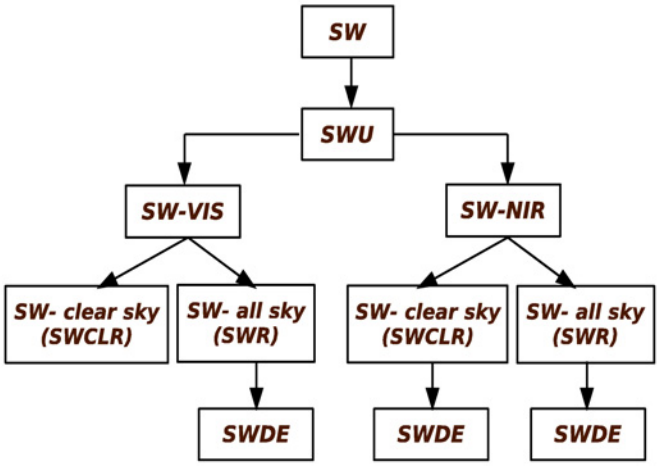


Figure 3.4: Schematic of the shortwave radiation scheme in ECHAM5.

### 3.4.1 Calculation of absorber amounts

Solar radiation is attenuated by some absorbing gases, mainly by water-vapor, uniformly mixed gases ( $CO_2$, $CH_4$, $N_2O$, CO and $O_2$) and $O_3$, and scattered by molecules (Rayleigh scattering), aerosols and cloud particles. In the near infrared region, water-vapor and carbon dioxide have numerous bands. Hence a combination of scattering and molecular band absorption has to be considered. Since scattering by particles and absorption by gases occur simultaneously, the exact amount of absorber along any photon path is unknown. So, the probability that a photon of a particular energy (or wavelength) has encountered an absorber amount is calculated approximately (*Fouquart and Bonnel* [1980]). Once the effective amounts of $H_2O$, uniformly mixed gases and ozone are found, the transmission functions are computed in each band in the form of Pade approximants (*Brezinski* [1973]), where absorber amounts are given as effective amounts for reference conditions of temperature and pressure: Tref = 296 K and Pref = 1000 hPa. As the ozone absorption is mainly restricted to upper layers, the interaction between scattering and ozone absorption is neglected. The interactions between gaseous absorption and scattering processes are accounted for only in the Near-IR interval.

### 3.4.2 Treatment of clouds, aerosols and gases in ECHAM5

Clouds are characterized by their microphysical properties such as liquid water content and drop-size distribution and by their optical properties which are described in the model by spectrally dependent optical depth, single scattering albedo and asymmetry parameter. The fraction of the atmosphere covered by clouds/aerosols depends on the overlap assumption assumed in the calculations. In ECHAM5, Maximum-Random Overlap assumption is used where 'Maximum overlap' is considered between clouds/aerosols in adjacent levels and 'Random overlap' is considered between the groups of clouds/aerosols separated by one or more clear layers (*Geleyn and Hollingsworth* [1979]; *Collins* [2001]). Scattering and absorption by molecules and aerosols are considered in the clear sky atmosphere. The calculations are carried out twice, once for the clear sky fraction of the atmospheric column and the second time for the clear sky fraction of each individual layer within the fraction of the column containing clouds. The final fluxes are calculated as the weighted average of the fluxes in the clear sky and cloudy fractions of the column.

In the *SWCLR* routine, the optical properties of individual aerosol species and Rayleigh scattering are combined. In the *SWR* routine, cloud optical properties are combined with those of the aerosols and molecules. This part is the same in both visible and in near-IR spectral interval, except that along with aerosols and clouds, the interaction of gaseous absorption and aerosol scattering is included in the near-IR calculations. The interaction between aerosol scattering and gaseous absorption are ignored in the *SW-VIS* routine, but are considered in the *SW-NIR* routine for all sky calculations. Optical properties (refer sec-

tion 3.2 for details) in a single layer are calculated as functions of the total optical thickness of the layer, total single scattering albedo and total asymmetry parameter, where "total" refers to the contributions from clouds, aerosols and gases. For co-located atmospheric particles (aerosols, clouds or molecules), their optical properties are combined by mixing rules. The combined optical depth ($\tau$) is the sum of the optical depths of the individual species and is given by,

$$\boldsymbol{\tau = \sum_i \tau_i} \tag{3.1}$$

The combined SSA ($\omega$) is the average of the individual SSAs, weighted by the optical depths of the individual species and is given by,

$$\boldsymbol{\omega = \frac{\sum_i \tau_i \cdot \omega_i}{\sum_i \tau_i}} \tag{3.2}$$

The combined asymmetry parameter (g) is the average of individual asymmetry parameters, weighed by the product of optical depths and single scattering albedo of the individual species given by,

$$\boldsymbol{g = \frac{\sum_i \tau_i \cdot \omega_i \cdot g_i}{\sum_i \tau_i \cdot \omega_i}} \tag{3.3}$$

### 3.4.3 Radiative transfer calculations

The radiative transfer through a scattering layer is calculated using the Delta-Eddington two stream approximation (*Joseph and Wiscombe* [1976]). This approximation is an efficient method of calculating radiative fluxes in an absorbing-scattering atmosphere. The delta-Eddington approximation combines the delta transformation of the scattering parameters (*Joseph and Wiscombe* [1976]) and the Eddington approximation for the radiative transfer through a plane parallel and homogeneous scattering layer (*Shettle and Weinman* [1970]). This approximation is realistic only if the scattering is isotropic. For this purpose a delta transformation is applied to the optical properties of aerosols, clouds and molecules to account for a large fraction of the radiation directly transmitted into the forward scattering peak. The transformed optical properties are given by,

$$\boldsymbol{\tau' = \tau \cdot (1 - \omega \cdot g^2)} \tag{3.4}$$

$$\boldsymbol{\omega' = \frac{\omega \cdot (1 - g^2)}{(1 - \omega \cdot g^2)}} \tag{3.5}$$

$$g' = \frac{g}{(1+g)} \tag{3.6}$$

where $\tau'$ is the transformed optical depth, $\omega'$ is transformed SSA and $g'$ is the transformed asymmetry parameter.

The addition of aerosols modifies the atmospheric radiative properties like absorptivity, reflectivity and transmissivity. The reflectivity, transmissivity and absorptivity of the layer are computed without reflection from the atmosphere below and with reflection from the atmosphere below. The calculations provide the contribution to reflectance and transmittance of those photons interacting only with the layer in consideration. It also includes the effect of the medium below the layer in consideration on the reflectivity at the top of the layer and the transmissivity at the bottom of the layer. The adding method (*Liou* [2002]) is adopted in ECHAM5 to combine the aerosol layer with the layers of the atmosphere below it. The reflectivity ($R_a$) and transmissivity ($T_a$) are given by,

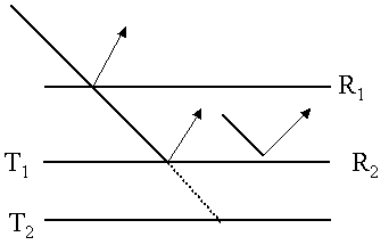


$$\boldsymbol{R_a = R_1 + \frac{(T_1 \cdot R_2 \cdot T_1)}{(1 - R_1 \cdot R_2)}} \tag{3.7}$$

$$\boldsymbol{T_a = \frac{(T_1 \cdot T_2)}{(1 - R_1 \cdot R_2)}} \tag{3.8}$$

where $R_1$, $R_2$ are the reflectivities and $T_1$, $T_2$ are the transmissivities of two consecutive atmospheric layers and the term $(1 - R_1 \cdot R_2)^{-1}$ account for multiple reflections within the layer. The interactions between aerosol scattering and gaseous absorption and the multiple reflection effect are considered negligible and hence are ignored in the near- infrared in clear sky atmospheres.

## 3.5 Possible causes for the over-estimation

It is evident that notable discrepancies exist in the shortwave heating rate anomalies. Model deficiencies that can cause this over-estimation and their improvements are described in detail in the following subsections

### 3.5.1 Multiple reflection effects and interactions between aerosol scattering and gaseous absorption

As mentioned in the previous section, Pinatubo aerosols are mostly scattering in the visible as well as in the Near-IR-1 (0.69 - 1.19) bands of ECHAM5. Hence, there could be significant

multiple reflections between the layers. Because of the increase in multiple scattering, the interactions between aerosol scattering and gaseous absorption becomes significant. Taking into account the high aerosol loading owing to the Pinatubo eruption, the aforementioned factors cannot be neglected. These factors were found to be incorporated only in the cloudy part of the column in the model and were neglected in the clear part in the Near-IR since the climatological aerosol loading is much smaller than that of the stratospheric aerosol layer related to the Mt. Pinatubo eruption. Minor modifications are made in the model to incorporate these factors. Shown in figure 3.5 is the flow chart of the radiation routine in ECHAM5.

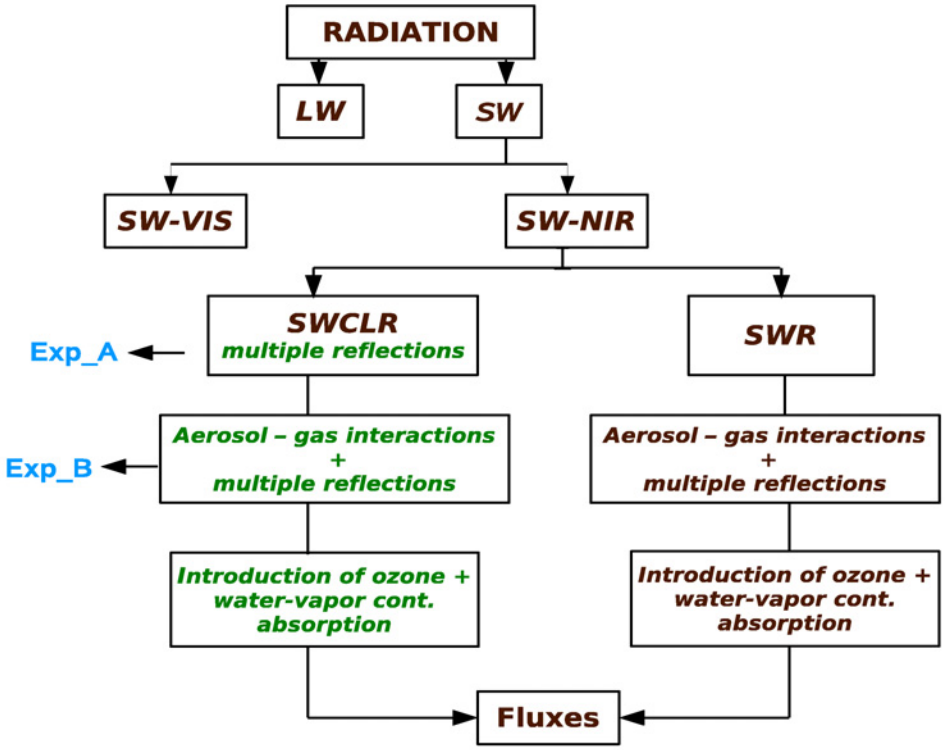


Figure 3.5: Schematic of the improvements made (shown in green) in the SW radiation scheme of ECHAM5. The subroutines of ECHAM5 are represented by capital letters and the processes taking place within the specific routines are presented by small letters.

The improvements incorporated are shown in green. The changes are made in the Near-IR (*SW_NIR*) routine for the clear sky fraction (CLEAR fraction) of the column. The UV/VIS (*SW_VIS*) part of the spectrum follows a more or less similar procedure except that the interactions between aerosols, clouds and gases are not included in the clear/cloudy fractions, but the effect of multiple reflections are included.

### 3.5.2 Modifying the way in which the different atmospheric particles are combined in ECHAM5 and avoiding the repetition of delta transformations

As mentioned in section 3.4.2, the optical properties of several species, such as aerosols, clouds and gases are combined for radiative transfer calculations. In ECHAM5, the way in which the optical properties of the individual species have been combined is found to be in part inconsistent with those shown in equations 3.1 - 3.3. Hence, this part in the model has been modified so as to follow the basic mixing rules. A detailed flow chart showing the part in the Near-IR routine (*SW-NIR*) where each species are combined is depicted in figure 3.6 and a similar procedure is carried out in the visible (*SW-VIS*) routine also. Here, $\tau$ is the optical thickness, $\omega$ is the single scattering albedo and g is the asymmetry parameter and each species are assigned with different subscripts.

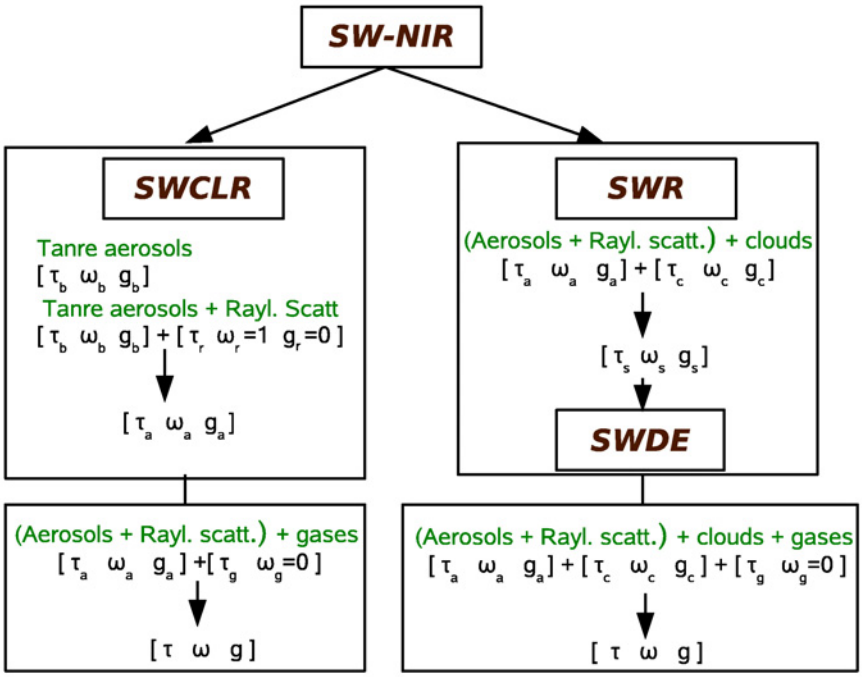


Figure 3.6: Schematic of the near-IR routine of ECHAM5 where individual atmospheric species are combined. $\tau$ is the optical depth, $\omega$ is the single scattering albedo and g is the asymmetry parameter. Different subscripts are given for the different species.

As mentioned in section 3.4.3, a delta transformation has to be applied to the combined optical properties before performing the reflectivity and transmissivity calculations following the Eddington approximation and these calculations are done in the subroutine *SWDE*. Currently in ECHAM5, this transformation is repeatedly carried out without necessity,

making the scattering more isotropic. This is schematically represented in the flow chart in figure 3.7. It can be seen that the delta transformation is repeatedly carried out and inconsistent in the fact that at several places one set of optical properties are delta transformed and the other set is not delta transformed. Note that for gases the delta transformation would not have an effect as the single scattering albedo for gases is zero.

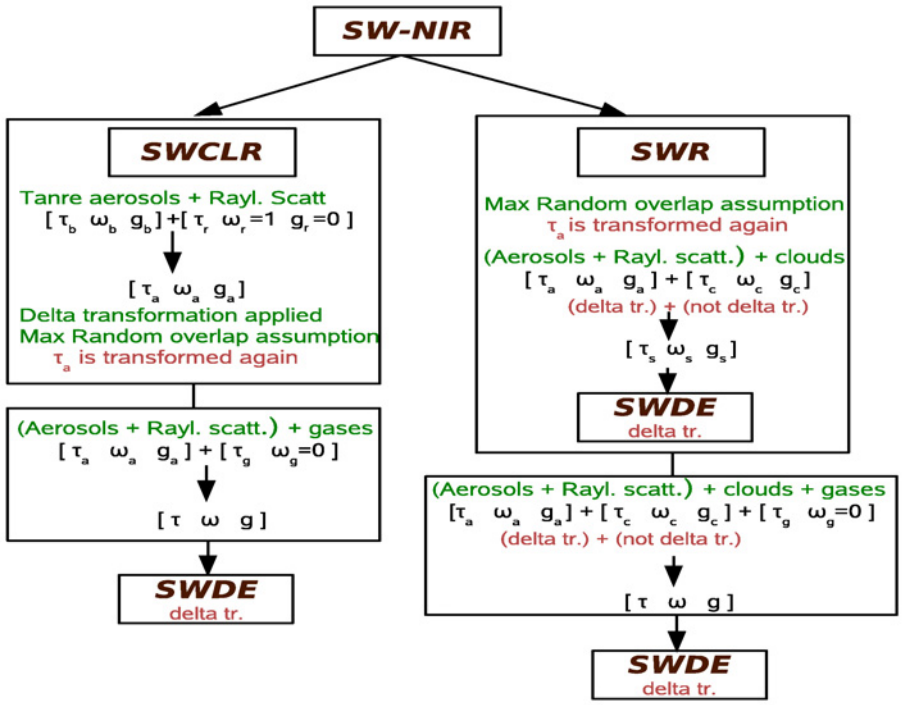


Figure 3.7: Schematic of the near-IR routine in ECHAM5 where the inconsistency in delta transformation (in red) is presented. Similar nomenclature as figure 3.6 is used here also.

### 3.5.3 From simplified two stream approximation to Delta-Eddington approximation

The radiative transfer for Rayleigh and aerosol scattering are computed using a very simplified two stream approximation (*Coakley and Chylek* [1975]) in order to reduce computing time. This is, of course, adequate if the aerosol loading is negligible which is not the case after large volcanic eruptions. Hence it is necessary to replace the simplified radiative transfer computations by the delta-Eddington approximations for a better estimate of the forcing in the case of high aerosol optical depths in clear sky conditions. In the model, the delta-Eddington approximation is already used for the calculation of radiative transfer due to the combined effect of aerosols and clouds, when high optical depths have to be expected.

Several model deficiencies and simplifications not justified for this study have been

identified in the SW radiation scheme and have been revealed. With a single column radiation model, the differences will be assessed.

## 3.6 Experiments using the stand-alone radiation code

### 3.6.1 Model setup and data description

A single column radiation model of ECHAM5 radiation scheme is used to investigate the effects of modifications of the SW scheme for selected atmospheric profiles thus excluding feedback effects that may occur in the full ECHAM5 GCM. This single column radiation model has 4 solar spectral wavelength bands instead of the 6 solar bands. The single column model consists of the radiation code extracted from ECHAM5 and hence, the effects of radiative forcing alone can be ascertained. The model is initialized with atmospheric profiles extracted from a control run of ECHAM5 for August, for the resolution T42L19. The surface conditions are specified by albedo, pressure and temperature and total cloud cover and vertical profiles of background aerosols, water-vapor, ozone, cloud cover, mass mixing ratios of liquid water and ice, saturation specific humidity and half and full level pressure and temperature. The single column model is run for the zenith angle specified for local noon in August. Optical properties of Pinatubo aerosols such as extinction, single scattering albedo and asymmetry parameter are fed into the model to assess the significance of the modifications in the case of high aerosol loading. All meteorological input parameters are derived as zonal means from the 3-dimensional model simulation. Constant volume mixing ratios are assumed for carbon dioxide (348 ppmv), methane (1.65 ppmv) and nitrous oxide (306 ppbv).

### 3.6.2 Description of experiments

Three sets of experiments given in table 3.1 are carried out to assess the parameterized radiative forcing. The details of these experiments are also mentioned in the table.

The change in fluxes for the sets of experiments in table 3.1 is investigated for the following cases shown in table 3.2.

| **Experiment** | **Description of the experiments** |
|---|---|
| CTRL | Simulations with original single column radiation model of ECHAM5 |
| Exp_A | Incorporating the effect of multiple reflection in the clear sky part in Near-IR |
| Exp_B | Incorporating the effect of multiple reflection in the clear sky part in Near-IR and the effects of the interactions between aerosol scattering and gaseous absorption |
| Exp_C | Using an improved set of mixing rules and avoiding the repetition of delta transformation (section 3.5.2) |
| Exp_D | Replacing the simplified two stream approximation by delta Eddington approximation (section 3.5.3) after including the changes from Exp_C |

Table 3.1: The sets of experiments carried out to assess radiative forcing

| **Cases** | **Experiments** |
|---|---|
| Case-1 (no_aer) | No aerosols: Only the effect of Rayleigh scattering and gas absorption are considered |
| Case-2 (bg_tanre) | Background Tanre aerosols (Tanre et al.,1984) only *The vertical profile of different types of Tanre aerosols as a function of optical thickness in shown in figure 3.8(a).* |
| Case-3 (tanre+pads) | Both Tanre and Pinatubo aerosols *The Pinatubo aerosol profile in the four solar spectral wavelengths are in shown in figure 3.8(b).* |
| Case-4 (high_aer) | High aerosol loading case for super volcanic eruptions. The optical depths are taken to be 100 times that of Pinatubo aerosol loading |
| Case-5 (single_aer) | A single aerosol layer at 100 hPa of optical depth 2.4 at 0.55 |

Table 3.2: The cases for which the sets of experiments given in table 3.1 are analyzed

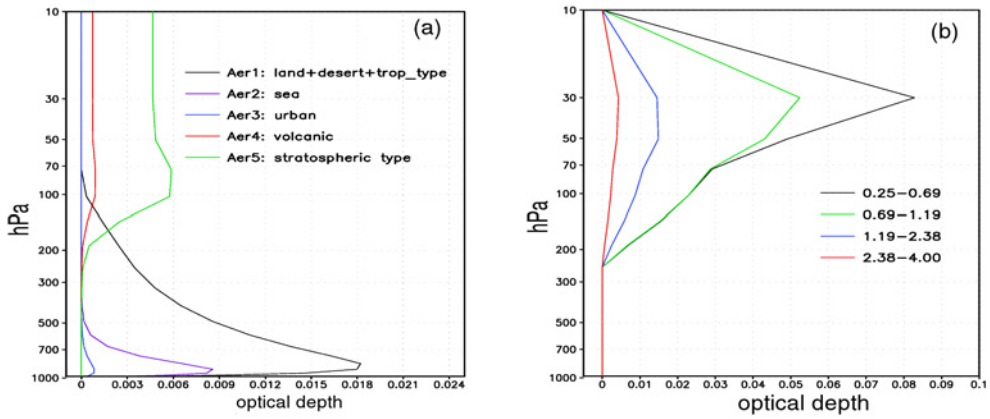


Figure 3.8: The zonally averaged profiles of optical thickness per layer of the (a) five background Tanre aerosol types at the equator at 0.55 $\mu$ and (b) Pinatubo aerosol at the equator for Aug 1991 for the ECHAM SW spectral bands. The pressure levels are in hPa.

### 3.6.3 Results and Discussion

Results are shown for net fluxes, downward and upward fluxes for all the cases explained in the previous sections for the differences Exp_A - CTRL, Exp_B - CTRL and Exp_C - CTRL. But, for Exp_D, instead of the deviations from CTRL, the difference Exp_D - Exp_C is considered where the delta modifications are also included in Exp_D. Clear and all sky values are shown for the experiments Exp_A and Exp_B, but, emphasis will be given for clear sky conditions and for all the other cases, results are shown for all sky conditions only. The figures are kept at the end of this section for brevity. Negative values of the fluxes imply that there is a decrease in the fluxes in the experiments compared to the original ECHAM5 run (CTRL) and vice versa.

For reference, the absolute values of net, downward and upward fluxes in the "No aerosol" case for the CTRL and the deviations Exp_B - CTRL and Exp_C - CTRL are presented in figure 3.9 to show the differences when only clouds and gas interacts with radiation. It can be seen that in both differences, the downward and upward fluxes are positive at lower layers (up to 200 hPa) indicating an increase in the fluxes in both the experiments compared to original ECHAM5. The high values beyond 60 N and S in Exp_B - CTRL are due to the high solar zenith angles encountered which emphasizes the effect of multiple reflection. The differences seen in this case even in the absence of aerosols are due to the presence of gases and Rayleigh scattering. Higher magnitudes in Exp_C - CTRL when compared to that of Exp_B - CTRL is because the mis-representations of mixing equations is considerable owing to large cloud optical depths and the results show an increase of up to 2 W/m$^2$ in the troposphere, in the region of clouds.

The zonally averaged net flux differences (figures 3.10 & 3.11) and the profiles at 15S (figure 3.12) for net, downward and upward fluxes for Case-2 (bg_tanre) is discussed below.

The clear sky deviations of Exp_A and Exp_B show a significant increase in net fluxes in the lower layers of up to 4 W/m$^2$ at the surface. Figure 3.10(b) shows the combined effect of multiple reflection as in figure 3.10(a) and interaction of aerosol scattering and gaseous absorption. There is an increase in net fluxes below 200 hPa and a decrease in net fluxes above. The same effect is also evident in all sky case (figure 3.10), but the magnitude and extent is less. This is because most of the radiation scattered by aerosols are absorbed by clouds or aerosols in the troposphere, thus reducing the amount of upward radiation. Compared to Case-1 (no_aer), the combined effects of aerosols and clouds can be seen in Exp_C - CTRL (figure 3.11), where there is a significant increase of net fluxes of 3 W/m$^2$ at the surface and a decrease of around 2.5-3 W/m$^2$ above the layer of aerosols and clouds. The differences in Exp_D - Exp_C are negligible as can be seen from figure 3.11 and therefore, the two stream method is a good approximation for low aerosol loadings.

The profiles at 15S in figure 3.12 explain in detail the change in fluxes after incorporating the modifications as in table 3.1 and after incorporating all the modifications when compared to original ECHAM5 in clear and all sky conditions. The latitude is chosen arbitrarily. Both downward and upward fluxes increase for all the experiments with respect to CTRL. For Exp_A - CTRL (black curve) and Exp_B - CTRL (green curve), the downward flux differences increase from the top of the model atmosphere (TOA) to a maximum difference at the surface. The magnitudes at the surface in all sky conditions are lower when compared to clear sky case due to the absorption by clouds. The difference in upward fluxes is negligible in Exp_A for both clear and all sky conditions, but significant in Exp_B signifying the importance of aerosol-gas interactions. The net fluxes in both clear and all sky conditions increase below the aerosol layer and decrease above or within the aerosol layer. The deviation in Exp_C - CTRL is shown as the blue line. The differences in downward fluxes in clear sky conditions is comparatively less than that in all sky conditions and there is a net flux decrease up to 2.5 W/m$^2$ at the TOA and up to 0.7 W/m$^2$ at the surface. The differences due to the changes from Exp_D (orange line) are seen to be minor. With all the modifications, denoted by the red line, the change in net fluxes at the TOA amounts to around 3 W/m$^2$ and to 2 W/m$^2$ at the surface.

The modifications due to Exp_C contribute to around 75% to the large fraction of the variance in the net fluxes including all the modifications compared to the CTRL at the TOA followed by Exp_B modifications that come to around 25% in clear sky conditions. These figures vary by only 5% in all sky conditions. The change in net fluxes after all the modifications at the surface for clear sky conditions are purely due to Exp_B (that includes the effects from Exp_A), whereas for all sky conditions the majority is contributed by the modifications due to Exp_B and partly by Exp_C. When compared to the red curve that includes all the modifications, the rate of increase in upward fluxes is dominated by the contributions from Exp_B and Exp_C.

The net fluxes of Case-3 single column calculations, where Pinatubo and background Tanre aerosols are included, are shown in the figures 3.13 and 3.14. The deviations for Exp_A and Exp_B, show well-marked net increase (decrease) below or within (above) the aerosol layer when compared to the Case-2 (bg_tanre) net fluxes. The changes due to modified mixing rules in Exp_C remain more or less the same. There is a slight decrease in net fluxes in Exp_D case, but they are still negligible.

The globally averaged noon values for net fluxes in August for Case-3 (tanre+pads) are shown in figure 3.15. Each color line follows the same code as in the previous case. It can be seen that the differences of the globally averaged net fluxes are higher in the stratosphere in Exp_C - CTRL (blue) compared to the other cases. The differences for each case in clear and all sky conditions magnify the role of clouds. After incorporating all the modifications, there is a decrease in TOA net fluxes by 5 $W/m^2$ in clear and by 3 $W/m^2$ in all sky conditions. At the surface, there is an increase around 3 $W/m^2$ in both clear and all sky conditions signifying the importance of these modifications.

Since changes in downward, upward and net fluxes in Exp_B also includes Exp_A and since Exp_D is more significant for high aerosol loadings, these two sets of experiments are only explained hereafter in detail for the remaining cases.

To assess how large these changes could be for extreme volcanic eruptions, Case-4 is defined as a hypothetical case where the optical depths are 100 times larger than Pinatubo. As mentioned before, limitations in the SW radiative transfer in ECHAM have to be taken into consideration when dealing with such high optical depths. The approximations used in radiative transfer are applicable when optical depths are less than 0.1 or 0.2. The approximation becomes less accurate for large optical depth and for large zenith angles. Hence, the results of such an extreme case should be dealt with caution as no improvements have been made in the radiative transfer calculations for the model to adapt to the huge optical depths. The results are presented here to examine a case of extremity and are shown in figure 3.16 in clear sky conditions for Exp_B and in all sky conditions for Exp_D. A huge increase in net fluxes below the aerosol layer and a decrease above is evident in Exp_B that corresponds to regions of high aerosol optical thickness and net fluxes decrease through out the layer with improved calculation of radiative transfer. The notable differences in fluxes with the inclusion of aerosol-gas interactions and improved methods for radiative transfer calculations highlight the significance of these effects.

Since both Pinatubo aerosols and background Tanre aerosols are widely dispersed around the globe and over several layers of the atmosphere, it is much simpler to understand the same effects with a single aerosol layer in the atmosphere. Hence, a single aerosol layer at 100 hPa with an aerosol optical depth that is 10 times the maximum Pinatubo aerosol optical depth is considered in Case-5. The difference, Exp_B - CTRL in clear sky case and Exp_D - Exp_C in all sky for net, downward and upward fluxes are presented figure 3.17.

A clear distinction in the increment of upward and downward fluxes is evident in Exp_B - CTRL. It can be also seen that there is no change in the downward fluxes until the radiation encounters the aerosol layer. The upward fluxes increase throughout the model layers. The increase in downward fluxes below the aerosol layer is higher than the increase in upward fluxes and the opposite is observed above or within the aerosol layer. The upward fluxes mainly depend upon the surface albedo and on the radiation reaching the surface. And since only the radiation reaching the surface is modified or increased by the inclusion of the afore-mentioned modifications the upward fluxes increase, whereas the downward fluxes are modified when the radiation encounters the aerosol layer. This explains the increase in the net fluxes below the aerosol layer and a decrease in the net fluxes above or within the aerosol layer. A single aerosol layer of significant optical depth can result in a maximum increase of surface downward fluxes up to 4 $W/m^2$ and a maximum increase of upward fluxes at the TOA up to 2 $W/m^2$ in clear sky conditions. These changes can result in an increase of up to 3 $W/m^2$ in the surface net fluxes and a decrease of net fluxes at the TOA up to 2 $W/m^2$ that cannot be neglected. Replacing the adding two stream approximation by the delta-Eddington approximation results in a decrease of both the downward and upward fluxes below and within the aerosol layer and an increase in upward fluxes above the aerosol layer, thus reducing the net fluxes throughout the layer in the latitudinal band of 30S - 60N and vice versa at the latitudes beyond this band. The reversal of the sign happens at these latitudes in August in noon because of the solar angle dependency of the Exp_D - Exp_C differences. The net fluxes change by a maximum of 0.6 $W/m^2$.

To summarize, the simplified SW radiation scheme of ECHAM5 has been modified to simulate the effect of volcanic eruptions more efficiently. Several cases were investigated such as the effects of multiple reflection and interactions between aerosol scattering and gaseous absorption, improved mixing rules for combining the optical properties of aerosols, clouds and gases and improved radiative transfer methods. There are significant changes with the improvements in mixing rules due to the high cloud optical depths, whereas the effects of multiple reflection and aerosol-gas interactions in clear sky conditions were important for high aerosol optical depths as in the Pinatubo case. The implementation of an improved radiative transfer method seems to be important for very high aerosol optical depths as in the case of super-volcanoes or dust aerosols.

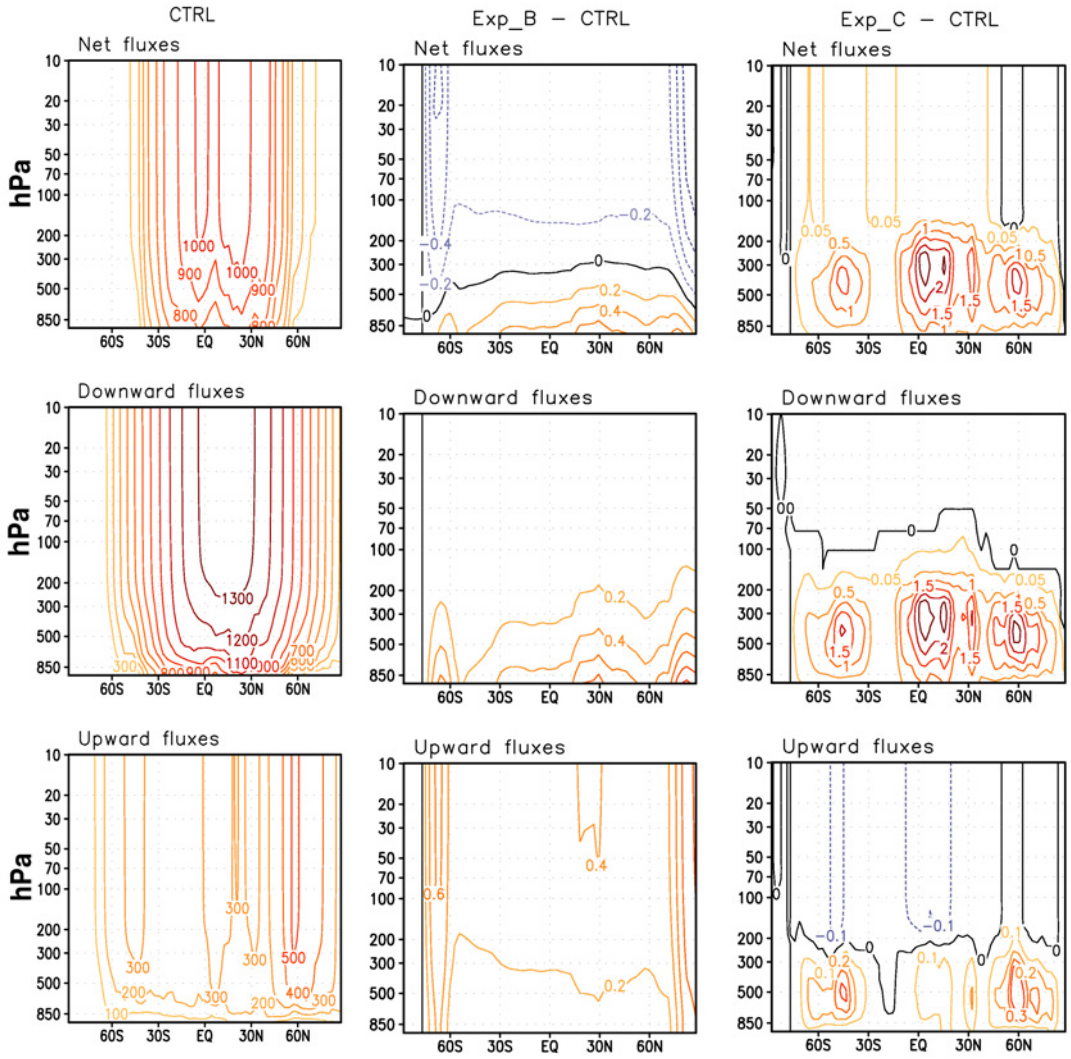


Figure 3.9: Net fluxes, downward and upward fluxes in W/m$^2$ for absolute values in CTRL and differences Exp_B - CTRL and Exp_C - CTRL in all sky conditions for the "No aerosol" case. The increase in fluxes when compared to that of the CTRL is shown in red (positive values) and the decrease in fluxes are shown in blue (negative values).

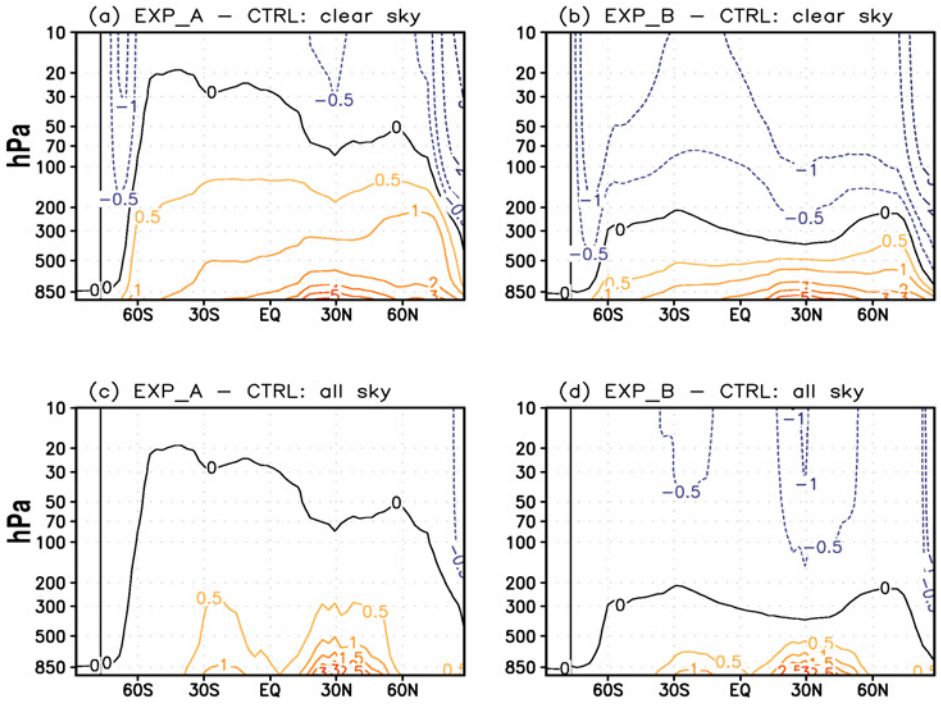


Figure 3.10: The differences in net fluxes in W/m$^2$ for the "background Tanre aerosols only" case in Exp_A - CTRL and Exp_B - CTRL in clear sky (upper row) and all sky (lower row) conditions. The contouring follows the same convention as in the previous figure.

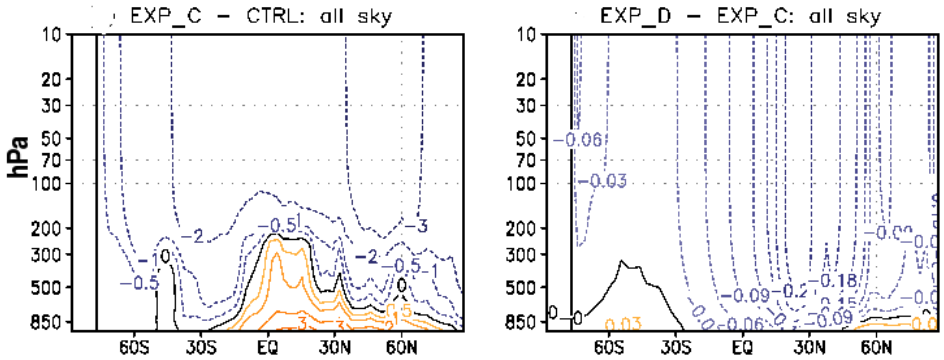


Figure 3.11: The differences in net fluxes in W/m$^2$ for the "background Tanre aerosols only" case in Exp_C - CTRL (left) and Exp_D - Exp_C (right) in all sky conditions. The contouring follows the same convention as in the previous figure.

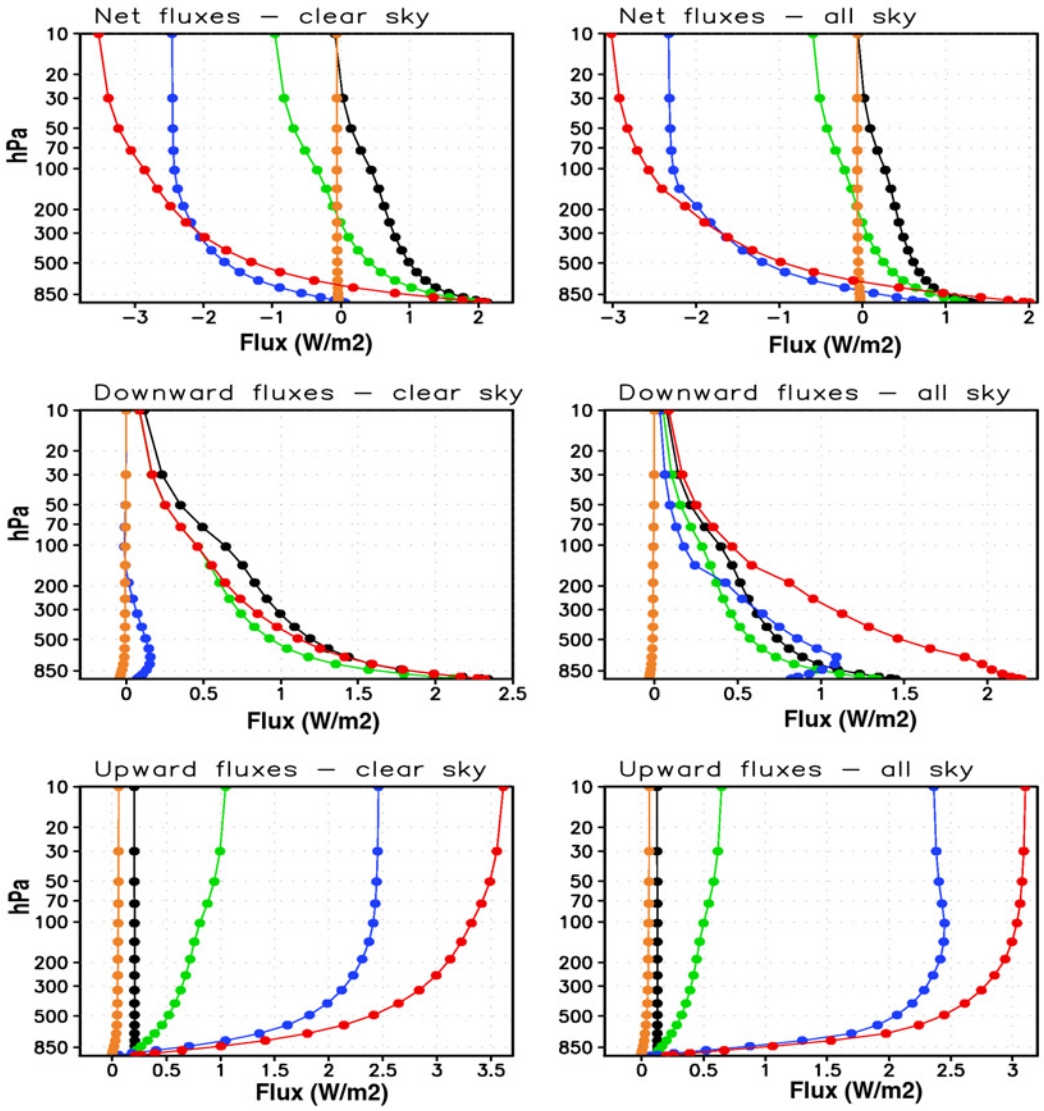


Figure 3.12: Vertical profiles at 15S of differences of net fluxes (upper panel), downward (middle panel) and upward fluxes (lower panel) in Exp_A - CTRL (black), Exp_B - CTRL (green), Exp_C - CTRL (blue), Exp_D - Exp_C (orange) and incorporating all the modifications (red) for clear (right column) and all (left column) sky conditions in the "background Tanre aerosols only" case. The fluxes are in W/m$^2$.

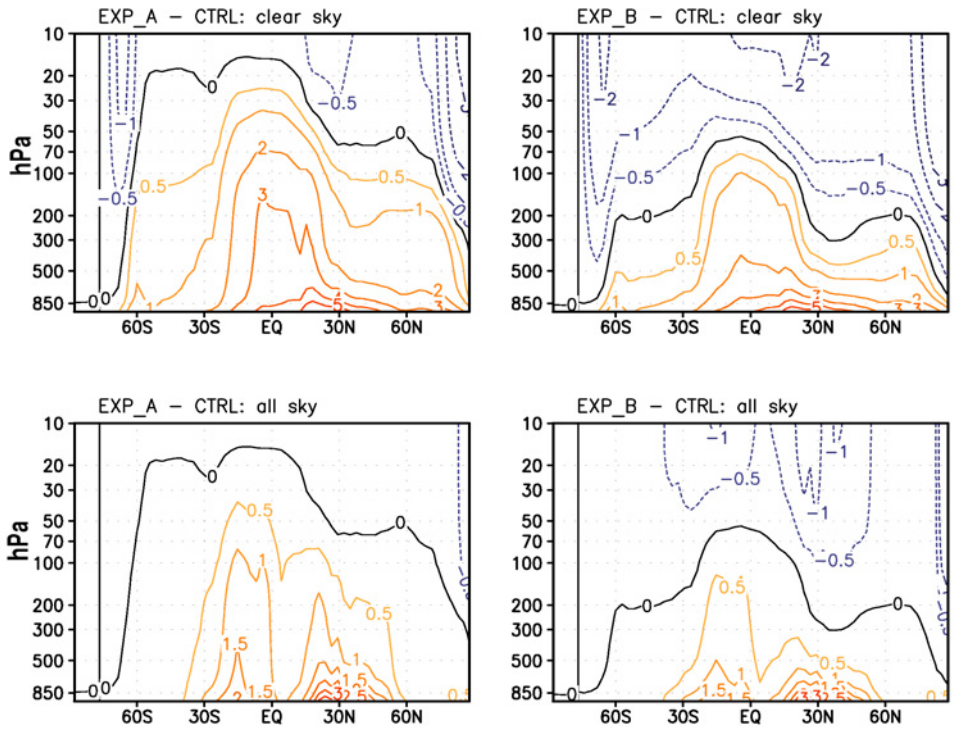


Figure 3.13: The differences in net fluxes in W/m$^2$ for the "Pinatubo and background Tanre aerosols" case in Exp_A - CTRL and Exp_B - CTRL in clear sky (upper row) and all sky (lower row) conditions. Positive values are in red and negative values in blue.

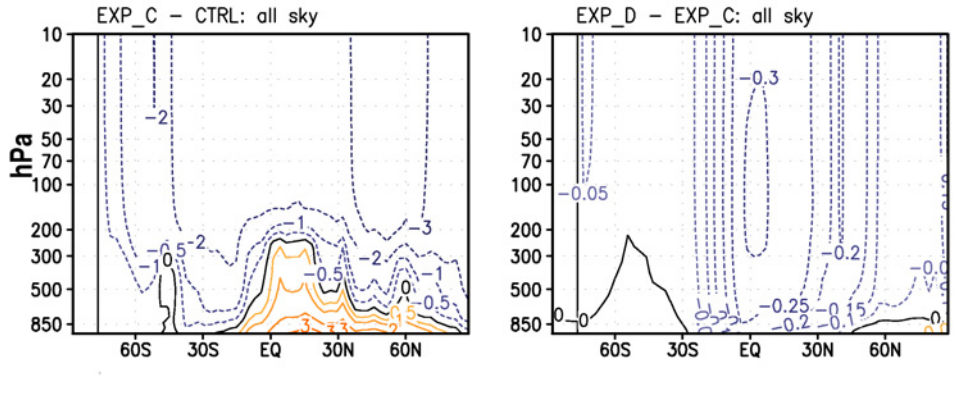


Figure 3.14: The differences in net fluxes in W/m$^2$ for the "Pinatubo and background Tanre aerosols" case in Exp_C - CTRL (left) and Exp_D - Exp_C (right) in all sky conditions. The contouring follows the same convention as in the previous figure.

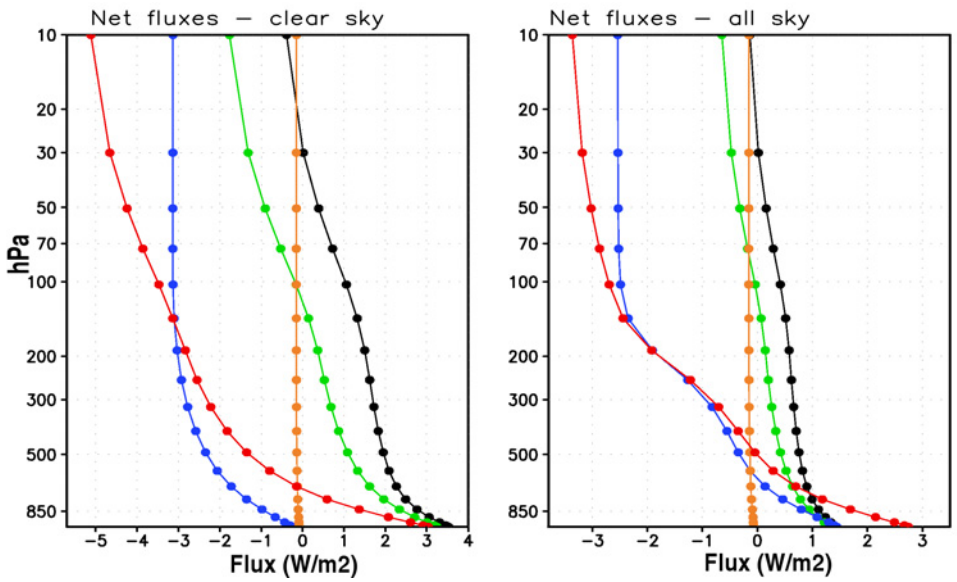


Figure 3.15: Globally averaged noon values of the net fluxes in W/m$^2$ in clear and all sky conditions in W/m$^2$ for Exp_A - CTRL (black), Exp_B - CTRL (green), Exp_C - CTRL (blue), Exp_D - Exp_C (orange) and incorporating all the modifications (red) for the "Pinatubo and background Tanre aerosols" case.

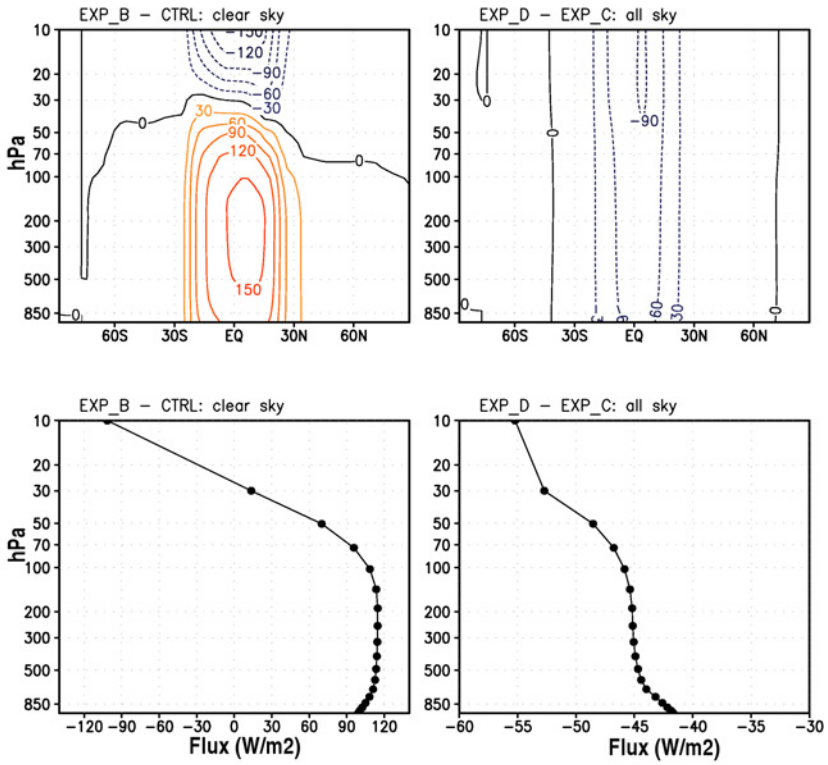


Figure 3.16: The differences in net fluxes in W/m$^2$ for Exp_B - CTRL in clear sky (left column) and Exp_D - Exp_C (right column) in all sky conditions and the profiles at 15S for the same for "super-volcano" case.

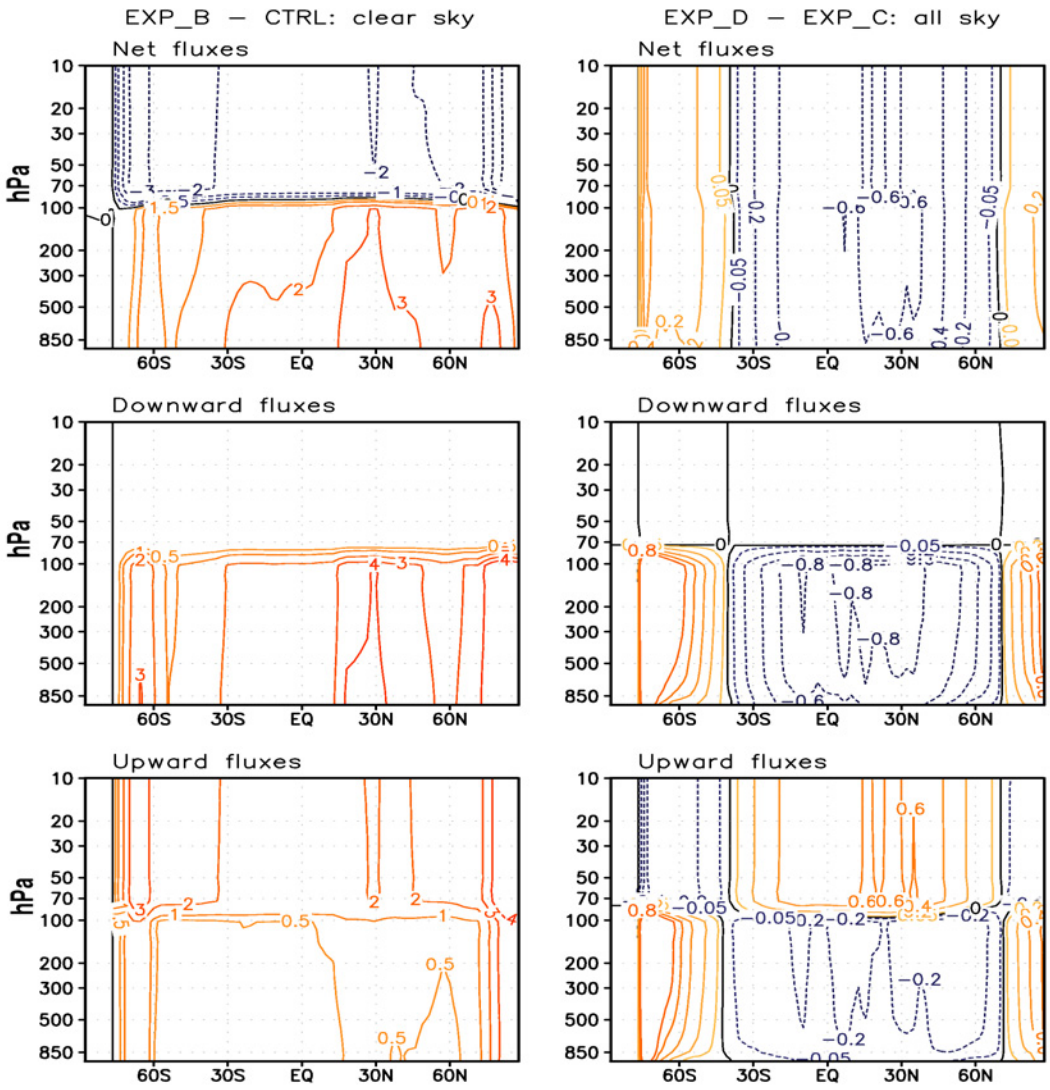


Figure 3.17: Changes in net fluxes (upper panel), downward (middle panel) and upward (lower panel)fluxes in Exp_B - CTRL (left panel) for clear sky and Exp_D - Exp_C (right panel) for all sky for "an aerosol layer at 100hPa" case. The fluxes are in W/m$^2$.

## 3.7 Analyzing the full model performance

The above-mentioned improvements used in the single column radiation calculations are incorporated in the full model to test the temperature response in the tropical atmosphere with prescribed Pinatubo aerosols. Model simulations were carried out at the T42L19 resolution. The heating rate anomalies in the shortwave for Aug 1991 after incorporating all the modifications are presented. As mentioned before, the simulated SW heating rate anomalies (figure 3.18(b)) were two times higher than the previous studies by ST-98. By incorporating all the modifications, it can be seen that the modelled SW heating rate is improved considerably (figure 3.18(c)) and are in good agreement with that of the previously published values (figure 3.18(a)).

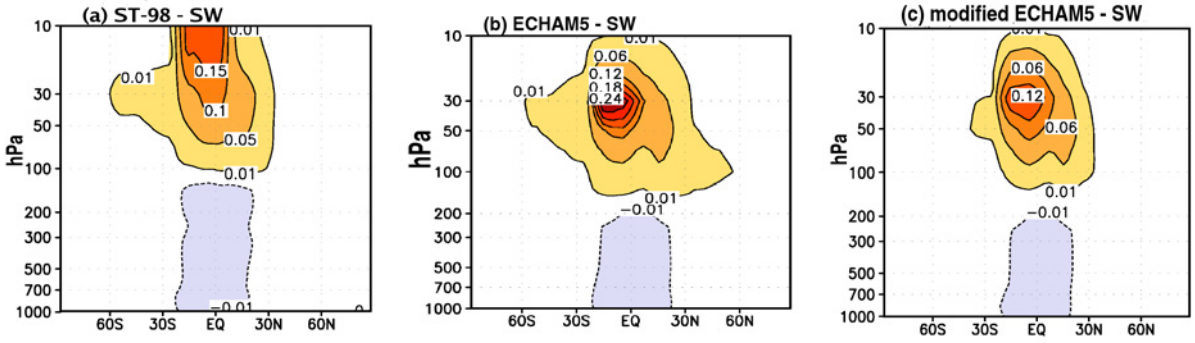


Figure 3.18: Solar heating rate anomalies (K/d) for Aug 1991 as in (a) Stenchikov et al., 1998 (b) simulations with original ECHAM5 and (c) improved ECHAM5 radiative parameters.

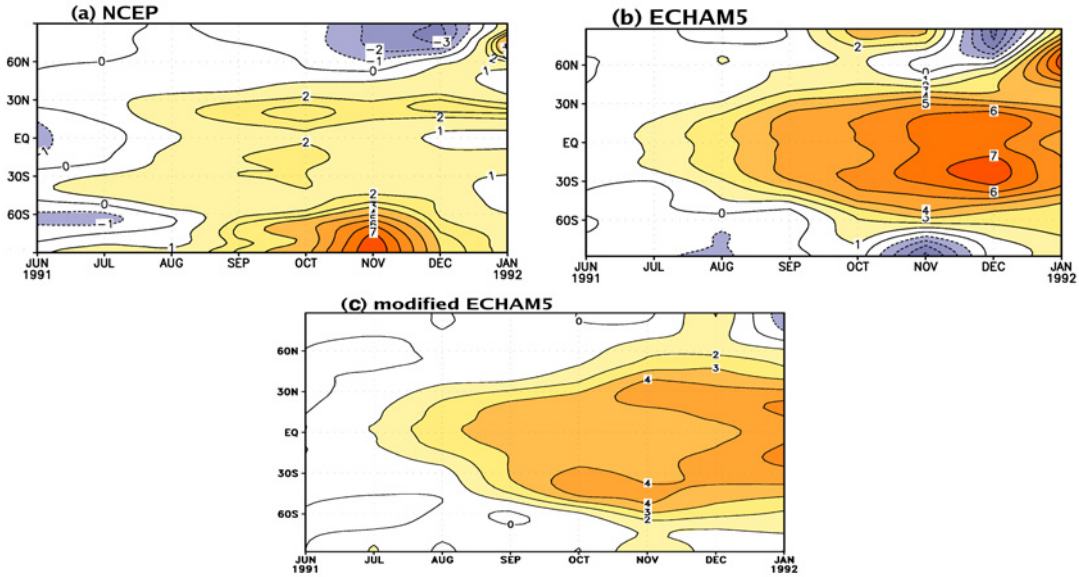


Figure 3.19: Temperature anomalies at 50 hPa (K) as in (a) NCEP (b) simulations with original ECHAM5 and (c) modified ECHAM5 for the period Jun 1991 - Jan 1992.

The lower stratospheric (50 hPa) temperature response is significantly reduced after incorporating the modifications with local maxima of 5K instead of 7K (figure 3.19(b)) and is shown in figure 3.19(c).

The results shown above are from only one realization. Deviations are expected because of neglected factors as for example, the ozone reduction, QBO effects and coarse vertical resolution.

## 3.8 Model sensitivity to the choice of aerosol dataset

Many aerosol datasets have been used for simulating the climate impact of Pinatubo eruption ( *Stenchikov et al.* [1998]; *Kirchner et al.* [1999]; *Ramachandran et al.* [2000]; *Stenchikov et al.* [2006]). In order to evaluate the model sensitivity to the choice of these datasets, this section discusses how much the resulting warming in the tropical lower stratosphere owing to Mt. Pinatubo eruption depends on the uncertainty in these datasets. We consider two datasets of aerosol optical depths differing slightly from one another. The datasets are named as PADS and SAD. PADS is Pinatubo Aerosol Data Set and SAD is Sato Aerosol Data described in detail in chapter 2.

The difference in extinction (1/m) values at 50 hPa in the visible band for the two datasets is shown in figure 3.20. It is clear that PADS has higher extinction values compared to SAD that show the level of uncertainty in the aerosol datasets retrieved using different spectral wavelength bands.

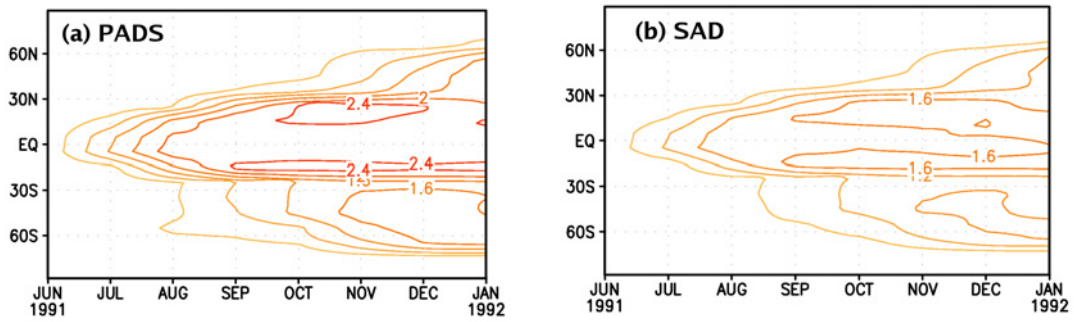


Figure 3.20: Extinction(1/m*1.0e+05) at 50 hPa in 0.55 micron for 2 datasets: (a) PADS (b) SAD for 8 months after the eruption.

To compare their effects, these aerosol datasets are used in ensembles of 3 integrations for each dataset differing in their initial conditions and an additional ensemble of 3 simulations without aerosol perturbations. The model runs for only 7 months after the eruption. Ensemble mean anomalies are calculated as the difference between ensembles with and without aerosols. The lower stratospheric temperature response at 50 hPa is presented in figure 3.21. Since the response is the average of only 3 ensemble members, in this study we

focus only on the tropical stratosphere. Due to the higher variability in the extratropics, one would need many more ensemble members so as to get a statistically significant signal in high latitudes.

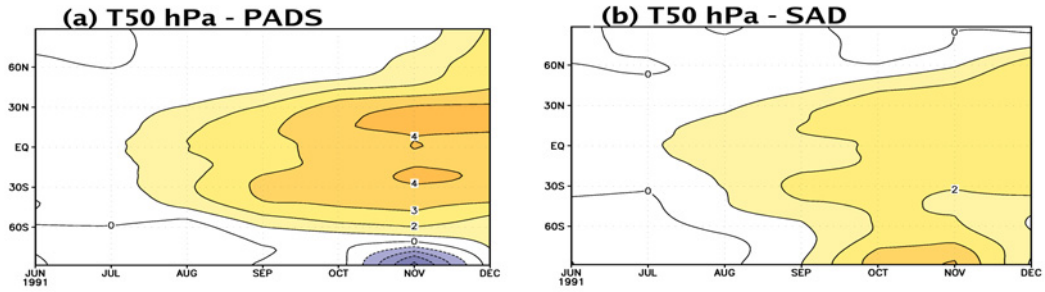


Figure 3.21: Stratospheric temperature anomalies (K) at 50 hPa using (a) PADS (b) SAD

The model sensitivity to the different datasets is clearly reflected in the simulated temperature response (refer fig. 3.21(a) and fig. 3.21(b)). There is a significant reduction in the tropical stratospheric warming up to 2K with SAD, that is very close to the observations. After including all the modifications in the radiation scheme, SAD seems to reproduce the observed stratospheric temperature response more realistically and hence is used for the following study.

## 3.9 Summary

ECHAM5 was overestimating the SW heating rate anomalies and hence, the lower stratospheric (50 hPa) temperature response after the Pinatubo eruption. The SW heating rate anomalies were two times higher than that of the previous studies from ST-98. This overestimation is due to the simplified assumptions for low aerosol loadings in the clear sky conditions, which are not valid for high aerosol loadings after volcanic eruptions. For efficiency reasons, the effects of multiple reflection and the interactions between aerosol scattering and gaseous absorption were neglected. The effect of aerosol-gas interactions and the multiple reflection effect are contradictory to one another. The inclusion of aerosol-gas interactions decreases the photon path, resulting in more absorption by the gas molecules resulting in heating. However, the multiple reflection effect increases the photon path, thereby reducing the energy for absorption resulting in cooling. And these effects depends upon the properties of aerosol particles. In the case of sulfate particles that are considered here, the aerosols formed are mostly scattering in the visible range, thereby reducing the photon path and resulting in cooling. Modifications were made in the model so as to include these effects, showing that the multiple reflection effect is a dominant effect for scattering particles.

Minor corrections were made to remove the inconsistencies in the way the individual atmospheric particles were combined in the model. These corrections are required irrespective

of high or low aerosol loadings. Moreover, a more complicated scheme is used to compute the radiative transfer. However, it is shown that this implementation seems to be important for very high aerosol optical depths as in the case of super-volcanoes or dust aerosols. After introducing all these effects, ECHAM5 shows a better agreement with observations in simulating the stratospheric temperature response after Pinatubo.

The notable differences in the responses with the inclusion of aerosol-gas interactions and multiple reflection effect and improved methods for radiative transfer calculations emphasizes the significance of these effects

The sensitivity of the model to different Pinatubo aerosol datasets is evaluated. Both these Pinatubo aerosol datasets (PADS and SAD) have been compiled by Gera Stenchikov (*Stenchikov et al.* [1998]) from SAGE and UARS satellite data. The only difference between these datasets is that PADS make use of the SAGE retrievals at 1.02 $\mu$m and SAD make use of retrievals at 0.55 $\mu$m. There is a significant difference in the lower stratospheric temperature response simulated with these two datasets.

# Chapter 4

# Evaluation of responses to individual and combined forcings by volcanic aerosols, SST variations and the QBO phases

## 4.1 Introduction

Large tropical volcanic eruptions can impact global climate by reducing the amount of solar radiation reaching the Earth's surface, lowering temperatures in the troposphere, increasing temperatures in the tropical stratosphere and thereby, changing atmospheric circulation patterns. The circulation in the lower atmosphere can be affected by short term stratospheric perturbations, for example, ozone changes (*Rind et al.* [1992]; *Grainger et al.* [1993]; *Kodera* [1994]). It is thus, interesting to explore the various ways in which the stratospheric perturbations can influence the tropospheric circulation. Both models and observations point out to the fact that the troposphere and middle atmosphere are coupled through wave mean flow interaction, especially with respect to planetary Rossby waves (*Sassi et al.* [2004]; *Graf et al.* [2007]).

The variability in the stratosphere is mainly due to anomalous boundary forcings or natural internal variations. Natural internal variability arises from the non linearity of the dynamics of the circulation in the middle atmosphere. Boundary forcing arises from variations in the tropospheric forcing such as changes in radiative budget due to changes in atmospheric composition such as ozone depletion via volcanic aerosols/anthropogenic influences or re-distribution of tropical heat source such as the ENSO events. This can in turn give rise to vertically propagating wave disturbances (*Holton* [1982]; *Matsuno* [1970]). But, in the real world, where the circulation evolves under the continuous influence of a

combination of factors, it is not simple to determine the responses to single influencing factors. For example, it is not possible to isolate the ENSO effects from other elements of natural variability if the signal is small and is strongly varying because of internal variability (*Hamilton* [1993]; *Baldwin and O'Sullivan* [1995]). However, it is possible to do so using a numerical model, for example, where ENSO is the only specified source of variability in addition to internal model dynamics and other surface properties like snow cover or soil moisture, which are computed by the model.

The observed climate evolution following a major volcanic eruption (discussed in introductory chapter) has significant anomalies compared to climatology, indicating a link between the major volcanic eruptions and the climate anomalies. These have, however, occurred under additional influences of SST anomalies (e.g. El Niño) and the specific phases of the QBO and possibly other influences. Hence while simulating this impact, one must consider all these interactions. In this chapter, the generalized climatic response to Mt. Pinatubo eruption with different boundary conditions is examined. The response of the tropospheric and stratospheric circulation to individual and combined factors including volcanic forcing, varying SST boundary conditions and different states of the QBO are assessed. This is important as this gives us insights on how the climate responds to the volcanic aerosol radiative forcing in which either one or more of the boundary conditions such as El Niño, QBO phase etc are included.

The main scientific questions addressed in this chapter are the following:

1. What is the pure effect of volcanic radiative forcing under different boundary conditions?
2. Is the combined aerosol and ocean response linear or non-linear?
3. What is the combined aerosol response with different boundary conditions?

This study is the first attempt to include all the important factors such as the effects of QBO, El Niño and volcanically induced ozone anomalies for the simulation of Mt. Pinatubo eruption and to analyze the response to individual and combined forcings using the same atmospheric general circulation model, which is the middle atmosphere ECHAM5 (MAECHAM5) model.

## 4.2 Violent volcanic eruptions

In the past, there were large volcanic eruptions that have been studied in detail from models and observations. Many of them caused observable impacts to the climate system (e.g. *Robock and Mao* [1992]; *Grant et al.* [1994]; *Robock and Mao* [1995]). Three major volcanic eruptions, namely, Agung (1963), El Chichón (1982) and Mt. Pinatubo (1991) are documented well since the start of the satellite measurements and due to the availability of re-analysis datasets such as NCEP and ERA-40. In this section, attempts are made to quantify the tropical and high latitude responses to these three major volcanic eruptions.

For this, a detailed description of the observed anomalies following the eruptions is presented.

An overview of the three volcanic eruptions in consideration is briefly summarized in the table A.1. Firstly, all these eruptions were of the explosive type (shown by VEI), injecting million tonnes of $SO_2$ into the stratosphere, which is chemically converted to $SO_4$ that forms sulfate aerosols. Secondly, these eruptions happened in the tropical belt and hence the aerosols were dispersed over the entire globe in a relatively short period of time by stratospheric winds. Finally, all the three volcanic eruptions occurred during an evolution of an El Niño event.

| **Volcano** | **Latitude** | **Longitude** | **Date of eruption** | **VEI** | **$SO_2$ (Mt)** |
|---|---|---|---|---|---|
| **Agung** | $8^0$S | $116^0$E | March 17, 1963 | 4 | 4 |
| **El Chichón** | $17^0$N | $93^0$W | April 3, 1982 | 4-5 | 5-9 |
| **Mt. Pinatubo** | $15^0$N | $120^0$E | June 15, 1991 | 5-6 | 17-20 |

Table 4.1: Details of the three major volcanic eruptions. The values for the amount of $SO_2$ are taken from *Krueger et al.* [1995].

Hence, these eruptions are chosen as representative cases to investigate the observed impacts of violent tropical eruptions on atmospheric circulation. ERA-40 re-analysis data are used for the analysis of climate anomalies following these eruptions.

## 4.3 ERA-40 Re-analysis data

ERA-40 is a re-analysis of meteorological observations from September 1957 to August 2002 produced by the European Center for Medium-Range Weather Forecasts (ECMWF) in collaboration with many institutions (*Uppala et al.* [2005]). The observations that entered the re-analysis were provided by surface and sonde observations and a succession of satellite-borne instruments from the 1970s onwards, supplemented by aircraft measurements and ocean-buoys. ERA-40 provides fields with higher vertical resolution compared to NCEP/NCAR Re-analysis (*Kalnay and coauthors* [1996]) and is the best data available for the purpose of this study.

In this study, the monthly data for 43 years from January 1958 to December 2001 are used for the computation of the mean climatology. The data is evaluated on a $2.5^0$x$2.5^0$ grid at 23 vertical pressure levels extending from 1000 to 1 hPa.

Here, the tropical and high latitude responses are discussed. The main idea behind

analyzing these responses is to quantify robustness and variability of the anomalies. For tropical responses, the lower stratospheric temperature anomaly at 30 hPa and 50 hPa for the three volcanic eruptions are investigated. Further, the wind profiles, surface temperature and 30 hPa geopotential height anomalies in two winters following the volcanic eruptions are analyzed for the winters of 1963-1964 and 1964-65 for Agung, 1982-83 and 1983-84 for El Chichón and 1991-92 and 1992-93 for Mt. Pinatubo eruption to understand the high latitude response. In order to understand the natural variability in temperature and geopotential, boreal winters are chosen excluding the volcanic years. 35 winters are chosen to represent the general winters excluding volcanic winters.

## 4.4 The observed volcanic responses

### 4.4.1 Tropical response

As the three largest volcanic eruptions in the last 50 years occurred in conjunction with El Niño events, it is important to look into the strength of the El Niño events during these eruptions. For this, the Niño3.4 index, which is the averaged sea surface temperature anomaly taken from ERA-40 over the region 5S-5N and 170W-120W is calculated. The Niño3.4 index, after a 3 month running mean is presented for all the eruptions in figure 4.1 for two years after the respective volcanic eruptions. To accommodate all the eruptions in one figure, the time axis is shown for three years and the eruption date for the volcanoes are shown by the vertical bar. Since the eruption occurred at different times and for comparison purposes, the time axis is labelled arbitrarily. The El Niño event was much stronger during El Chichón eruption compared to Mt. Pinatubo eruption. Weaker positive anomalies were observed during Agung eruption

The lower stratospheric temperature response at 30 hPa and 50 hPa after Agung, El Chichón and Mt. Pinatubo is shown in figure 4.2. Here, the main focus is on the tropical response as the high latitude response is highly variable. The maximum standard deviation in lower stratospheric temperature in the tropics calculated from ERA-40 data is $\pm$2K, where the QBO dominates the variability in the equatorial stratosphere whereas in the high latitude winter hemisphere it is $\pm$12K. It can be seen that the tropical responses vary largely from eruption to eruption in magnitude and pattern. This may be due to the differences in the spatial distribution of aerosols and the wind patterns. For the first few months after the eruption, the maximum temperature anomaly is observed at the equator and reaching a maxima of up to 4 K in the case of Agung and El Chichón (*Newell* [1970]; *Labitzke et al.* [1983]; *Angell* [1997a]) and straddling around the equator reaching a maxima up to 3 K in the case of the Mt. Pinatubo eruption (*Hansen et al.* [1992]; *Labitzke and McCormick* [1992]; *Labitzke* [1994]). This difference in the responses can also be attributed to the amount of ozone loss and to the phase of the QBO.

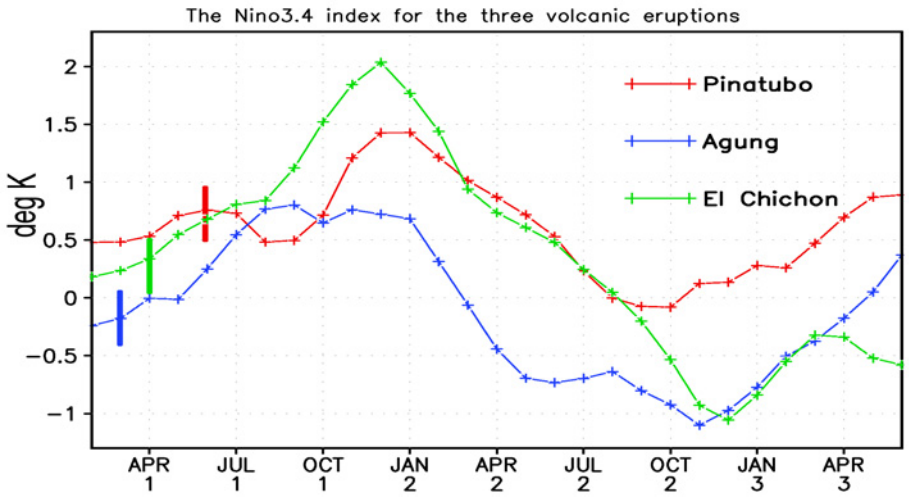


Figure 4.1: Three month running mean of SST anomalies (K) from ERA-40 averaged over the region 5S-5N and 170W-120W (Niño3.4 index) calculated for the three volcanic eruptions: Agung - March 1963 (blue line); El Chichón - April 1982 (green line) and Mt. Pinatubo - June 1991 (red line). The x-axis is the time axis that goes from February for 3 years. The eruption time is shown for all the eruptions by the vertical bar.

To understand the phase of the QBO during these eruptions, the vertical profiles of zonal mean zonal wind anomalies averaged over 5N-5S is presented for all the three volcanic eruptions (fig 4.3) for the years following the eruption. As can be seen, Agung and El Chichón erupted during the QBO's easterly phase at 30 and 50 hPa. The QBO phase then changed within a few months to westerlies. The westerly phase lasted longer in the case of Agung eruption. For the El Chichón case, the descent of the easterly phase was more rapid, therefore, phase changes occur at 30 hPa twice. Mt. Pinatubo erupted during QBO's easterly shear at 30 hPa and then phase change took place in July 1992 at 30 hPa and in January 1993 at 50 hPa. This can have different consequences on the stratospheric response, even though all the three eruptions had some features in common.

As cited before, the sulfate aerosols are highly scattering in the visible range of the spectrum, thereby reflecting the solar radiation and hence, cooling the atmosphere below the aerosol layer. Figure 4.4 shows the spatial pattern of the summer temperature anomalies (JJA averaged) following the eruptions. Since Mt. Pinatubo erupted in mid June, only the summer following the eruption is considered here. As expected, global surface cooling up to 1-2K is observed after volcanic eruptions depending on the aerosol optical depths. It has to be noted that a warm anomaly is observed over central Europe following all the eruptions. The El Niño events are also evident during the summers of 1963, 1982 and 1983.

**Agung, March 1963**

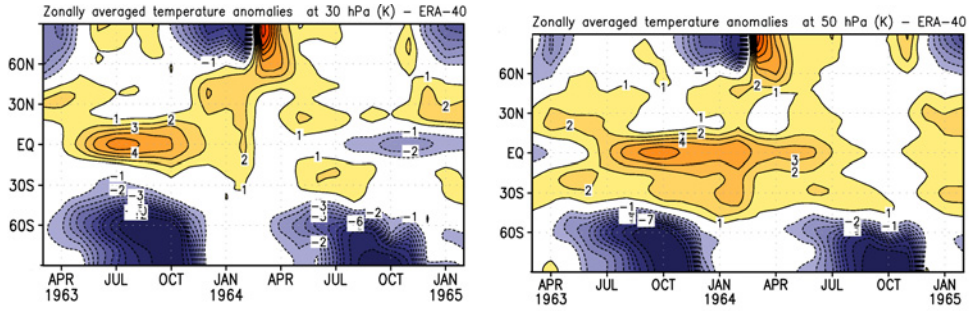


**El Chichón, April 1982**

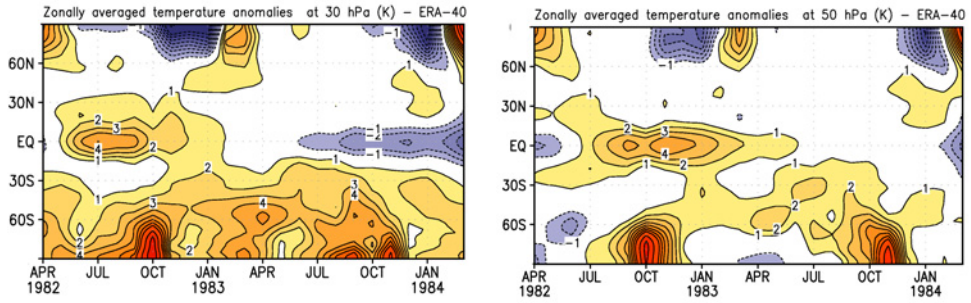


**Mt. Pinatubo, June 1991**

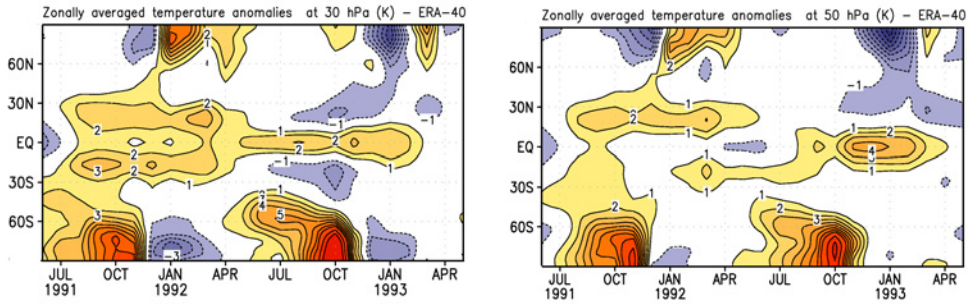


Figure 4.2: The lower stratospheric zonal mean temperature (K) anomaly at 30 hPa (left column) and at 50 hPa (right column) for the three volcanic eruptions: Agung (top row); El Chichón (middle row) and Mt. Pinatubo (bottom row).

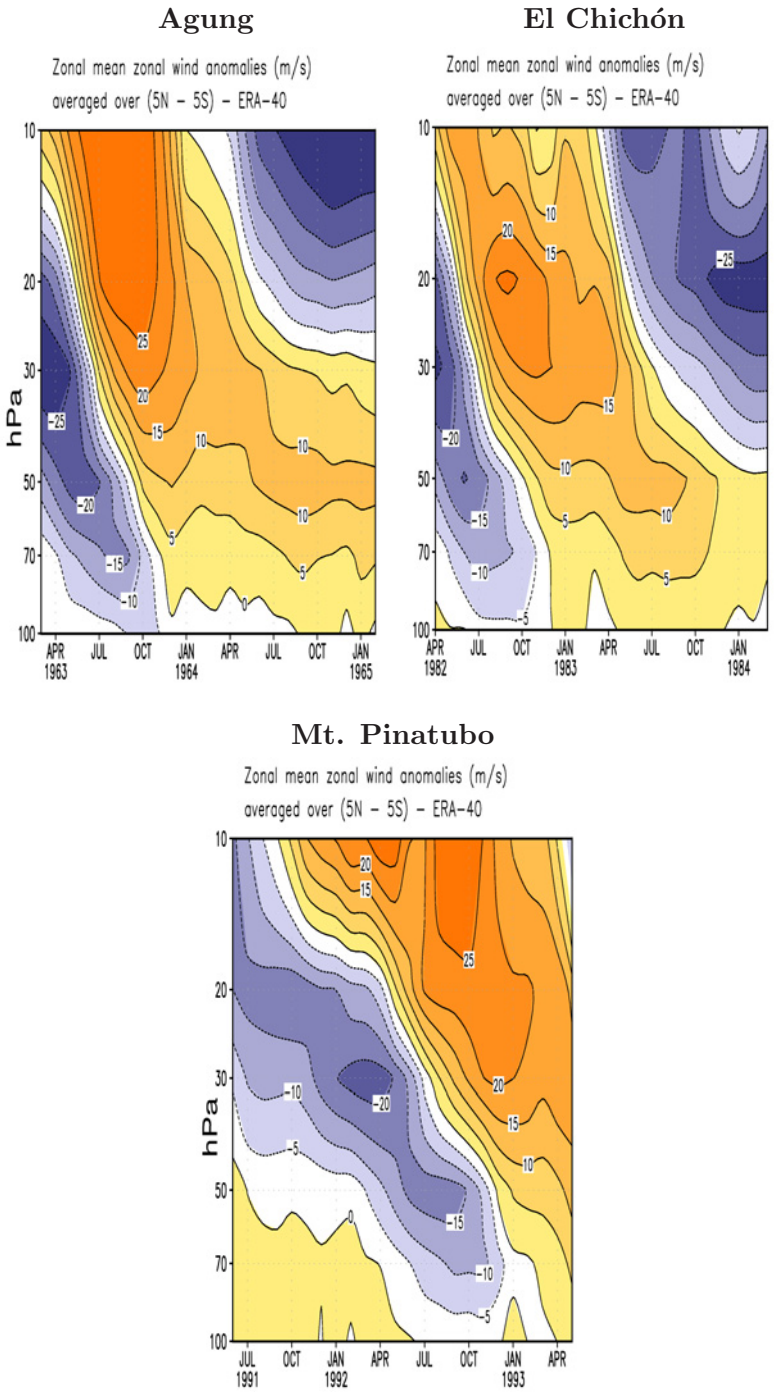


Figure 4.3: Vertical profile of zonal mean zonal wind anomalies (m/s) averaged over 5N-5S (m/s) for Agung (left, top row); El Chichón (right, top row) and Mt. Pinatubo (bottom row).

**Agung, March 1963**

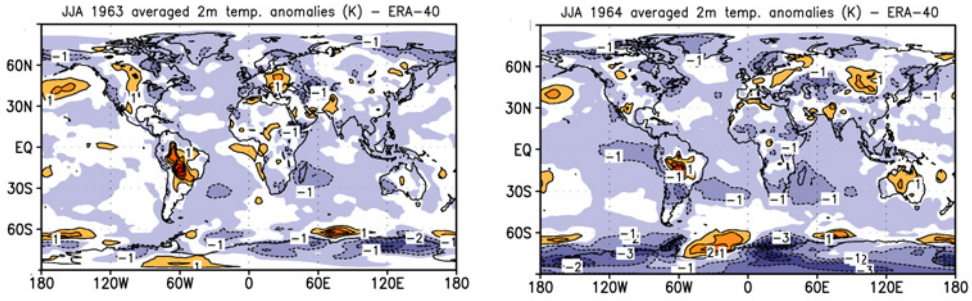


**El Chichón, April 1982**

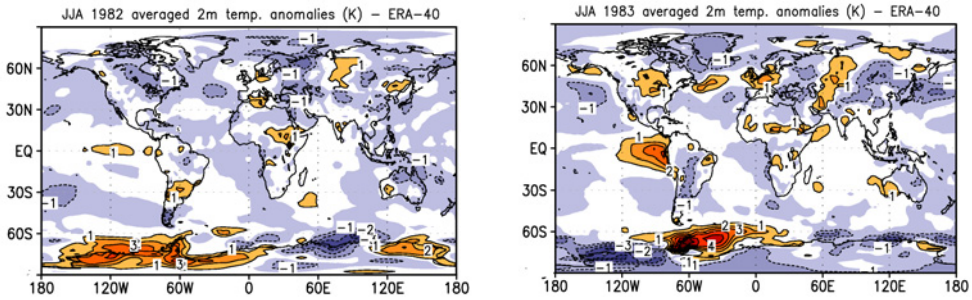


**Mt. Pinatubo, June 1991**

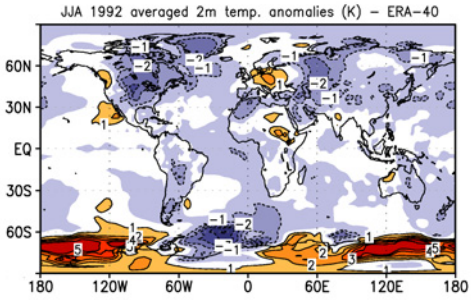


Figure 4.4: The JJA averaged 2m temperatures (K) for the three volcanic eruptions: Agung - JJA/63 and JJA/64 (top row); El Chichón - JJA/82 and JJA/83 (middle row) and Mt. Pinatubo - JJA/92 (bottom row).

### 4.4.2 Natural climate variability

To facilitate better understanding and quantification of the observed extratropical impacts of volcanic eruptions that will be discussed in the next section, it is necessary to evaluate the natural climate variability. This is important as there is a significant variability in the winter hemisphere. Hence, this section focusses on the climatology and the standard deviation of the key parameters for the Northern Hemisphere winter. Here, the climatology is based on 43 winters (averaged December, January and February (DJF) months) from 1958-2002 taken from ERA-40. Figures 4.5 - 4.8 show the climatological mean and the standard deviation (SD) for 2m temperature, 30 hPa geopotential heights, zonal mean zonal winds (hereafter, referred to as U) and zonal mean temperature.

The climatology of the surface temperatures for boreal winter is presented in figure 4.5. It can be seen that the temperatures are warmer in the tropical belt compared to the mid and high latitude regions. The temperatures reach as high as 300 K in the tropics and as low as 240 K in the high latitudes. The variability is strong in the winter high latitudes as can be seen in the SD of the climatological winter means. This is due to the prominent mode of interannual variabilities such as the North Atlantic Oscillation, the Arctic Oscillation and the ENSO. In the tropics, the variability is around 1K, but in the mid and high latitudes the variability is around 3-4 K.

The climatological mean of the 30 hPa winter geopotential heights is shown in figure 4.6. The figure shows low climatological mean values of $22*10^3$ gpm at the polar latitudes and comparatively high values at mid-latitudes. The variability as seen from the corresponding SD plot is high in the high latitudes (up to 500 gpm) and very low (below 100 gpm) in the NH tropics.

The distribution of U is shown in figure 4.7. U shows a strong polar vortex with westerly winds reaching a maximum of 40 m/s in the upper stratosphere. The subtropical jet is also evident with westerly winds as high as 35-40 m/s. The climatology of the winds in the tropics in the stratosphere depends on the phase of the QBO. In the tropics, relatively weak easterlies prevail at the surface up to 300 hPa and weak westerlies in the upper troposphere. The variability in U in the winter stratosphere is high due to the variations in the strength and structure of the polar vortex that has a wide range of time scales (e.g. *Labitzke* [1981]; *Andrews et al.* [1987]; *Limpsuvan et al.* [2004]) and is evident from the SD plot given for the same. The SD in U is highest beyond $50^o$ in the winter hemisphere in the stratosphere, reaching values up to 20 m/s. The SD in the subtropical jet is around 4-8 m/s. High variability is also seen in the tropical stratosphere and this is due to the zonal wind variability of the QBO and the DJF standard deviation is around 16 m/s between 10 and 30 hPa (*Giorgetta et al.* [2006]). SD is relatively less in the NH lower troposphere.

The climatological mean zonal mean temperature in figure 4.8 shows warm temperatures close to the surface, reaching a minimum to 200K, which corresponds to the tropical

tropopause, around 100 hPa. The tropopause height is higher in the tropics compared to the mid-latitudes. The steady increase in temperatures is also evident in the stratosphere. The standard deviation in temperature in the winter hemisphere is much higher in the mid and high latitudes reaching a maxima up to ±12 K. In the lower stratosphere, the temperature fluctuation due to the QBO is around ±2 K at 2 hPa. In the tropical troposphere, the variability is less, but maximizes in high latitudes between 500 hPa and the surface.

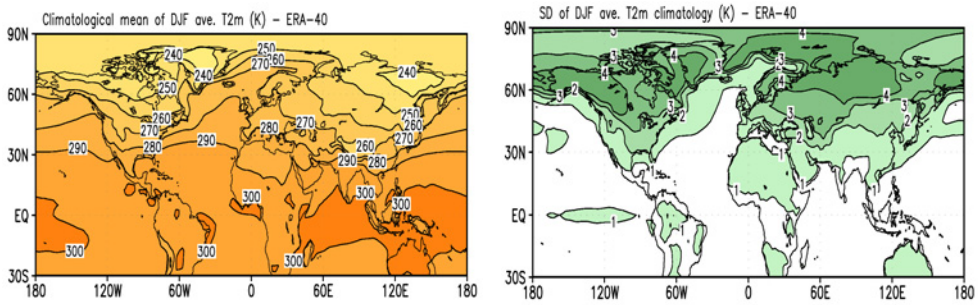


Figure 4.5: Climatological mean of DJF averaged 2m temperature (K) from ERA-40 calculated from 43 winters (left figure). The standard deviation (SD) of the winter temperatures (K) (right figure).

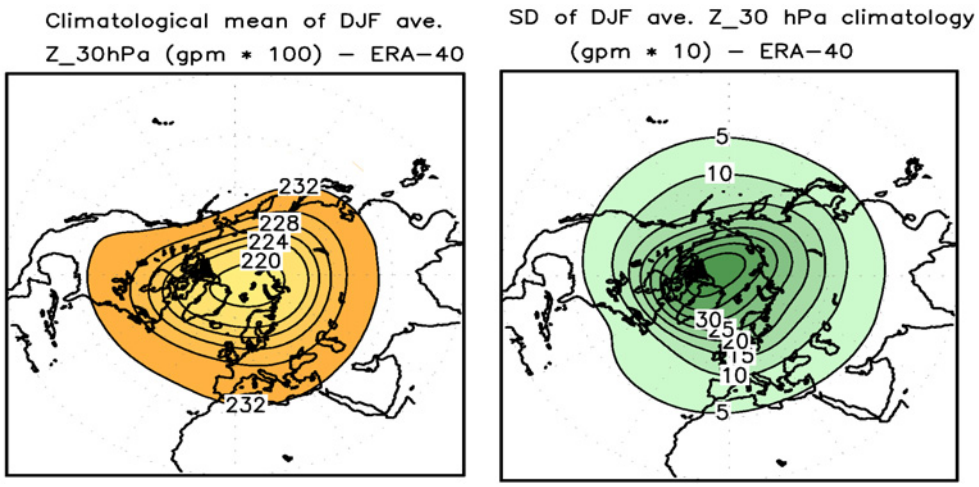


Figure 4.6: Same as above but for the 30 hPa geopotential height (gpm).

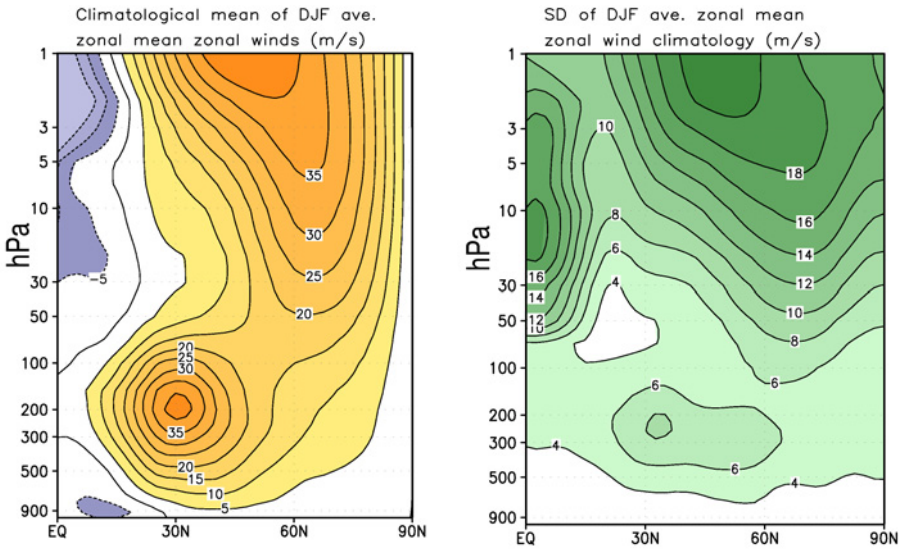


Figure 4.7: Same as above but for the zonal mean zonal winds (m/s).

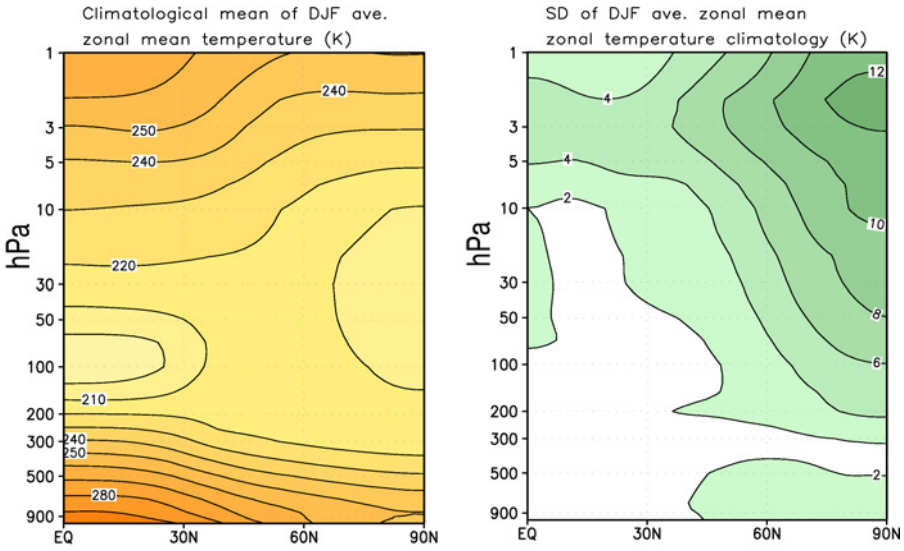


Figure 4.8: Same as above but, for the zonal mean temperature (K).

### 4.4.3 High latitude response

Stratospheric sulfate aerosol particles from strong tropical volcanic eruptions produce significant warming in the lower equatorial stratosphere thereby increasing the equator to pole temperature gradient in the lower stratosphere of the winter hemisphere and hence force a positive phase of the Arctic Oscillation during northern winter. This is manifested at the surface as a winter warming pattern in the NH high latitude continents (refer section 1.2.4 of introductory chapter). This dynamical response is typical of low latitude volcanic eruptions.

This pattern has been observed for two consecutive winters after volcanic eruptions and is presented in figure 4.9 for all the three volcanic eruptions. The first winter following Agung (DJF 1963/64) shows mainly three centers of warming - in Siberia, Scandinavia and Greenland, whereas the response is much weaker in the second winter. For the El Chichón eruption, the anomalies are much stronger than for Agung, with a primary center of warming, mostly in Northern and eastern Europe and Siberia and the whole pattern is shifted further north in the second winter. But, significant cooling is observed over Greenland during the first and second winters of El Chichón eruption. The winters following Mt. Pinatubo eruption shows two centers of warming over Eurasia - one over Northern and Eastern Europe and the other over Siberia. Significant cooling is evident over Greenland as in the two winters following El Chichón eruption and over the Middle East. The positive temperature anomalies reach as high as 6K. It has to be noted that these eruptions occurred in conjunction with an El Niño event as can be seen in the positive temperature anomalies in the eastern and central tropical Pacific for the first winters following these eruptions. Another prominent center of warming is also seen over northern and central North America during the winters of 1963/64, 1982/83 and 1991/92 and studies (*Halpert and Ropelewski* [1992]; *Trenberth et al.* [2002]) have shown that this warming is mainly due to the influence of the El Niño events.

The mean of the 2m temperature anomalies for the first winters and second winters are shown in figure 4.10. The mean picture shows three centers of warming in the first winter and cooling over Greenland and the Middle East, where as, there is a single center of warming over Europe and cooling over Greenland during the second winter. Moreover, the presence of the El Niño event and the related warming in northern and central North America during the first winter is also evident. Hence, here, the so-called "winter warming pattern" is re-defined as "volcanic winter pattern" and is referred to as the warming over Northern and eastern Europe and Siberia and cooling over Greenland and Middle east. As can be seen this dynamical response is highly variable from winter to winter of the eruptions and the presence of El Niño during these three volcanic eruptions complicate the efforts to quantify the effects from volcanoes alone.

The "volcanic winter pattern" can be due to several factors. It may be (1) solely due

to El Niño or (2) solely due to volcanoes or (3) due to the combined effects of volcanoes and El Niño or (4) due to the internal variability of the system or (5) due to the processes we are not aware of. To analyze the aforementioned factors, first, we consider the surface temperature response in those El Niño winters not affected by volcanic eruptions (winters of 1965/66, 1972/73, 1977/78, 1986/87, 1987/88, 1994/95 and 1997/98). Figure 4.11 shows the 2m temperature anomaly excluding the winters affected by volcanic eruptions. As a consequence of the warming over the central and eastern tropical Pacific, statistically significant positive anomalies are seen over Northern North America (*Halpert and Ropelewski* [1992]; *Trenberth et al.* [2002]). Statistically significant anomalies are also seen over Siberia and eastern China. An EOF [1] analysis is applied to the 2m temperature winter anomalies excluding volcanic winters over the region 30S-90N; 180W-180E. The EOF patterns generated (not shown) are highly variable with the first EOF, second EOF and the third EOF explaining only 20%, 15% and 12% respectively of the total variability. Neither of the EOF patterns produce the observed "volcanic winter pattern". Considering the fact that the main effects due to El Niño are over Northern North America and over Siberia, one can dismiss El Niño as a necessary cause of the "volcanic winter pattern" observed after volcanic eruptions.

To understand the natural variability, the standard deviation of surface winter temperature excluding the volcanic winters is evaluated and is shown in figure 4.12. The variability is seen to be high and is around 2 - 3 K over Europe and Siberia. The three cases of volcanic eruptions considered here limits robust statistical tests. Instead, the minimum value and the maximum value at each grid point from the 2m temperature anomalies of the six volcanic winters considered here is calculated (figure 4.13) and is compared with the standard deviation of the 2m winter temperature estimated without the volcanic winters. It is assumed that the local anomalies are significant if the anomalies are coherent and the maximum value exceeds the standard deviation. Figure 4.13 clearly shows that the maximum value exceeds the standard deviation of non-volcanic winters. To evaluate the consistency of the pattern, the probability of the six volcanic winters to show the respective anomaly pattern is evaluated and is shown in fig. 4.14. It can be seen that there is more than 83% probability to produce positive anomalies over Northern Europe and Siberia and around 66% probability to produce negative anomalies over Greenland, northern Africa and Middle east after explosive volcanic eruptions. This affirms that the "volcanic winter pattern" is significant and is an outcome of large volcanic eruptions.

Since the availability of long term datasets, there were only three explosive type volcanic eruptions and all these eruptions occurred during an El Niño event. Attempts were made to separate the El Niño signal from the volcanic signal (*Kirchner and Graf* [1995]; *Robock and Mao* [1995]; *Mao and Robock* [1998]) by statistical methods and it has been shown that

[1] EOF: Empirical Orthogonal Function

this pattern is a characteristic of tropical explosive volcanic eruptions.

Considering the aspects explained above, it can be concluded with certain degree of confidence that this pattern is mostly due to volcanic eruptions. However, one has to note that this pattern is highly variable in space and magnitude.

The geopotential height anomalies at 30 hPa gives the strength of the polar vortex. As mentioned in the previous chapter, the volcanic winter pattern is associated with the strengthening of the polar vortex. Figure 4.15 shows the geopotential height anomalies for the three volcanic eruptions. Depending on how low the geopotential height anomalies are, the polar vortex is stronger and colder. The geopotential height anomalies reach a low of -450 m during the first winter and the polar vortex is relatively weak during the second winter following Agung eruption (fig. 4.15 top row). However, during the two winters following El Chichón, the vortex is stable with geopotential height anomalies reaching a minimum of -300 to -350 m (fig. 4.15 middle row). In the case of Mt. Pinatubo eruption, the vortex is slightly disturbed in the first winter, but, stronger in the second winter, when the geopotential height anomaly reaches -450 m.

Deeper polar vortices, through geostrophic balance, imply strengthening of the westerly winds. This can be noted in the vertical profile of zonally averaged wind anomalies (fig. 4.16). The polar wind anomalies are seen to extend into the troposphere during the winters of all the volcanic eruptions except for the winter of 1991/92 and 1964/65 (e.g. *Graf et al.* [1993]; *Graf et al.* [1994]; *Kodera* [1994]). In addition to a strong polar vortex, relatively weak easterlies (of the order of 2-3 m/s) can be observed in the tropical and extratropical troposphere. Westerly wind anomalies reach a maximum of up to 18 m/s during the winter of 1963/64 and up to 9-11 m/s during the winters of 1982/83, 1983/84 and 1992/93. The westerly anomalies are weak in the winter of 1991/92 reaching up to 3 m/s and relatively strong easterlies up to 10 m/s are observed in the middle and upper stratosphere. This dipole type structure in the wind anomalies following the winter of 1991/92 is not seen for the other volcanic winters. The second winter following Agung eruption also exhibits relatively weak westerlies, but, is more confined to the stratosphere with weak easterlies in the troposphere. The phase of the QBO is also evident in the tropical stratosphere in these figures, where westerly phases occur in 1963/64, 1982/83 and 1992/93 and easterly phases in 1964/65, 1983/84 and 1991/92.

The difference of zonal mean temperature between volcanic winters compared to the climatology is also analyzed and is shown in figure 4.17. A dipole structure is observed in the meridional plane with one center of strong cooling in the polar lower stratosphere and relatively weak center of warming in the tropical-extratropical stratosphere for the two winters following Agung and El Chichón. The amplitude of the tropical and extratropical warming is much smaller than the polar stratosphere cooling. This meridional temperature gradient may result in the strengthening of the stratospheric polar vortex extending down

to the troposphere (e.g. *Graf et al.* [1993]; *Graf et al.* [1994]; *Kodera* [1994]). The dipole structures vary in amplitude and structure. During the winter of 1991/92, the dipole structure is not present in the stratosphere. However, strong cooling is observed in the polar stratosphere and relatively weak negative anomalies extend to the subtropical stratosphere during 1992/93. It has to be noted that the positive temperature anomalies in the stratosphere in 1992/93 are mostly confined to the tropics. The meridional temperature gradients is weaker in 1991/92 compared to the other cases.

To sum up, the dynamical response that is manifested as the "volcanic winter pattern" is highly variable from winter to winter and is also different from eruption to eruption, for example, the surface winter anomalies show a single center of warming over Eurasia after El Chichón, but, there are two centers of warming following the winters of Mt. Pinatubo and the first winter after Agung. The anomalies are very weak after the second winter in the case of Agung eruption. The maximum warming is more shifted to the north in the case of 1983/84 winter. It has been concluded that the "volcanic winter pattern" is mostly due to volcanic eruptions.

The "volcanic winter pattern" is mostly associated with the strengthening of the polar vortex. The polar vortex is colder and stronger for the winters of 1963/64 and 1992/93. However, during the winters of 1964/65 and 1991/92, the vortex was relatively weak and shifted, but the dynamical response was much weaker in the former winter and a stronger response was observed in the latter. The polar vortex was stronger following the two winters of El Chichón eruption producing different dynamical responses. The polar vortex extends to the troposphere and the westerlies are much stronger in all the winters except for the winters of 1964/65 and 1991/92. During the winters of 1964/65 and 1991/92, the wind anomalies look different. Weak westerlies of the order of 5 m/s extending to the tropopause in the winter of 1964/65 and weak easterlies are seen in the troposphere, whereas, during the winter of 1991/92, weak westerlies extend from the lower stratosphere to the surface and strong easterlies are seen above. This strengthening of the winds in the winter hemisphere is associated with the strong meridional temperature gradients. The meridional temperature gradient exhibits a dipole structure with a center of strong cooling in the polar lower stratosphere and a relatively weak center of warming in the tropical-extratropical stratosphere for the two winters following the volcanic eruptions except for the Pinatubo winters. This analysis shows that the patterns are highly variable from eruption to eruption and also from winter to winter. It has to be noted that the anomalies in 1991/92 after Mt. Pinatubo eruption and 1964/65 after Agung eruption are unusual compared to the other volcanic eruptions.

**Agung**

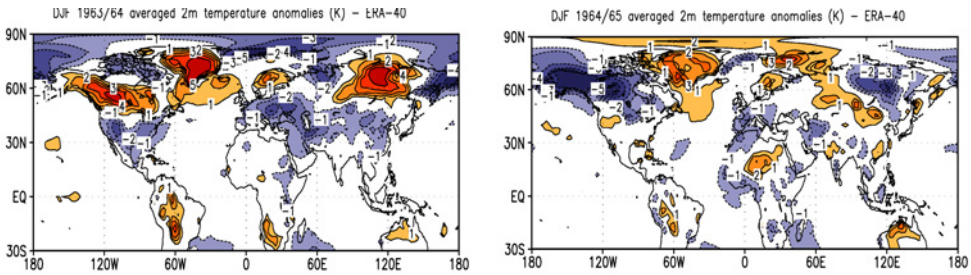


**El Chichón**

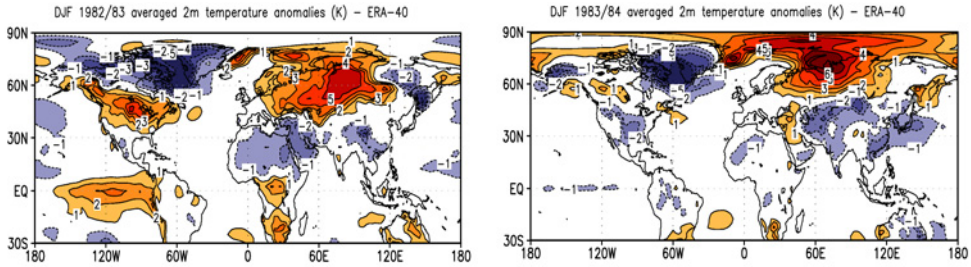


**Mt. Pinatubo**

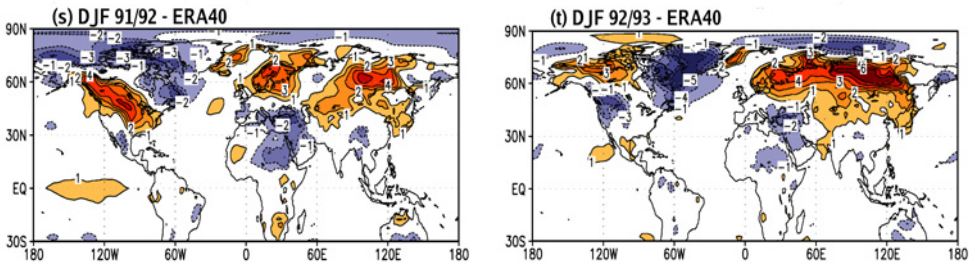


Figure 4.9: DJF averaged 2m temperature anomalies (K) after Agung - DJF/6364 and DJF/6465 (top row); El Chichón - DJF/8283 and DJF/8384 (middle row) and Mt. Pinatubo - DJF/9192 and DJF/9293 (bottom row).

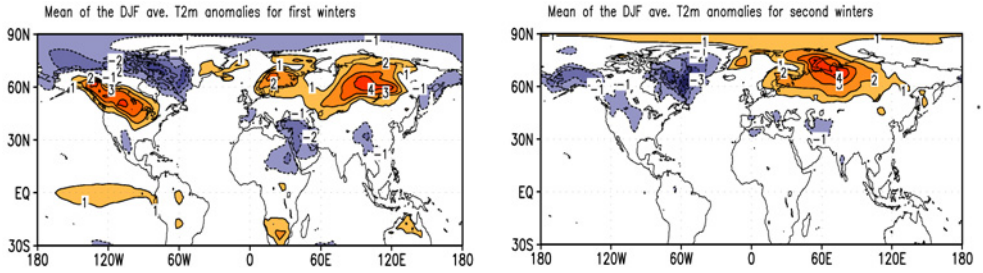


Figure 4.10: The mean of DJF averaged 2m temperature anomalies (K) of the first winters of Agung - DJF/6364, El Chichón - DJF/8283 and Mt. Pinatubo - DJF/9192 (left) and of the second winters of Agung - DJF/6465, El Chichón - DJF/8384 and Mt. Pinatubo - DJF/9293 (right).

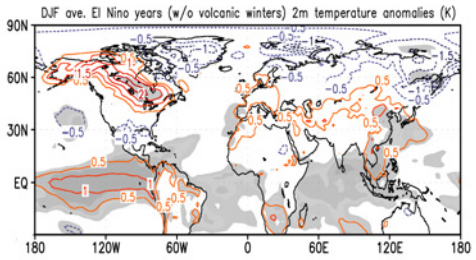


Figure 4.11: DJF averaged 2m temperature anomalies (K) in El Ni$\widetilde{n}$o winters excluding volcanic years. The statistical significance above 80%, 90% and 95% confidence levels is shown as increasing order of grey shading.

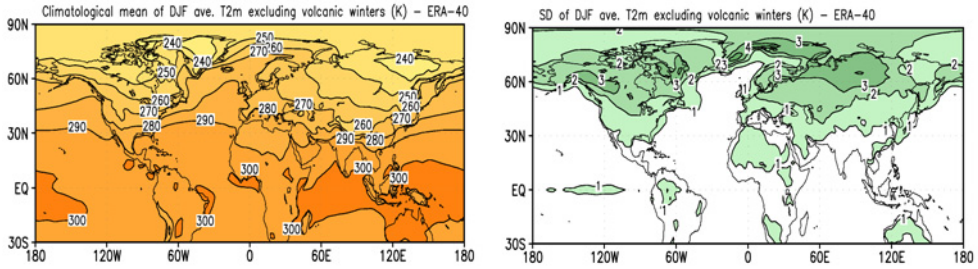


Figure 4.12: Climatological mean of DJF averaged 2m temperature (K) from ERA-40 calculated from 35 winters excluding volcanic years (left). The standard deviation (SD) of the winter temperatures (K) (right).

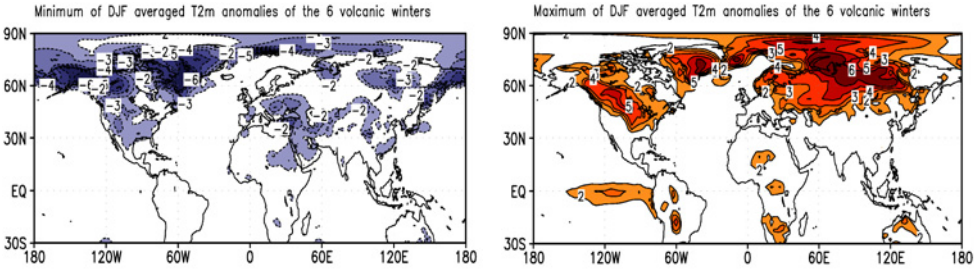


Figure 4.13: The minimum at each grid point of the mean of DJF averaged 2m temperature anomalies (K) from the 6 winters considered here (left) and the maximum at each grid point (right).

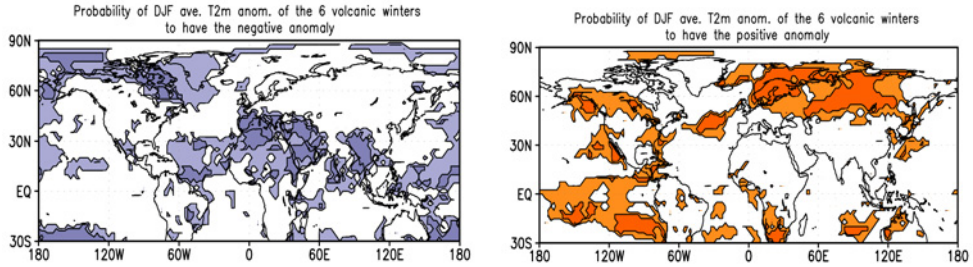


Figure 4.14: The probability of the DJF averaged 2m temperature anomalies from the 6 winters considered here to have the negative anomalies (left) and the positive anomalies (right) at each grid point. The lightly shaded are areas of probability 4/6 and heavily shaded of 5/6.

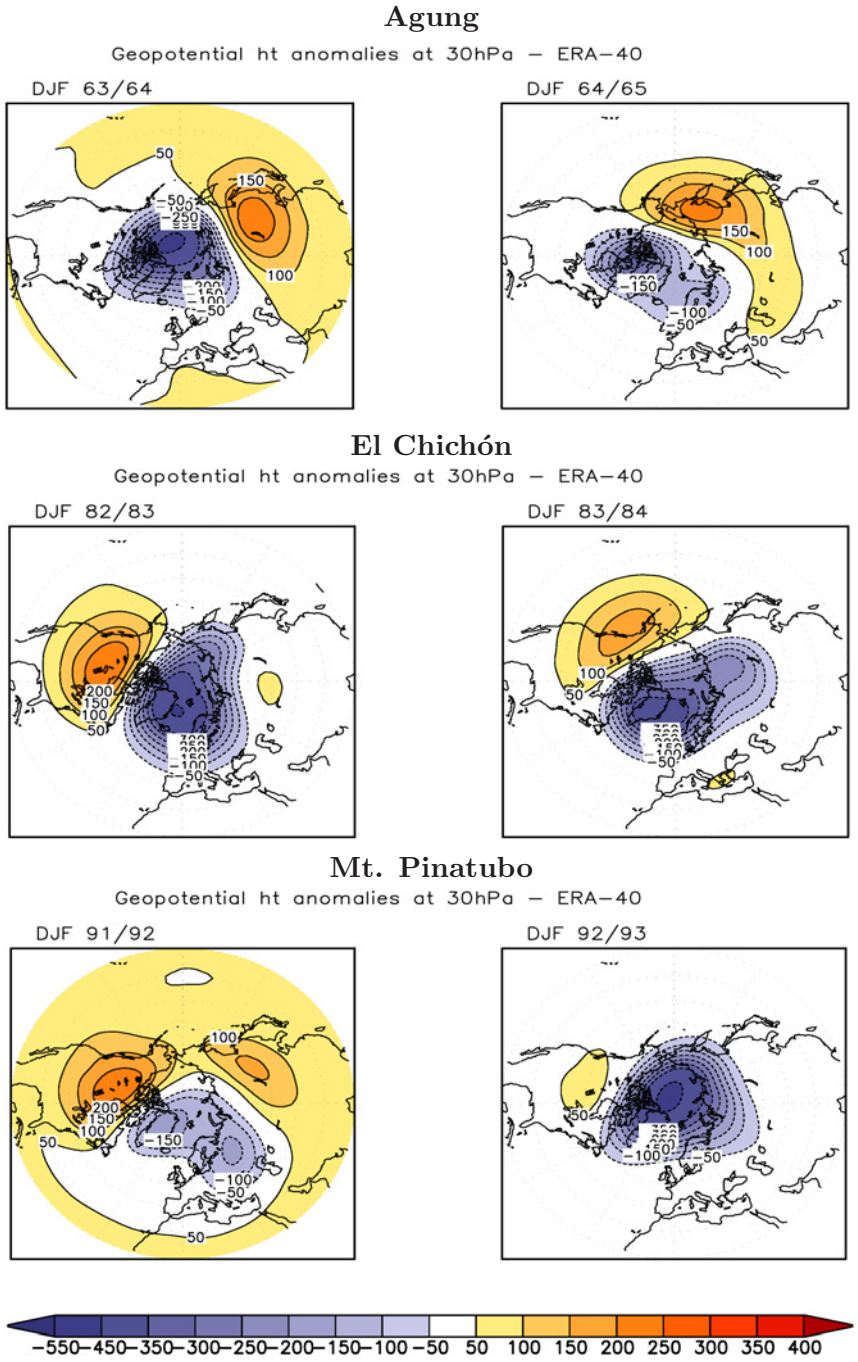


Figure 4.15: DJF averaged geopotential height anomalies at 30 hPa (m) for Agung (top row); El Chichón (middle row) and Mt. Pinatubo (bottom row); The anomalies for the first winter following the eruptions are shown in the left column and for the second winter in the right column.

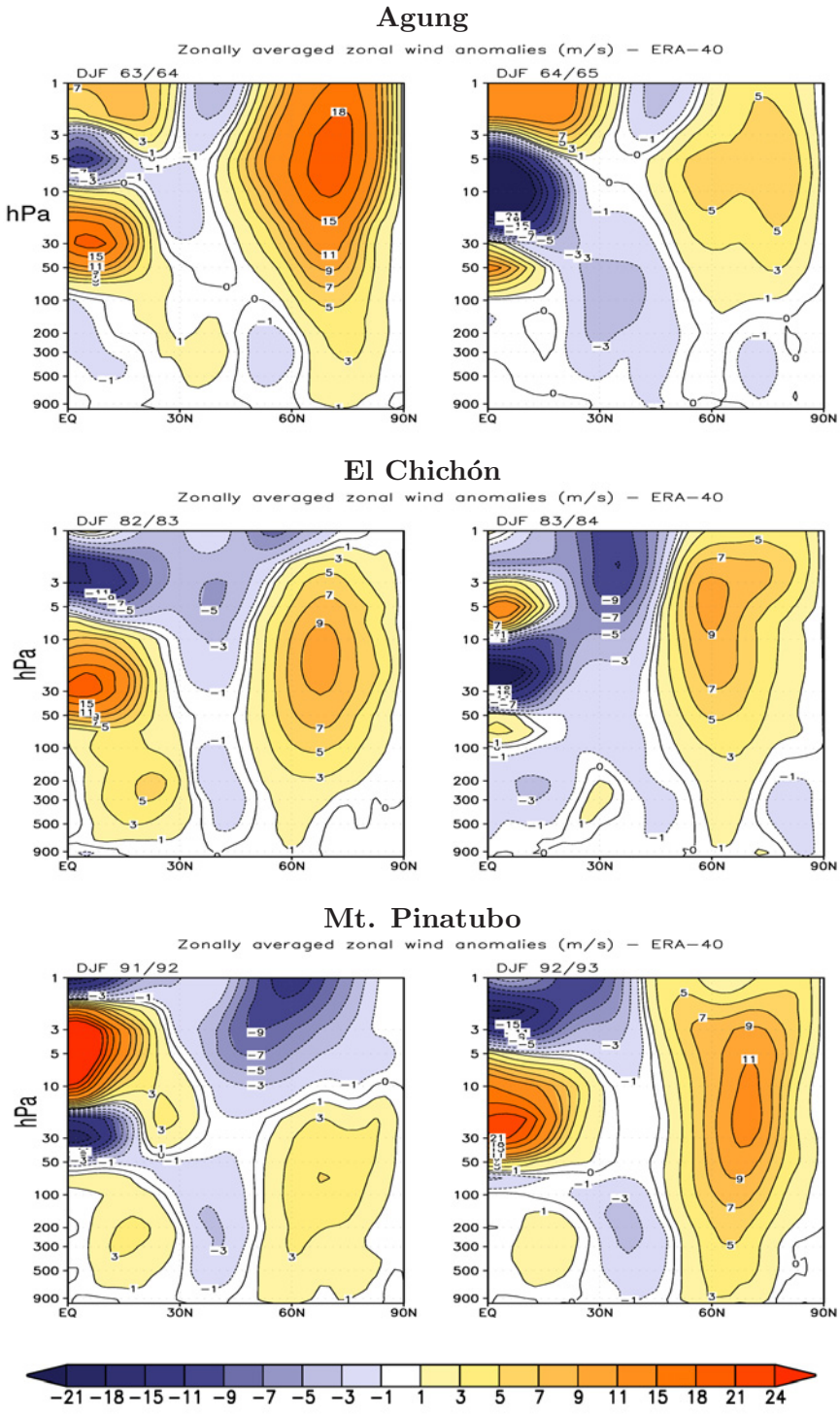


Figure 4.16: Vertical profiles for zonal mean zonal wind anomalies (m/s) for Agung (top row); El Chichón (middle row) and Mt. Pinatubo (bottom row); The anomalies for the first winter following the eruptions are shown in the left column and for the second winter in the right column.

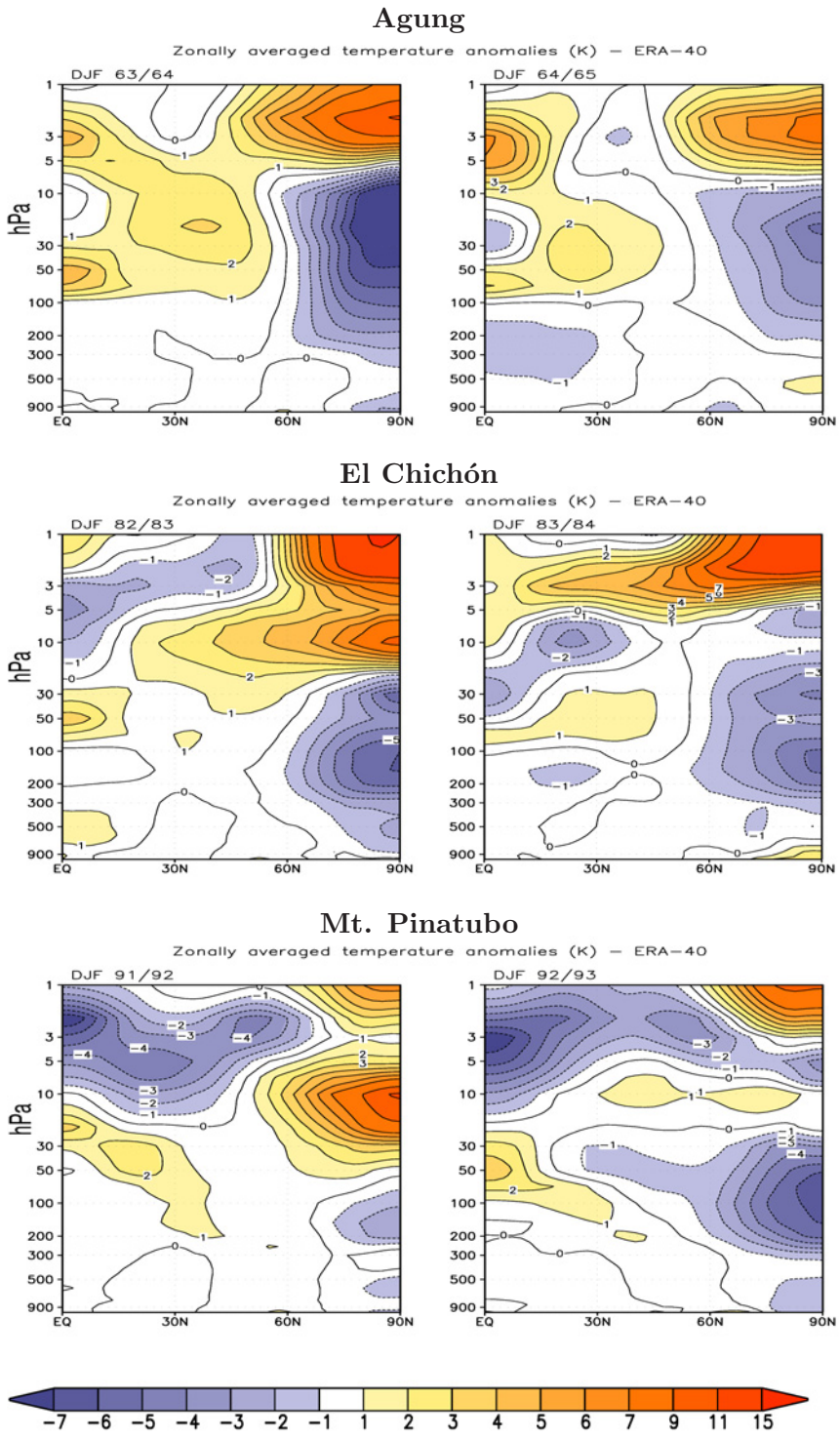


Figure 4.17: Vertical profiles for zonal mean temperature anomalies (K) for Agung (top row); El Chichón (middle row) and Mt. Pinatubo (bottom row); The anomalies for the first winter following the eruptions are shown in the left column and for the second winter in the right column.

## 4.5 Ensemble runs and Forcing Experiments

The ensembles of perturbed and unperturbed runs carried out with different boundary conditions are presented in table 4.2. The perturbed runs include the zonally and monthly averaged volcanic aerosol distribution, represented by their optical properties and volcanically induced ozone anomalies. The set up of the ensemble experiments and the data sets used are discussed in detail in chapter 2. The subscript "c" is used to denote the unperturbed runs and "p" for the corresponding perturbed runs. Runs are carried out with climatological SST (Clim_SST), observed SST (Obs_SST) and with boundary conditions combining observed SST and QBO (O_QBO). The main advantage of these experiments is that it is possible to isolate the effects of volcanic aerosol, the ocean and the QBO and also to assess their combined effects so as to better understand the observed responses.

| **Experiments** | **Clim_SST (C)** | **Obs_SST (O)** | **O_QBO (OQ)** |
|---|---|---|---|
| **CTRL** | $C_c$ | $O_c$ | $OQ_c$ |
| **Perturbed runs** | $C_p$ | $O_p$ | $OQ_p$ |

Table 4.2: Perturbed and unperturbed (CTRL) ensemble experiments. The subscript 'c' is used to denote the unperturbed runs and "p" is used for perturbed runs. C stands for climatological SST; O stands for observed SST; Q for QBO

The ensemble runs can be analyzed in different ways as shown in table 4.3 to obtain forcing differences to address the scientific questions. The boxes show the differences between the corresponding perturbed ensemble (in the row) and the unperturbed control ensemble (in the column). For example, Aer1 is the ensemble mean difference $C_p$ - $C_c$ and Aer + ocean + QBO is the difference $OQ_p$ - $C_c$. Hence, Aer1, Aer2 and Aer3 give the aerosol response under different boundary conditions. Aer1 gives the aerosol response under climatological SST as boundary conditions, Aer2 the aerosol response under observed SST as boundary conditions and Aer3 under both observed SST and QBO. The table also gives the individual responses of the ocean (O) and QBO (Q). The other responses discussed in this chapter are (1) the combined aerosol and ocean response (AO), (2) the combined aerosol and QBO response (AQ) and (3) the combined aerosol, ocean and QBO response (AOQ).

| Control runs (CTRL) | | | Perturbed runs + $O_3$ anomalies | | |
|---|---|---|---|---|---|
| $O_c$ | $C_c$ | — | $C_p$ | $O_p$ | $OQ_p$ |
| | — | $C_c$ | Aer1 | Aer+O (AO) | Aer+O+QBO (AOQ) |
| — | Ocean (O) | $O_c$ | | Aer2 | Aer+QBO (AQ) |
| QBO (Q) | QBO+O (OQ) | $OQ_c$ | | | Aer3 |

Table 4.3: Ensemble mean differences between perturbed and unperturbed runs. The text in red within the table are the difference between the corresponding perturbed runs and unperturbed control runs.

## 4.6 Analysis of individual and combined aerosol responses

A comparison of the different experiments in simulating the tropical and high latitude response to the Mt. Pinatubo eruption is presented in the following sections.

### 4.6.1 Stratospheric temperature response

Aer1 and Aer2 give the aerosol responses for different SST boundary conditions. In this case, Aer1 is the pure aerosol response neglecting all other sources of variability, whereas Aer2 is the aerosol response where the boundary condition includes interannual variability in SST and ice, this includes the effects of El Niño. In figure 4.18(a + b), the tropical responses are similar in pattern, but the response is slightly higher with observed SST as boundary conditions, with a maximum of up to 3K. The magnitude of the response is well simulated when compared to the observations. Both ENSO and QBO are prescribed as boundary conditions in the runs of Aer3 (fig. 4.18 (c)). The tropical response in Aer3 remains more or less the same as Aer1 and Aer2 simulations. The response for Aer1, Aer2 and Aer3 in the latitudinal belt of 50N - 50S is statistically significant at the 99% significance level from Aug 1991 to Apr 1993. The main point to be noted here is that the warming during the period Jan'92 - April'92 in the NH high latitudes in Aer3 corresponding to the weak polar vortex is consistent with observations (fig. 4.18 (j)) and is statistically significant at 95% confidence level, with temperatures reaching as high as 7K, whereas, this signal is much weaker and is not significant in Aer1 and Aer2.

Before analyzing the combined responses, it is important to analyze the ocean (O) and QBO (Q) alone ensemble differences to see whether the model reproduces the effect of El Niño and QBO circulation realistically.

Figure 4.18 (d) accounts for the effects of El Niño alone. ENSO signal propagates into the middle atmosphere by means of planetary Rossby waves and this propagation is strong when the stratospheric winds are westerly and peaks during boreal winter in the mid-latitudes (*Garcia-Herrera et al.* [2006]). Studies by *Sassi et al.* [2004]; *Manzini et al.* [2006] and *Chen et al.* [2003] have shown that during an El Niño event, the enhancement of vertical propagation and divergence of E-P flux cools the tropics and warms the high latitudes. Figure 4.18 (d) shows a similar pattern except that the cooling in the tropics is less, but, more evident in the 50 hPa temperature anomalies (shown in Appendix-B, fig. B1).

Figure 4.18 (e) shows the QBO-related lower stratospheric temperature anomalies at 30 hPa. A cooling of about 1-2K associated with the easterly phase of QBO is observed in the latitudinal belt from 15N-15S from June 1991 to June 1992 and warm anomalies in mid-latitudes. The opposite is observed during the westerly phase of QBO though the warming is only of about 0.5K. This cold bias along the equator is because the reference model have no QBO and are therefore too cold at 30 hPa. This can be seen in the other responses with QBO (figures 4.18 (e), (f), (h) and (i)). This is consistent with previous studies (*Baldwin et al.* [2001]). The combined ocean and QBO effects is shown in 4.18 (f) and the responses are linear except in high latitudes, which means that the combined ocean and QBO temperature responses in the tropics is the sum of ocean response and QBO response.

The AO ensemble difference accounts for the effects of both aerosol and ocean (fig. 4.18 (g)). The maximum temperature anomaly of 2K is simulated and here too, the responses are linear in the tropics.

Figure 4.18 (h) is the 30 hPa temperature response when both aerosol and QBO (AQ) effects are considered. The effect of easterly and westerly phase of QBO can be clearly seen. In the easterly phase, the AQ response shows a dual peak with relative maximum in the subtropics and a minimum at the equator and in the westerly phase, the AQ response shows a single equatorial peak. The significant warming beyond 60N during the winter of 1991/92 and the cooling during the winter of 1992/93 is not seen in the runs without the QBO and is consistent with observations. Comparing with the observed response as in figure 4.18 (j), the simulated response is most realistic when A, O and Q forcings are included (figure. 4.18 (i)). There is not much difference between the AQ and AOQ, except that the high latitude response in first boreal winter is much stronger. Though the NH high latitude response is realistically simulated, it has to be noted that large discrepancies exist in the southern hemisphere high latitudes. Hence, to simulate the pattern and the magnitude of the observed lower stratospheric temperature anomalies realistically, it is best to include all three forcings, namely, volcanic radiative forcing, observed SST/ice and the correct QBO phase.

Moreover, the combined responses are seen to be linear in the tropics. For example, the AOQ lower stratospheric temperature response is the sum of the aerosol-related response, ocean-related response and QBO-related response.

### 4.6.2 2m temperature response

Before analyzing the ensemble mean differences, the climatological means of 2m temperatures used in the calculation of the anomalies are investigated and shown in the Appendix-C. The figure shows the mean of 15 years of the unperturbed run with climatological SST as boundary conditions (fig. C.1(a)) and the figures C.1 (b)- (e) display the mean of the unperturbed runs from the 10 ensemble members. The climatological means with different boundary conditions are similar and are close to the observations shown in figure 4.12 (a). The differences between these runs are discussed in detail later in this section.

Figures 4.19 (a) - (r) show the ensemble mean surface temperature anomalies for two winters following the Pinatubo eruption. The shading in the figures corresponds to the level of significance. Areas with significance level above 95% are heavily shaded and above 90% lightly shaded.

As discussed in section 4.4.3, the observed pattern corresponds to a warming over Northern Europe, Siberia and parts of Asia and cooling in the Middle East (fig. 4.9). The warming over Central and northern North America is attributed to the positive ENSO phases observed during this period, rather than any volcanic effect (fig. 4.11).

For the two winters, the warming over northern Europe and Siberia is weakly simulated by the model with climatological SST as boundary conditions (Aer1) (fig. 4.19 (a) and (b)) and is shifted further north, but the anomalies are not significant. The cooling over the middle east is simulated by the model in the Aer1 experiments reasonably well, though the magnitudes are over-estimated. With observed SST as boundary conditions (fig. 4.19 (c)), the aerosol response cannot reproduce the volcanic winter pattern during the first winter. This may be because of El Ni$\tilde{n}$o that is present during the first winter and the signal is stronger than the effects due to the volcanic aerosols. However, the volcanic winter pattern is weakly simulated in the second winter (fig. 4.19 (d)), but they are not statistically significant. With both observed SST and QBO as boundary conditions, the aerosol response show significant cooling over Eurasia. Hence, we can conclude that model is not able to reproduce the observed volcanic winter pattern in the ensemble means with respect to the volcanic radiative forcing alone under the set of boundary conditions considered here.

The individual responses of El Ni$\tilde{n}$o SST in the winter circulation is discussed in figures 4.19 (g) - (h). The warm anomalies associated with El Ni$\tilde{n}$o over the eastern Pacific are clearly seen in the ocean response alone experiments (fig. 4.19 (g) - (h)) which is expected as the SST in this case is prescribed from observations. The ENSO-related warming (ref. figure 4.11) over central and northern North America during the winter of 91/92 is also well

simulated by the model. However, statistically significant above normal temperatures are observed beyond north of 60N and cooling over middle east and parts of Europe and China for both the winters following the eruption. These anomalies cannot be attributed to El Nino effects as can be seen from the temperature anomalies in El Nino winters excluding volcanic eruptions in figure 4.11. It has to be noted that these anomalies are evident in the second winter, when the El Nino effects are negligible.

The QBO effects on the winter circulation of 1991/92 and 1992/93 are presented in fig. 4.19 (i) and (j) respectively. Significant warming over Europe, parts of Russia and over eastern China and cooling over northern North America, Canada and Greenland is simulated for the two winters. However, the warming is slightly weaker in the second winter. The combined ocean and QBO effects (fig. 4.19 (k) - (l)) produces the spatial patterns to some extend in both the winters and is closest to the observed winter warming, but the magnitude of the anomalies are less than the observed and there is a northward shift as in the winter following El Chichón eruption.

The AO experiment that accounts for the effects of both aerosol and the state of the ocean for the two winters are shown in figures 4.19 (m) and (n). The patterns associated with ENSO during the first winter is clearly seen in the figures and the interactions between aerosol and ocean seems to be minimal. Comparing the AO-related response with the ocean response, the only difference is that the warming over Eurasia in the first winter is more pronounced in the AO response and colder temperatures are observed over Greenland in the second winter in the AO response which is typical of volcanic winters. This may be because the ocean response is more stronger in the model, thereby, over-riding the effects due to volcanic eruptions.The combined effects of aerosol and QBO in the AQ experiment (fig. 4.19 (o) - (p)) do not reproduce the observed volcanic winter patterns in both the winters. Even in the case where all effects, aerosol, ENSO and QBO are included (fig. 4.19 (q) - (r)), the pattern is shifted poleward.

The ensemble mean responses to individual and combined forcings for two NH winters cannot reproduce the observed warming, though the cooling is simulated fairly well by some of the forcing experiments. One of the possible reasons can be that this model may not have sufficient vertical resolution in the upper troposphere and lower stratosphere to resolve the stratospheric tropospheric interactions accurately. The analysis shows that the ENSO signal is dominating and modulated by QBO, partly masks the effects due to volcanic forcing. Also, the recent IPCC models used for the same analysis (*Stenchikov et al.* [2006]) could not reproduce this dynamical response. However, it should be noted that about 30% of the individual ensemble members for some of the forcing experiments do simulate this response realistically (Appendix-D). Hence, detailed analysis on why some of the ensemble members show this pattern is discussed later in this chapter.

### 4.6.3 Geopotential height response at 30hPa

The climatological means of geopotential heights used in the calculation of the anomalies are shown in the Appendix-E. The figure E.1 (a) - (e) follows the similar convention as figure C.1 (a) - (e). Here, the difference between the geopotential height mean climatology generated with climatological SST as boundary conditions differ with the other climatologies. The polar vortex looks similar for all the cases and agrees well with observations (figure 4.6). The geopotential height reaches a low at the poles to about $22*10^3$ gpm and reaches a maximum at the tropics to about $23*10^3$ gpm.

In the two winters following the major eruptions, the observed surface pattern is hypothesized as a characteristic of the anomalously positive AO index (*Thompson and Wallace* [1998]; *Baldwin and Dunkerton* [1999]). Figures 4.20 (a) - (r) shows the 30 hPa geopotential height anomaly as a representative of the strength of the polar vortex for all the forcing experiments considered here. In both winters, the aerosol response simulated under climatological SST as boundary conditions (figures 4.20 (a) & (b)) does not capture the magnitude and spatial pattern of the polar vortex (refer figure 4.15). However, under observed SST as boundary conditions (fig. 4.20 (c) & (d)), the aerosol response shows an anomalously strong stratospheric polar vortex in the second winter that is consistent with the observations, but the anomaly is weaker and not statistically significant. The geopotential height anomaly reaches -100 m.

The ENSO effect on the winter circulation is shown in figures 4.20 (g) & (h). A dipole structure is seen with above normal geopotential height anomalies over northern N. America and Russia and below normal anomalies over northern Atlantic and Europe during the first winter, whereas in the second winter, the dipole is shifted clockwise, with above normal anomalies over the poles and Russia and below normal geopotential heights over northern Atlantic. During a warm ENSO, enhanced wave propagation in boreal winter disturbs the polar vortex (*Sassi et al.* [2004]; *Manzini et al.* [2006]).

In the westerly phase of QBO the polar vortex is expected to be anomalously strong and in the easterly phase anomalously weak (*Holton and Tan* [1980]; *Holton and Tan* [1982]) in the absence of the aerosol effects. This is evident in the QBO experiment, where QBO is the only source of variability (fig. 4.20 (i) & (j)). Figure 4.20 (j) shows that the geopotential height anomalies at high latitudes is lower reaching a minimum value -140 m and is surrounded by above normal anomalies in the second winter when QBO is in its westerly phase.

The combined effects of ENSO and QBO (OQ) do not simulate a strong vortex in neither of the two winters. This is because, during the first winter, neither ENSO nor the easterly phase of QBO favors an anomalously strong polar vortex. But, during the second winter, with the ENSO effects relatively weak and with QBO in its westerly shear, the model still cannot produce a strong polar vortex, reflecting the non-linearity in the way

QBO modulates the circulation. Figures 4.20 (k) & (l) show a dipole structure with low values over Europe, Russia and northern Atlantic and high values over Canada in the first winter and the opposite is observed in the second winter.

The polar vortex is disturbed in the combined aerosol and ocean responses in both winters. The same is seen in the combined aerosol and QBO response in the first winter. However, in the second winter of AQ response, the polar vortex is more stable. This may be because, the westerly shear of the QBO favors a polar vortex with values reaching as low as 220 m. With all the effects included, the model simulates the deepening of the geopotential height anomaly in the second winter, though the magnitudes are relatively weak (around -100m). This pattern is more or less similar to the geopotential height anomaly observed during the second winter following Agung eruption. It should be noted that the polar vortex was much weaker after the first winter following Mt. Pinatubo eruption. This study suggests that there is significant non-linearity between aerosol and QBO effects and the strengthening of the polar vortex is more effective when the QBO is in the westerly phase.

### 4.6.4 Zonal mean zonal wind anomalies

As mentioned before, deeper polar vortices imply strengthening of the westerly winds. Detailed analysis of observed zonal mean zonal wind anomalies show strong westerly winds in high latitudes, extending down to the troposphere in all the winters except for the winters of 1991/92 and 1964/65. Here, the ability of the model to simulate this anomalously strong westerlies in the NH high latitudes is assessed in the experiments. The vertical profiles of the ensemble mean zonal mean zonal wind anomalies for the two winters following Mt. Pinatubo are analyzed for all the forcing experiments and is shown in Appendix-F, figures F.1 (a)-(r). The shading in the figures corresponds to the level of significance. Areas with significance level above 95% are heavily shaded and above 90%, lightly shaded.

The simulated zonal mean zonal wind anomalies with different boundary conditions in Aer1, Aer2 and Aer3 for the two winters are presented in figures F.1 (a)-(f). It is seen that the aerosol response cannot produce anomalously strong westerly winds in the winters in the high latitudes. The individual aerosol forcing simulates weak easterly winds in the upper stratosphere in figures F.1 (a + b +d), whereas the easterly winds extend down to the troposphere in figures F.1 (c + e + f). Strong easterly winds are observed of magnitude up to 8 m/s is observed during the first winter in Aer3.

Ocean-related zonal mean zonal wind anomalies also exhibit strong easterlies in the upper stratosphere, but, weak westerlies prevail in the lower stratosphere in the high latitudes in the first winter. However, the winds are easterly throughout the atmospheric layer during the second winter.

The differences in the tropical stratosphere in Aer1, Aer2, Aer3 and ocean forcing experiments in comparison with the observations (fig. 4.16) is due to absence of QBO.

The QBO-related individual response show strengthening of the westerly winds in the high latitudes as in figure F.1(j) during the second winter when QBO is in its westerly phase and weak easterlies during the easterly QBO phase, again, supporting the studies by *Holton and Tan* [1980]. Moreover, the strengthening of the westerly winds associated with the westerly QBO phase (figure F.1 (l)+(p)+(r) in 91/92) is also evident in the combined responses of OQ, AQ and AOQ and strong easterlies, during the second winter. Though the QBO-related easterly anomalies are much weaker in the easterly QBO phase following the first winter after the eruption, the combined responses with ENSO effects as in OQ, AO and AOQ exhibit stronger easterlies in the high latitudes (figure F.1 (k)+(m)+(q)).

### 4.6.5 Zonal mean temperature anomalies

The vertical profiles of zonal mean temperature anomalies are analyzed for the ensemble means of the different forcing experiments and is shown in the Appendix-G, figure G.1 (a)-(r) for the two winters following Mt. Pinatubo eruption. As explained in the introductory section of this chapter, the anomalously strong westerly winds are thought to be a result of the strong temperature gradient in the lower stratosphere between the tropics and the high latitudes in winter (e.g. *Graf et al.* [1994]; *Kodera* [1994]). However, the analysis of the six volcanic winters show that this meridional temperature gradient after the Pinatubo winters was relatively weak (during the first winter, in particular) compared to the other volcanic winters and this pattern is highly variable from winter to winter and spatially. A dipole structure is observed in the meridional plane with a center of strong cooling in the polar lower stratosphere and a relatively weak center of warming in the tropical-subtropical stratosphere.

The forcing experiments carried out here simulate this warming in the lower stratosphere associated with the volcanic aerosol loading in the tropics in both the winters in the individual responses such as, Aer1, Aer2 and Aer3 (figure G.1 (a) - (f)) and in the combined responses such as, AO, AQ and AOQ (figure G.1 (m) - (r)). However, the anomalously cold temperatures in the high latitudes is not simulated by any of the cases here.

The ocean-related zonal mean temperature anomalies are relatively weak during the second winter, but, warm anomalies in the subtropics and cold anomalies in the tropics are observed in the lower stratosphere in consistent with the studies by *Manzini et al.* [2006] and *Sassi et al.* [2004].

The QBO related temperature anomalies attempt to simulate the anomalously cold temperature over the high latitudes during the second winter as can be seen in figure G.1 (j). However, the magnitude is much weaker compared to the observations. These high latitude cold anomalies are seen in the combined responses with QBO in OQ, AQ and AOQ (figure G.1 (l) + (p) + (r) respectively) during the second winter when the westerly phase of QBO prevails.

The meridional temperature gradient is weakly simulated in the combined AQ and AOQ responses during the second winter where the aerosol forcing produce warm temperature anomalies over the tropics and the westerly phase of QBO results in the cold temperature anomalies in the high latitudes. This relatively weak meridional temperature gradient produces strong westerly wind anomalies as described in the previous section.

The ensemble mean picture of the individual and combined responses in 30 hPa geopotential fields and surface temperature for NH winter could not reproduce the observed response. However, the observed response is simulated by some of the ensemble members. The individual ensemble members for all the cases for the anomalies in geopotential and surface temperature for the two winters following the eruption is shown in the Appendix-D. It can be seen that, there are several cases when the response is simulated realistically for the right reasons and some cases irrespective of the forcing. Some of these cases are studied in detail to get a more vivid picture that result in the difference in the responses.

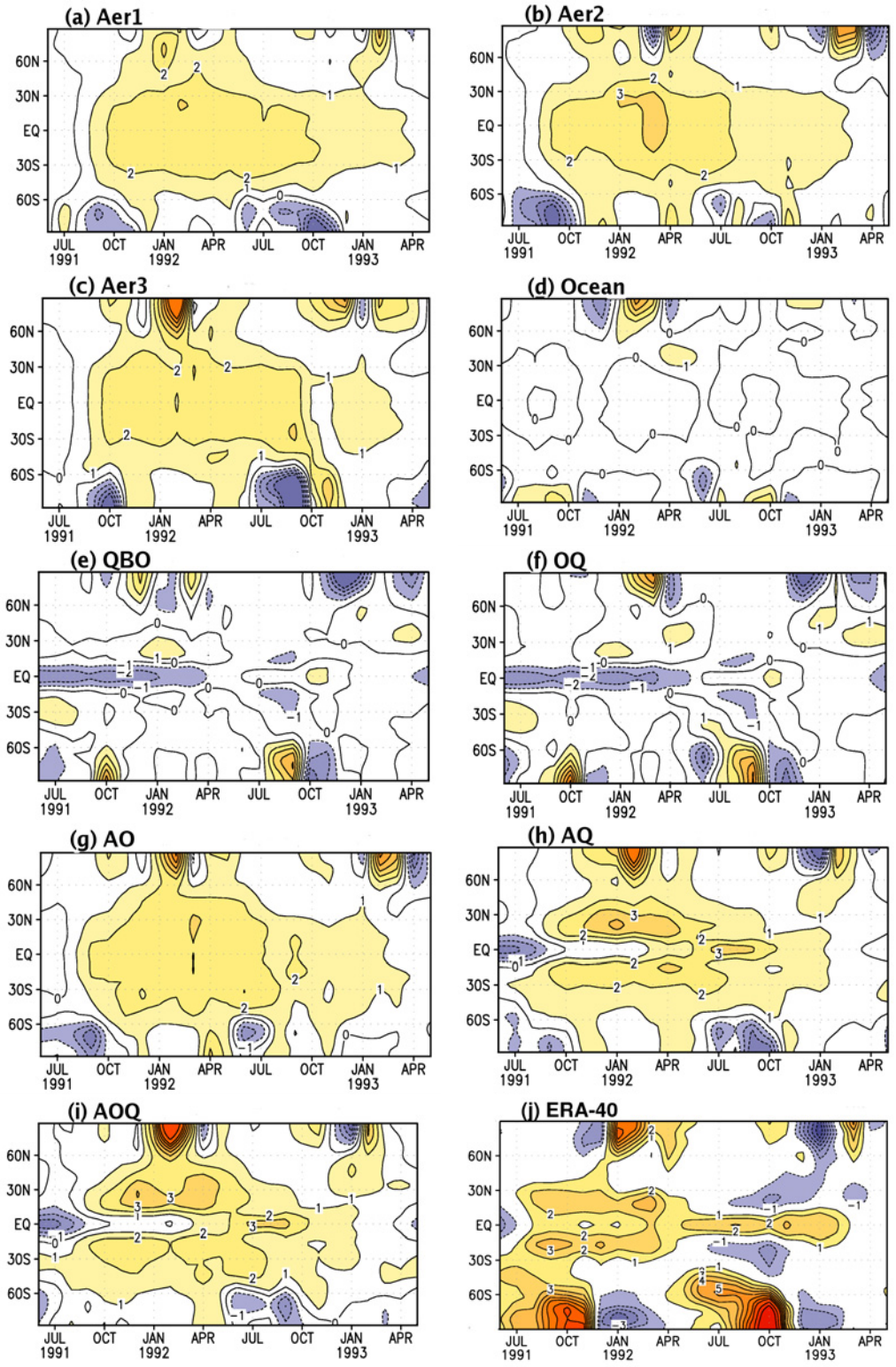


Figure 4.18: Lower stratospheric temperature anomalies at 30 hPa (K) for (a) Aer1 (b) Aer2 (c) Aer3 (d) ocean response (e) QBO response (f) combined ocean and QBO – OQ (g) combined aerosol and ocean – AO (h) combined aerosol and QBO – AQ (i) combined aerosol, ocean and QBO – AOQ (j) ERA-40.

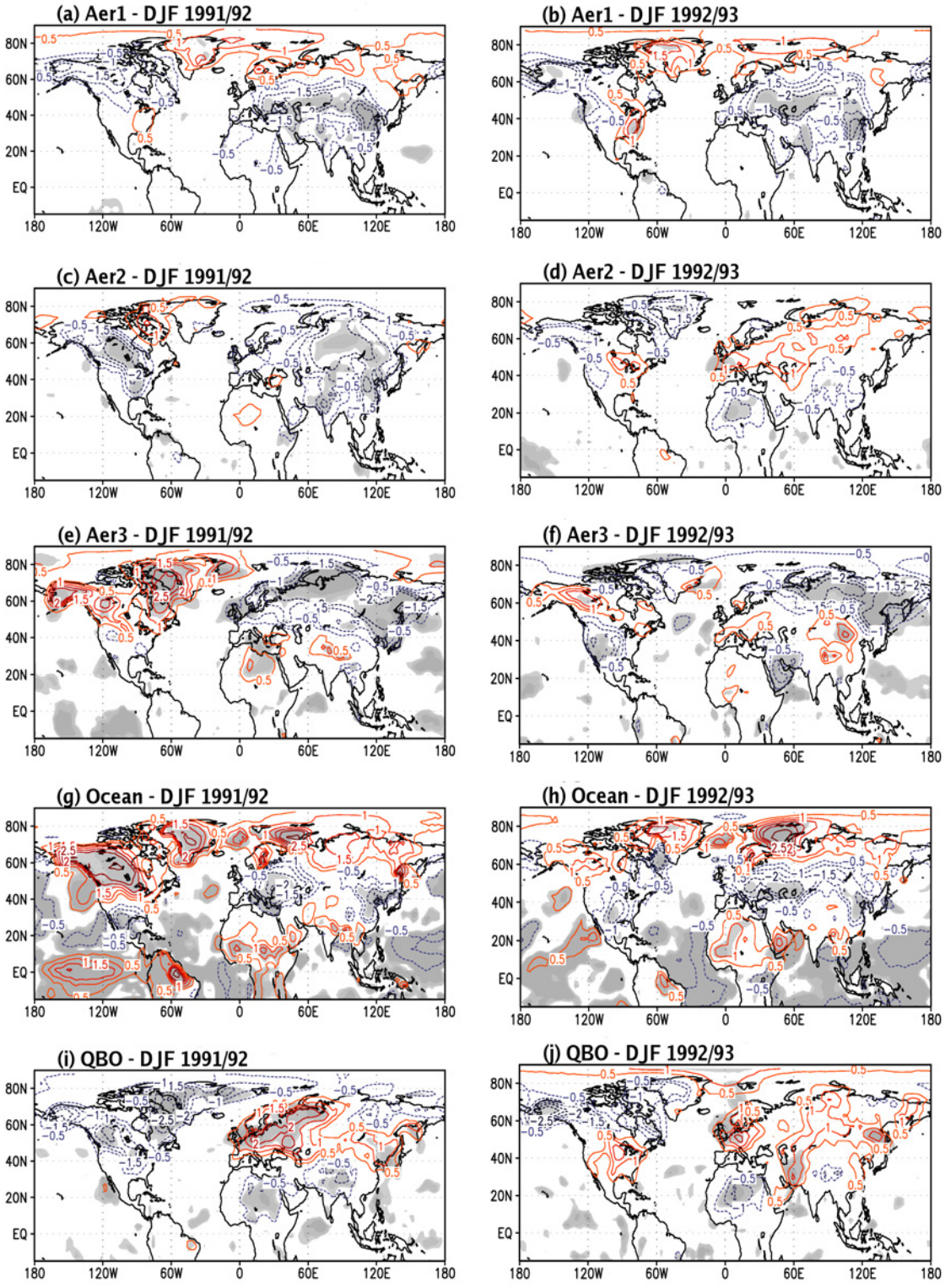
(a) Aer1 - DJF 1991/92
(b) Aer1 - DJF 1992/93
(c) Aer2 - DJF 1991/92
(d) Aer2 - DJF 1992/93
(e) Aer3 - DJF 1991/92
(f) Aer3 - DJF 1992/93
(g) Ocean - DJF 1991/92
(h) Ocean - DJF 1992/93
(i) QBO - DJF 1991/92
(j) QBO - DJF 1992/93
80N
60N
40N
20N
EQ
180
120W
60W
0
60E
120E
180

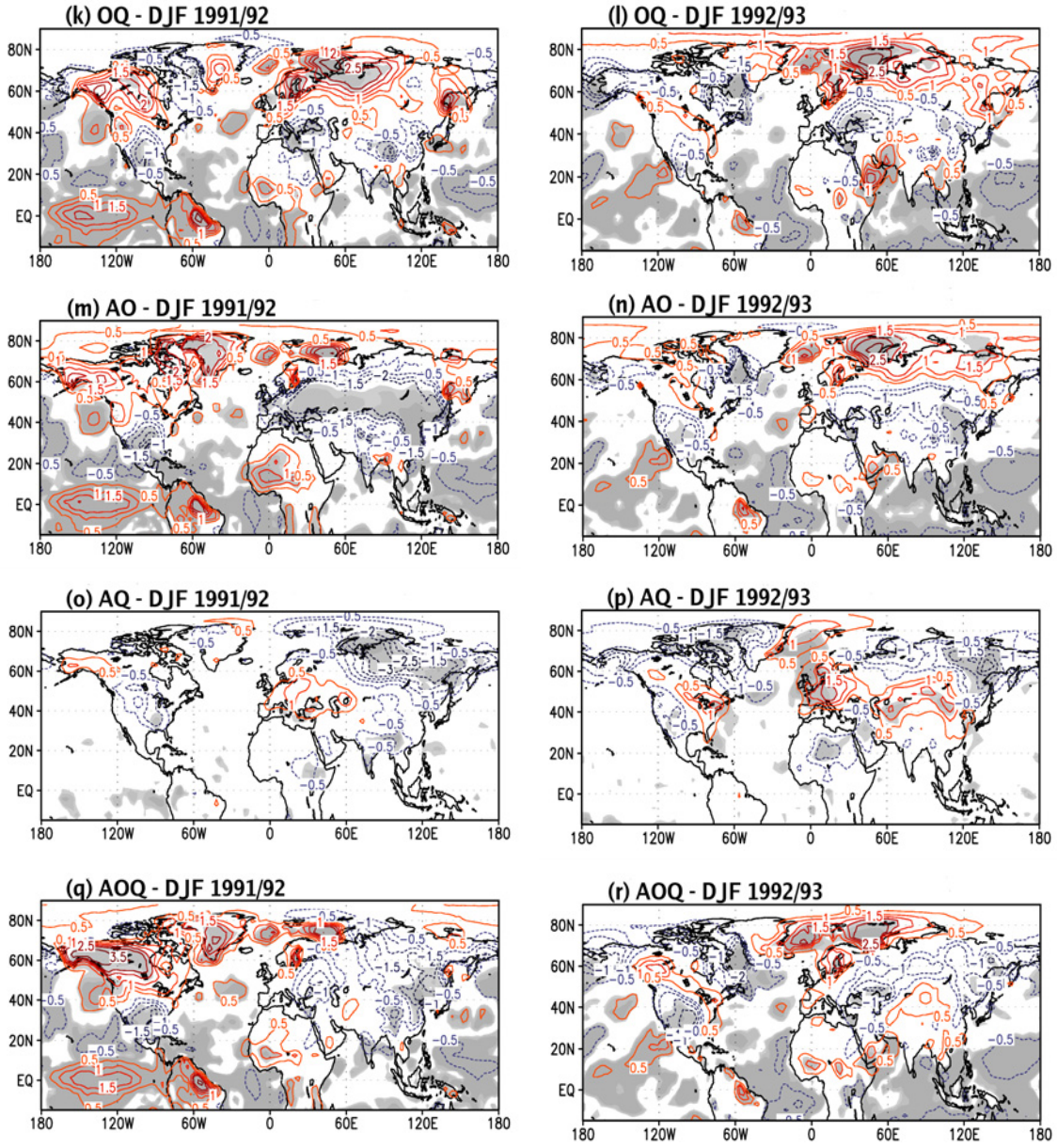


Figure 4.19: 2m temperature anomalies (K) for Aer1 (a & b); Aer2 (c & d); Aer3 (e & f); ocean response (g & h); qbo response (i & j); combined ocean and qbo (OQ) (k & l); combined aerosol and ocean (AO) (m & n); combined aerosol and QBO (AQ) (o & p); combined aerosol, ocean and QBO (AOQ) (q & r); for DJF 1991/92 (left column) and DJF 1992/93 (right column).

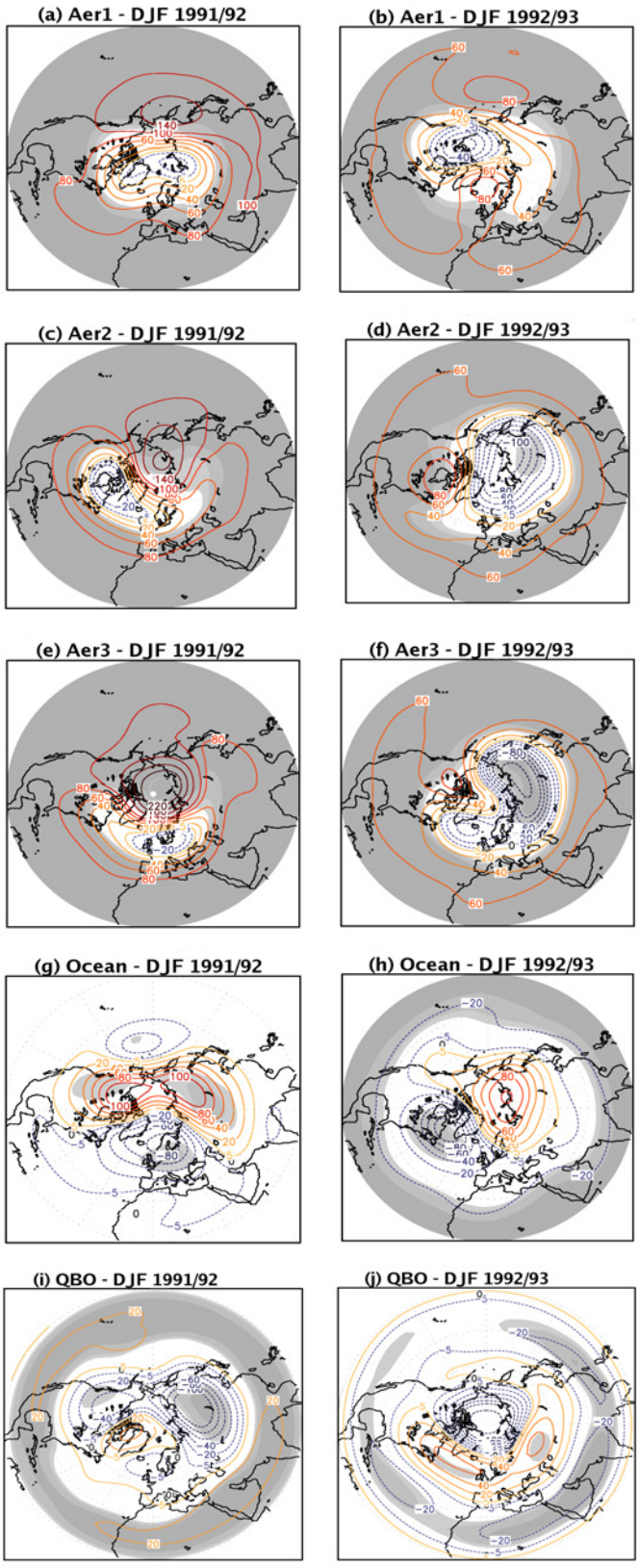
(a) Aer1 - DJF 1991/92
(b) Aer1 - DJF 1992/93
(c) Aer2 - DJF 1991/92
(d) Aer2 - DJF 1992/93
(e) Aer3 - DJF 1991/92
(f) Aer3 - DJF 1992/93
(g) Ocean - DJF 1991/92
(h) Ocean - DJF 1992/93
(i) QBO - DJF 1991/92
(j) QBO - DJF 1992/93

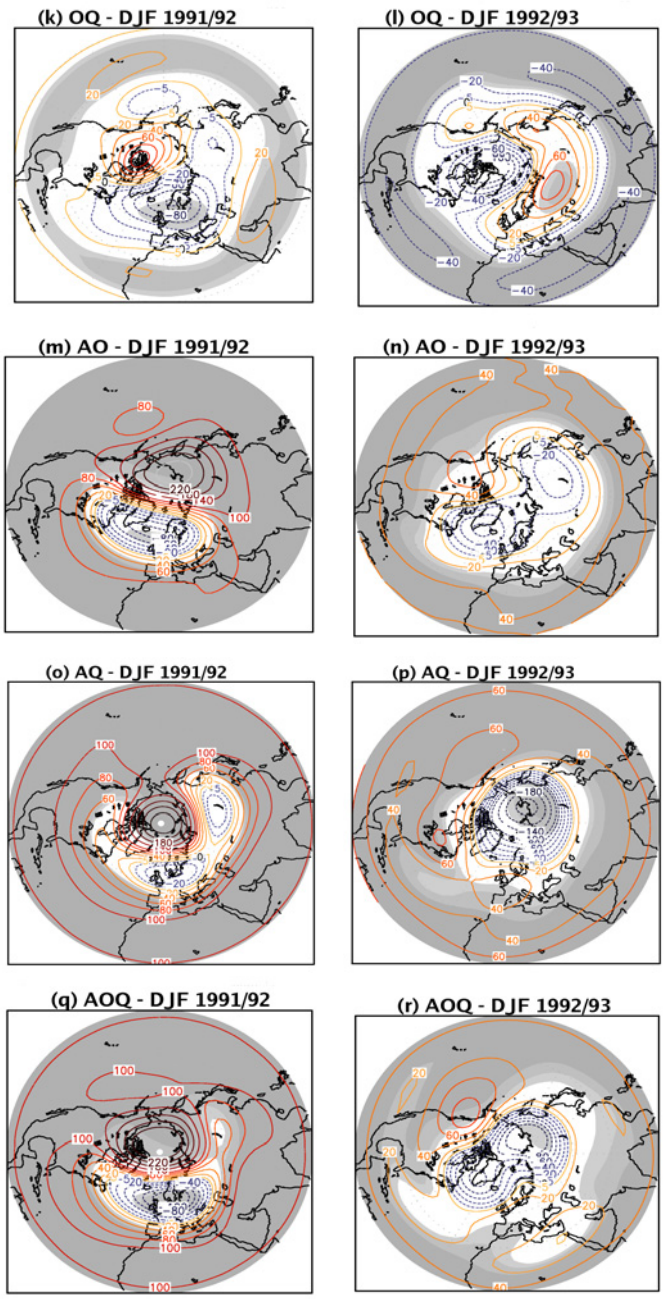


Figure 4.20: Geopotential height anomalies at 30 hPa (m) for Aer1 (a & b); Aer2 (c & d); Aer3 (e & f); ocean response (g & h); qbo response (i & j); combined ocean and qbo (OQ) (k & l); combined aerosol and ocean (AO) (m & n); combined aerosol and QBO (AQ) (o & p); combined aerosol, ocean and QBO (AOQ) (q & r); for DJF 1991/92 (left column) and DJF 1992/93 (right column). Heavily shaded areas are significant at 99% level, lightly shaded at 90% significance level.

## 4.7 Analysis of planetary wave propagation in NH winter

### 4.7.1 Introduction

In this section, the dynamical influence of the Pinatubo eruption on the climate system is discussed. As mentioned before, for two winters following explosive type volcanic eruptions, the so-called "volcanic winter pattern" is observed in the surface temperature anomalies. There are many interpretations or speculations to this dynamical response. The interpretation is such that the meridional temperature gradient between low and high latitudes in the stratosphere would lead to the strengthening of westerlies in winter and these strong westerlies prevent the planetary waves from penetrating high into the stratosphere and their reflection back to the troposphere creates such a pattern at the surface (*Graf* [1992]; *Graf et al.* [1993]; *Kodera* [1994]). Recently, *Graf et al.* [2007] showed from observations that there is, instead, more planetary wave propagating in to the higher altitudes. The previous sections of this chapter address the simulation of this dynamical response. The simulated geopotential height anomalies and the surface temperature anomalies could not realistically display the observed response, even though some of the members of the forcing experiments did simulate the response realistically. Here, in this section analysis is carried out to try to explain why some of the ensemble members show this pattern, while others do not.

Planetary waves are generated by topography and diabatic heating in the troposphere and they have zonal wavelengths of the scale of the earth's radius. Planetary waves can induce forcing on the mean flow. The E-P [2] flux and its divergence (*Eliassen and Palm* [1961]; *Andrews et al.* [1987]) that represent the wave activities and eddy forcing respectively are used to analyze the planetary wave propagation and this diagnostic has been adopted in many previous studies (e.g. *Chen and Robinson* [1991]; *Chen et al.* [2002]; *Christiansen* [2003]; *Hitoshi and Hirooka* [2004]). Here, the quasi-geostrophic version of E-P flux is used to study the planetary wave mean flow interaction in the troposphere and stratosphere in NH winter. The equations used are shown in the Appendix-H. Basically, the E-P flux has two components. One is the meridional E-P flux component that corresponds to eddy momentum flux and the other is the vertical E-P flux component that corresponds to the eddy heat flux. Convergence (or negative divergence) of the E-P flux implies that zonal easterly forcing is induced by waves on the mean flow that leads to the deceleration of the westerly winds.

Variations in the strength of the polar vortex are mainly caused by the interaction of the upward propagating planetary waves from the troposphere with the mean flow in the stratosphere (*Matsuno* [1970]). However, several external forcings, such as volcanic eruptions, QBO phases, anthropogenic emissions (e.g. *Holton and Tan* [1980]; *Grant et al.* [1994]; *Perlwitz and Graf* [1995]; *Baldwin et al.* [2001]) can also influence the strength of

[2] Eliassen-Palm

the polar vortex. But, the interaction between the background zonal flow which influences the wave propagation and the waves which change the flow where they dissipate, is complex. Here, we chose four ensemble members to understand how the planetary wave propagation differs from one another.

### 4.7.2 Selected ensemble members

The 30 hPa geopotential height anomalies and the corresponding volcanic winter patterns are shown respectively in the figures 4.21 and 4.22 for the first winters of the ensemble members, ens5 and ens7 and the second winters of ens1 and ens6 following the Pinatubo eruption. These ensemble member anomalies are taken from the AOQ experiment calculated with respect to the climatology of the $C_c$ (control run with climatological SST as boundary conditions) experiment.

These cases are chosen such that for,

→ ens1 (1992/93): the polar vortex is anomalously strong and a clear volcanic winter pattern is seen at the surface (hereafter referred to as ens1-PW).

→ ens5 (1991/92): the polar vortex is warm and unstable and no signal of a volcanic winter pattern at the surface (hereafter referred to as ens5-NN).

→ ens6 (1992/93): the polar vortex is anomalously strong, but, could not produce a volcanic winter pattern at the surface (hereafter referred to as ens6-P) and

→ ens7 (1991/92): the polar vortex is weak as in ens5, but, produces a significant volcanic winter pattern at the surface (hereafter referred to as ens7-W).

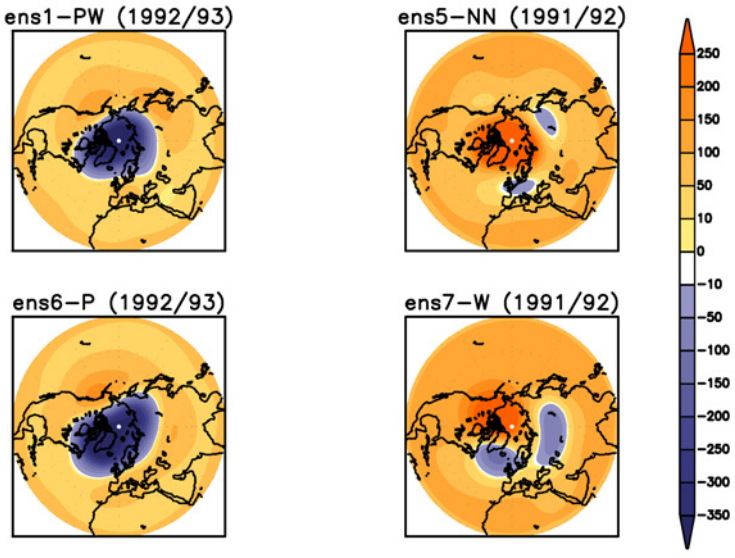


Figure 4.21: DJF averaged geopotential height anomalies (m) of the ensemble members selected from the AOQ runs.

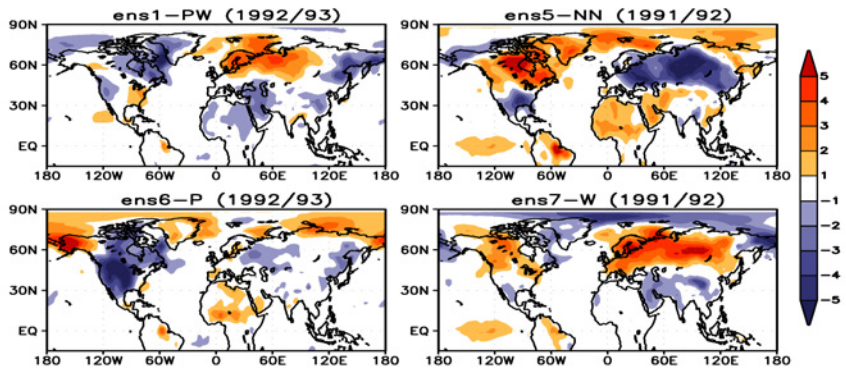


Figure 4.22: DJF averaged surface temperature anomalies (K) of the ensemble members selected from the AOQ runs.

### 4.7.3 Discussion

The differences of the zonal mean zonal wind (U) and the zonal mean temperature of these cases from the climatological mean of the control run ($C_c$) are analyzed and shown in figure 4.23 and 4.24 respectively. The westerly wind anomalies during the winters after volcanic eruptions that extend to the tropopause and weak easterlies in the tropical and extratropical troposphere can be seen in the ens1-PW and ens6-P cases and the opposite is observed in ens5-NN and ens7-W cases where the polar vortex is weak and unstable. The U anomalies in the high latitude troposphere show westerlies in ens1-PW and ens7-W and easterlies in ens5-NN and ens6-P. As in the case of U anomalies, clear differences are evident in the zonal mean temperature anomalies also. There are two major centers that occur in the lower stratosphere - one is a stronger cooling in the polar lower stratosphere and the other is relatively weaker warming in the tropical and extratropical lower stratosphere in ens1-PW and ens6-P as discussed in section 4.4.3. This dipole means that there exists a strong anomalous meridional temperature gradient whereas this gradient is not present for ens5-NN and ens7-W. This increased meridional temperature gradient can cause the strengthening of the polar vortex extending down to the troposphere. This is consistent with the ens1-PW and and ens6-P cases where strong polar vortices are displayed. It should be noted that the zonal temperature anomalies for the cases ens1-PW and ens7-W are entirely different, but, the high latitude tropospheric winds are simialr. However, both exhibits the volcanic winter pattern in winter. This implies that the generation of this pattern cannot be explained entirely and exclusively based on the strengthening of the polar vortex. In-depth analysis is required to consider other factors such as, the NAO [3] patterns, tropospheric wind patterns etc, but, is beyond the scope of this study.

Stronger winds prevent the planetary waves to propagate into the stratosphere, leading to a colder atmosphere in the high latitudes and then as a dynamical response, strengthen

[3]NAO: North Atlantic Oscillation

the polar vortex (eg. *Graf et al.* [1993]; *Kodera* [1994]; *Graf et al.* [1994]). However, a recent study by *Graf et al.* [2007] shows that during the winters after volcanic eruptions there is, instead, more planetary wave propagation from the troposphere to the stratosphere and at the same time the polar vortex is strong and stable. Here, the cross-sections of E-P flux and its divergence which represent the planetary wave activities and wave momentum forcing on the mean flow are analyzed for these four cases. Figure 4.25 shows the E-P flux and divergence of stationary planetary waves of the first three zonal wave numbers (ZWN1+2+3) for the cases selected above. The same analysis is applied to ERA-40 data for the two winters following Mt. Pinatubo eruption for easy comparison and is also shown in 4.25 (E-P flux and divergence of the winters of Agung and El Chichón are shown in the Appendix-I). Two major branches of E-P flux vectors are seen in all the ensemble members - vertical E-P flux indicating meridional heat flux into the sub polar stratosphere and momentum flux into the sub tropical upper troposphere and this is similar to the wave activity computed from observations. This means that in NH winter, the poleward eddy heat flux is dominant between troposphere and lower and mid stratosphere and eddy momentum flux is dominant over the subtropical upper troposphere. Relatively weaker vertical wave activity flux is evident in ens1-PW compared to the other cases. Ens1-PW and ens7-W have stronger wave activity flux in to the subtropics compared to the other cases. ens6-P shows wave reflection from the polar stratosphere down to the high latitude upper troposphere. It has to be noted that there is an increase in vertical wave activity between 10 and 2 hPa in 1991/92 and 1992/93 in ERA-40 analysis and this feature is not captured by any of the ensemble cases considered here.

Two major convergence zones are evident in the analysis from ERA-40 (refer fig. 4.25 third column) - one in the extratropical troposphere with a maxima around 45-55N and the other in the stratosphere. The convergence zone over the extratropical troposphere is stronger (around 5 /m/s/day) during the first winter compared to the second (around 3 /m/s/day). The second convergence zone in the stratosphere is mostly confined to the upper stratosphere, but, extends to the lower stratosphere in the extratropics. These two centers of convergence are well represented by the four cases with some minor differences. The convergence zone in the extratropical troposphere is over-estimated in ens6-P case compared to the other cases. The center of maxima in the extratropical troposphere is realistically simulated in ens5-NN and ens7-W, but, is slightly shifted to around 55-65N in ens1-PW and ens6-P cases. During the winters of 1991/92 for the cases ens5-NN and ens7-W, the stratospheric convergence zone in the lower and upper levels is realistically simulated when compared to the 1991/92 analysis from ERA-40, but the amplitude is much weaker. ERA-40 show a region of strong divergence beyond 60N and between 20 and 5 hPa in the upper stratosphere. This may be because of increased horizontal diffusion in the upper levels of ERA-40. If horizontal diffusion is increased, waves are damped stronger and is diagnosed

as divergence of E-P flux. It would be interesting to see whether the horizontal diffusion in ERA-40 is changing above 10 hPa. This is much stronger in the first winter than in the second winter following the eruption in ERA-40. This region of divergence, which means more zonal westerly forcing on the mean flow, is also observed in the upper stratosphere between 60N and 70N in ens1-PW, whereas this is much stronger and extends down to the lower stratosphere in high latitudes in ens6-P. Hence, there are only minor differences in the pattern of E-P flux vertical and meridional components. In order to investigate this further, the magnitude of the vertical wave activity is analyzed as this is the most important term through which the troposphere modulates the stratosphere and vice versa.

The vertical component of the E-P flux (hereafter referred to as Fz) of ZWN1+2+3 at two different levels: 200 hPa and 20 hPa is analyzed. The meridional profiles of the vertical component of ZWN1+2+3 related E-P flux ($kg/s^2$) are shown for ens1-PW (green), ens5-NN (blue), ens6-P (red), ens7-W (yellow) and also for the climatological mean unperturbed run (black) in figure 4.26. The figure also presents the standard deviation of the Fz of the unperturbed mean (shown as the black line with unfilled circles). The maximum vertical E-P flux in 200 hPa is seen between 45N and 55N and is between 120,000 and 140,000 $kg/s^2$ for most of the cases except for ens1-PW, where we actually get both a volcanic winter pattern at the surface and a stronger polar vortex. Comparing these values with the climatology (Max. Fz = 90,000 $kg/s^2$ at 200hPa), it can be seen that there is more or slightly less vertical wave activity during volcanically disturbed winters. Ens6-P shows downward eddy heat flux beyond 60N which could mean that there is reflection of the waves and this could in turn lead to the surface volcanic winter pattern, but in this case, the model could not reproduce the observed pattern. The maxima for the vertical component of E-P flux at 20 hPa is more shifted to the higher latitudes between 60N and 65N and here, too, there is more or slightly less vertical wave activity flux in the runs perturbed with volcanic forcing. This supports the study by *Graf et al.* [2007] that more eddy heat flux penetrates into the higher altitudes during volcanic winters, but, it has to be noted that this is seen for most of the cases considered here irrespective of whether they produce a volcanic winter pattern or not. The maxima of the standard deviation of vertical wave activity flux of the unperturbed run is close to 30,000 $kg/s^2$ at 200 hPa and around 15,000 $kg/s^2$ at 20 hPa.

In order to understand if the simulated Fz values for these cases agree with the observations, the Fz component at 200 hPa and 20 hPa is analyzed for all the volcanic winters following the three major volcanic eruptions discussed in the beginning of this chapter. For comparison purposes, the same analysis is applied to the long term climatological mean from ERA-40 data calculated from all the 43 years from 1958. These values are shown in fig. 4.27. It can be seen that for the winters of 1992/93, 1963/64 and 1964/65, the vertical wave activity flux at 200 hPa and 20 hPa is nearly equal or less than the climatological mean in comparison with other volcanic winters. There is a clear signal of the volcanic winter

pattern at the surface and the polar vortex is stronger too for the winter of 1992/93, but for the two winters following Agung, the vortex was stronger and the dynamical response is much weaker in the second winter than the first. Stronger vertical wave activity flux is seen for the winters of 1991/92, 1982/83 and 1983/84 when a strong El Niño was present. This is an indication that during El Niño years accompanied by volcanic eruptions there is more vertical wave activity compared to those volcanic winters that occurred during a non El Niño period. This explains why in the model simulations, there is a relatively weaker Fz component in ens1-PW and ens6-P (non El Niño cases) compared to ens1-NN and ens7-W (El Niño cases). The values of Fz during volcanic winters in conjunction with an El Niño lies between 180,000 and 240,000 kg/s$^2$ at 200 hPa and between 60,000 and 70,000 kg/s$^2$ at 20 hPa. Apart from this, there is strong downward wave activity beyond 65N at 200 hPa and this, as explained earlier may be a representation of wave reflection. As can be seen there are differences in the responses between the individual winters of volcanic eruptions.

Although there is a good agreement in the main features of the vertical wave activity component (such as the location of maximum Fz, differentiation between El Niño and non El Niño cases, more Fz compared to the mean in volcanic winters) between model simulations and observations, major discrepancies exist in the magnitude of Fz. The magnitude of the Fz component in the simulations is much lower than in ERA-40. To understand the reasons for this discrepancy, first, the Fz values in the model climatology is examined and comparisons with ERA-40 climatology is discussed in the next section.

### 4.7.4 Intercomparison of model (ECHAM5.4) and ERA-40 climatologies of vertical wave activity flux, Fz

A comparison of the vertical wave activity flux is made between the long term climatological monthly means from observations (ERA-40) and model simulations to see whether the model simulates the planetary wave propagation reasonably well. This is shown in 4.28. Since the monthly means are used for this analysis, the transient waves are filtered out and the stationary waves remain. The maximum value of Fz component at 200 hPa and 20 hPa calculated from ERA-40 data is 178,300 kg/s$^2$ at 50N and 51,300 kg/s$^2$ at 62.5N respectively. The simulated values without the effects of volcanic forcing, El Niño and QBO are 93,300 kg/s$^2$ at 48N and 33,400 kg/s$^2$ at 62.5N respectively. If the ensemble mean of the unperturbed runs including the observed SSTs and the right QBO phases in the calculation of Fz, the maximum values are 110,000 kg/s$^2$ at 48 N and 42,000 kg/s$^2$ at 62.5 N at 200 hPa and 20 hPa respectively. Hence, there is relatively more vertical wave activity flux when the observed SSTs and the right shear of QBO are included. Though the latitude of maximum Fz is simulated reasonably well in model simulations at the levels considered here, the magnitude of the vertical wave activity flux is about 48% less in the model at 200 hPa and about 35% less at 20 hPa compared to ERA-40. This means that

48% less planetary stationary waves generated in the troposphere reaches the stratosphere and hence, can transfer much less eddy heat fluxes to the stratosphere.

Further, the E-P flux analysis is applied to the 6-hourly model and ERA-40 data so that both the stationary and transient waves are included. The Fz component at 20 hPa and 200 hPa for both model and ERA-40 data is shown in 4.29. At 20 hPa, the maxima in Fz differs by 33%, where the model Fz values are still less than the ERA-40. However, at 200 hPa, the difference in the Fz values are comparatively lower (20%). It should be noted that the percentage difference at 20 hPa remains more or less the same even when both stationary and transient waves are considered. But, at 200 hPa, the difference between observations and model data is reduced considerably. This may be due to the fact that the transient waves are overestimated in the model thus compensating the total vertical wave activity flux. However, it has to be noted that at 200 hPa, there are differences beyond 40 N. This may be because the subtropical jet is stronger in the model, thereby creating a wave guide, preventing the propagation of the waves from the tropics to higher latitudes.

The vertical component of E-P flux is also analyzed for the stationary waves for zonal wave numbers (ZWN), ZWN-1, ZWN-2 and ZWN-3 to understand which wave contributes most to this discrepancy. This is shown for both model and ERA-40 climatology at 20 hPa and 200 hPa in figures 4.30 and 4.31 respectively. It is seen that the first two wave numbers contribute most to eddy heat flux transfer to high altitudes at 20 hPa, whereas, all the three wave numbers contribute, at 200 hPa. At 20 hPa, ZWN-1 and ZWN-2 contributes to 63% and 37% respectively to the total difference between the model and observed climatological values of Fz. At 200 hPa, the percentages are 28%, 49% and 20% for ZWN-1, ZWN-2 and ZWN-3 respectively. As can be seen, all the waves contribute equally to the discrepancy in Fz values between model and observed climatology. However, at 200 hPa, ZWN-2 contributes more and at 20 hPa, ZWN-1 contributes more than the other zonal wave numbers. Moreover, negative values of Fz means the wave is reflected at this level. This can be seen in the Fz at 200 hPa in ZWN-2 and ZWN-3 in ERA40 around 70N. The model climatology estimates more wave reflection in ZWN-1 than ERA40 and comparatively less in ZWN-2.

Hence, the previous paragraphs describe the inconsistency in the planetary wave propagation characteristics in the model climatology in comparison with the ERA40 climatology. This is an important point which might be a reason behind the poor simulation of the dynamical response. This would improve the coupling between the stratosphere and the troposphere coupling. An in-depth analysis is required to understand the reasons behind this disparity. But, this is beyond the scope of this thesis.

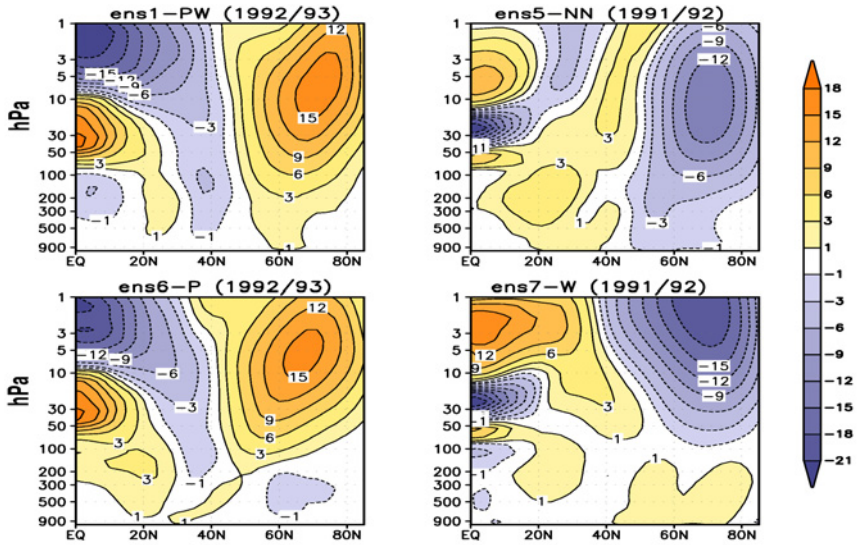


Figure 4.23: Zonal mean zonal wind (m/s) anomalies for the selected cases averaged over the DJF months.

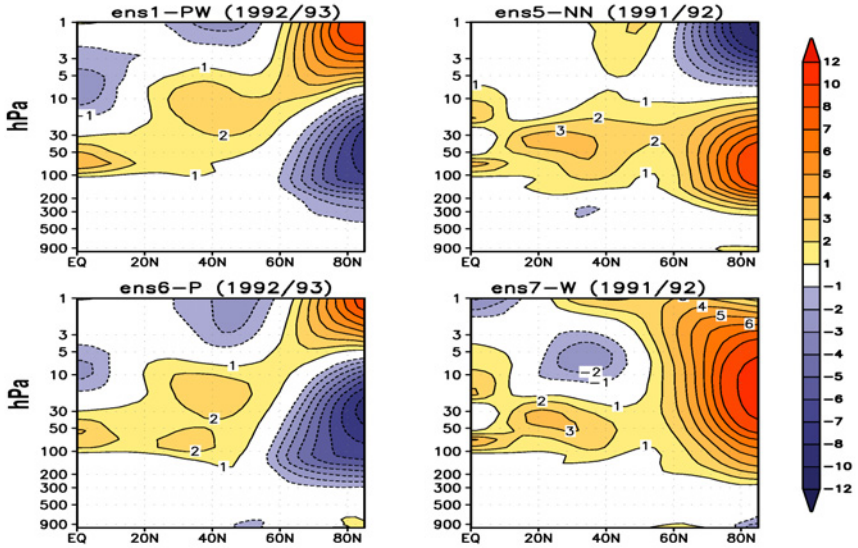


Figure 4.24: Zonal mean temperature (K) anomalies for the selected cases averaged over the DJF months.

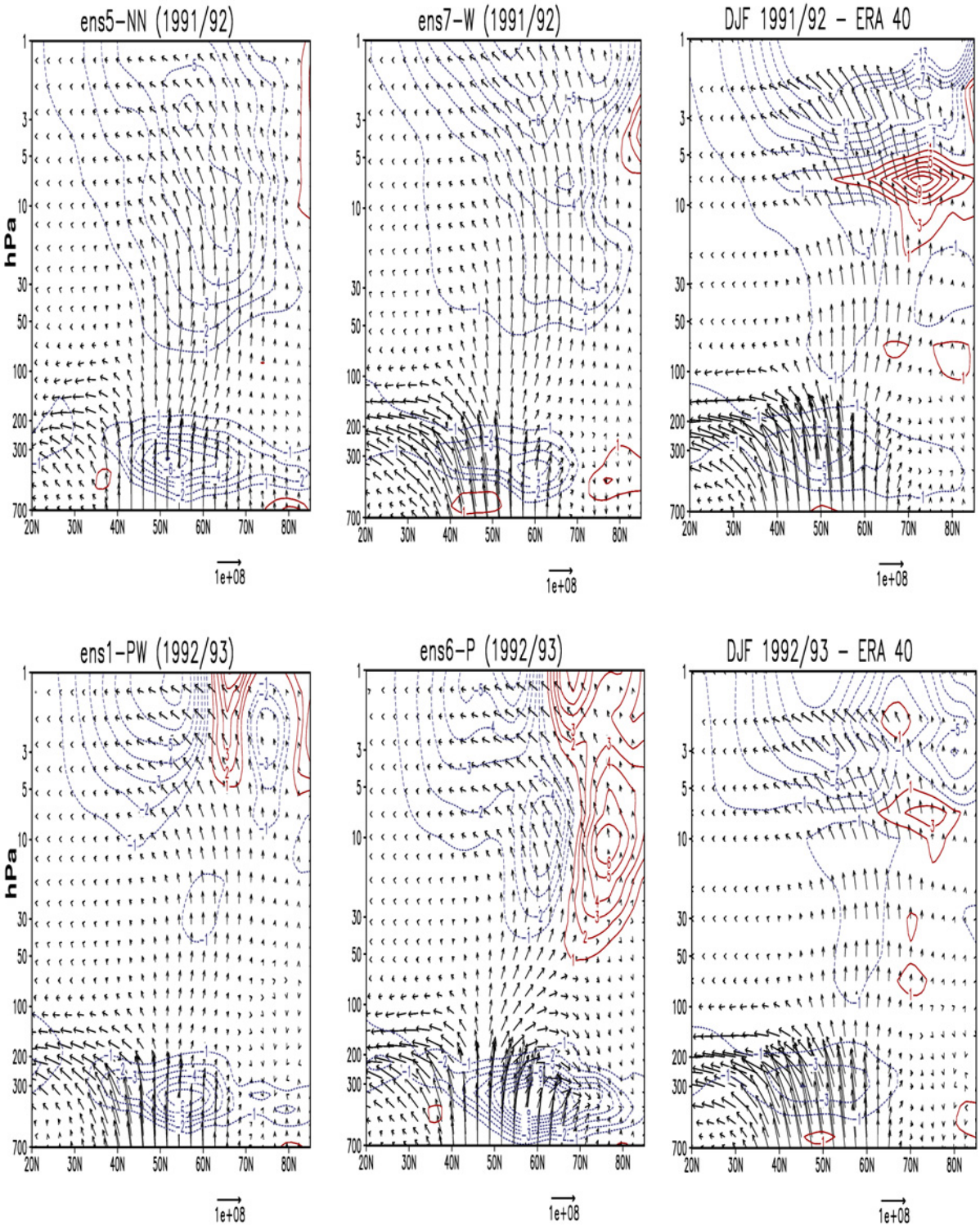


Figure 4.25: E-P flux and divergence for stationary planetary waves in DJF of the selected cases - ens1-PW, ens5-NN, ens6-P, ens7-W and from ERA-40 for the winters of 1991/92 and 1992/93 for ZWN1+2+3. Divergence contour interval is 1 m/s/day. The unit of the vector is kg/s$^2$.

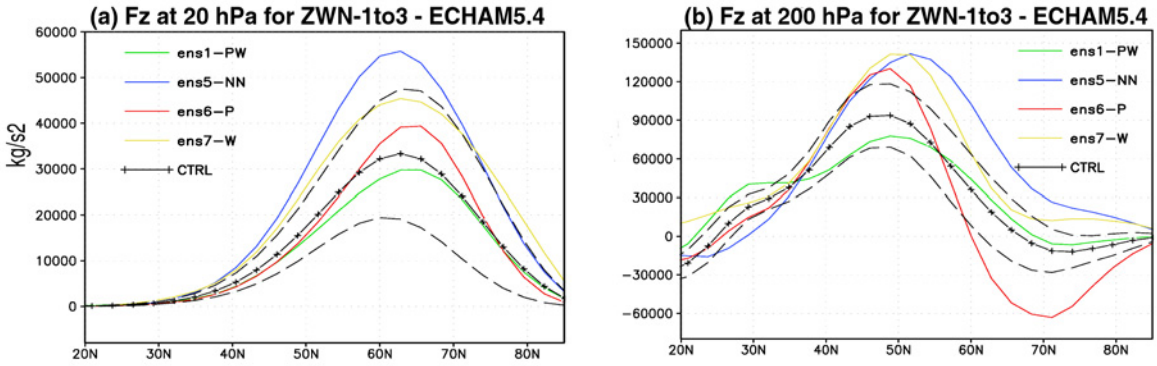


Figure 4.26: Meridional profiles of the vertical component of stationary planetary waves for ZWN1+2+3 related E-P flux (kg/s$^2$) across (a) 20 hPa and (b) 200 hPa for four selected ensemble members - ens1-PW in green; ens5-NN in dark blue; ens6-P in red; ens7-W in yellow and climatological mean from $C_c$ run in black. The standard deviation of the $C_c$ run is shown as the dashed line.

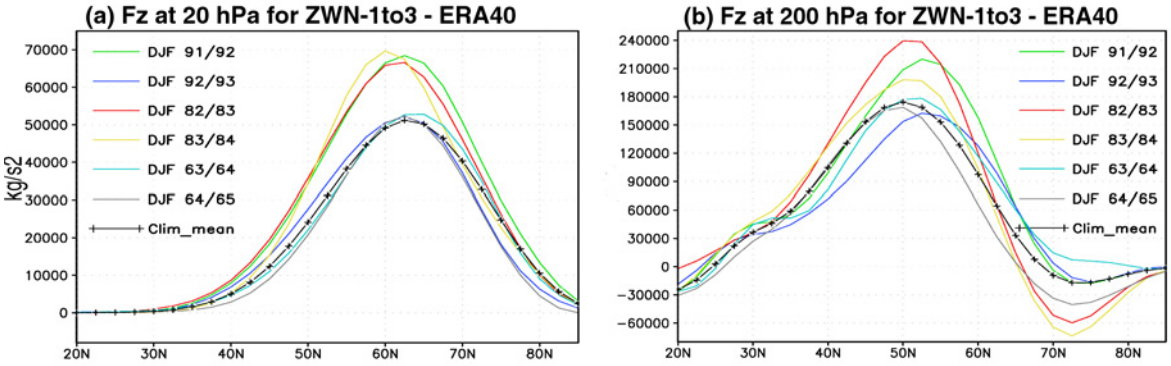


Figure 4.27: Meridional profiles of the vertical component of of stationary planetary waves for ZWN1+2+3 related E-P flux (kg/s$^2$) across (a) 20 hPa and (b) 200 hPa in the six winters following the volcanic eruptions from ERA-40. The winters of 1991/92 in green; 1992/93 in dark blue; 1982/83 in red; 1983/84 in yellow; 1963/64 in light blue; 1964/65 in grey and the long term mean climatology in black.

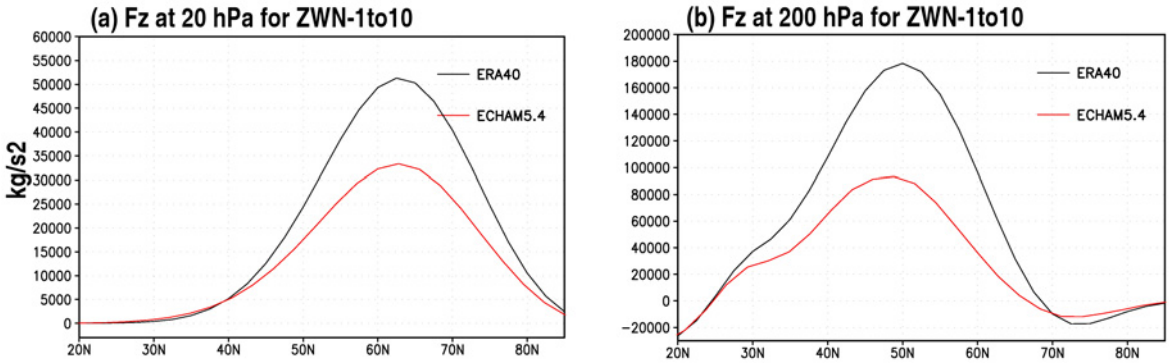


Figure 4.28: Meridional profiles of vertical component of of stationary planetary waves for ZWN-1to10 related E-P flux (kg/s$^2$) across (a) 20 hPa and (b) 200 hPa calculated for model climatology and ERA40 climatology

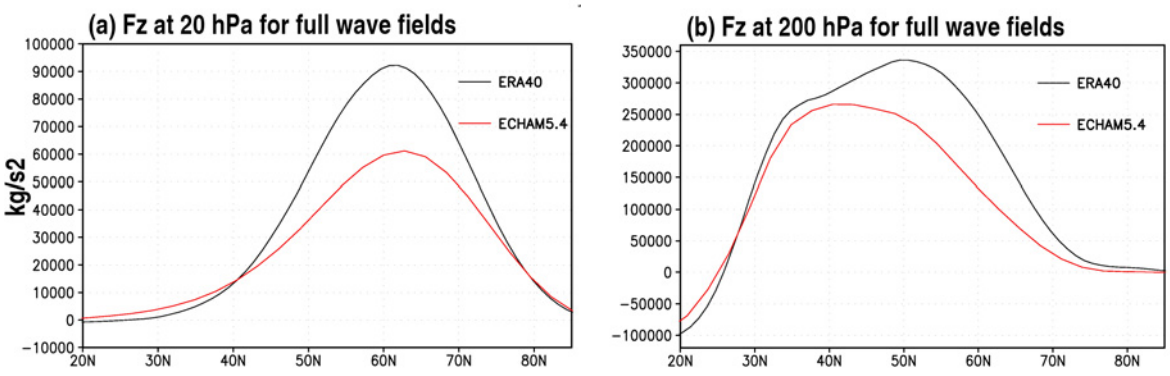


Figure 4.29: Meridional profiles of vertical component of the full wave fields (both stationary and transient) related E-P flux (kg/s$^2$) across (a) 20 hPa and (b) 200 hPa calculated for model climatology and ERA40 climatology

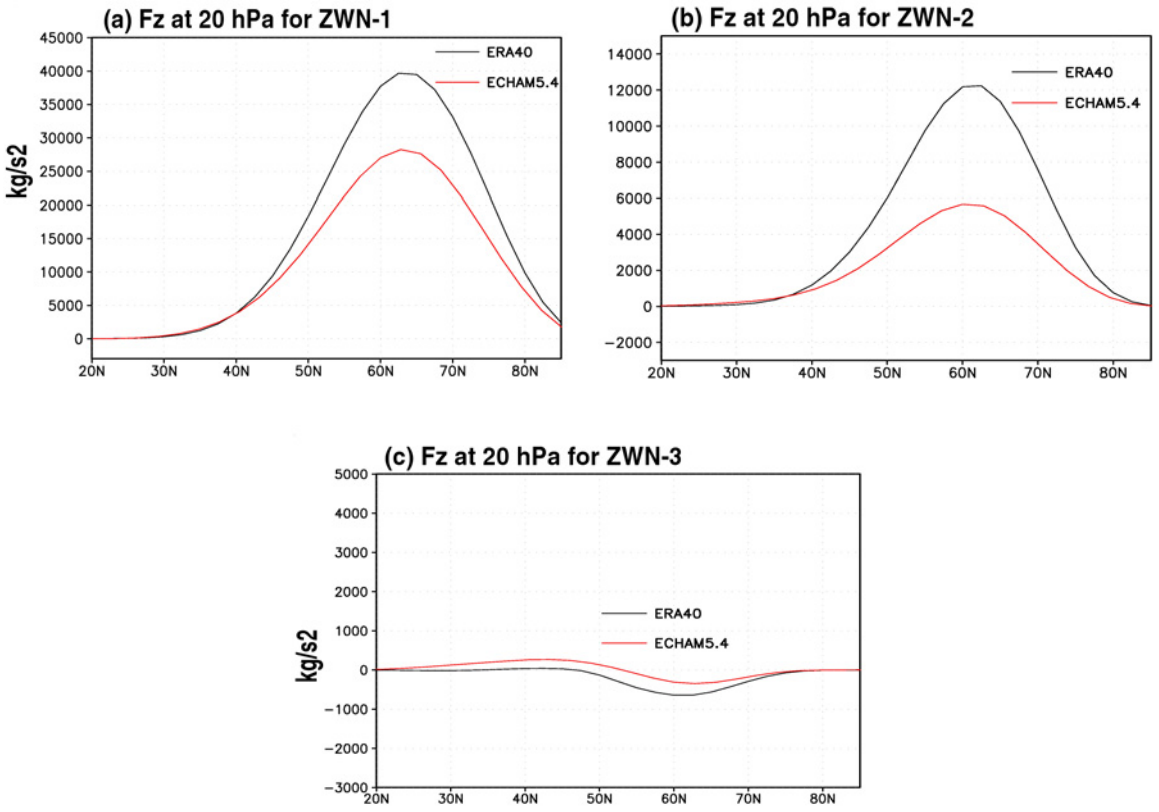


Figure 4.30: Meridional profiles of vertical component of stationary planetary wave related E-P flux (kg/s$^2$) across 20 hPa for (a) ZWN-1 (b) ZWN-2 and (c) ZWN-3 calculated for model climatology and ERA40 climatology

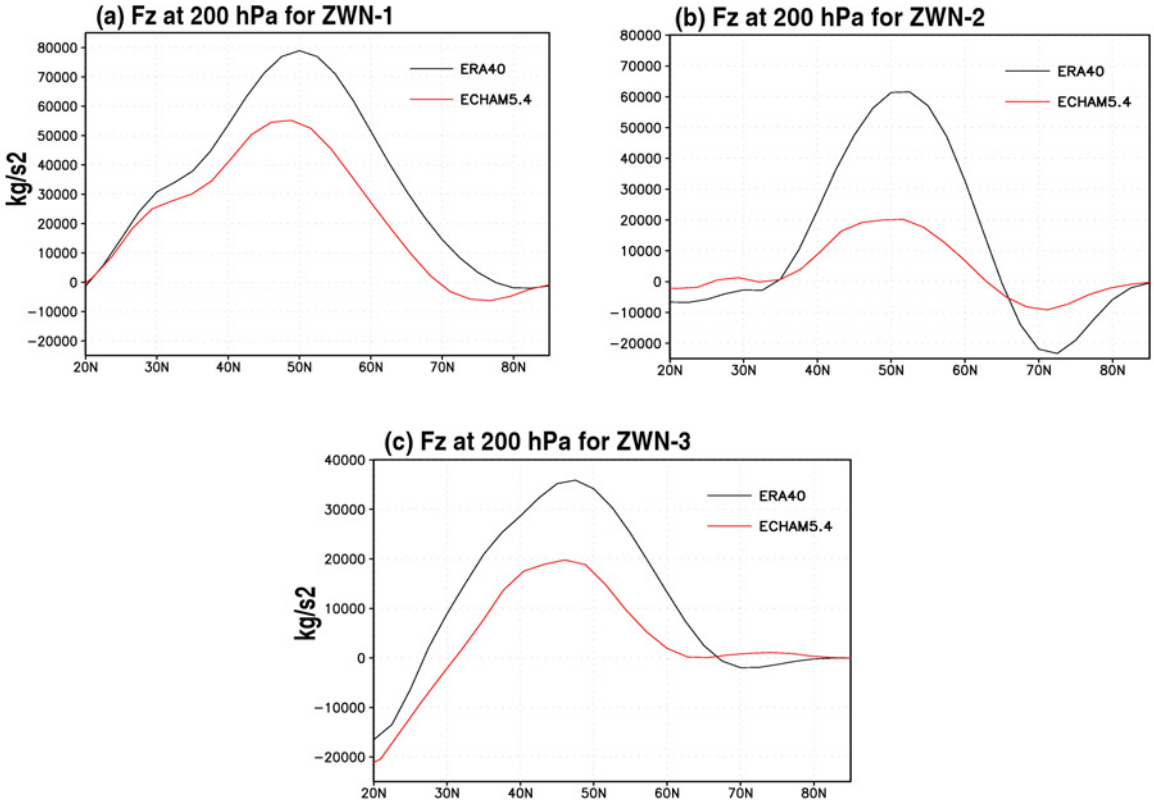


Figure 4.31: Meridional profiles of vertical component of stationary planetary wave related E-P flux ($kg/s^2$) across 200 hPa for (a) ZWN-1 (b) ZWN-2 and (c) ZWN-3 calculated for model climatology and ERA40 climatology

## 4.8 Summary

In this chapter, the generalized climatic response to Mt. Pinatubo eruption is investigated. The response of the tropospheric and stratospheric circulation to individual and combined factors such as volcanic forcing, varying SST boundary conditions and different states of QBO are assessed. This study is important as it provides insights on how the climate responds to the volcanic forcing when either one or more of the boundary conditions are included.

The first part of this chapter deals with the observed climate impacts of three major volcanic eruptions, namely, Agung (1963), El Chichón (1982) and Mt. Pinatubo (1991) and how the impacts vary from eruption to eruption. To understand the significance of the observed response, the natural variability of the climate system is also addressed. Significant warming up to 4 K is observed in the lower stratosphere for the three eruptions depending up on the dispersal of the sulfate aerosols which in turn depends on the QBO phase and on the amount of ozone loss. One of the prominent impacts is the dynamical response manifested as "volcanic winter pattern" observed for two winters after the volcanic eruptions. Based on the arguments given in section 4.4.3, "volcanic winter pattern" hereafter is referred to as the warming over Northern and eastern Europe and Siberia and cooling over Greenland and Middle east and is re-defined as "volcanic winter pattern". This pattern is highly variable from winter to winter and from eruption to eruption. The volcanic winter pattern is mostly associated with the strengthening of the polar vortex. Deeper polar vortices mean strengthening of the westerly winds and this in turn is due to the strengthening of meridional temperature gradient. The zonal mean zonal wind and temperature anomalies and the associated 30 hPa geopotential height anomalies for the three eruptions exhibit variations in magnitude and pattern.

To evaluate how well the model simulates these observed impacts, ensembles of perturbed and unperturbed runs are carried out with different boundary conditions and the differences between the several combinations of perturbed and unperturbed runs give the individual and combined responses due to volcanic forcing, El Ni$\tilde{n}$o and QBO effects. For example, Aer1, Aer2 and Aer3 gives the pure aerosol response under different boundary conditions. Hence, Aer1 is the aerosol response under climatological SST as boundary conditions, Aer2 under observed SST as boundary conditions and Aer3 under both observed SST and QBO. The individual responses of QBO and SST is also investigated. The other responses discussed in this chapter are 1. combined aerosol and SST response (AO), 2. combined aerosol and QBO response (AQ) and 3. combined aerosol, SST and QBO response (AOQ). So, the ensemble mean differences gives an idea on how different the responses would be if El Ni$\tilde{n}$o was not present or if only the volcanic forcing exists, which otherwise, would have been possible to estimate without these sets of experiments.

The ensemble mean lower stratospheric temperature response is simulated realistically

when all the known factors such as El Niño and QBO effects are included. Moreover, the combined response are seen to be linear in the tropics. For example, the lower stratospheric temperature response in AOQ is the sum of the aerosol related response, ocean response and the QBO response. The individual and the combined forcings for two winters following the eruption could not reproduce the warming over northern and eastern Europe and Siberia and the cooling over Middle east and Greenland, though this pattern was simulated by 30% of the ensemble members. One of the possible reasons could be that the model has insufficient vertical resolution in the upper troposphere and lower stratosphere to resolve the interactions between troposphere and stratosphere. Another reason would be that zonally averaged volcanic forcing and volcanically induced ozone anomalies are used in the model simulations. The omission of the zonal asymmetric component of volcanic forcing and ozone forcing may produce differences in the response. It is shown that the zonally asymmetric component of ozone has an effect on the stratospheric temperature and planetary wave propagation (*Gabriel et al.* [2007]). This surface pattern is hypothesized as a characteristic of anomalously positive AO index. The magnitude and strength of the polar vortex is more or less captured in the second winter by the individual aerosol response with observed SST as boundary conditions. However, the polar vortex is shifter over Russia and Siberia during the second winter when observed SST + QBO are prescribed as boundary conditions. The QBO-related 30 hPa geopotential height anomalies tries to simulate the polar vortex realistically in the westerly QBO phase and the vortex is weaker and warm in the easterly phase of QBO. This is in agreement with the studies by *Holton and Tan* [1980]. Similar characteristic is observed in the combined responses of (aerosol+QBO) forcing and (aerosol+ocean+QBO) forcing.

There are several ensemble members where the response is simulated realistically and in some cases, they did not. Hence, the second part of this chapter addresses the reasons selecting four ensemble members as a case study.

The stationary planetary wave propagation is analyzed for selected ensemble member cases and for the 6 volcanic winters from ERA-40 data. For this, E-P flux analysis is diagnosed for both the observations and simulations. Four cases are selected in a way that the "volcanic winter pattern (W)" at the surface and polar vortex (P) are simulated or not. Of the cases that exhibit a stable polar vortex, ens1-PW and ens6-P, ens1-PW exhibits the volcanic winter pattern at the surface. ens5-NN does not reproduce the surface pattern whereas ens7-W does without a strong polar vortex. The observed E-P flux of 1991/92 and 1992/93 shows two centers of convergence one in the extratropical troposphere and the other in the stratosphere and this is simulated realistically by all the four cases selected here, irrespective of whether they exhibit the volcanic winter pattern or not. However, the center of divergence between 60N and 80N and between 10 and 5 hPa is not simulated. All the cases selected here also try to simulate realistically the eddy heat flux in the mid-

latitude stratosphere and the horizontal momentum flux to subtropical troposphere. One notable difference is that the increase in vertical wave activity between 5 and 2 hPa is not simulated by any of the cases. To be more specific, the vertical wave activity flux at 200 hPa and 20 hPa is investigated. There is relatively more vertical eddy flux component during the El Niño winters (ens5-NN and ens7-W) compared to the non El Niño winters (ens1-PW and ens6-P). This is consistent with the observations and earlier studies (*Calvo et al.* [2004]; *Manzini et al.* [2006]) where there is more vertical wave activity flux during volcanic winters with El Niño events than the volcanic winters without El Niño events. The model simulates the location of maximum vertical eddy flux realistically at 200 hPa and 20 hPa. However, the simulated Fz values during the volcanic winters are significantly lower than the observations. A comparison of the climatology of vertical wave activity flux for the stationary waves from observations and model simulations show that Fz is two times less in the model climatology than the observations. However, E-P flux analysis on the full wave field that comprises of both stationary and transient waves do not show a large difference between model climatology and ERA-40 climatology. This would mean that the model is over-estimating the transient waves. It should be noted that the climatology of wind and temperature of the model compare well with ERA-40. This could be one of the reasons of inability of the model in simulating the correct amplitude of the tropospheric anomalies after big volcanic eruptions. Hence, it is important that the model be able to resolve the stratosphere region realistically in order to simulate the dynamical response.

# Chapter 5

# Sensitivity of the climate impact of Mt. Pinatubo eruption to the phase of the QBO

## 5.1 Introduction

The quasi-biennial oscillation (QBO) in the zonal winds in equatorial lower stratosphere is a well known mode of interannual variability. The zonally symmetric easterly and westerly wind regimes alternate regularly with a period of 20-30 months. The alternating wind regimes develop in the upper stratosphere near 3 hPa and propagate downward at an approximate rate of 1Km/month to the tropopause. The amplitude of the easterly phase is stronger than the westerly phase. The easterly zonal winds can reach as high as 35-40 m/s, whereas the westerly zonal winds reach 15-20 m/s. The broad spectrum of waves in the tropics provide the momentum flux required to drive the QBO (refer *Baldwin et al.* [2001] for details). There is considerable variability of the QBO in period and amplitude.

The QBO influences the extratropical northern stratosphere. Studies have shown that the geopotential height at high latitudes is significantly lower during the westerly phase of QBO than during the easterly phase (*Holton and Tan* [1980]; *Holton and Tan* [1982]). *Labitzke* [1987] and *Labitzke and Loon* [1988] found a strong relation of the QBO signal to the 11-year solar cycle during January and February and it was shown that during the easterly phase, for solar maxima, there exists an intensified cold polar vortex and vice versa for solar minima. The 30-hPa North Pole temperatures are positively correlated with the 11-year sunspot cycle during the westerly phase of the QBO while no correlation exists for the easterly phase of the QBO directly over the North Pole. QBO also affects the winter stratospheric temperatures depending on the ENSO phase (*Garfinkel and Hartmann* [2007]), for example, our model simulations show with observed SSTs and QBO show that

when ENSO is in its warm state, the influence of QBO is reduced. Even the height of tropical deep convection have a strong correlation with QBO wherein the height of the tropopause is higher than normal allowing convection to penetrate more deeper during the easterly phase of QBO (*Collimore et al.* [2003]). Moreover, there is a strong relationship between the phase of the QBO and seasonal hurricane activity in the north Atlantic basin with more storms in the westerly QBO phase at 50 hPa (*Gray* [1984]; *Gray et al.* [1992]). The QBO plays an important role in the distribution of chemical constituents like ozone, water vapor and methane and aerosols (*Trepte and Hitchman* [1992]; *Trepte et al.* [1993]; *Baldwin et al.* [2001]). Once the aerosols reach the stratosphere, their dispersal strongly depends on the phase of the equatorial wind. Planetary wave activity is much less in the easterly phase of the QBO compared to the westerly phase, which means that the aerosols are trapped in the equatorial belt during the easterly phase of QBO and are dispersed during the westerly phase (*Trepte et al.* [1993]).

The easterly and westerly phases of the QBO have different effects on the stratospheric extratropical circulation. Here, the sensitivity of the effect of large volcanic eruptions on the high latitude circulation to the QBO phase is evaluated. Mt. Pinatubo erupted on June 15, 1991 during the easterly phase of the QBO at 30 hPa and the change to the westerly phase took place in Aug 1992 at 30 hPa and remained in the same phase till May 1993. It would be interesting to understand the climate impact of Mt Pinatubo eruption if it had erupted during the opposite phase. Here, in this study, a sensitivity analysis is carried out to explain if there is any systematic difference of the effect of the QBO phase on the response of the extratropical circulation to the Mt. Pinatubo eruption. As explained in chapter 2, most GCMs are not able to simulate a spontaneous QBO. But, in the recent years, attempts have been made to include the QBO forcing in GCMs either by assimilating the zonal winds at Singapore to the model winds or by considering a sufficient spatial resolution, a realistic simulation of tropical convection and the consideration of the effects of gravity waves (*Hamilton* [1998]; *Bruhwiler and Hamilton* [1999]; *Giorgetta et al.* [2002]; *Stenchikov et al.* [2004]; *Giorgetta et al.* [2006]). For this study, the middle atmosphere version of ECHAM5 is modified to include the QBO forcing by nudging the zonal mean zonal winds in the tropics towards the prevailing zonal wind observations at Singapore following *Giorgetta and Bengtsson* [1999].

The individual and combined responses with QBO in the opposite phase are discussed in detail in the following sections. The responses in the observed phase are already discussed in the previous chapter, but, are shown here for quick comparison.

## 5.2 Experimental setup

The setup for the runs including the QBO is discussed in detail in chapter 2 (section 2.4) and the same procedure is followed for the computation of the ensemble members of both perturbed and unperturbed runs with the opposite QBO phase. Ten 2-year runs are carried out with Pinatubo aerosol perturbation and without the aerosol perturbation after a 17 month spinup. The opposite QBO phase is prescribed along with observed SST and sea ice as boundary conditions for both the perturbed and unperturbed runs. Here, easterly winds are denoted by negative values and westerly winds, by positive values.

As mentioned before, there is significant variability of the QBO in period and amplitude. To extract the QBO-related zonal winds that are exactly opposite of that occurred during Pinatubo eruption, the correlation co-efficient is calculated between the 50 hPa zonal mean zonal winds at Singapore for the years 1953-2004 and the 50 hPa zonal winds of 1991/93. The time period of maximum negative correlation co-efficient is chosen as the opposite QBO phase (hereafter referred to as $\overline{QBO}$) and in this case, the best anti-correlated years are from June 1975 - May 1977. The zonal mean zonal winds averaged over 5N-5S from observations for the period June 1991 - May 1993 and for the period June 1975 - May 1977 are presented in figure 5.1. It can be seen that the amplitudes of the westerly and easterly winds are comparable in both these cases. The phase change at 30 hPa takes place in month 14 after June 1991 (around August 1992) and in $\overline{QBO}$, this phase change occurs in month 11 after June 1975 (around mid May 1976). It can be seen that the zonal winds of opposite sign for the period 1991/93 are well represented by the period 1975/77. Since each of the QBO cycles are unique, this is the best correlation possible.

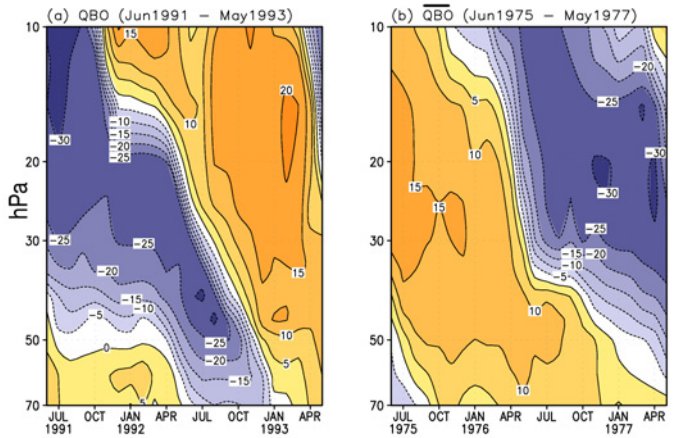


Figure 5.1: Zonally averaged observed zonal winds (m/s) at Singapore for (a) June 1991 - May 1993 and (b) June 1975 - May 1977. Negative values are shaded in colors of blue and are easterlies and the positive values are shaded in colors of yellow and are the westerlies. The contour intervals are 5 m/s.

The model is run with the winds of these two periods and the simulated winds for the same are shown in figure 5.2. These runs are made with observed SST conditions and volcanically induced ozone anomalies. Although there are very slight differences in the magnitude and pattern, the model simulated winds seem to agree in general with the observed winds (slight underestimation of the magnitude).

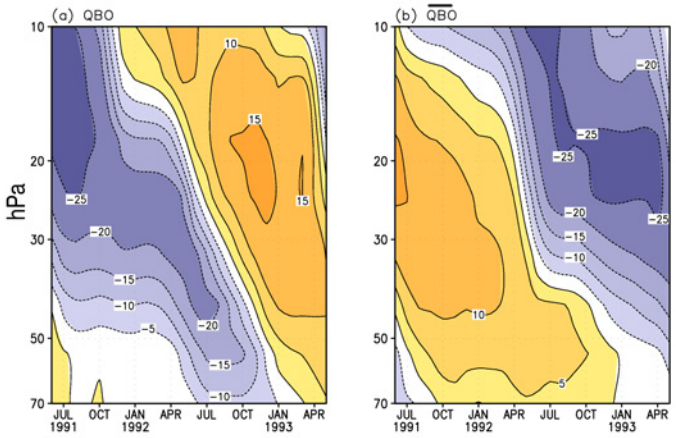


Figure 5.2: Simulated zonal mean zonal winds (m/s) averaged over 5N-5S for two years following Mt. Pinatubo eruption using the wind observations at Singapore from (a) June 1991 - May 1993 and (b) June 1975 - May 1977.

## 5.3 Pure $QBO$ and $\overline{QBO}$ responses

The individual $QBO$ ($\overline{QBO}$) response is calculated as a difference between the unperturbed combined ocean+QBO run (combined ocean+$\overline{QBO}$ run) and the unperturbed run with observed SST as boundary conditions. The following subsections describe the differences in high latitude and low latitude responses owing to the change in QBO phases.

### 5.3.1 Lower stratospheric temperature response at 30 hPa

The QBO exhibits a clear signature in stratospheric temperature with pronounced signals in tropics and extratropics (*Baldwin et al.* [2001]). The tropical temperature QBO is in thermal wind balance (*Andrews et al.* [1987]) with the vertical shear of the zonal winds. For QBO variations centered on the equator with meridional scale, L, the thermal wind balance at the equator is approximated as

$$\frac{du}{dz} = \frac{R}{H * \beta} * \frac{T}{L^2} \tag{5.1}$$

where R is the gas constant, H is scale height, $\beta$ is the latitudinal derivative of the Coriolis parameter, T is temperature deviation and u is the zonal wind. This means that the vertical shear of zonal winds is proportional to the temperature. Figure 5.3 shows the equatorial

temperature anomalies at 30 hPa multiplied by $\frac{R}{H*\beta*L^2}$ (where L = 1500 km) denoted by the red line and the vertical zonal wind shear in 30 - 50 hPa level, by the black line, associated with both $QBO$ and $\overline{QBO}$ phases. It can be seen that both the terms co-vary and the 30 hPa temperature anomalies are negative during the easterly shear of the QBO and positive when the westerly shear is strongest.

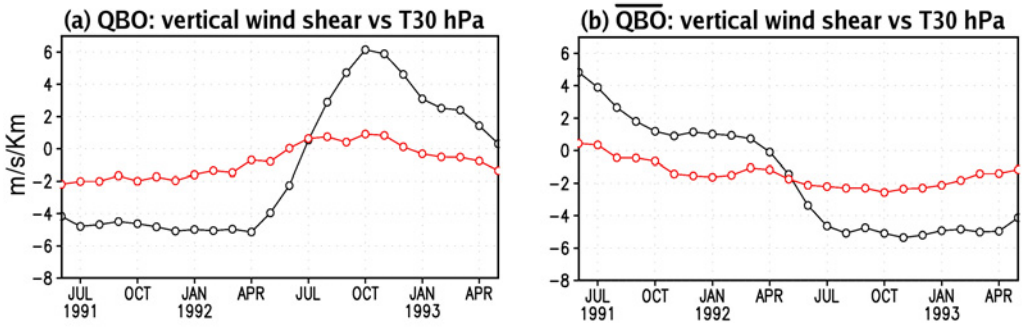


Figure 5.3: Right hand side of the equation 5.1 (red line) and the vertical wind shear in 30 - 50 hPa level (m/s/Km) (black line) for (a) $QBO$ and (b) $\overline{QBO}$.

The stratospheric temperature response at 30 hPa to the two QBO phases, namely, one for the phase change from from easterly to westerly ($QBO$) and the other from westerly to easterly ($\overline{QBO}$) is investigated. Figure 5.4 shows the lower stratospheric temperature response to (a) the observed $QBO$ and (b) $\overline{QBO}$. A cooling of about 1-2 K is observed in the latitudinal belt from 10N-10S from June 1991 - Apr 1992 in fig. 5.4 (a) and from Jan 1992 - May 1993 in fig. 5.4 (b) and warm anomalies are observed in the mid latitudes. As mentioned in chapter 4, negative temperature anomalies are observed in the equatorial belt associated with the easterly wind shear of the QBO and positive anomalies in the mid latitudes. The opposite is observed during the westerly wind shear of QBO. However, the temperature response associated with the westerly phase of the QBO in figures 5.4 (a) and (b) is comparatively weaker. To better understand this, the zonally averaged vertical wind shear in 30 - 50 hPa level is shown in figure 5.5. It can be seen that the easterly shear lasts longer than the westerly shear. The westerly shear is stronger during the observed QBO phase (fig. 5.5 (a)) and is weaker during the opposite QBO phase (fig. 5.5 (b)). As the magnitude of both the shears are comparable, the weaker temperature anomalies associated with the westerly phase of QBO cannot be justified. To investigate this further, the climatological mean differences in temperature anomalies in the simulations with QBO and without a QBO is analyzed. Since, the simulations carried out here are for two years, long term climatology is not possible. Hence, the 22 year simulations carried out with MAECHAM4 with the same QBO set up is used to calculate the climatological mean differences (H. Punge, personal communication). This is presented in Appendix-J. The figures J.1 (a) and (b) show the vertical temperature profile differences of (with QBO) runs minus the (without QBO) runs. It can be seen that at 30 hPa, there is a cold bias of up

to -1.5 K. This means that the 30 hPa stratospheric temperature climatology without a QBO is colder in the model than with a QBO. This explains why the warm temperature anomalies observed during the westerly QBO shear are weaker.

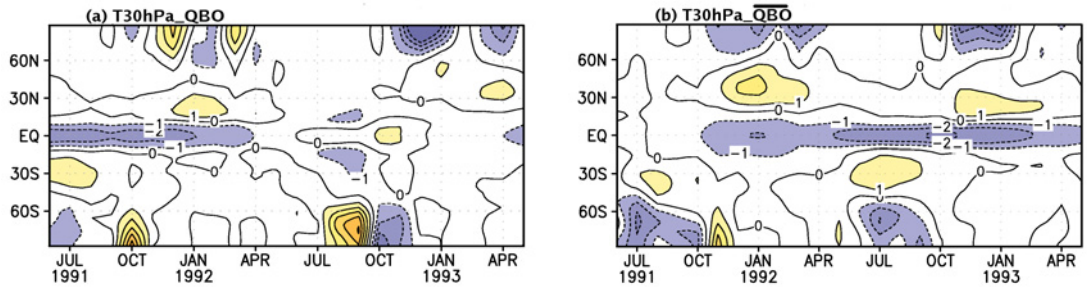


Figure 5.4: Zonally averaged lower stratospheric temperature anomalies (K) at 30 hPa for (a) QBO in the observed shear and (b) QBO in the opposite shear.

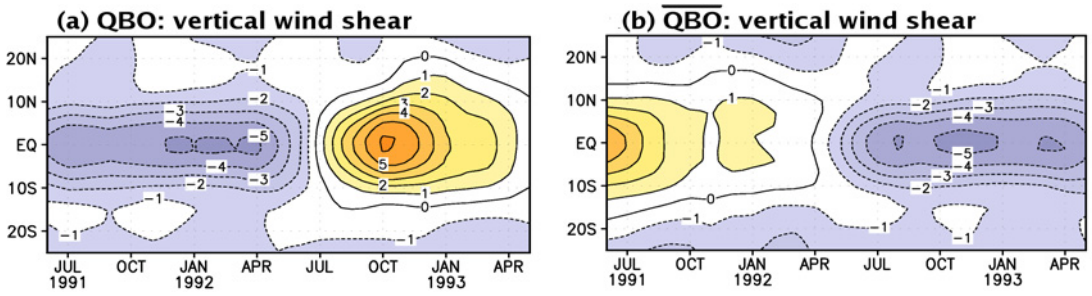


Figure 5.5: Zonally averaged vertical wind shear (m/s/Km) for (a) QBO in the observed shear and (b) QBO in the opposite shear.

### 5.3.2 2m temperature response in boreal winter

The differences in the 2m temperature pattern following the two winters after the eruption simulated for the two QBO phases are analyzed. Figures 5.6 (a + b) show the winter warming pattern for the two winters when the opposite QBO phase is prescribed and figures 5.6 (c + d), when the observed QBO phase is used in the simulations. During 1991/92, statistically significant warm anomalies are observed over Europe, parts of Russia and China and cold anomalies over Greenland and northern Canada in fig. 5.6 (c) with the observed QBO phase and these anomalies are much weaker and not significant in fig. 5.6 (a) in $\overline{QBO}$. Significant cold temperature anomalies are observed over the Himalayan region irrespective of the phase of the QBO during the first winter. Following the second winter after Pinatubo eruption, warm anomalies are observed over Europe and also over eastern and central N. America and cooling over Greenland irrespective of the QBO phase. The main difference is over Asian subcontinent where weak positive anomalies are observed when the observed QBO phase is prescribed. It can be seen that the model tries to simulate statistically significant warming over Europe and cooling over Greenland during the easterly

QBO phase, in figure 5.6 (b) and (c), though the anomalies are much weaker and the cooling over Greenland is not statistically significant in (b).

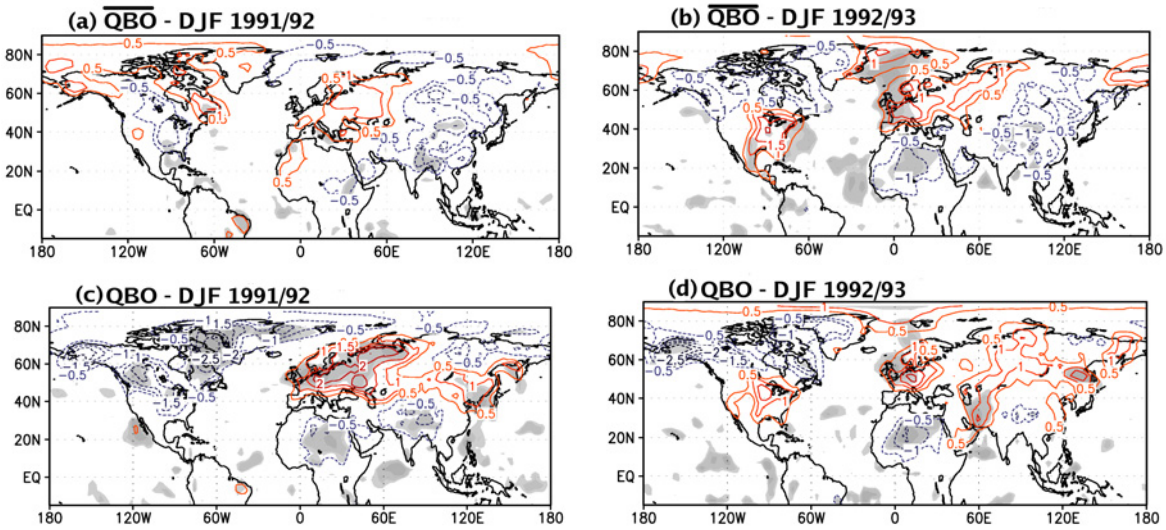


Figure 5.6: 2m temperature anomalies (K) for (a) $\overline{QBO}$: DJF 1991/92 (b) $\overline{QBO}$: DJF 1992/93, when the opposite QBO phase is prescribed; and for (c) $QBO$: DJF 1991/92 and (d) $QBO$: DJF 1992/93, when the observed QBO phase is prescribed. The shading denotes three levels (99%, 95% and 90%) of statistical significance in the order of lighter shading.

### 5.3.3 30 hPa geopotential height response in boreal winter

The differences in the 30 hPa geopotential height anomaly in response to the $\overline{QBO}$ phase is presented in figure 5.7 (a + b) for the two boreal winters following the eruption. The anomalies are weaker in DJF 1991/92 in the $\overline{QBO}$ where positive anomalies are observed over southern Europe, Russia and Siberia (up to 40 m) and negative anomalies over Scandinavia, parts of Greenland and northern Canada (up to -40 m). The second winter shows a strong and larger area of below normal geopotential height anomalies (as low as -160 m) over Northern Eurasia and Greenland and above normal geopotential height anomalies over Canada and northern Atlantic. The vortex observed in the winter of 1992/93 is not symmetric over the poles, but, is slightly shifted over northern Eurasia.

For comparison, the response with the observed $QBO$ phase is shown in figures 5.7 (c + d). In the first winter following the eruption, the $QBO$ is in its easterly phase and $\overline{QBO}$ is in its westerly phase at 30 hPa and the opposite is observed during the second winter. During the first winter, the anomaly patterns do not simulate the strengthening of the polar vortex in either of the cases, though the $\overline{QBO}$ favors a strong polar vortex (*Holton and Tan* [1980]). This may be because of the strong feedbacks between El Niño and the QBO that disturbs the vortex, even though they are individual responses. Comparing the response of $\overline{QBO}$ for the second winter with the response of $QBO$ in the observed phase, the model simulates deeper geopotential height anomalies in both the QBO phases. This means that

the model simulates the anomalously cold polar vortex irrespective of the QBO phase. This contradicts the study by *Holton and Tan* [1980] that the westerly phase of QBO favors a strengthening of the polar vortex or may be the interactions between the QBO and the vertically propagating wave flux is reduced in the second winter when El Niño effects are reduced, thereby strengthening the polar vortex irrespective of the QBO phase.

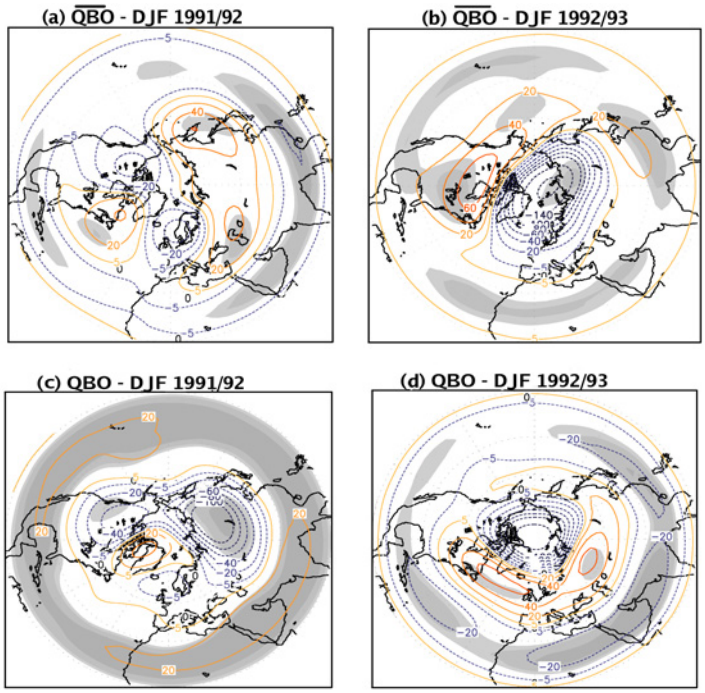


Figure 5.7: Geopotential height anomalies (m) at 30 hPa for (a) $\overline{QBO}$: DJF 1991/92 (b) $\overline{QBO}$: DJF 1992/93, when the opposite QBO phase is prescribed; and for (c) $QBO$: DJF 1991/92 and (d) $QBO$: DJF 1992/93, when the observed QBO phase is prescribed. The shading denotes three levels (99%, 95% and 90%) of statistical significance in the order of lighter shading.

## 5.4 Differences in the response to volcanic aerosol forcing in $QBO$ and $\overline{QBO}$ phases

This section gives a detailed description on the tropical and high latitude response to Mt. Pinatubo eruption when the opposite shear of the QBO is prescribed. The anomalies are calculated as the difference between the combined AOQ/AO$\bar{Q}$ experiment and the unperturbed run with climatological SST ($C_c$) as boundary conditions.

### 5.4.1 Lower stratospheric temperature response

Figure 5.8 shows the 30 hPa temperature response when the aerosol forcing, El Niño and QBO effects are included for two years following the eruption. The only difference is that fig. 5.8 (a) has the observed QBO phase and the fig. 5.8 (b) has the opposite phase as

can be seen in the color bars given at the bottom of the figure. The effects due to the contrasting QBO phases are clearly evident. A cooling of about 1-2 K from June 1991 - Apr 1992 in (a) and from Jan 1992 - May 1993 in (b) is seen in the latitudinal belt 10N - 10S and warmer temperatures are observed in the subtropics. This dual peak with a relative maximum in the subtropics and minimum at the equator during the easterly phase of QBO is well simulated by both the experiments. The response in the latitudinal belt 50N - 50S is statistically significant at $> 90\%$ significant level.

Colder temperature anomalies are observed during the westerly phase of QBO in NH winter (Nov-Dec-Jan) in the polar latitudes associated with the strengthening of the polar vortex. Strong warm anomalies are observed in the northern high latitudes in winter (Jan-Feb-Mar) during the easterly phase of QBO as in fig. 5.8 (a + b) in AOQ forcing. However, in the AO$\bar{Q}$ case, strong warming is observed in northern high latitudes for the two winters following the eruption irrespective of the QBO phase. These warmings are statistically significant at 90% significance level. This means that the change of the QBO phase can bring about changes in the extratropical winter circulation in the lower stratosphere.

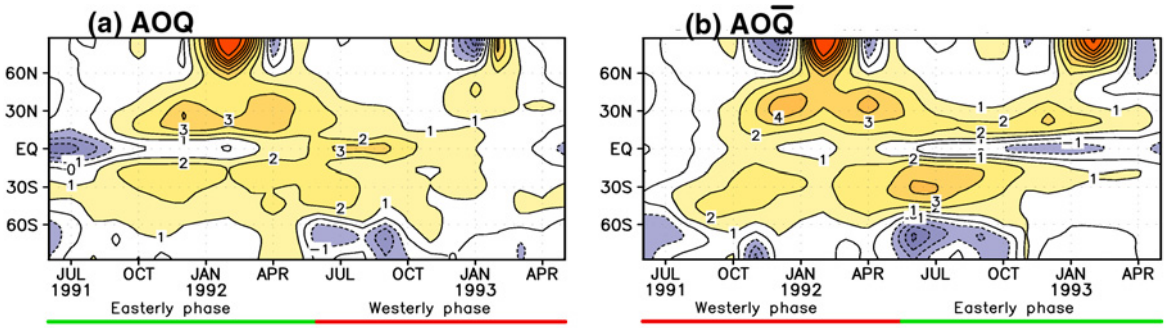


Figure 5.8: Zonally averaged lower stratospheric temperature anomalies (K) at 30 hPa for two years following Mt. Pinatubo eruption for (a) AOQ experiment with observed QBO phase and (b) AO$\bar{Q}$ with the opposite QBO phase. The QBO phases encountered during (a) and (b) are shown by the colored lines.

### 5.4.2 2m temperature response

Figures 5.9 (a) and (b) show the ensemble mean surface temperature anomalies for the first and second winters respectively in AO$\overline{Q}$. For comparison purposes, the ensemble mean surface temperature anomalies in AOQ are also shown in 5.9 (c) and (d). It can be seen that one of the main features of the volcanic forcing, the so-called "volcanic winter pattern" (refer introductory chapter and chapter4 for details), is not simulated by the model in both the winters. The tropical warming in the Pacific due to the El Ni$\tilde{n}$o event of 91/92 is clearly seen in (a). During the first winter, the anomalies in AO$\overline{Q}$ and AOQ are more or less the same, except for some minor differences. The warming over northern N. America associated with El Ni$\tilde{n}$o is statistically significant in AOQ, though the magnitude of the anomalies are captured irrespective of the phases. The pattern exhibited in fig. 5.9 (a) and (c) is similar to the ocean response (refer figure 4.19 (g)), thereby clearly signifying the dominance of

ENSO effects over the effects due to the change of QBO phase. However, during the second winter when the effects of El Niño are negligible, the combined effects due to aerosols and the change of phase of QBO are seen. The warming over northern parts of Europe, Russia and Greenland and cooling over N. America and parts of Canada are simulated irrespective of the phase of the QBO. But, strong statistically significant cooling Middle East, India and China is observed during the easterly QBO phase as in fig. 5.9 (b), whereas these anomalies are weaker and not significant during the westerly phase of QBO as seen in fig. 5.9 (d). Hence, it can be seen that the surface temperature response is independent of the phase of the QBO during the first winter after Mt. Pinatubo eruption due to the presence of El Niño, but differs over Asian subcontinent during the second winter when El Niño effects are reduced.

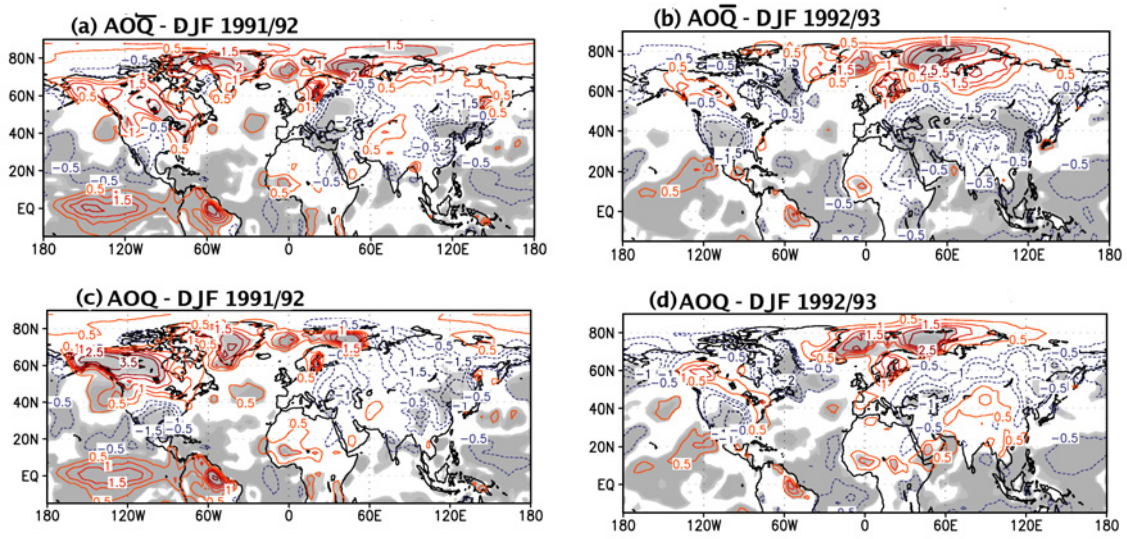


Figure 5.9: 2m temperature anomalies (K) for (a) AO$\overline{Q}$: DJF 1991/92 (b) AO$\overline{Q}$: DJF 1992/93, when the opposite QBO phase is prescribed; and for (c) AOQ: DJF 1991/92 and (d) AOQ: DJF 1992/93, when the observed QBO phase is prescribed. The shading denotes three levels (99%, 95% and 90%) of statistical significance in the order of lighter shading.

### 5.4.3 30 hPa geopotential height response

The geopotential height anomalies for the two winters following the eruption are shown in figures 5.10 (a + b) in AO$\overline{Q}$ and in figures 5.10 (c + d) in AOQ runs. The anomalies in AO$\overline{Q}$ during the winters of 1991/92 and 1992/93 exhibit a wave number one pattern with positive anomalies over northern Pacific, Canada, Alaska and Siberia and negative anomalies over north western Europe and northern Atlantic. The geopotential height anomalies reach as low as -100 m and as high as 140 - 160 m. There is no notable differences between the anomalies of the two winters except that the anomalies in the second winter following the eruption are relatively stronger than in the first winter. As mentioned before, the westerly phase of the QBO favors a strong polar vortex. But, in AO$\overline{Q}$, the westerly phase occurs

during the El Niño winter, which in turn, disturbs the polar vortex.

Comparing the combined responses due to the observed QBO phase with the opposite QBO phase, it can be seen that the anomaly pattern is more or less similar in the first winter, where positive anomalies are more or less positioned over the Arctic circle and the negative anomalies cover a smaller region compared to the anomalies in the AO$\bar{Q}$ response. This similarity in the responses is due to the fact that the El Niño effects override the effects due to the phase change of QBO. However, the response in the second winter differs considerably with a large center of low geopotential height anomalies over the Arctic circle, Greenland and north eastern Europe and Siberia in AOQ when the QBO is in the westerly phase that favors a strong polar vortex and is not seen in AO$\bar{Q}$, when the QBO is in the easterly phase, again, supporting the studies by *Holton and Tan* [1980] and *Holton and Tan* [1982].

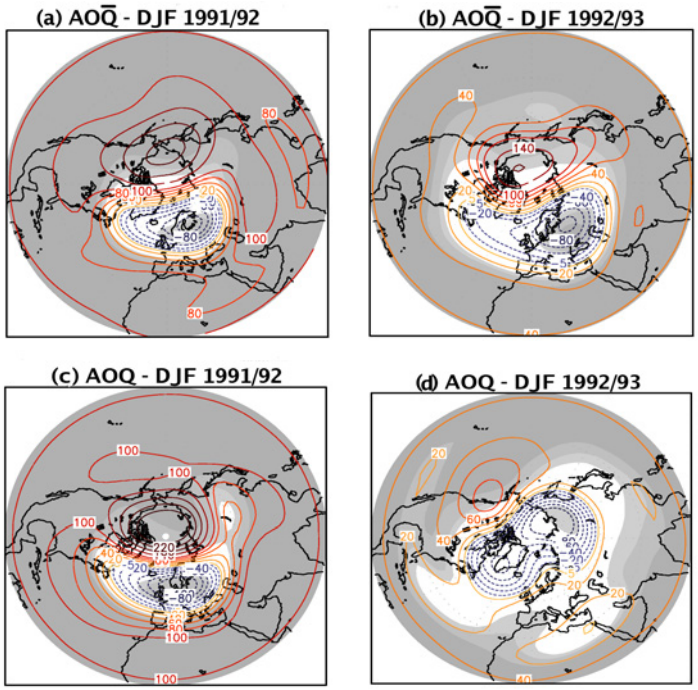


Figure 5.10: Same as above, but, for, Geopotential height anomalies (m) for (a) AO$\overline{Q}$: DJF 1991/92 (b) AO$\overline{Q}$: DJF 1992/93, and for (c) AOQ: DJF 1991/92 and (d) AOQ: DJF 1992/93.

## 5.5 Summary

The sensitivity of the impact of Mt. Pinatubo eruption on tropical and extratropical responses to the different QBO phases is investigated. Here, two cases are considered, one in which the QBO phase is the same as observed during the eruption of Mt. Pinatubo and the other, in which the phase is reversed. Mt. Pinatubo erupted during the easterly phase

of QBO and the phase change took place 14 months after the eruption. In this study, the consequences are analyzed if the eruption had taken place in the westerly phase of QBO. The opposite phase of the observed 91/93 QBO phase is chosen by computing the correlation co-efficient between the observed 50 hPa zonal mean zonal winds at the equator for the period 1953-2004 and the period 1991/93. In doing so, the best anti-correlated years are from June 1975 to May 1977 and this is chosen as the opposite QBO phase, $\overline{QBO}$. Runs are carried out with volcanic forcing and observed SSTs with the opposite phase of $QBO$ and the differences in the responses are discussed.

The individual $QBO$ and $\overline{QBO}$ responses in 30 hPa temperature shows a dual peak with minimum temperatures along the equator and maximum temperatures in the subtropics associated with the easterly QBO shear and the opposite is observed during the westerly QBO shear. The temperature anomalies associated with the westerly phase of QBO is relatively weaker than that with the easterly phase of QBO. This because the lower stratospheric temperatures are colder (up to -1.5 K) in the model without a QBO. The geopotential height anomalies show a strong vortex in the second winter for $QBO$ and $\overline{QBO}$ phases, except that the vortex is more symmetric over the poles when the observed $QBO$ phase is prescribed. The vortex is disturbed in the first winters irrespective of the QBO phase. This may be due to the strong feedbacks between El Niño and the QBO. The model tries to simulate statistically significant warming over Europe and cooling over Greenland during the easterly phase of QBO in $QBO$-91/92 and $\overline{QBO}$-92/93

The combined response to volcanic forcing with observed SSTs and QBO phases are also discussed in this chapter. The lower stratospheric response over the tropics shows a dual peak as explained above and this peak differs from one another based on the QBO phases. A prominent warming is seen in the high latitudes in the two winters following the eruption during the $\overline{QBO}$ phase, whereas, this warming is observed only in the first winter when the observed $QBO$ phase is included. This means that the change of phase of QBO can not only affect the tropics, but also the high latitudes in winter. This warming is statistically significant at 90% significance level. The 30 hPa geopotential height anomalies for the AOQ is more or less the same as that in AO$\bar{Q}$ in the first winter. This is because the effects of El Niño in the first winter after Mt. Pinatubo eruption override the effects due to phase of QBO and may be the El Niño is too strong in the model. However, the pattern is different in the second winter. In the second winter, negative geopotential height anomalies in AOQ are more or less symmetric over the poles with two lobes, one over eastern Europe and Russia and the other over Greenland, in the westerly phase of QBO. But, in AO$\bar{Q}$, negative anomalies are shifted over Europe. It is also shown that the simulated surface temperature pattern is independent of the phase of the QBO during the first winter due to the presence of El Niño, but differs mainly over the Asian subcontinent during the second winter.

# Chapter 6

# Conclusions and outlook

Large explosive volcanoes can inject huge amounts of gases and particulate matter high up into the atmosphere to heights up to 20-30 Km. The most significant impacts from these injections come from the conversion of sulfur dioxide to sulfuric acid, which condenses rapidly in the stratosphere to form fine sulfate aerosols. The aerosols increase the Earth's albedo by reflecting the solar radiation and thus cool the Earth's lower atmosphere. However, they also absorb solar-IR and terrestrial radiation, thereby warming the atmospheric layer they reside. Apart from their radiative impacts, the sulfate aerosols influence the climate system through their interactions with chemical constituents and also by modulating the microphysical properties of clouds. An accurate and realistic simulation of such large perturbations over a relatively short period can serve as important guidelines for understanding the anthropogenic influences on climate, such as the effects of increasing greenhouse gases, aerosols in the stratosphere and ozone depleting chemicals. Studying such climate responses also helps in the evaluation of important radiative and dynamical processes that respond to both natural and anthropogenic forcings. These studies could be used to test our climate models so as to see how well they can simulate this natural climate experiment. Moreover, the simulation of such events can serve as an ideal case scenario for the feasibility and sensitivity of new concepts such as geo-engineering (*Crutzen* [2006]). Many studies, both modeling and observational have been carried out to understand the climate impacts of volcanic eruptions, in particular the Mt. Pinatubo eruption as this is the best documented volcanic eruption so far. However, the major volcanic eruptions of the last century occurred in conjunction with an El Niño event, thereby complicating the efforts of retrieving the volcanic signal.

The main objective of this study is to investigate the climate impact of Mt. Pinatubo eruption on the tropical and extratropical circulation. Here, the climate response is evaluated under varying boundary conditions including one at a time, thereby, assessing the radiative and dynamical responses to individual and combined forcings by observed SST, QBO and volcanic effects. For example, this study helps to answer the questions such as,

how would the response be if El Niño was not present or how different would the response be if the QBO is not included in the model simulations etc. This is the first study that includes all the known processes such as observed SST and QBO effects and volcanically induced ozone anomalies for the simulation of Mt. Pinatubo eruption using the middle atmosphere version of ECHAM5.4. Moreover, the sensitivity of the climate response to the phase of the QBO is also assessed in this study by carrying out the model simulations in an opposite QBO phase. This gives an estimate on how different the response be if the eruption had occurred in the opposite phase of QBO. In order to simulate the impact of volcanic eruption, first, a few improvements are made in the radiation parameterization scheme to simulate the response as realistically as possible.

### ECHAM5.3 radiation scheme:

ECHAM5.3 was overestimating the SW heating rate anomalies and, hence, the lower stratospheric temperature response in the simulations with Pinatubo aerosols. The SW heating rate anomalies were two times higher than that of previous studies from e.g. *Stenchikov et al.* [1998]. This overestimation was due to the simplified assumptions made for low aerosol loadings in the clear sky conditions which are not valid for high aerosol loadings after volcanic eruptions. Thus, for efficiency reasons, the effects of multiple reflection and the interactions between aerosol scattering and gaseous absorption were neglected. These two effects are opposing one another. The aerosol-gas interactions decrease the photon path, thereby, increasing the absorption by the gas molecules resulting in heating. However, the multiple reflection effect increases the photon path, thereby, reducing the energy for absorption resulting in cooling. The dominance of these effects depend on the optical properties of the aerosol particles and their concentration. Here, the sulfate aerosols are mostly scattering in the solar spectrum. So, in this study, the multiple reflection effect overrides the aerosol-gas interaction effect. Minor corrections are also made to remove the inconsistencies in the way the individual atmospheric particles were combined in the model and a more complex scheme is used to compute radiative transfer. The notable differences in the responses after the improvement of the radiative routines emphasizes the significance of these effects. After the improvement, the model simulates the radiative response realistically.

### Response to individual and combined forcings:

The second part of the thesis evaluates the response of the climate to the volcanic forcing when either one or more of the boundary conditions are included. First, an analysis of ERA-40 data was carried out to examine the observed impacts from the large volcanic eruptions such as Agung, El Chichón and Mt. Pinatubo. They reveal warming of the lower stratosphere by up to 4 K and strengthening of the polar vortex for two consecutive winters after the eruptions and one of the prominent impacts during the winters is the warming

up to 4-6 K over northern and eastern Europe and Siberia and cooling over Greenland and Middle east and is referred to as the "volcanic winter pattern". These impacts vary from eruption to eruption, though all the three eruptions were of the explosive type and tropical and co-occurred with El Niño events.

Ensembles of perturbed and unperturbed runs were carried out with different boundary conditions to see how realistically the model simulates the observed impacts. The difference between combinations of perturbed and unperturbed runs gives the individual and combined responses due to volcanic forcing, El Niño and QBO effects. The individual responses considered here are the aerosol responses under different boundary conditions, ocean response and QBO response. The combined responses include AO (aerosol+ocean), AQ (aerosol+QBO) and AOQ (aerosol+ocean+QBO).
The main conclusions are:

1) The pure lower stratospheric temperature aerosol response is insensitive to boundary conditions in the tropics and subtropics.

2) The lower stratospheric temperature response in the tropics is simulated most realistically in the AOQ experiment compared to all the others. The anomalies in the latitudinal belt of 50N-50S are statistically significant at 99% confidence level.

3) The warming observed in the high latitudes in winter in the lower stratosphere is also simulated in the AOQ experiment and the pattern is close to observations. This warming is also significant at 95% significant level.

4) The dynamical response manifested as the "volcanic winter pattern" at the surface is not simulated by any of the ensemble mean experiments considered here. Although, 30% of the ensemble members try to simulate the observed pattern.

5) The analysis shows that the response of the ocean to the atmosphere is very strong in the model that it partially masks the effects due to the volcanic forcing. For example, the ocean-related 2m temperature anomalies during the two winters following the eruption show a warming beyond 60N and cooling in the middle east and parts of Europe and China. This ocean-related response is evident in the combined responses such as AO, OQ and AOQ and this explains the dominance of El Niño over other effects.

6) The volcanic winter pattern observed at the surface after volcanic eruptions in winter is hypothesized as a characteristic of anomalously positive AO index. In the absence of aerosol or El Nino effects, the polar vortex is expected to be anomalously strong during

the westerly phase of the QBO and weak, during the easterly QBO phase (*Holton and Tan* [1980]; *Holton and Tan* [1982]). This is clearly evident in the simulated QBO-related geopotential height anomalies.

7) Detailed analysis of the observed volcanic eruptions shows that aerosol forcing from explosive volcanic eruptions tends to strengthen the polar vortex irrespective of the QBO phase. The magnitude and pattern of the strong polar vortex is more or less captured in the second winter, when the QBO is in its westerly phase in individual Aer3 response and in the combined responses of AQ and AOQ are in agreement with the studies of *Holton and Tan* [1980]. The vortex is disturbed during the first winters in the combined responses and this is due to the enhanced wave propagation in boreal winter that in turn disturbs the vortex.

8) Studies by *Sassi et al.* [2004], *Manzini et al.* [2006] and *Chen et al.* [2003] have shown that during an El Niño event, the enhancement of vertical propagation and divergence of E-P flux cools the tropics and warms the high latitudes. This feature is simulated realistically in the first winter when an EL Niño is ongoing and is evident in the ocean-related lower stratospheric temperature response at 50 hPa.

9) The combined responses in temperature are seen to be linear in the tropics. This means that it is possible to compute the combined AOQ temperature response by adding the responses of the individual terms.

10) The vertical component of E-P flux for stationary waves is about 48% less in the model climatology at 200 hPa and 35% less at 20 hPa compared to the ERA-40 climatology. This means that very less planetary stationary waves generated in the troposphere reaches the stratosphere and hence, the transfer of eddy heat fluxes are less.

11) The percentage difference in the Fz values at 20 hPa in the full wave field (stationary + transient) remains the same to that when the stationary waves are considered. However, this difference is much lower in the Fz values at 200 hPa. This may be due to the overestimation of transient waves in the model compared to the ERA40 climatology.

### Sensitivity to the QBO phase:

The sensitivity of the impact of Mt. Pinatubo eruption in the tropics and extratropics to the different QBO phases is investigated. Mt. Pinatubo erupted during the easterly phase of QBO and the phase change took place 14 months after the eruption. Here, the consequences are analyzed if the eruption had taken place in the opposite QBO phase ($\overline{QBO}$).

The main conclusions are:

1) The individual $QBO$ (when observed QBO phase is included) and $\overline{QBO}$ responses in the lower stratospheric temperature at 30 hPa show a dual peak with cooling along the equator and warming over the subtropics associated with the easterly phase of the QBO and the opposite is observed during the westerly QBO phase.

2) The 30 hPa geopotential height anomalies show a strong polar vortex in the second winter for $QBO$ and $\overline{QBO}$ phases, except the vortex is more symmetric in when the QBO is in its westerly phase as in the case of the observed QBO phase. The vortex is disturbed in the first winters irrespective of the phase of the QBO. This may be due to the increased vertical wave activity during El Niño winters (*Calvo et al.* [2004]; *Manzini et al.* [2006]), though the responses shown here are the individual responses. Similar features are also seen during the first winter in the $AOQ$ and AO$\bar{Q}$ responses. Though a strong polar vortex is seen in the pure $\overline{QBO}$ response when QBO is in its easterly phase in second winter, the combined AO$\bar{Q}$ response do not simulate a strong polar vortex. This may be again due to the strong ocean response to the atmosphere in the model.

3) The model more or less tends to simulate statistically significant warming over Europe and cooling over Greenland and Middle East during the easterly QBO phase. Above normal temperatures over Europe and cooling over Middle east and over the Himalayan region are simulated irrespective of the QBO phase in the individual QBO experiments.

4) The combined lower stratospheric temperature response of volcanic forcing with observed SSTs and QBO phases shows notable changes in the high latitudes. Colder temperature anomalies are observed during the westerly phase of QBO in NH winter (Nov-Dec-Jan) in the polar latitudes associated with the strengthening of the polar vortex. Strong warm anomalies are observed in northern high latitudes in late winter during the easterly phase of QBO. This warming is statistically significant at 90% confidence level and is also evident during the westerly QBO phase in the AO$\bar{Q}$ experiment.

## Outlook

The dynamical response after the Mt. Pinatubo eruption is not well simulated by the applied version of the model. The simulation of the dynamical response still remains a challenge. A recent analysis of the IPCC models used for the simulations for volcanic perturbations showed that none of the models could reproduce this response correctly (*Stenchikov et al.* [2006]). The models underestimate the coupling of stratospheric changes to annular variations at the surface and hence, may not be able to simulate the dynamical response (*Miller*

*et al.* [2006]). One of the reasons could be that the model has insufficient vertical resolution in the upper troposphere and lower stratosphere to resolve the troposphere - stratosphere interactions. It would be interesting to see whether this response can be simulated better with a model with higher vertical resolution (for example, L90 model). Another reason could be that zonally averaged volcanic forcing and volcanically induced ozone anomalies are used in the model simulations carried out here. The omission of the zonally asymmetric component of volcanic forcing and ozone forcing may produce differences in the responses. In this study, the inconsistency in the planetary wave propagation characteristics is pointed out in the model climatology in comparison with the ERA40 climatology and this may have an impact on the simulation of the dynamical response. Hence, it is important to assess the reasons behind this discrepancy. It is shown that the zonally asymmetric component of ozone has an effect on the stratospheric temperature and planetary wave propagation (*Gabriel et al.* [2007]). This could be carried out either by including the zonally asymmetric component of aerosol and ozone forcing or by using a chemistry climate model where sulfate aerosols and the gases are transported by the winds. This can give an idea on how different the response would be and also give an estimate on the error in using such simplified simulations. Moreover, it would be also interesting to see whether the coupled ocean-atmosphere GCMs can provide us with additional information compared to prescribing the observed SSTs in an atmospheric GCM in simulating the climate impact of volcanic eruptions. Apart from these, it would be desirable to look into the water vapor feedback resulting from explosive volcanic eruptions to see whether the model can realistically account for the amount of water-vapor (*Soden et al.* [2002]). Several other parameters such as the frequency of radiation time step and varying cloud overlap assumptions can be major challenges in radiation parameterizations for GCMs and are also found to have a strong effect on the heating rates. Hence, this study points out to the importance of model performance for future climate experiments.

# Appendix A

# Longwave spectral bands in ECHAM5

| *Band* | *Spectral interval* | *Trop.abs* | *Strat.abs* |
|---|---|---|---|
| 1 | 10 - 250 | $H_2O$, SC, FC | $H_2O$, FC |
| 2 | 250 - 500 | $H_2O$, SC, FC | $H_2O$, FC |
| 3 | 500 - 630 | $H_2O$, $CO_2$, $N_2O$, SC, FC | $H_2O$, $CO_2$, $N_2O$, FC |
| 4 | 630 - 700 | $H_2O$, $CO_2$, SC | $O_3$, $CO_2$ |
| 5 | 700 - 820 | $H_2O$, $CO_2$, SC | $O_3$, $CO_2$ |
| 6 | 820 - 980 | $H_2O$, $CO_2$, CFC11, CFC12, SC | CFC11, CFC12 |
| 7 | 980 - 1080 | $H_2O$, $O_3$, $CO_2$, SC | $O_3$, $CO_2$ |
| 8 | 1080 - 1180 | $H_2O$, CFC12, CFC22, $CO_2$, $N_2O$, SC | $O_3$, $CO_2$, CFC12, CFC22, $N_2O$ |
| 9 | 1180 - 1390 | $H_2O$, $CH_4$, $N_2O$, SC | $CH_4$ |
| 10 | 1390 - 1480 | $H_2O$ | $H_2O$ |
| 11 | 1480 - 1800 | $H_2O$, SC | $H_2O$ |
| 12 | 1800 - 2080 | $H_2O$, $CO_2$, SC | – |
| 13 | 2080 - 2250 | $H_2O$, $N_2O$, SC | – |
| 14 | 2250 - 2380 | $CO_2$, SC | $CO_2$ |
| 15 | 2380 - 2600 | $CO_2$, $N_2O$, SC | – |
| 16 | 2600 - 3000 | $H_2O$, $CH_4$, SC | – |

Table A.1: Spectral intervals ($cm^{-1}$), gaseous absorbers used in troposphere and in stratosphere in ECHAM5. SC and FC denote self and foreign continuum

# Appendix B

# Zonal mean T-50hPa anomaly

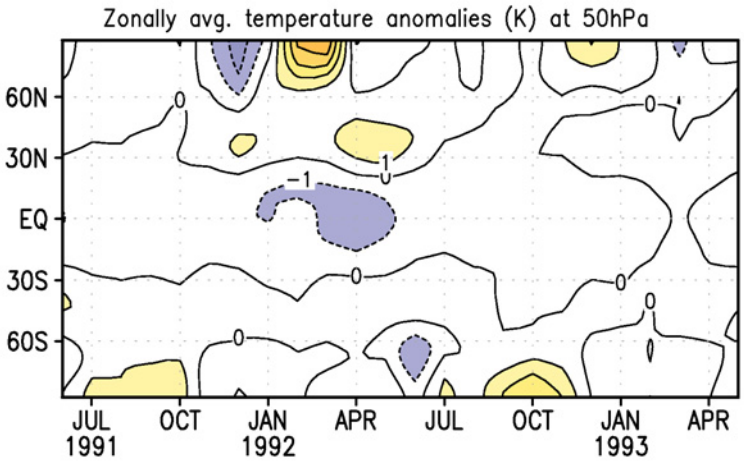


Figure B.1: Zonally averaged lower stratospheric temperature (K) anomalies at 50 hPa for the ocean response

# Appendix C

# T-2m model climatology

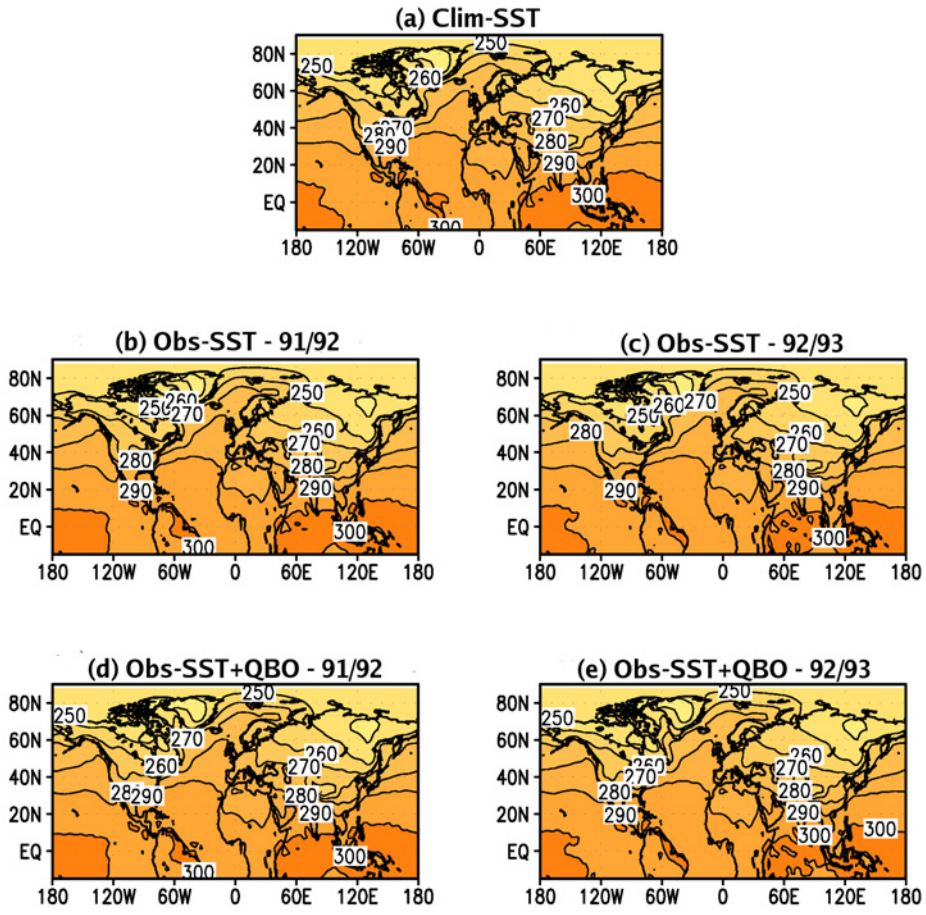


Figure C.1: Climatology used in the calculation of the 2m temperature anomalies (K) for the set of experiments (a) Clim_SST climatology, Obs_SST climatology for (b) 1991/92 and (c) 1992/93, Obs_SST + QBO climatology for (d) 1991/92 and (e) 1992/93.

# Appendix D

# Ensemble member T-2m and Z-30hPa anomalies

### Ensemble member anomalies for Aer1 - DJF 1991/92

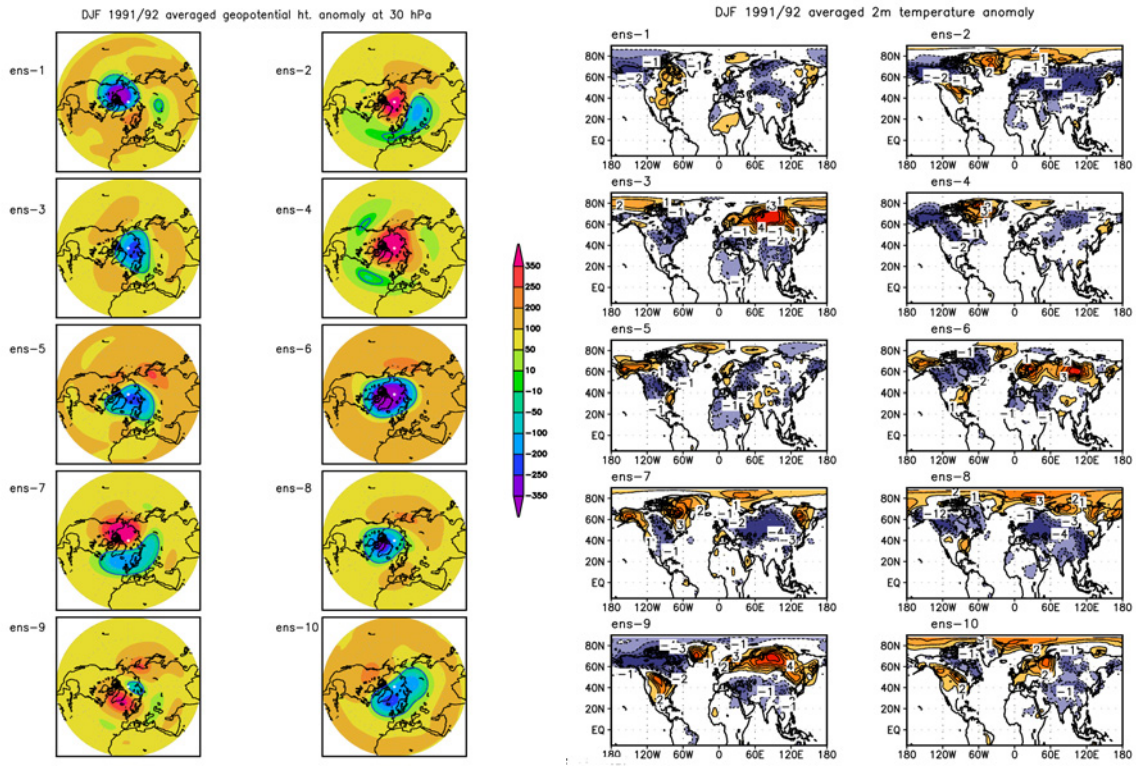


Figure D.1: Ensemble member anomalies for averaged DJF 91/92 in aer1 case for (a) 30 hPa geopotential height (m) and (b) 2m temperature (K).

## Ensemble member anomalies for Aer1 - DJF 1992/93

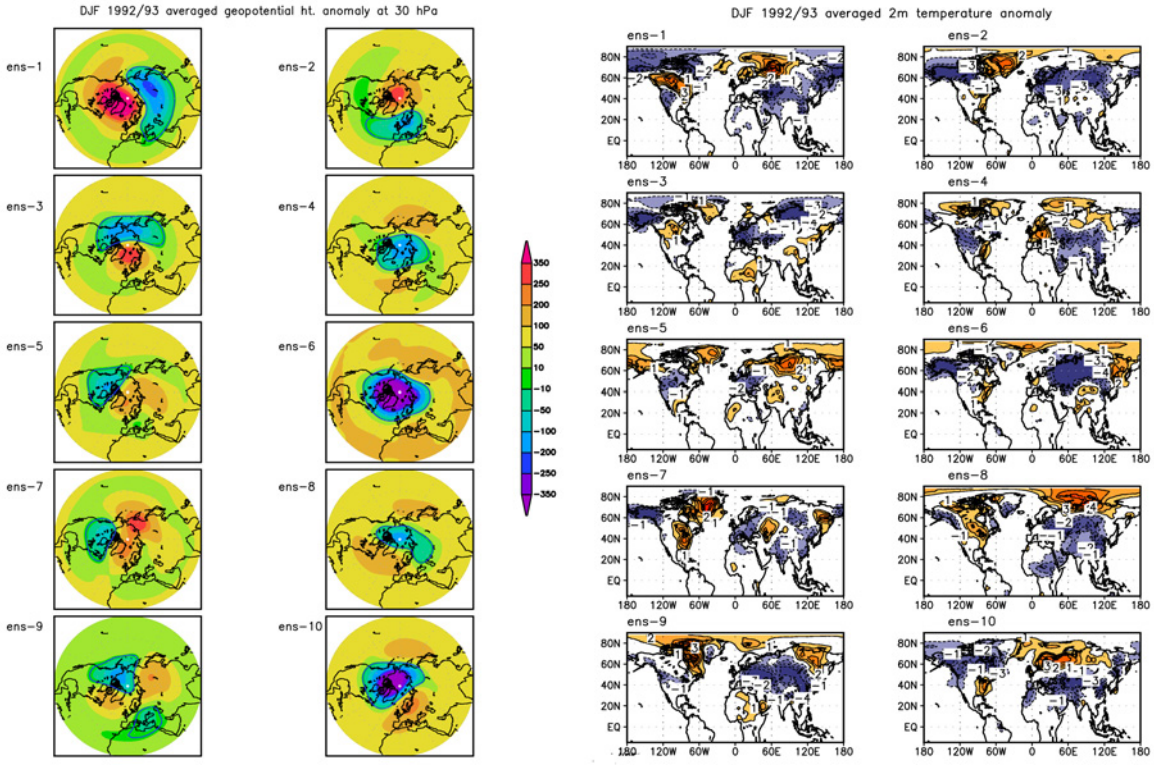


Figure D.2: Ensemble member anomalies for averaged DJF 92/93 in aer1 case for (a) 30 hPa geopotential height (m) and (b) 2m temperature (K).

## Ensemble member anomalies for Aer2 - DJF 1991/92

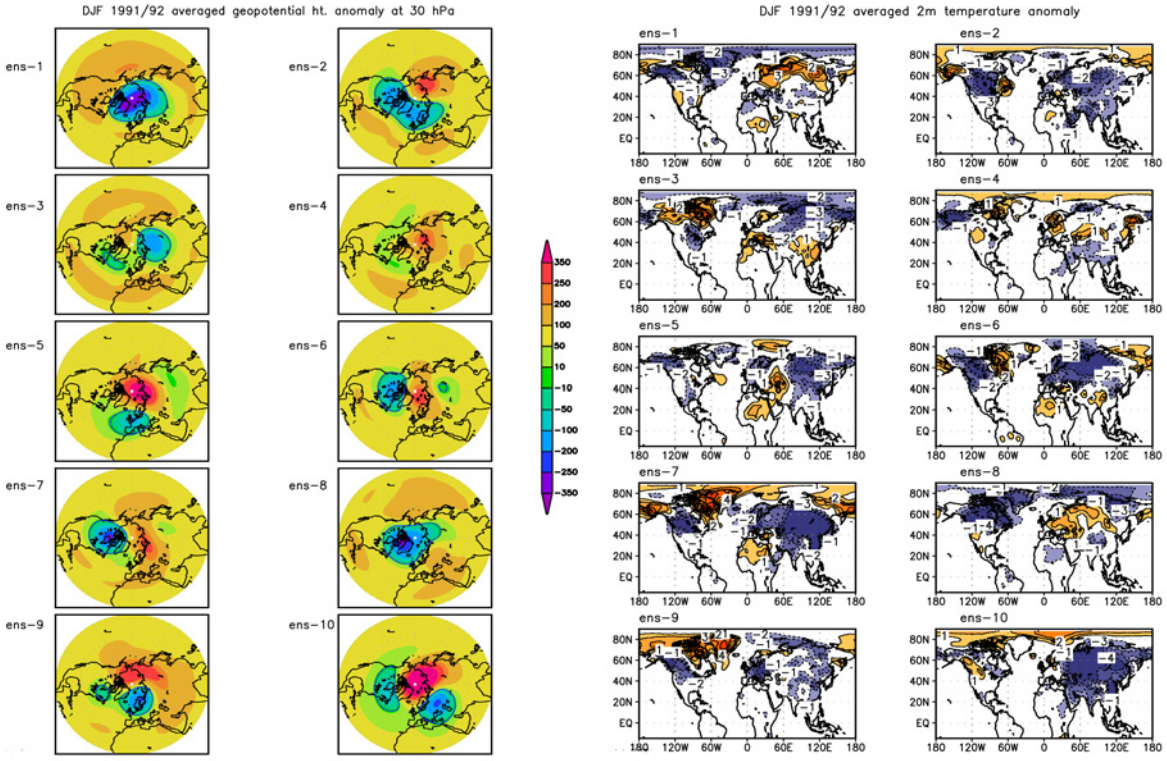


Figure D.3: Ensemble member anomalies for averaged DJF 91/92 in aer2 case for (a) 30 hPa geopotential height (m) and (b) 2m temperature (K).

## Ensemble member anomalies for Aer2 - DJF 1992/93

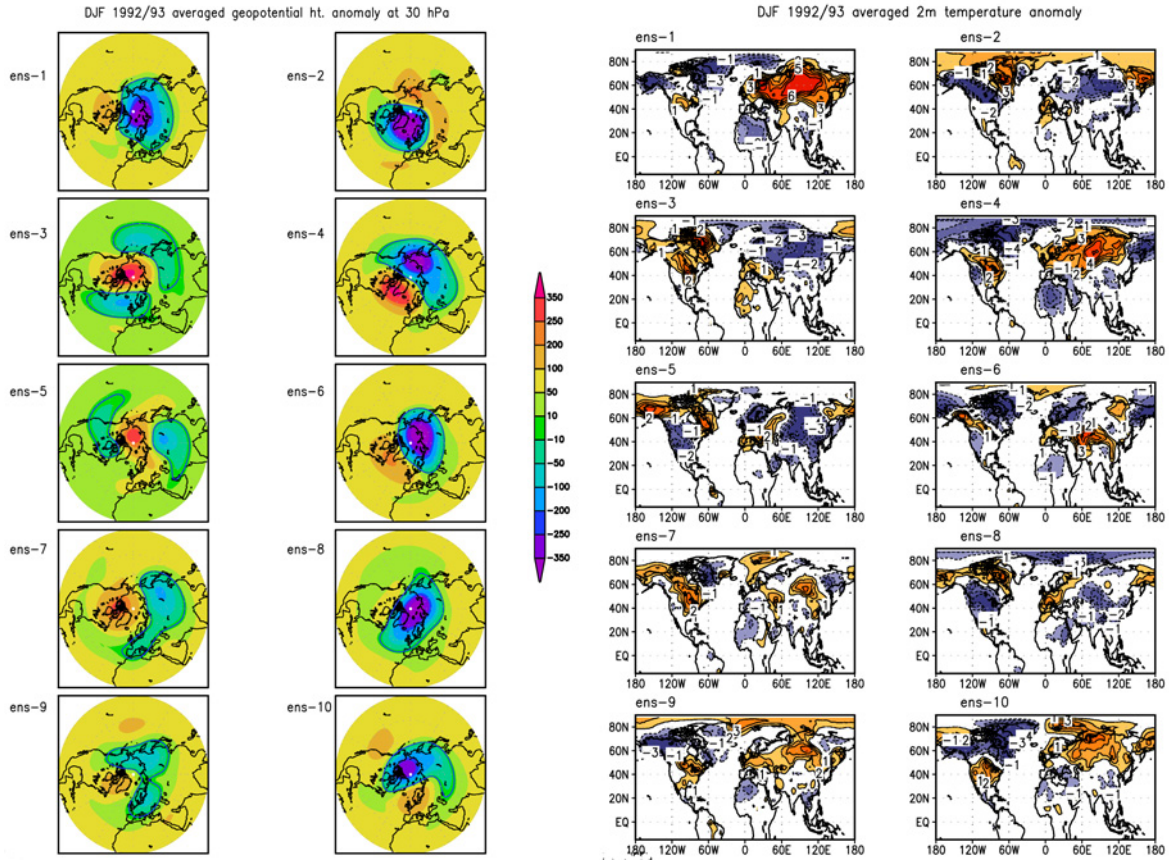


Figure D.4: Ensemble member anomalies for averaged DJF 92/93 in aer2 case for (a) 30 hPa geopotential height (m) and (b) 2m temperature (K).

## Ensemble member anomalies for Aer3 - DJF 1991/92

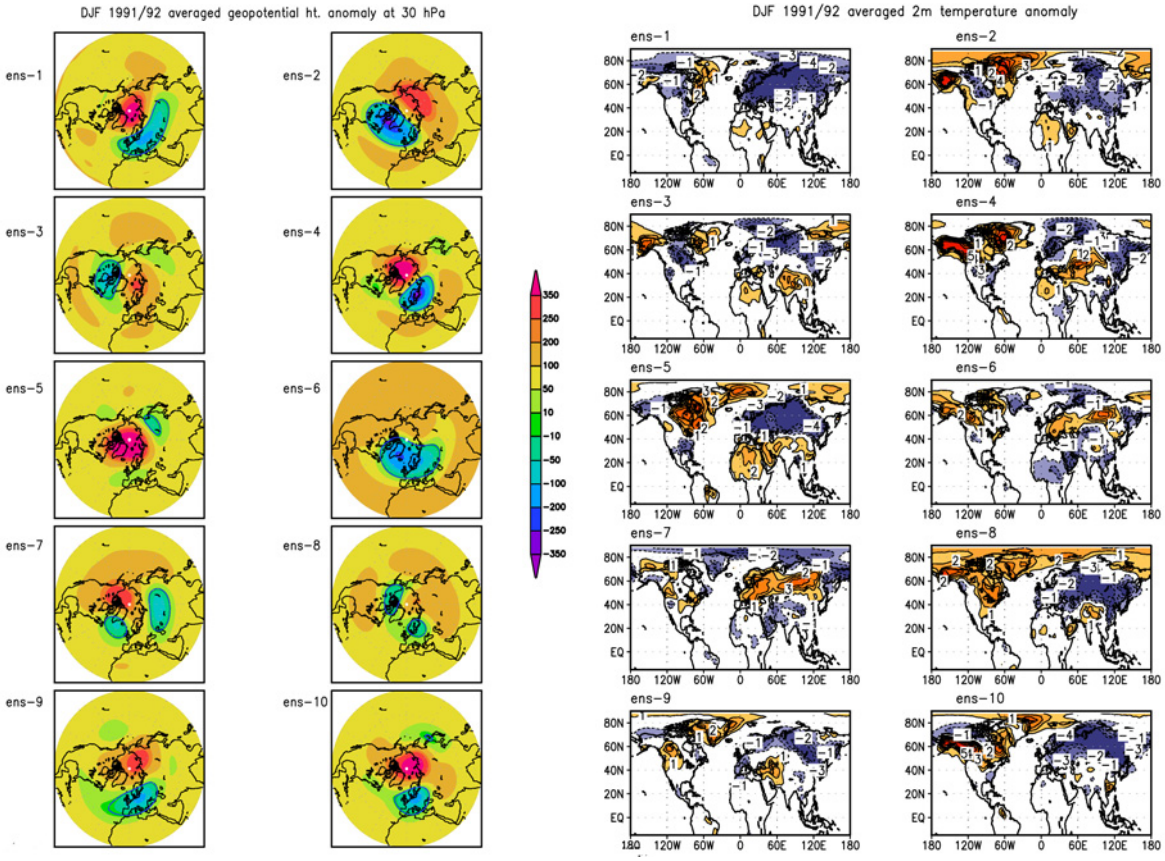


Figure D.5: Ensemble member anomalies for averaged DJF 91/92 in aer3 case for (a) 30 hPa geopotential height (m) and (b) 2m temperature (K).

## Ensemble member anomalies for Aer3 - DJF 1992/93

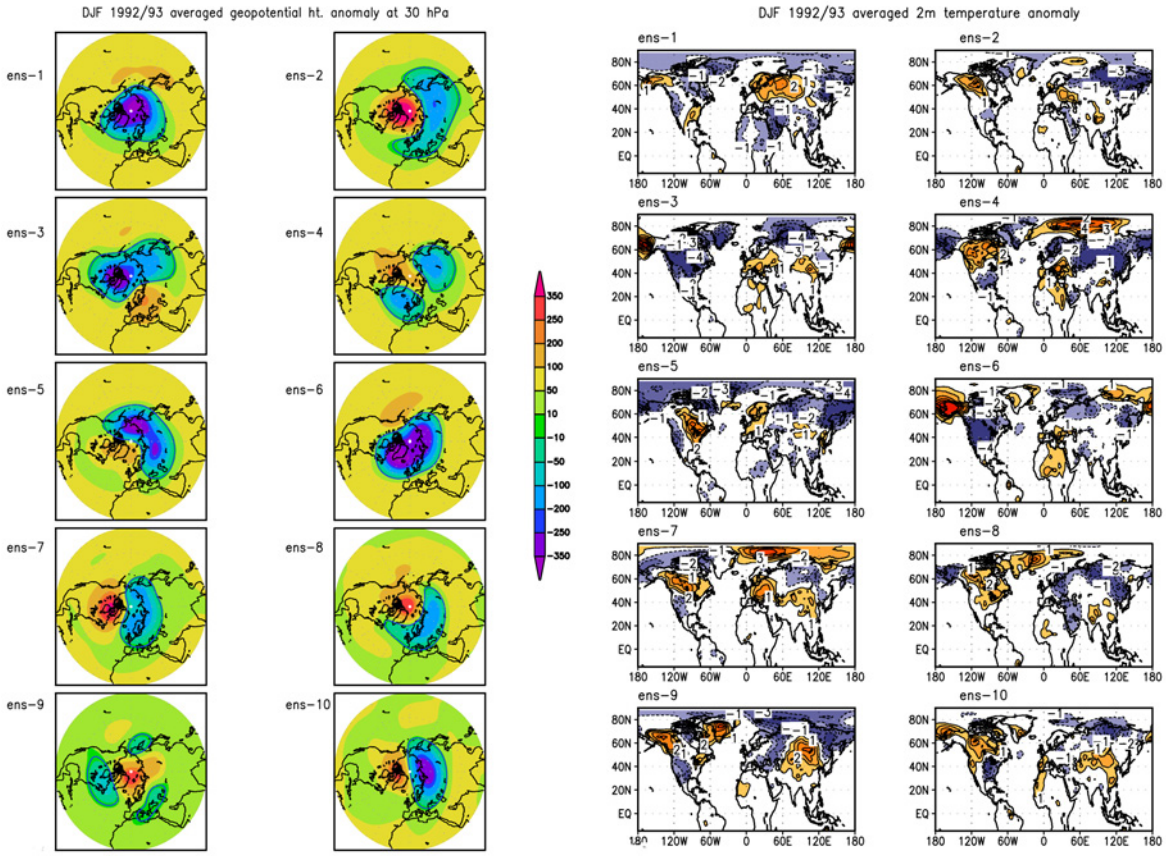


Figure D.6: Ensemble member anomalies for averaged DJF 92/93 in aer3 case for (a) 30 hPa geopotential height (m) and (b) 2m temperature (K).

## Ensemble member anomalies for AQ - DJF 1991/92

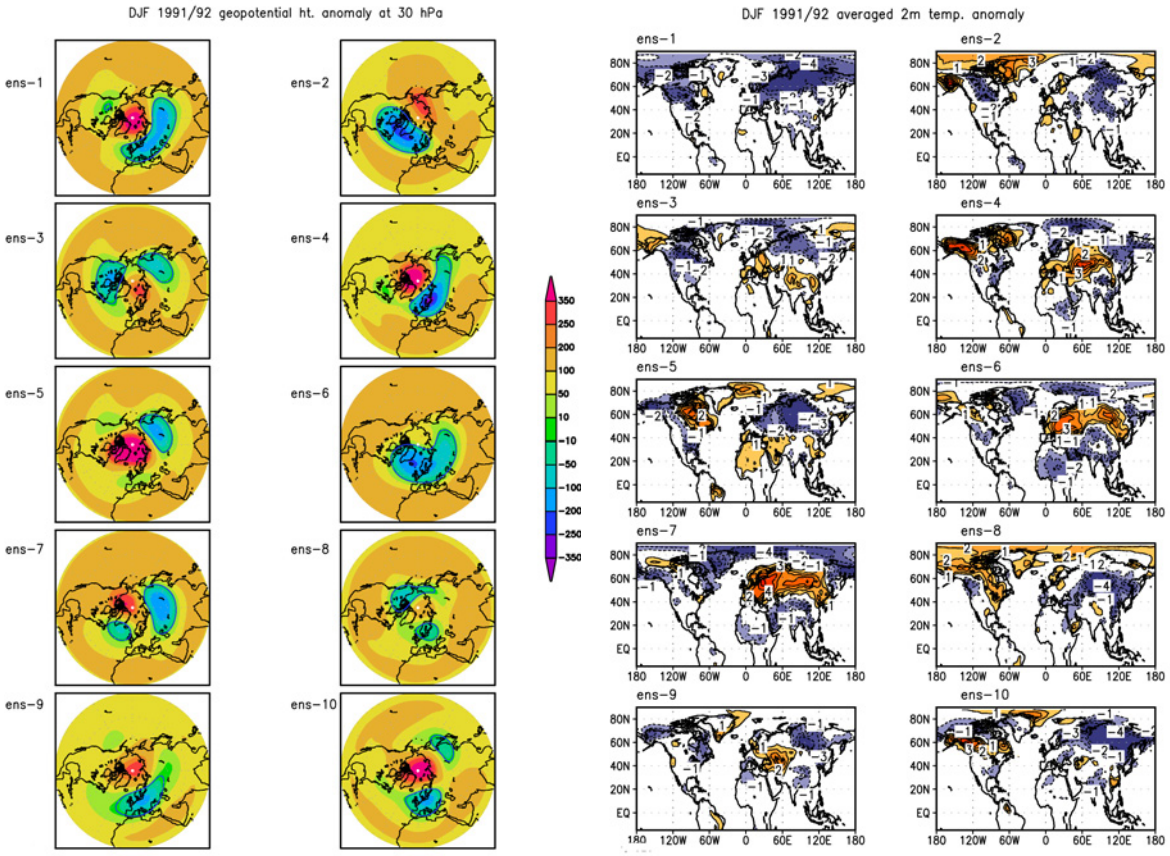


Figure D.7: Ensemble member anomalies for averaged DJF 91/92 in AQ case for (a) 30 hPa geopotential height (m) and (b) 2m temperature (K).

## Ensemble member anomalies for AQ - DJF 1992/93

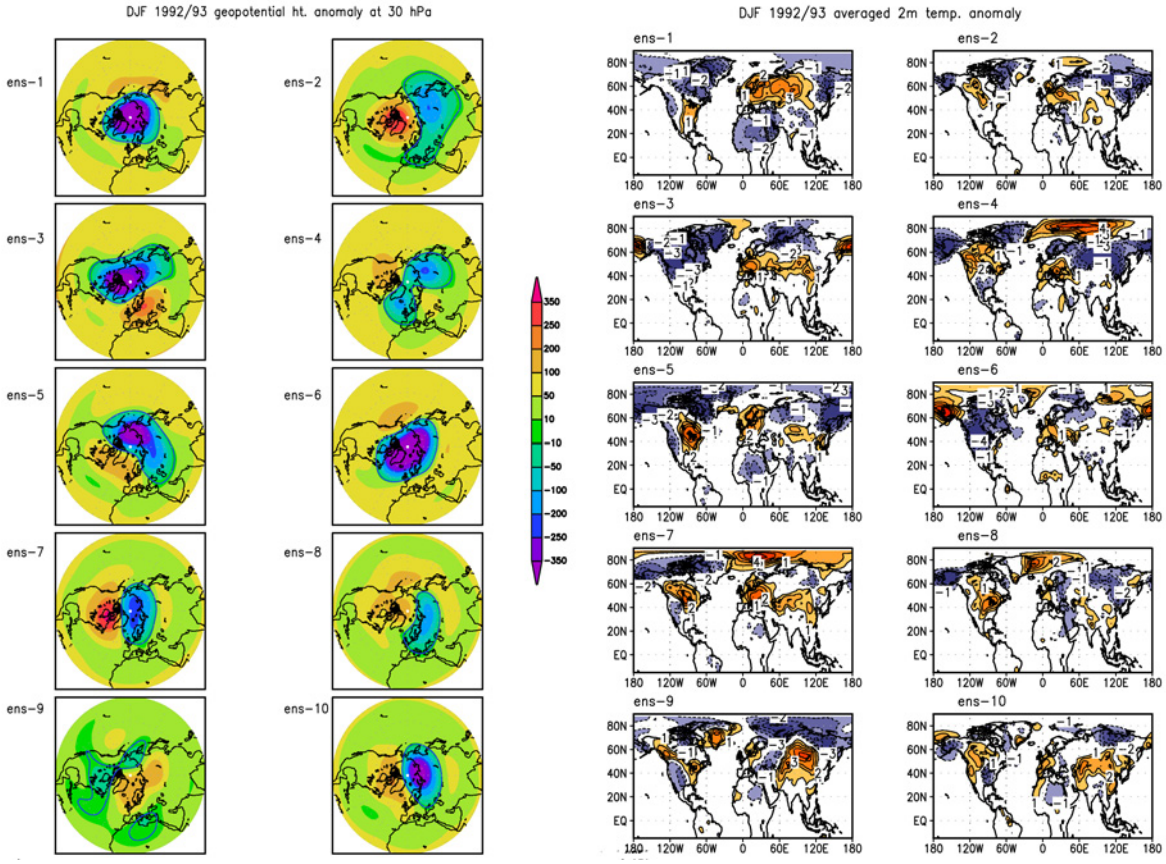


Figure D.8: Ensemble member anomalies for averaged DJF 92/93 in AQ case for (a) 30 hPa geopotential height (m) and (b) 2m temperature (K).

## Ensemble member anomalies for AO - DJF 1991/92

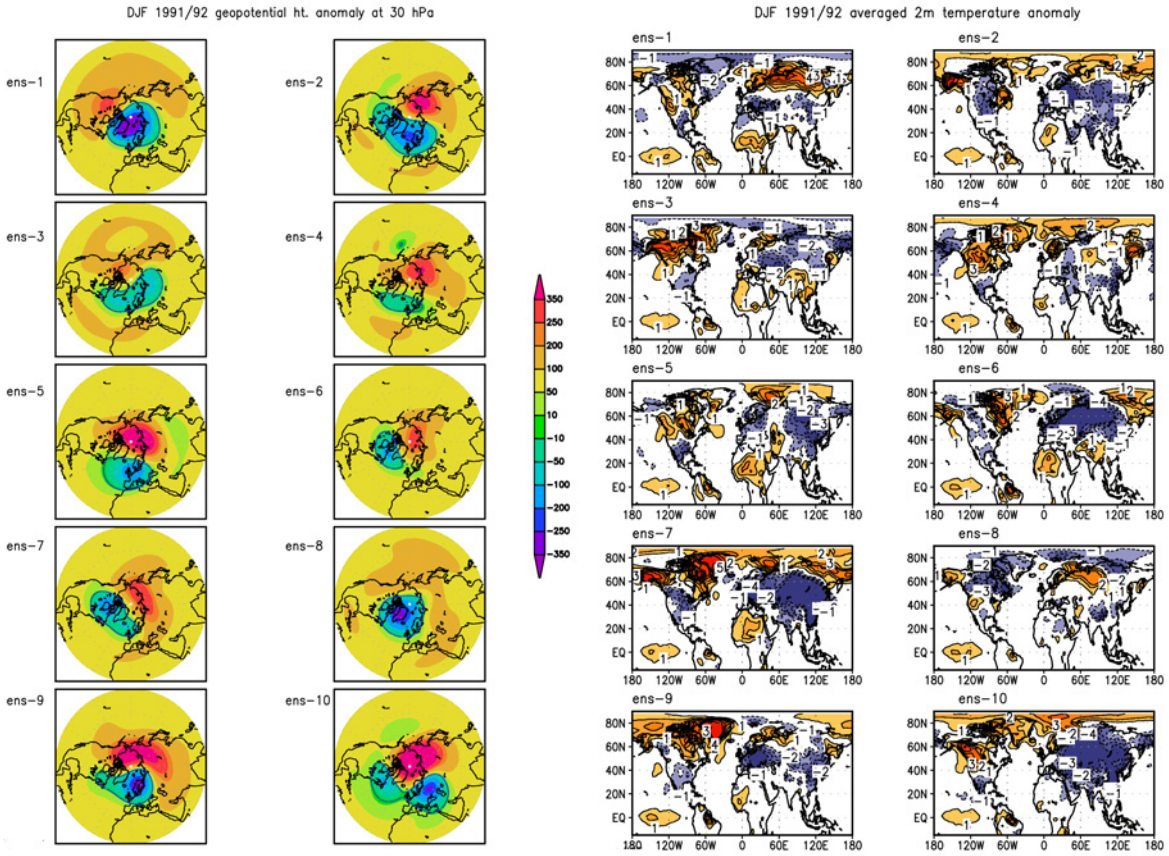


Figure D.9: Ensemble member anomalies for averaged DJF 91/92 in AO case for (a) 30 hPa geopotential height (m) and (b) 2m temperature (K).

## Ensemble member anomalies for AO - DJF 1992/93

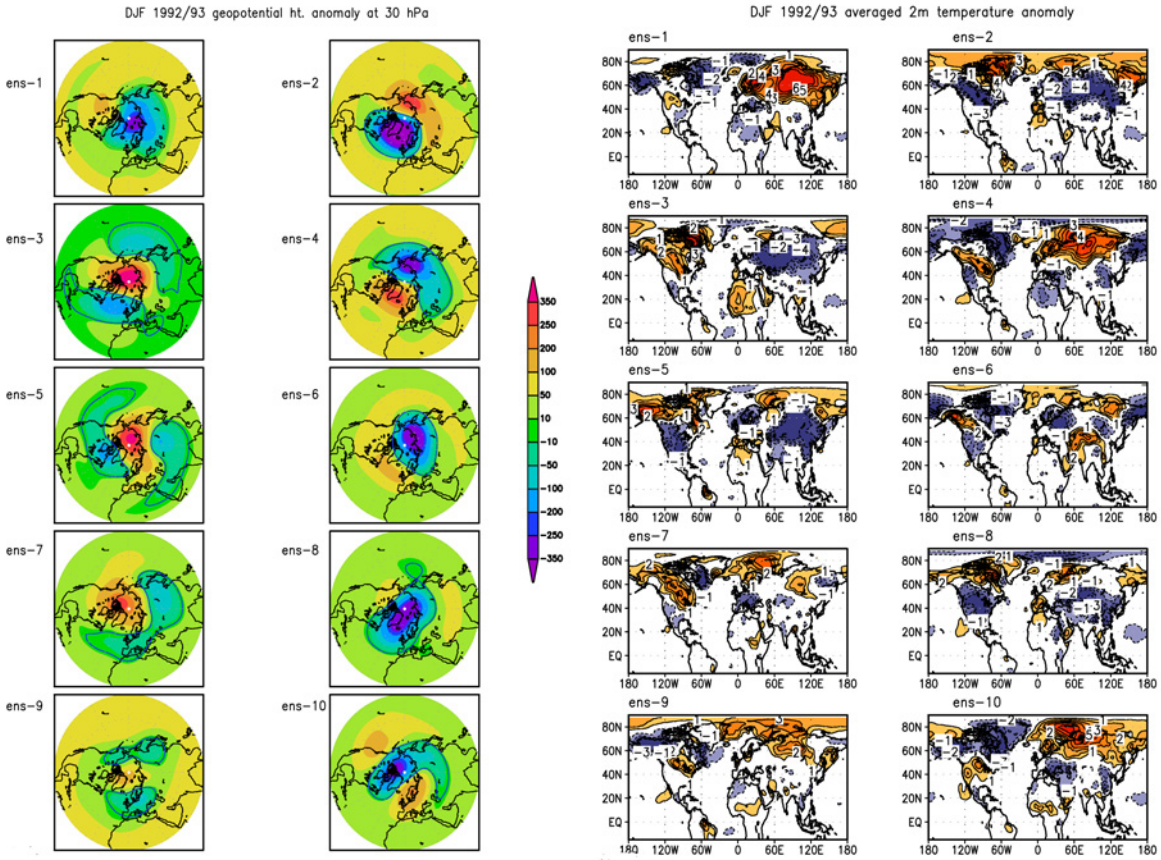


Figure D.10: Ensemble member anomalies for averaged DJF 92/93 in AO case for (a) 30 hPa geopotential height (m) and (b) 2m temperature (K).

## Ensemble member anomalies for AOQ - DJF 1991/92

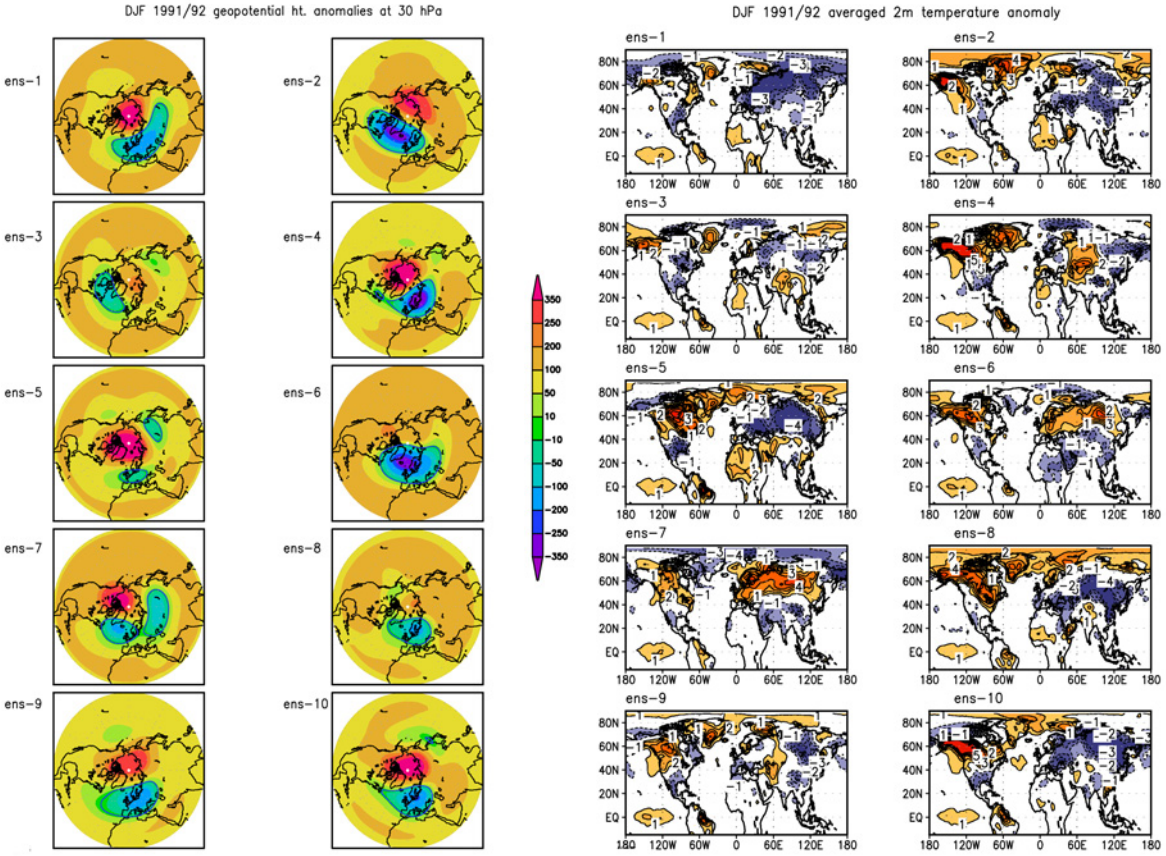


Figure D.11: Ensemble member anomalies for averaged DJF 91/92 in AOQ case for (a) 30 hPa geopotential height (m) and (b) 2m temperature (K).

## Ensemble member anomalies for AOQ - DJF 1992/93

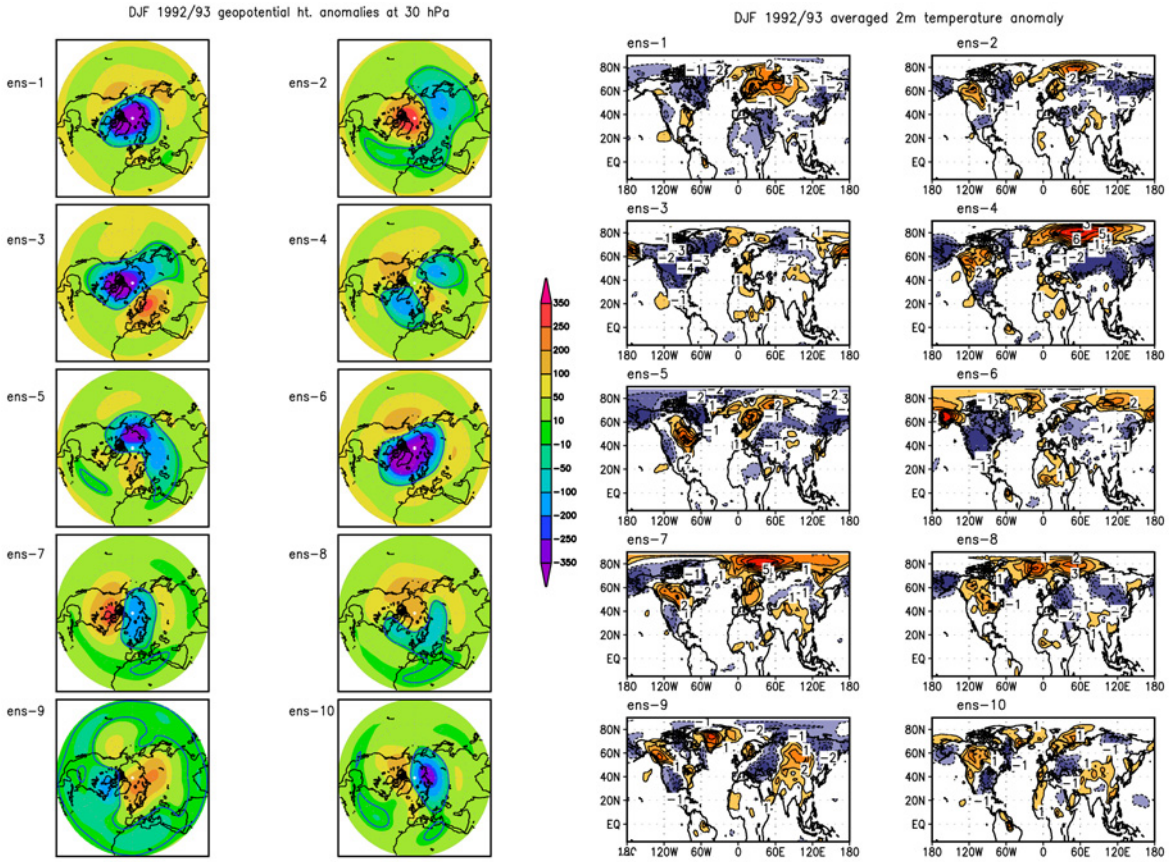


Figure D.12: Ensemble member anomalies for averaged DJF 92/93 in AOQ case for (a) 30 hPa geopotential height (m) and (b) 2m temperature (K).

# Appendix E

# Z-30hPa model climatology

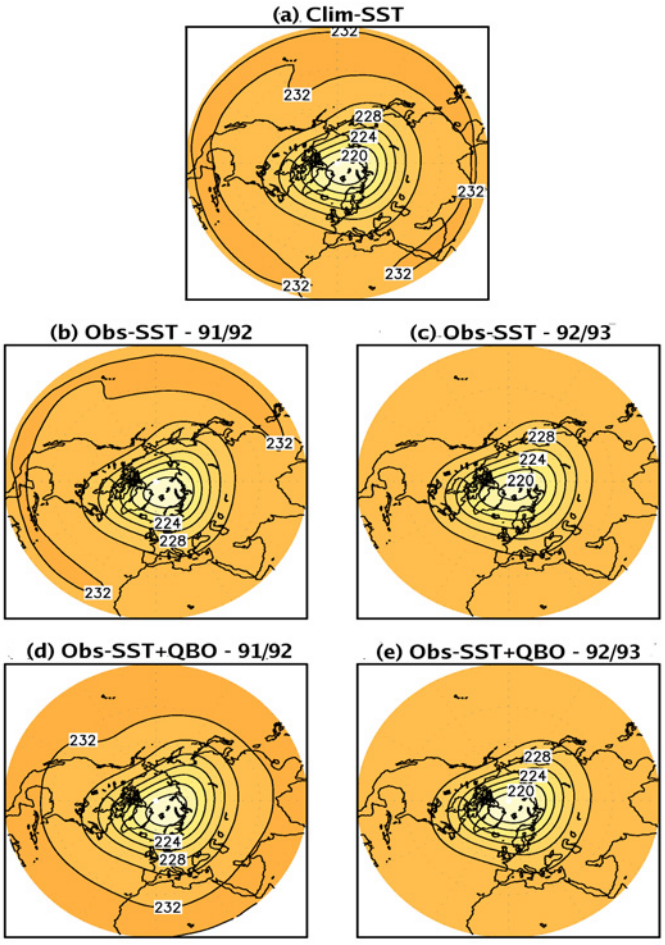


Figure E.1: Climatology used in the calculation of the geopotential height anomalies for the set of experiments (multiply by 100) (a) Clim_SST climatology, Obs_SST climatology for (b) 1991/92 and (c) 1992/93, Obs_SST + QBO climatology for (d) 1991/92 and (e) 1992/93.

# Appendix F

# Zonal mean zonal wind anomalies

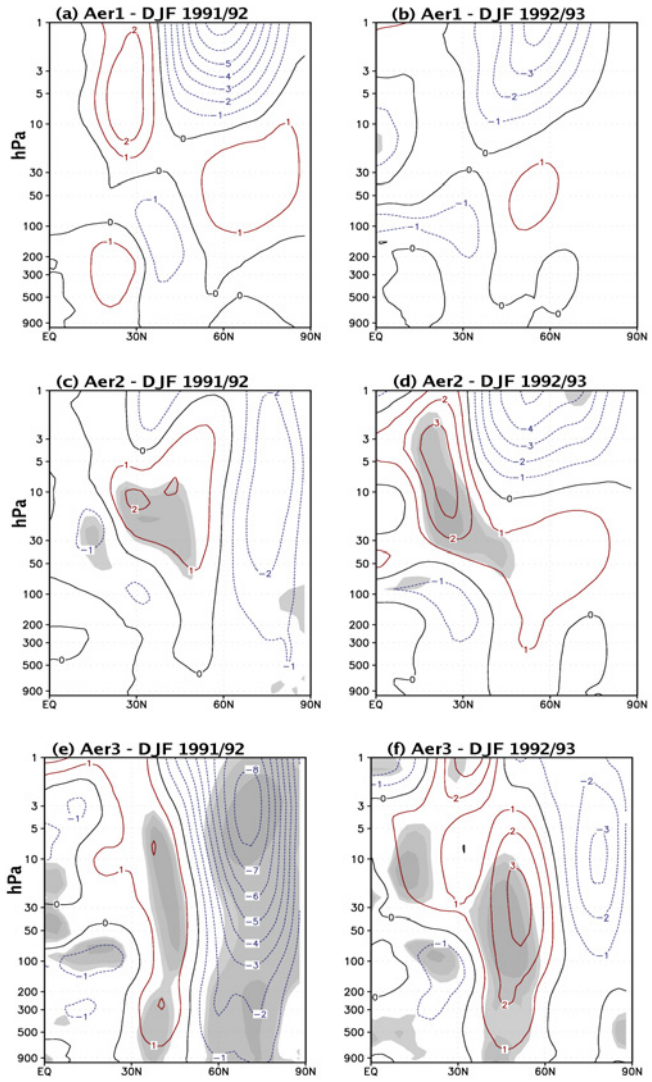

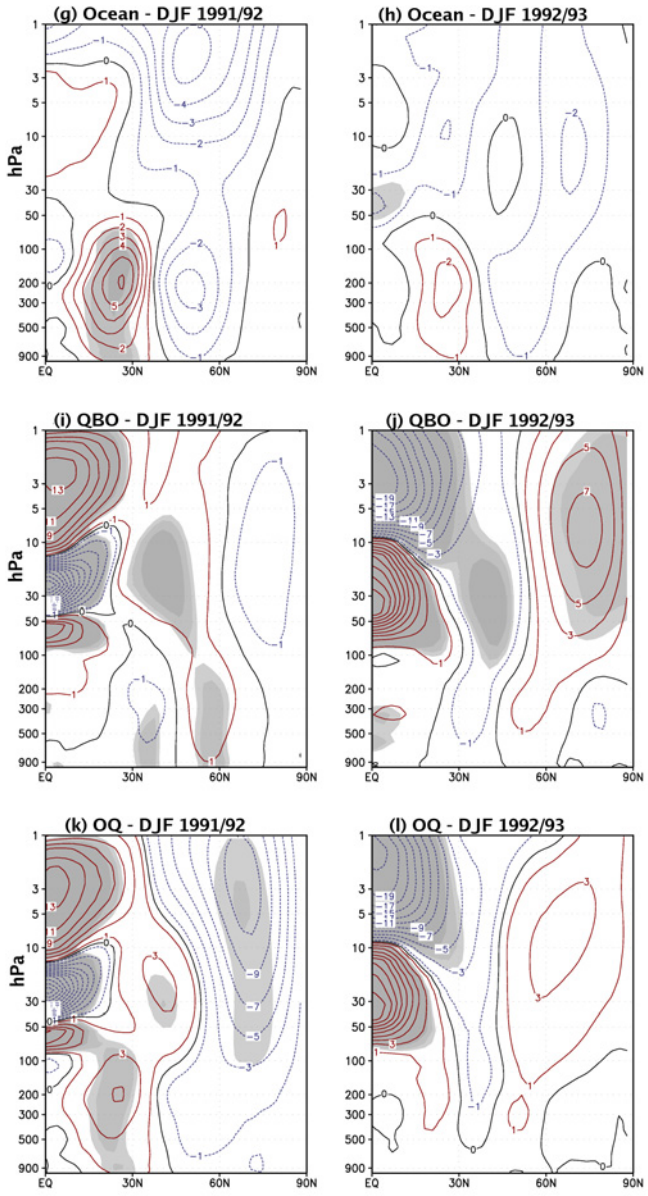
(g) Ocean - DJF 1991/92
(h) Ocean - DJF 1992/93
(i) QBO - DJF 1991/92
(j) QBO - DJF 1992/93
(k) OQ - DJF 1991/92
(l) OQ - DJF 1992/93
hPa
1
3
5
10
30
50
100
200
300
500
900
EQ
30N
60N
90N

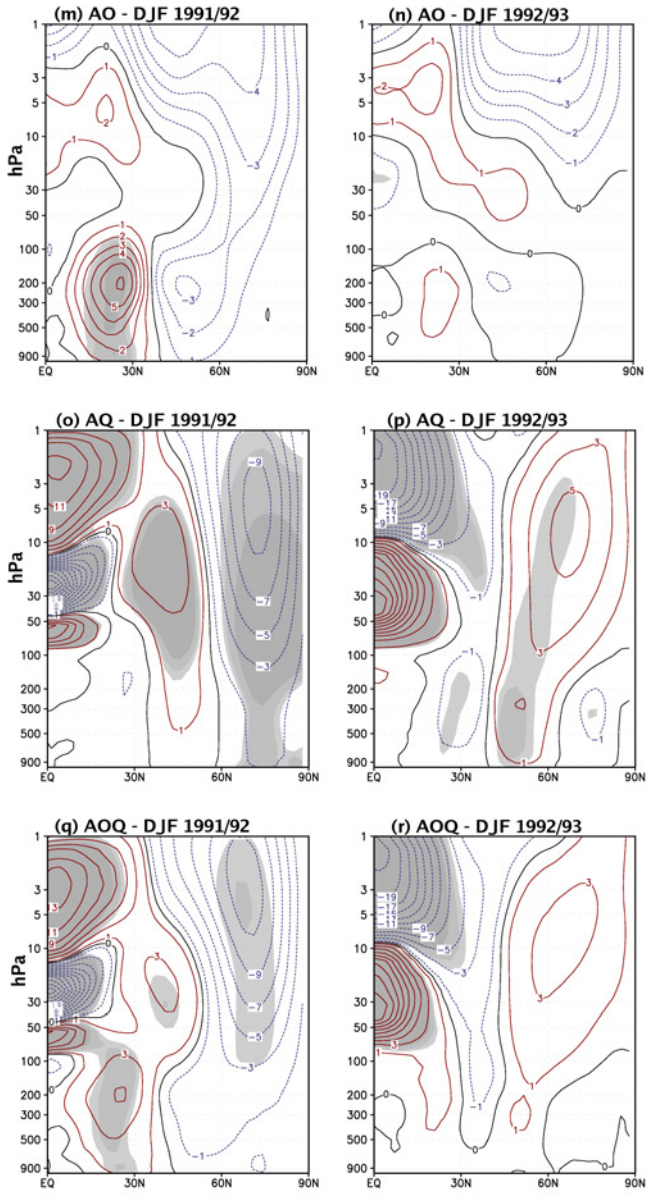


Figure F.1: Zonal mean zonal wind anomalies (m/s) for Aer1 (a + b); Aer2 (c + d); Aer3 (e + f); ocean response (g + h); qbo response (i + j); combined ocean and qbo (OQ) (k + l); combined aerosol and ocean (AO) (m + n); combined aerosol and QBO (AQ) (o + p); combined aerosol, ocean and QBO (AOQ) (q + r); for DJF 1991/92 (left column) and DJF 1992/93 (right column).

# Appendix G

# Zonal mean T anomalies

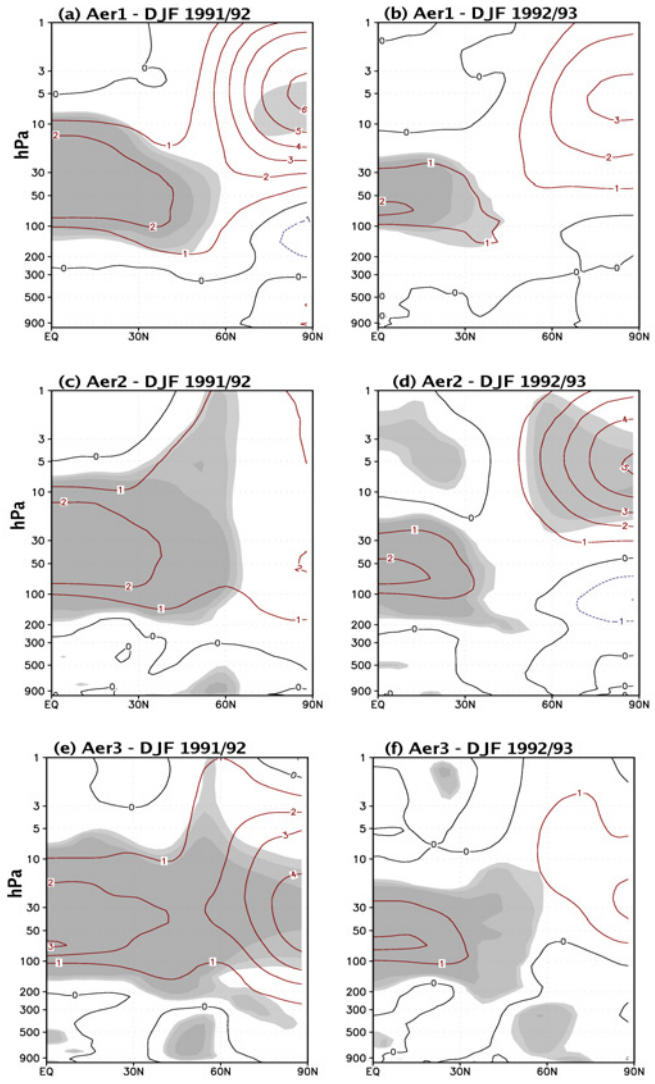

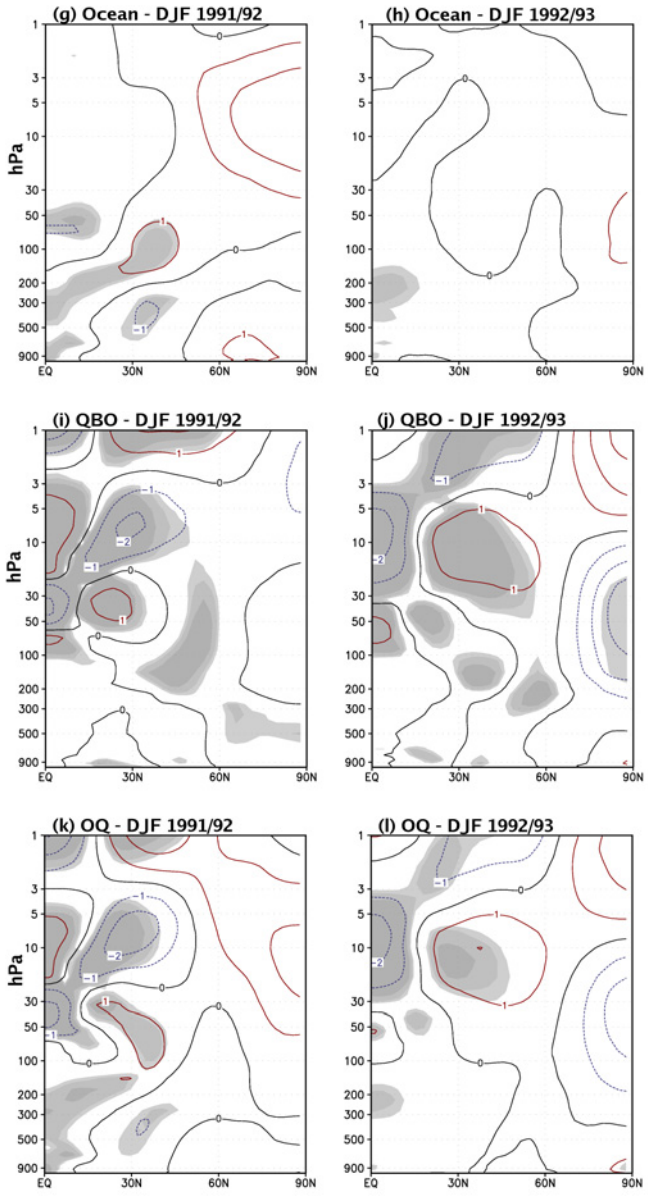
(g) Ocean - DJF 1991/92
(h) Ocean - DJF 1992/93
(i) QBO - DJF 1991/92
(j) QBO - DJF 1992/93
(k) OQ - DJF 1991/92
(l) OQ - DJF 1992/93
hPa
1
3
5
10
30
50
100
200
300
500
900
EQ
30N
60N
90N

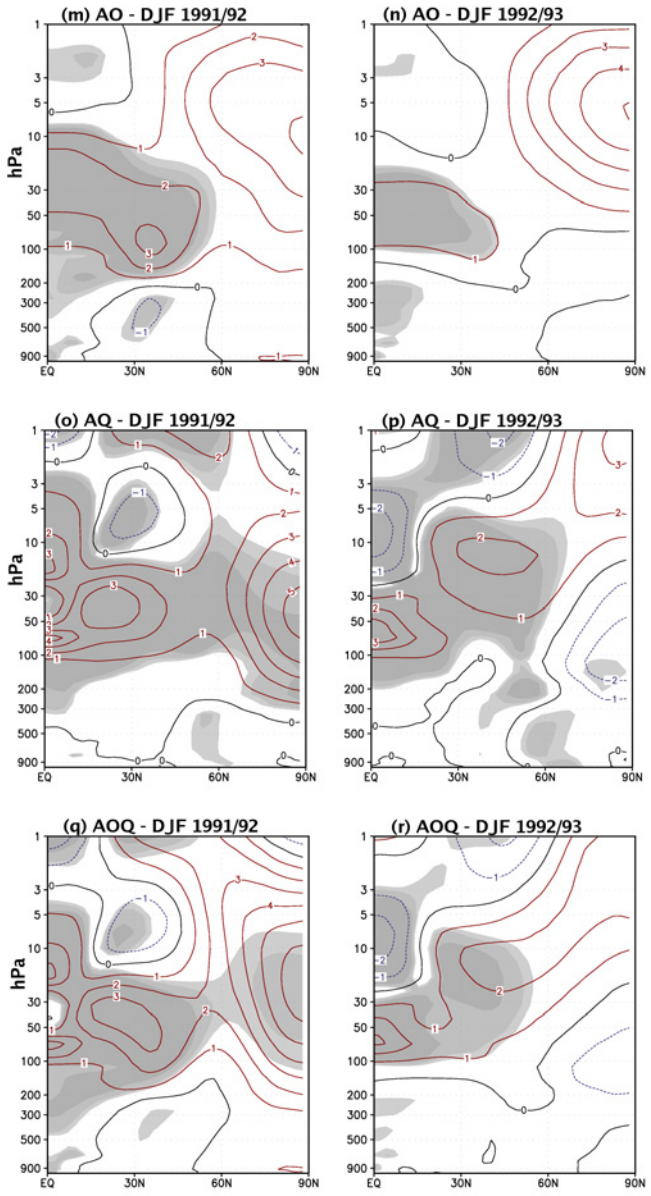


Figure G.1: Zonal mean temperature anomalies (K) for Aer1 (a + b); Aer2 (c + d); Aer3 (e + f); ocean response (g + h); qbo response (i + j); combined ocean and qbo (OQ) (k + l); combined aerosol and ocean (AO) (m + n); combined aerosol and QBO (AQ) (o + p); combined aerosol, ocean and QBO (AOQ) (q + r); for DJF 1991/92 (left column) and DJF 1992/93 (right column).

# Appendix H

# E-P flux and divergence

Planetary waves can induce forcing on the mean flow. The Eliassen-Palm flux (E-P flux) and its divergence (*Eliassen and Palm* [1961]; *Andrews et al.* [1987]) represent the wave activities and eddy forcing are used to analyze the planetary wave propagation.

The quasi-geostrophic version of E-P flux vector, $\vec{F}$ in spherical geometry is shown below.

$$\vec{F} = [0, -\rho_o * a * (cos\phi) * \overline{v'u'}, \rho_o * a * (cos\phi) * f * \frac{\overline{v'\theta'}}{\theta_o}] \tag{H.1}$$

where,

$$\rho_o = \rho_s * exp(\frac{-Z}{H}) \tag{H.2}$$

is the background air density

Then meridional and vertical components of E-P flux are,

$$F_y = -\rho_o * a * (cos\phi) * \overline{v'u'} \tag{H.3}$$

$$F_z = \rho_o * a * (cos\phi) * f * \frac{\overline{v'\theta'}}{\theta_o} \tag{H.4}$$

and the divergence of E-P flux is

$$D_F = \frac{\nabla.\vec{F}}{\rho_o * a * (cos\phi)} \tag{H.5}$$

Using the following approximate geostrophic formulas in spherical co-ordinates,

$$u' = -(f * a)^{-1} * \Phi'_\phi \tag{H.6}$$

$$v' = (f * a * (cos\phi))^{-1} * \Phi'_\lambda \tag{H.7}$$

together with with eqn.1 gives

$$\vec{F} = \rho_o[0, \frac{\overline{\Phi'_\phi * \Phi'_\lambda}}{f^2 * a}, \frac{\overline{\Phi'_z * \Phi'_\lambda}}{N^2}] \tag{H.8}$$

where
Φ': departure of the climatological mean geopotential from its zonal mean value
N: buoyancy frequency
H: scale height
f: Coriolis parameter
a: Earth's radius
Z: geometric height
u: zonal winds
v: meridional winds
$\phi$: zonal wave number
$\lambda$: latitude

The geostrophic equations are not valid near the equator where f is small. The meridional and vertical E-P flux components (eqn.3 and eqn. 5) correspond with the eddy momentum flux ($\overline{v'u'}$) and eddy heat flux ($\overline{v'\theta'}$) respectively. The divergence of E-P flux (eqn. 5) represents the eddy momentum forcing on the mean flow.

# Appendix I

# E-P flux and divergence for Agung and El Chichon

### E-P flux and divergence for DJF 1963/64 from ERA-40

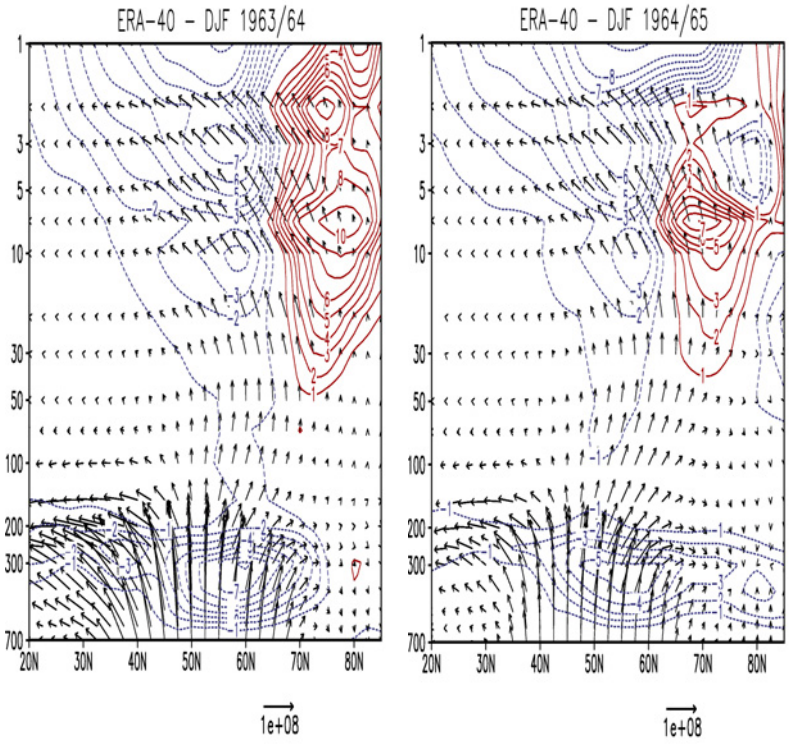


Figure I.1: E-P flux and divergence for stationary planetary waves in DJF from ERA-40 for the winters of 1963/64 and 1964/65 for ZWN1+2+3. The unit of vector is kg/s$^2$.

## E-P flux and divergence for DJF 1982/84 from ERA-40

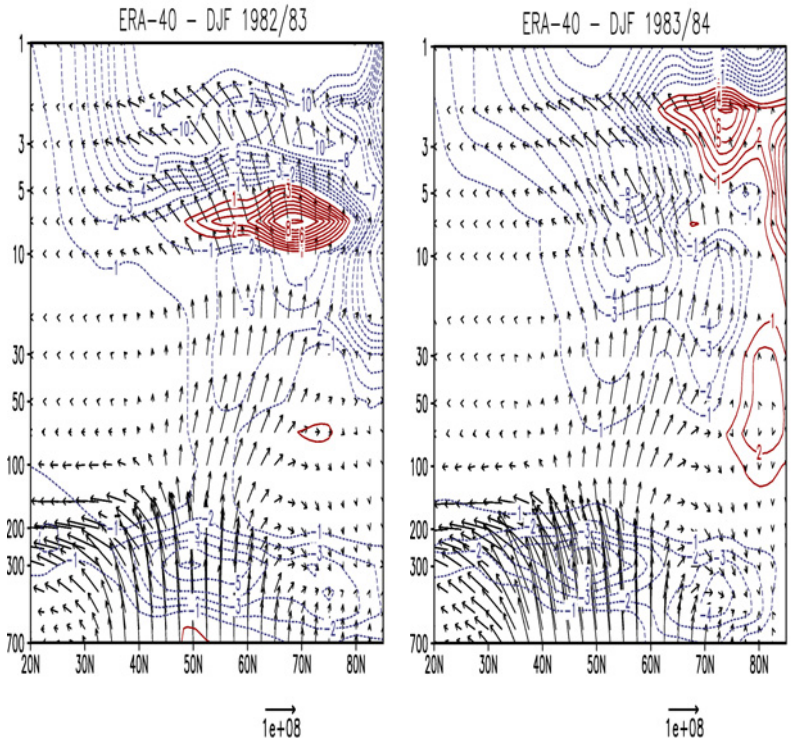


Figure I.2: E-P flux and divergence for stationary planetary waves in DJF from ERA-40 for the winters of 1982/83 and 1983/84 for ZWN1+2+3. The unit of vector is kg/s$^2$.

# Appendix J

# T in [(with QBO) runs - (without QBO) runs]

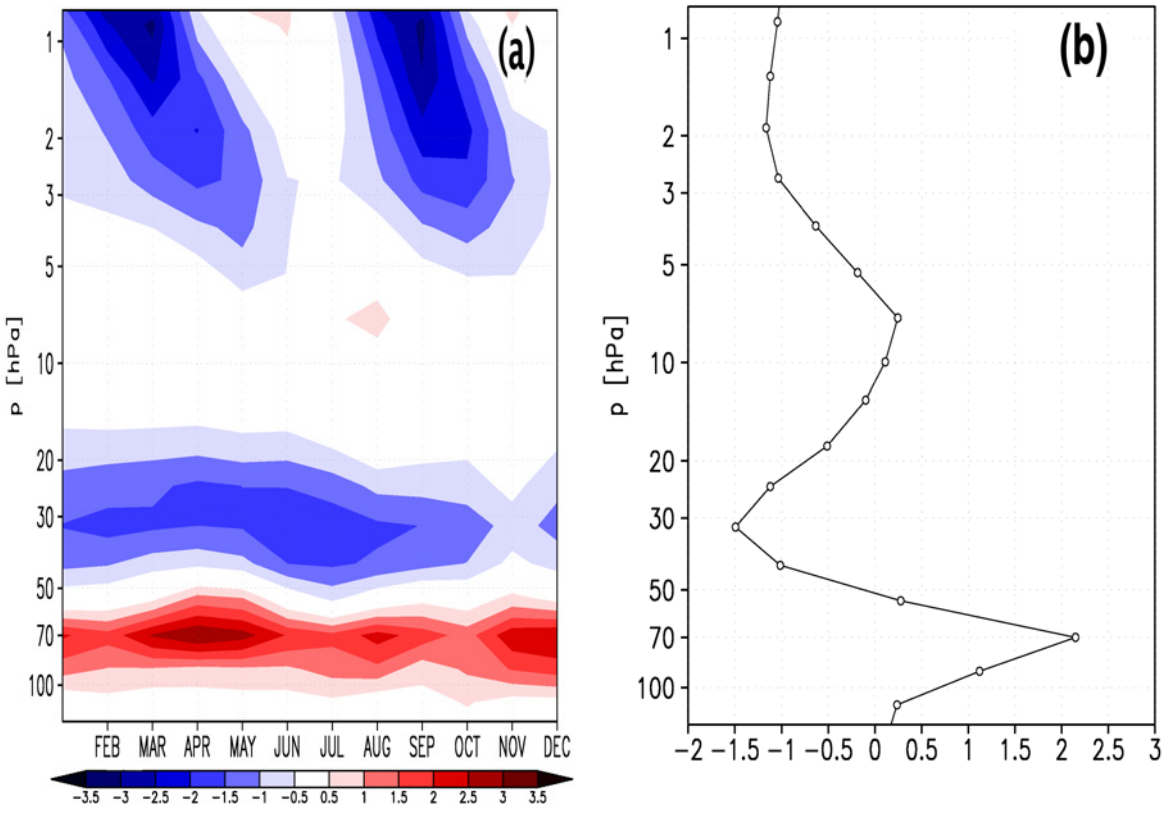


Figure J.1: Results from MAECHAM4 simulations: (a) Climatological mean temperature differences (K) between simulations with QBO and without QBO (with QBO runs minus without QBO runs) averaged over 5N-5S and (b) climatology of the vertical profile of the temperature difference (K), (with QBO - without QBO) runs (by H. Punge).

# Bibliography


Adams, J. B., M. E. Mann, and C. M. Ammann, Proxy evidence for an El niño like response to volcanic forcing, *Nature*, *426*, 274–278, 2003.

Andrews, D. J., J. R. Holton, and C. B. Leovy, Middle atmosphere dynamics, *Academic Press*, p. 489pp, 1987.

Angell, J. K., Estimated impact of Agung, El Chichón and Pinatubo volcanic eruptions on global and regional total ozone after adjustment for the QBO, *Geophys. Res. Lett.*, *24*, 647–650, 1997a.

Baldwin, M. P., and T. J. Dunkerton, Propagation of the Arctic Oscillation from the stratosphere to the troposphere, *J. Geophys. Res.*, *104*, 30,937–30,946, 1999.

Baldwin, M. P., and D. O'Sullivan, Stratospheric effects of ENSO related tropospheric circulation anomalies, *J. Clim.*, *8*, 649 – 667, 1995.

Baldwin, M. P., et al., The quasi-biennial oscillation, *Rev. of Geophys.*, *39*, 179–229, 2001.

Bluth, G. J. S., S. D. Doiron, S. C. Schnetzler, A. J. Krueger, and L. S. Walter, Global tracking of the SO2 clouds from the june 1991 Mount Pinatubo eruptions, *Geophys.Res. Lett.*, *19*, 151–154, 1992.

Brasseur, G., and C. Granier, Mount Pinatubo aerosols, chlorofluorocarbons and ozone depletion, *Science*, *257*, 1239–1241, 1992.

Brasseur, G., and E. Roeckner, Impact of improved air quality on the future evolution of climate, *Geophys. Res. Lett.*, *32*, 2005.

Brezinski, C., Accélération de la convergence en analyse numérique, *Publications de l'Université des Sciences et Techniques de Lille*, 1973.

Bruhwiler, L., and K. Hamilton, A numerical simualtion of the stratospheric ozone quasi biennial oscillation using a comprehensive general circulation model, *J. Geophys. Res.*, *104*, 30,523–30,557, 1999.

Cagnazzo, C., E. Manzini, M. A. Giorgetta, and P. M. D. F. Forster, Impact of an improved radiation scheme in the MAECHAM5 general circulation model, *Atmos. Chem. Phys*, *7*, 2503–2515, 2007.

Calvo, N., R. R. Garcia, R. G. Herrera, D. G. Puyol, L. G. Presa, E. H. Martin, and P. R. Rodriguez, Analysis of the ENSO signal in tropospheric and stratospheric temperatures observed by MSU, 1979 - 2000., *J. Clim.*, *17*, 3934–3946, 2004.

Chandra, S., Changes in stratospheric ozone and temperature due to the eruption of Mt. Pinatubo, *Geophys. Res. Lett.*, *20*, 33–36, 1993.

Chen, P., and W. A. Robinson, Propagation of planetary waves between the trosposphere and stratosphere, *J. Atmos. Sc.*, *49*, 2533–2545, 1991.

Chen, W., H.-F. Graf, and M. Takahashi, Observed interannual oscillation of planetary wave forcing in the Northern Hemisphere winter, *Geophys. Res. Lett.*, *29*, 2002.

Chen, W., M. Takahashi, and H.-F. Graf, Interannual variations of stationary planetary wave activity in the northern winter troposphere and stratosphere and their relations to NAM and SST, *J. Geophys. Res.*, *108*, 4797, 2003.

Christiansen, B., Evidence of nonlinear climate change: Two stratospheric regimes and a regime shift, *J. Clim.*, *16*, 3681–3690, 2003.

Church, J. A., N. J. White, and J. M. Arblaster, Significant decadal-scale impact of volcanic eruptions on sea level and ocean heat content, *Nature*, *438*, 74–77, 2005.

Coakley, J. A. J., and P. Chylek, The two stream approximation in radiative transfer: Including the angle of the incident radiation, *J. Atmos Sci.*, *32*, 409–418, 1975.

Collimore, C. C., D. W. Martin, M. W. Hitchman, A. Huesmann, and D. E. Waliser, On the relationship between the QBO and tropical deep convection, *J. Clim.*, *16*, 2552–2569, 2003.

Collins, W. D., Parameterization of generalized cloud overlap for radiative calculations in general circulation models, *J. Atmos. Sc.*, *58*, 3224–3242, 2001.

Crutzen, P. J., The possible importance of CSO for the sulfate layer of the stratosphere, *Geophys. Res. Lett.*, *3*, 73–76, 1976.

Crutzen, P. J., Albedo enhancement by stratospheric sulfur injections: A contribution to resolve a policy dilemma?, *Climate Change*, *77*, 211–220, 2006.

Delworth, T. L., V. Ramaswamy, and G. L. Stenchikov, The impact of aerosols on simulated ocean temperature and heat content in the 20th century, *Geophys. Res, Lett.*, *32*, L24,709, 2005.

Dutton, E. G., and J. R. Christy, Solar radiative forcing at selected locations and evidence for global lower tropospheric cooling following the eruption of El Chichón and Pinatubo, *Geophys. Res. Lett.*, *19*, 2313–2316, 1992.

Eliassen, A., and E. Palm, On the transfer of energy in stationary mountain waves, *Geophys. Publ.*, *22-3*, 1–23, 1961.

Farquhar, G. D., and M. L. Roderick, Pinatubo, diffuse light and the carbon cycle, *Science*, *299*, 1997–1998, 2003.

Fortuin, J. P. F., and H. Kelder, An ozone climatology based on ozonesonde and satellite measurements, *J. Geophys. Res.*, *103*, 31,709–31,734, 1998.

Fouquart, Y., and B. Bonnel, Computations of solar heating of the earth's atmosphere: A new parameterization, *Contrib. Atmos. Phys.*, *53*, 35–62, 1980.

Gabriel, A., D. Peters, I. Kirchner, and H.-F. Graf, Effect of zonally asymmetric ozone on stratospheric temperature and planetary wave propagation, *Geophys. Res. Lett.*, *34*, 2007.

Garcia-Herrera, R., N. Calvo, R. R. Garcia, and M. A. Giorgetta, Propagation of ENSO temperature signals into the middle atmosphere: A comparison of two general circulation models and ERA-40 reanalysis data, *J. Geophys. Res.*, *111*, D06,101, 2006.

Garfinkel, C. I., and D. L. Hartmann, Effects of El Niño -Southern Oscillation and the Quasi-Biennial Oscillation on polar temperatures in the stratosphere, *J. Geophys. Res.*, *112*, 2007.

Geleyn, J.-F., and A. Hollingsworth, An economical analytical method for the computation of the interaction between scattering and line absorption of radiation, *Beitr. Phys. Atmos.*, *52*, 1–16, 1979.

Giorgetta, M., and L. Bengtsson, The potential role of the quasi-biennial oscillation in the stratosphere-troposphere exchange as found in water vapour in general circulation model experiments., *J. Geophys. Res.*, *104*, 6003–6019, 1999.

Giorgetta, M., E. Manzini, and E. Roeckner, Forcing of the quasi-biennial oscillation from a broad spectrum of atmospheric waves, *Geophys. Res. Lett.*, *29*, 86–90, 2002.

Giorgetta, M., E. Manzini, E. Roeckner, M. Esch, and L. Bengtsson, Climatology and forcing of the Quasi-Biennial Oscillation in the MAECHAM5 model, *J. Clim.*, *19*, 3882–3901, 2006.

Gleason, J. F., et al., Record low global ozone in 1992, *Science*, *260*, 523–525, 1993.

Gleckler, P. J., T. M. Wigley, B. D. Santer, J. M. Gregory, K. AchutaRao, and K. E. Taylor, Krakatoa's signature persists in the ocean, *Nature*, *439*, 675, 2006.

Graf, H.-F., Arctic radiation deficit and climate variability, *Clim. Dyn.*, *7*, 19–28, 1992.

Graf, H.-F., I. Kirchner, A. Robock, and I. Schultz, Pinatubo eruption winter climate effects: Model versus observations, *Clim. Dyn.*, *9*, 81–93, 1993.

Graf, H.-F., J. Perlwitz, and I. Kirchner, Northern Hemisphere tropospheric and mid-latitude circulation after violent volcanic eruptions, *Contrib. Atm. Phys.*, *67*, 3–13, 1994.

Graf, H.-F., Q. Li, and M. A. Giorgetta, Volcanic effects of climate: Revisiting the mechanisms, *Atmos. Chem. and Phys.*, *7*, 4503–4511, 2007.

Grainger, R. G., A. Lambert, F. W. Taylor, J. J. Remedios, C. D. Rogers, and M. Corney, Infrared absorption by volcanic stratospheric aerosols observed by ISAMS, *Geophys. Res. Lett.*, *20*, 1287–1290, 1993.

Grant, W. B., et al., Observations of reduced ozone concentrations in the tropical atmosphere after the eruption of Mount Pinatubo, *Geophys. Res. Lett.*, *19*, 1109–1112, 1992.

Grant, W. B., et al., Aerosol-associated changes in tropical stratospheric ozone following the eruption of Mt. Pinatubo, *J. Geophys. Res.*, *99*, 8197–8211, 1994.

Gray, W. M., Atlantic seasonal hurricane frequency: part i: El Niño and 30 mb quasi-biennial oscillation, *Mon. Wea. Rev.*, *112*, 1669–1683, 1984.

Gray, W. M., C. W. Landsea, P. W. Mielke, and K. J. Berry, Predicting atlantic seasonal hurricane activity 611 months in advance, *Wea. Forecasting*, *7*, 440,455, 1992.

Gregory, J. M., H. T. Banks, P. A. Scott, J. A. Lowe, and M. D. Palmer, Simulated and observed decadal variability in ocean heat content, *Geophys. Res. Lett.*, *31*, L15,312, 2004.

Gu, L., D. D. Baldocchi, S. C. Wofsy, J. W. Munger, J. J. Michalsky, S. P. Urbanski, and T. A. Boden1, Response of a deciduous forest to the Mount Pinatubo eruption: enhanced photosynthesis, *Science*, *299*, 2035–2038, 2003.

Halpert, M. S., and C. F. Ropelewski, Surface temperature patterns associated with the Southern Oscillation, *J. Clim.*, *5*, 577–593, 1992.

Hamilton, K., An examination of observed Southern Oscillation effects in the Northern Hemisphere stratosphere, *J. Atmos. Sci.*, *50*, 3468–3473, 1993.

Hamilton, K., Effects of an imposed quasi-biennial oscillation in a comprehensive trsoposphere-stratosphere-mesosphere general circulation model, *J. Atmos. Sc.*, *55*, 2393–2418, 1998.

Handler, P., Possible association between the climatic effects of stratospheric aerosols and sea surface temperatures in the eastern tropical Pacific Ocean, *J. Climatol.*, *6*, 31–41, 1986.

Hansen, J., A. Lacis, R. Ruedy, and M. Sato, Potential climate impact of Mt. Pinatubo eruption, *Geophys. Res, Lett.*, *19*, 215–218, 1992.

Hansen, J., R. Ruedy, M. Sato, and R. Reynolds, Global surface air temperature in 1995, return to pre-Pinatubo level, *Geophys. Res. Lett.*, *23*, 1665–1668, 1996.

Hervig, M. E., M. R. James, L. G. Larry, H. P. Jae, and S. R. Drayson, Observations of aerosol by the haloe experiment on board UARS: a preliminary validation, *Geophys. Res. Lett.*, *20*, 1291–1294, 1993.

Hirono, M., On the trigger of El Niño Southern Oscillation by the forcing of early El Chichón volcanic aerosols, *J. Geophys. Res.*, *93*, 5365–5384, 1988.

Hitoshi, M., and T. Hirooka, Predictability of stratospheric sudden warming: A case study for 1998/99 winter, *Mon. Wea. Rev.*, *132*, 1764–1766, 2004.

Holton, J. R., The role of gravity waves induced drag and diffusion on the momentum budget of the mesosphere, *J. Atmos. Sci.*, *40*, 2497 – 2507, 1982.

Holton, J. R., and H. C. Tan, The influence of the equatorial quasi-biennial oscillation on the global circulation at 50mb, *J. Atmos. Sci.*, *37*, 2200–2208, 1980.

Holton, J. R., and H. C. Tan, The quasi biennial oscillation in the Northern Hemisphere lower stratosphere, *J. Meteo. Soc. Japan*, *60*, 140–148, 1982.

Jones, G. S., J. M. Gregory, P. A. Stott, S. F. B. Tett, and R. B. Thorpe, An AOGCM simulation of the climate response to a volcanic super-eruption, *Clim. Dyn.*, *45*, 725–738, 2005.

Jones, P. D., and K. R. Briffa, Global surface air temperature variations during the twentieth century, *The Holocene*, *2*, 165–179, 1992.

Joseph, J. H., and W. J. Wiscombe, The delta-Eddington approximation for radiative transfer, *J. Atmos Sci.*, *33*, 2452–2459, 1976.

Kalnay, E., and coauthors, The NCEP/NCAR Reanalysis Project, *Bull. Amer. Met. Soc.*, *77*, 437–471, 1996.

Kinne, S., O. Toon, and M. Prather, Buffering of stratospheric circulation by changing amounts of tropical ozone: A Pinatubo case study, *Geophys. Res. Lett.*, *19*, 1927–1930, 1992.

Kirchner, I., and H.-F. Graf, Volcanoes and El Niño: Signal separation in Northern Hemisphere winter, *Clim. Dyn.*, *11*, 341–358, 1995.

Kirchner, I., G. L. Stenchikov, H.-F. Graf, A. Robock, and J. C. Antuna, Climate model simulation of winter warming and summer cooling following the 1991 Mount Pinatubo volcanic eruption, *J. Geophys. Res.*, *104*, 19,039–19,055, 1999.

Kodera, K., Influence of volcanic eruptions on the troposphere through stratospheric dynamical processes in the northern hemisphere winter, *J. Geophys. Res.*, *99*, 1273–1282, 1994.

Krueger, A. J., L. S. Walter, P. K. Bhartia, C. C. Schnetzler, N. A. Krotkov, I. Sprod, and G. J. S. Bluth, Volcanic sulfur dioxide measurements from the total ozone mapping spectrometer instruments, *J. Geophys. Res.*, *100*, 14,057–14,076, 1995.

Labitzke, K., Stratospheric-mesospheric midwinter disturbances: A summary of observed characteristics., *J. Geophys. Res.*, *86*, 9665–9678, 1981.

Labitzke, K., Sunspots, the QBO and the stratospheric temperature in the North Polar region, *Geophys. Res. Lett.*, *14*, 535–537, 1987.

Labitzke, K., Stratospheric temperature changes after the Pinatubo eruption, *J. Atmos. Terr. Phys.*, *56*, 1027–1034, 1994.

Labitzke, K., and H. V. Loon, Association between the 11-year solar cycle, the QBO, and the atmosphere, Part I, The troposphere and the stratosphere in the Northern Hemisphere in winter, *J. Atmos. Terr. Phys.*, *50*, 197–207, 1988.

Labitzke, K., and M. P. McCormick, Stratospheric temperature increases due to Pinatubo aerosols, *Geophys. Res. Lett.*, *19*, 207–210, 1992.

Labitzke, K., B. Naujokat, and M. P. McCormick, Temperature effects on the stratosphere of the April 4, 1982 eruption of El Chichón, Mexico, *Geophys. Res. Lett.*, *10*, 24–26, 1983.

Lambert, A., R. G. Grainger, C. D. Rogers, F. W. Taylor, L. L. Mergenthaler, J. B. Kumar, and S. T. Massie, Global evolution of the Mount Pinatubo volcanic aerosols observed by the infrared limb-sounding instruments CLAES and ISAMS on the Upper Atmosphere Research Satellite, *J. Geophys. Res.*, *102*, 1495–1512, 1997.

Limpsuvan, V., D. W. J. Thompson, and D. L. Hartmann, The life cycle of the Northern hemisphere sudden stratosphere warmings, *J. Clim.*, *17*, 2584–2596, 2004.

Liou, K. N., An introduction of atmospheric radiation, *2nd edition Academic Press*, p. 583pp, 2002.

Lohmann, U., B. Kaercher, and C. Timmreck, Impact of the Mount Pinatubo eruption on cirrus clouds formed by homogeneous freezing in the ECHAM4 GCM, *J. Geophys. Res.*, *108*, 2003.

Long, C. S., and L. L. Stowe, Using the NOAA/AVHRR to study stratospheric aerosol optical thicknesses following Mt. Pinatubo eruption, *Geophys. Res. Lett.*, *21*, 2215–2218, 1994.

Manzini, E., M. A. Giorgetta, M. Esch, L. Kornblueh, and E. Roeckner, The influence of sea surface temperatures on the northern winter stratosphere: Ensemble simulations with the MAECHAM5 model, *J. Clim.*, *19*, 3863–3881, 2006.

Mao, J., and A. Robock, Surface air temperature simulations by AMIP general circulation models: Volcanic and ENSO signals and systematic errors, *J. Clim.*, *11*, 1538–1552, 1998.

Mass, C. F., and D. A. Portman, Major volcanic eruptions and climate: A critical evaluation, *J. Clim.*, *2*, 566–593, 1989.

Matsuno, T., Vertical propagation of stationary planetary waves in the winter Northern Hemisphere, *J. Atmos. Sci.*, *27*, 871–883, 1970.

McCormick, M. P., and R. E. Veiga, SAGE II measurements of early Pinatubo aerosols, *Geophys. Res, Lett.*, *19*, 155–158, 1992.

McCormick, M. P., T. J. Swissler, W. P. Chu, W. H. Fuller, and M. T. Osborne, Post-volcanic aerosol decay as measured by lidar, *J. Atmos. Sc.*, *35*, 1296–1301, 1978.

McCormick, M. P., L. W. Thomason, and C. R. Trepte, Atmospheric effects of Mt. Pinatubo eruption, *Nature*, *373*, 399–404, 1995.

Menon, S., and V. K. Saxena, Role of sulfates in cloud-climate feedback mechanisms, *Atmos. Res.*, *47-48*, 299–315, 1998.

Menon, S., A. D. D. Genio, D. Koch, and G. Tselioudis, GCM simulations of the aerosol indirect effect: Sensitivity to cloud parameterization and aerosol burden, *J. Atmos. Sci.*, *59*, 692–713, 2002.

Miller, R. L., G. A. Schmidt, and D. Shindell, Forced annular variations in the 20th century Intergovernmental Panel on Climate Change Fourth Assessment Report models, *J. Geophys. Res.*, *111*, 2006.

Minnis, P., E. F. Harrison, L. L. Stowe, G. G. Gison, F. M.Denn, D. R. Doelling, and W. L. S. Jr., Radiative climate forcing by the Mount Pinatubo eruption, *Science*, *259*, 1411–1415, 1993.

Mlawer, E. J., S. Taubman, P. D. Brown, M. J. Iacono, and S. A. Clough, Radiative transfer for inhomogeneous atmospheres: RRTM, a validated correlated-k model for the longwave, *J. Geophys. Res.*, *102*, 16,663–16,682, 1997.

Morcrette, J. J., S. A. Clough, E. J. Mlawer, and M. J. Iacono, Impact of a validated radiative transfer scheme, RRTM on the ECMWF model climate and 10-day forecasts, *Technical Memorandum, ECMWF, Reading, UK*, *252*, 1998.

Newell, R. E., Stratospheric temperature change from the Mt. Agung volcanic eruption of 1963, *J. Atmos. Sc.*, *27*, 977–978, 1970.

Palmer, K. F., and D. Williams, Optical constants of sulfuric acid: Application to the clouds of venus, *Applied Optics*, *14*, 208–219, 1975.

Perlwitz, J., and H.-F. Graf, The statistical connection between tropospheric and stratospheric circulation of the northern hemisphere in winter, *J. Clim.*, *8*, 2281–2295, 1995.

Philander, S. G. H., El Niño, La Nina and the Southern Oscillation, *Academic Press, San Diego, CA*, p. 289pp, 1990.

Pitari, G., A numerical model for the possible perturbations of stratospheric dynamics due to Pinatubo aerosols: Implications for tracer transport, *J. Atmos. Sc.*, *50*, 2443–2461, 1993.

Ramachandran, S., V. Ramaswamy, G. L. Stenchikov, and A. Robock, Radiative impact of the Mount Pinatubo volcanic eruption: Lower stratospheric response, *J. Geophy. Res.*, *105*, 24,409–24,429, 2000.

Randel, W. J., F. Wu, J. M. R. III, J. W. Waters, and L. Froidevaux, Ozone and temperature changes in the stratosphere following the eruption of Mount Pinatubo, *J. Geophys. Res.*, *100*, 16,753–16,764, 1995.

Rind, D., N. K. Balachandran, and R. Suozzo, Climate change and the middle atmosphere. Part II, The impact of volcanic aerosols, *J. Clim.*, *5*, 189–208, 1992.

Robock, A., Review of year without summer? World climate in 1816, *Clim. Change*, *26*, 105–108, 1994.

Robock, A., Volcanic eruptions and their effect on climate, *Earth in Space*, *12*, 9–10, 2000.

Robock, A., Cooling following large volcanic eruptions corrected for the effect of diffuse radiation on tree rings, *Geophys. Res. Lett.*, *32*, 2005.

Robock, A., and M. P. Free, Ice cores as an index of global volcanism from 1850 to the present, *J. Geophys. Res.*, *100*, 11,549–11,567, 1995.

Robock, A., and J. Mao, Winter warming from large volcanic eruptions, *Geophys. Res. Lett.*, *19*, 2405–2408, 1992.

Robock, A., and J. Mao, The volcanic signal in surface temperature observations, *J. Clim.*, *8*, 1086–1103, 1995.

Roeckner, E., and co authors, The atmospheric general circulation model echam 5. part i: Model description, *MPI-Report*, *349*, 2003.

Roeckner, E., et al., The atmospheric general circulation model ECHAM5 - Part i, *MPI Report*, *Report No. 349*, 126, 2003.

Rosenfield, J., D. Considine, P. Meade, J. Bacmeister, C. Jackman, and M. Schoeberl, Stratospheric effects of Mount Pinatubo aerosol studied with a coupled two dimensional model, *J. Geophys. Res.*, *102*, 3649–3670, 1997.

Rozanov, E., M. Schlesinger, F. Yang, S. Malyshev, N. Andronova, V. Zubov, and T. Egorova, Study of the effects of the Pinatubo volcanic eruption using the UIUC stratosphere/troposphere GCM with interactive photochemistry, *J. Geophys. Res.*, *107*, 2002.

Sarmiento, J. L., Atmospheric CO2 stalled, *Nature*, *365*, 697–698, 1993.

Sassi, F., D. Kinnison, B. A. Boville, R. R. Garcia, and R. Roble, Effect of El Niño-Southern Oscillation on the dynamical, thermal and chemical structure of the middle atmosphere, *J. Geophys. Res.*, *109*, D17,108, 2004.

Sato, M., J. Hansen, M. McCormick, and J. Pollack, Stratospheric aerosol optical depths, 1850-1990, *J. Geophys. Res*, *98*, 22,987–22,994, 1993.

Schatten, K. H., H. G. Mayr, I. Harris, and H. A. Taylor, A zonally symmetric model for volcanic influence upon atmospheric circulation, *Geophys. Res. Lett.*, *11*, 303–306, 1984.

Schoeberl, M. R., P. K. Bhartia, and E. Hilsenrath, Tropical ozone loss following the eruption of Mt. Pinatubo, *Geophys. Res. Lett.*, *20*, 29–32, 1993.

Self, S., The effects and consequences of very large explosive volcanic eruptions, *Phil. Trans. R. Soc. A.*, pp. 2073–2097, 2006.

Self, S., M. R. Rampino, J. Zhao, and M. G. Katz, Volcanic aerosol perturbations and strong El Niño events: No general correlation, *Geophys. Res. Lett.*, *24*, 1247–1250, 1997.

Shettle, E. P., and J. A. Weinman, The transfer of solar irradiance through inhomogeneous turbid atmospheres evaluated by Eddington's approximation, *J.Atmos. Sci.*, *27*, 1048–1055, 1970.

Soden, B. J., R. T. Wetherald, G. L. Stenchikov, and A. Robock, Global cooling after the eruption of Mount Pinatubo: A test of climate feedback by water vapor, *Science*, *296*, 727–730, 2002.

Solomon, S., Stratospheric ozone depletion: A review of concepts and history, *Rev. Geophys.*, *37*, 257–316, 1999.

Stenchikov, G., I. Kirchner, A. Robock, H.-F. Graf, J. C. Antuna, R. G. Grainger, A. Lambert, and L. Thomason, Radiative forcing from the 1991 Mount Pinatubo volcanic eruption, *J. Geophys. Res.*, *103*, 13,837–13,857, 1998.

Stenchikov, G., A. Robock, V. Ramaswamy, M. D. Schwartzkopf, K. Hamilton, and S. Ramachandran, Arctic Oscillation response to the 1991 Mount Pinatubo eruption: Effects of volcanic aerosols and ozone depletion, *J. Geophys. Res.*, *107*, 1–16, 2002.

Stenchikov, G., K. Hamilton, A. Robock, V. Ramaswamy, and M. D. Schwartzkopf, Arctic Oscillation response to the 1991 Pinatubo eruption in the SKYHI general circulation model with a realistic quasi-biennial oscillation, *J. Geophys. Res.*, *109*, D03,112, 2004.

Stenchikov, G., K. Hamilton, R. J. Stouffer, A. Robock, V. Ramaswamy, B. Santer, and H.-F. Graf, Arctic Oscillation response to volcanic eruptions in the IPCC AR4 climate models, *J. Geophys. Res.*, *111*, 2006.

Stommel, H., and E. Stommel, Volcano Weather - The story of 1816, the Year Without Summer, *Seven Seas Press, Newport, R. I*, p. 177, 1983.

Stowe, L. L., R. M. Carey, and P. P. Pellegrino, Monitoring the Mount Pinatubo aerosol layer with NOAA-11 AVHRR data, *Geophys. Res. Lett.*, *19*, 159–162, 1992.

Strong, A. E., Monitoring El Chichón aerosol distribution using NOAA-7 satellite AVHRR sea surface temperature observations, *Geofis. Int.*, *23*, 129–141, 1984.

Strong, A. E., The effect of El Chichón on the 82/83 El Niño, *EOS Trans. AGU*, *67(44)*, 1986.

Tanre, D., J.-F. Geleyn, and J. M. Slingo, First results of the introduction of an advanced aerosol-radiation interaction in the ECMWF low resolution global model, *In Aerosols and Their Climatic Effects*, pp. 133–177, 1984.

Textor, C., H.-F. Graf, M. Herzog, and J. M. Oberhuber, Injection of gases into the stratosphere by explosive volcanic eruptions, *J. Geophys. Res.*, *108*, 2003.

Thompson, D. W. J., and J. M. Wallace, The Arctic Oscillation signature in the wintertime geopotential height and temperature fields, *Geophys. Res. Lett.*, *25*, 1297–1300, 1998.

Tie, X., and G. Brasseur, The response of the stratospheric ozone to volcanic eruptions: Sensitivity to atmospheric chlorine loading, *Geophys. Res. Lett.*, *22*, 3035–3038, 1995.

Tie, X., G. Brasseur, C. Granier, A. D. Rudder, and N. Larsen, Model study of polar stratospheric clouds and their effect on stratospheric ozone - Model results, *J. Geophys. Res.*, *101*, 12,575–12,584, 1996.

Timmreck, C., and H.-F. Graf, The initial dispersal and radiative forcing of a Northern Hemisphere mid-latitude super volcano: a model study, *Atmos. Chem. and Phys.*, *6*, 35–49, 2006.

Timmreck, C., H.-F. Graf, and I. Kirchner, A one and a half year interactive MAECHAM4 simulation of Mount Pinatubo aerosol, *J. Geophys. Res.*, *104*, 9337–9359, 1999.

Timmreck, C., H.-F. Graf, and B. Steil, Aerosol chemistry interactions after the Mt. Pinatubo eruption, *Volcanism and the Earth's Atmosphere, AGU Monograph*, *139*, 213–225, 2003.

Trenberth, K. E., D. P. Stephaniak, and S. Worley, Evolution of El Niño-Southern Oscillation and global atmospheric surface temperatures, *J. Geophys. Res.*, *107*, 2002.

Trepte, C. R., and M. H. Hitchman, Tropical stratospheric circulation deduced from satellite aerosol data, *Nature*, *355*, 626–628, 1992.

Trepte, C. R., R. E. Veiga, and M. P. McCormick, The poleward dispersal of Mount Pinatubo volcanic aerosol, *J. Geophys. Res.*, *98*, 18,5563–18,573, 1993.

Uppala, S., et al., The ERA-40 re-analysis, *Quart. J. Roy. Meteor. Soc.*, *131*, 2961–3012, 2005.

Wiscombe, W., Improved Mie scattering algorithms, *Appl. Opt.*, *19*, 1505–1509, 1980.

Yang, F., and M. E. Schlesinger, Identification and separation of Mount Pinatubo and El Niño - Southern Oscillation land surface temperature anomalies, *J. Geophys. Res.*, *106*, 14,757–14,770, 2001.

Yang, F., and M. E. Schlesinger, On the surface and atmospheric temperature changes following the 1991 Pinatubo volcanic eruption: A GCM study, *J. Geophys. Res.*, *107*, No. D8 4073, 2002.

Yue, G. K., M. P. M. Cormick, and E. W. Chiou, Stratospheric aerosol optical depth observed by the Stratospheric Aerosol Gas Experiment ii: Decay of El Chichón and Ruiz volcanic perturbations, *J. Geophys. Res.*, *96*, 5209–5219, 1991.

Zielinski, G. A., Use of paleo-records in determining varaibility within the volcanism-climate system, *Quart. Sci. Rev.*, *19*, 417–438, 2000.

# Acknowledgements

I would like to express my gratitude to my supervisor, Dr. Claudia Timmreck for her supervision, guidance and advice from the very early stages of this work. She provided me unflinching encouragement and support in various ways. I am also very grateful to my supervisors Prof. Hans-F. Graf and Dr. Marco Giorgetta for the scientific discussions and crucial contribution that became the backbone of this thesis. Their timely and valuable guidance helped a lot in the completion of this thesis. I am thankful for using their precious time to read this thesis and for the critical comments about it.

I greatly appreciate the supervision of my advisory panel chair, Prof. Guy Brasseur for his strong interest in my work and for reviewing my work at several stages of my PhD term.

I would also like to thank Prof. Gera Stenchikov for his useful discussions and providing me with the necessary datasets for my study.

Many many thanks to Ulrich Schlese, Sebastian Rast and Monika Esch who helped me understand the technical details of the model.

I am glad to be enrolled in the International Max Planck Research School on Earth System Modelling and it was a great experience to meet with students from different backgrounds and to know about their field of research. I am also grateful to the executive committee members of the IMPRS-ESM for their support. I am also thankful to all those who supported me, especially, Dr. Antje Weitz, Ms. Cornelia Kampmann, Ms. Elke Lord and Ms. Hanna Stadelhofer.

I would like to thank all my colleagues Qian Li, Angelika Heil, Rene Hommel, Elina Marmer, Xuefeng Cui, Kristof Sturm, Semeena, Melissa Pfeffer, Heinz Juergen Punge, Hui Wan, Abhay Devasthale, Martin Keller, Swati Gehlot and this list goes on.. for their help during my stay here. It was wonderful to know you all.

Last but not the least, I would like to thank my father and my sisters for their love, confidence and support all these years. And thanks to my friends, Chirag and Pragya, Sunil and Himanshu who made me feel at home here.

**Publikationsreihe des MPI-M**
**„Berichte zur Erdsystemforschung“ , „*Reports on Earth System Science*“, ISSN 1614-1199**
**Sie enthält wissenschaftliche und technische Beiträge, inklusive Dissertationen.**

| | |
|---|---|
| **Berichte zur Erdsystemforschung Nr.1** Juli 2004 | **Simulation of Low-Frequency Climate Variability in the North Atlantic Ocean and the Arctic** Helmuth Haak |
| **Berichte zur Erdsystemforschung Nr.2** Juli 2004 | **Satellitenfernerkundung des Emissionsvermögens von Landoberflächen im Mikrowellenbereich** Claudia Wunram |
| **Berichte zur Erdsystemforschung Nr.3** Juli 2004 | **A Multi-Actor Dynamic Integrated Assessment Model (MADIAM)** Michael Weber |
| **Berichte zur Erdsystemforschung Nr.4** November 2004 | **The Impact of International Greenhouse Gas Emissions Reduction on Indonesia** Armi Susandi |
| **Berichte zur Erdsystemforschung Nr.5** Januar 2005 | **Proceedings of the first HyCARE meeting, Hamburg, 16-17 December 2004** Edited by Martin G. Schultz |
| **Berichte zur Erdsystemforschung Nr.6** Januar 2005 | **Mechanisms and Predictability of North Atlantic - European Climate** Holger Pohlmann |
| **Berichte zur Erdsystemforschung Nr.7** November 2004 | **Interannual and Decadal Variability in the Air-Sea Exchange of CO2 - a Model Study** Patrick Wetzel |
| **Berichte zur Erdsystemforschung Nr.8** Dezember 2004 | **Interannual Climate Variability in the Tropical Indian Ocean: A Study with a Hierarchy of Coupled General Circulation Models** Astrid Baquero Bernal |
| **Berichte zur Erdsystemforschung Nr9** Februar 2005 | **Towards the Assessment of the Aerosol Radiative Effects, A Global Modelling Approach** Philip Stier |
| **Berichte zur Erdsystemforschung Nr.10** März 2005 | **Validation of the hydrological cycle of ERA40** Stefan Hagemann, Klaus Arpe and Lennart Bengtsson |
| **Berichte zur Erdsystemforschung Nr.11** Februar 2005 | **Tropical Pacific/Atlantic Climate Variability and the Subtropical-Tropical Cells** Katja Lohmann |
| **Berichte zur Erdsystemforschung Nr.12** Juli 2005 | **Sea Ice Export through Fram Strait: Variability and Interactions with Climate**- Torben Königk |
| **Berichte zur Erdsystemforschung Nr.13** August 2005 | **Global oceanic heat and fresh water forcing datasets based on ERA-40 and ERA-15** Frank Röske |
| **Berichte zur Erdsystemforschung Nr.14** August 2005 | **The** HAM**burg** O**cean** C**arbon** C**ycle Model HAMOCC5.1 - Technical Description Release 1.1** Ernst Maier-Reimer, Iris Kriest, Joachim Segschneider, Patrick Wetzel |
| **Berichte zur Erdsystemforschung Nr.15** Juli 2005 | **Long-range Atmospheric Transport and Total Environmental Fate of Persistent Organic Pollutants - A Study using a General Circulation Model** Semeena Valiyaveetil Shamsudheen |

**Publikationsreihe des MPI-M**
**„Berichte zur Erdsystemforschung“ , „*Reports on Earth System Science*“, ISSN 1614-1199**
**Sie enthält wissenschaftliche und technische Beiträge, inklusive Dissertationen.**

**Publikationsreihe des MPI-M**
**„Berichte zur Erdsystemforschung“ , „*Reports on Earth System Science*“, ISSN 1614-1199**
**Sie enthält wissenschaftliche und technische Beiträge, inklusive Dissertationen.**

| | |
|---|---|
| **Berichte zur Erdsystemforschung Nr.30** November 2006 | **Long-term interactions between ice sheets and climate under anthropogenic greenhouse forcing Simulations with two complex Earth System Models** Miren Vizcaino |
| **Berichte zur Erdsystemforschung Nr.31** November 2006 | **Effect of Daily Surface Flux Anomalies on the Time-Mean Oceanic Circulation** Balan Sarojini Beena |
| **Berichte zur Erdsystemforschung Nr.32** November 2006 | **Managing the Transition to Hydrogen and Fuel Cell Vehicles – Insights from Agent-based and Evolutionary Models –** Malte Schwoon |
| **Berichte zur Erdsystemforschung Nr.33** November 2006 | **Modeling the economic impacts of changes in thermohaline circulation with an emphasis on the Barents Sea fisheries** Peter Michael Link |
| **Berichte zur Erdsystemforschung Nr.34** November 2006 | **Indirect Aerosol Effects Observed from Space** Olaf Krüger |
| **Berichte zur Erdsystemforschung Nr.35** Dezember 2006 | **Climatological analysis of planetary wave propagation in Northern Hemisphere winter** Qian Li |
| **Berichte zur Erdsystemforschung Nr.36** Dezember 2006 | **Ocean Tides and the Earth’s Rotation - Results of a High-Resolving Ocean Model forced by the Lunisolar Tidal Potential** Philipp Weis |
| **Berichte zur Erdsystemforschung Nr.37** Dezember 2006 | **Modelling the Global Dynamics of Rain-fed and Irrigated Croplands** Maik Heistermann |
| **Berichte zur Erdsystemforschung Nr.38** Dezember 2006 | **Monitoring and detecting changes in the meridional overturning circulation at 26°N in the Atlantic Ocean- The simulation of an observing array in numerical models** Johanna Baehr |
| **Berichte zur Erdsystemforschung Nr.39** Februar 2007 | **Low Frequency Variability of the Meridional Overturning Circulation** Xiuhua Zhu |
| **Berichte zur Erdsystemforschung Nr.40** März 2007 | **Aggregated Carbon Cycle, Atmospheric Chemistry, and Climate Model (ACC2) – Description of the forward and inverse modes –** Katsumasa Tanaka, Elmar Kriegler |
| **Berichte zur Erdsystemforschung Nr.41** März 2007 | **Climate Change and Global Land-Use Patterns — Quantifying the Human Impact on the Terrestrial Biosphere** Christoph Müller |
| **Berichte zur Erdsystemforschung Nr.42** April 2007 | **A Subgrid Glacier Parameterisation for Use in Regional Climate Modelling** Sven Kotlarski |

**Publikationsreihe des MPI-M**
**„Berichte zur Erdsystemforschung“ , „*Reports on Earth System Science*“, ISSN 1614-1199**
**Sie enthält wissenschaftliche und technische Beiträge, inklusive Dissertationen.**



ISSN 1614-1199